Phase Relations, Structural Studies and Physical Properties of Mixed Metal Oxides and Sulphides

Iwona Szkoda

A Thesis Submitted for the Degree
of
Doctor of Philosophy

Heriot-Watt University
Department of Chemistry
October 2008

Abstract

The phase relations in three oxide systems; ZnO–$BiVO_4$, $Pb_2V_2O_7$–$BiVO_4$ and PbO–$BiVO_4$, have been studied and their phase diagrams over the whole component concentration range up to 1273 K have been established. As a result of solid-state reaction between ZnO and $BiVO_4$ mixed at a molar ratio of 2:1 or among ZnO, V_2O_5 and Bi_2O_3, mixed at a molar ratio of 4:1:1, a new double vanadate $BiZn_2VO_6$ has been obtained. Its crystallographic system was determined, its unit cell parameters were calculated and its incongruent melting temperature was established. A new compound is also formed in the $Pb_2V_2O_7$–$BiVO_4$ system. It has been shown that $BiVO_4$ and $Pb_2V_2O_7$ react with each other forming a compound of the formula $Pb_2BiV_3O_{11}$, when their molar ratio is equal to 1:1, or between PbO, Bi_2O_3 and V_2O_5, mixed at a molar ratio of 4:1:3. This material melts congruently and it crystallises in the triclinic system.

A new series of non-stoichiometric sulphides $Ga_{1-x}Ge_xV_4S_8$ ($0 \leq x \leq 1$) has been synthesised by standard solid-state reaction. The samples have been characterised by powder X-ray and neutron diffraction, SQUID magnetometry and electrical transport-property measurements. Structural analysis reveals that a solid solution is formed throughout this composition range. Magnetic measurements suggest that the ferromagnetic behaviour of the end-member phase GaV_4S_8 is retained at $x \leq 0.7$. By contrast $Ga_{0.25}Ge_{0.75}V_4S_8$ appears to undergo antiferromagnetic ordering at *ca.* 15 K. All materials with $x \neq 1$ are *n*-type semiconductors whose resistivity falls by almost six orders of magnitude with decreasing gallium content, whilst the end-member phase GeV_4S_8 is a *p*-type semiconductor. Powder neutron diffraction studies show that the cubic unit cell is retained for non-stoichiometric materials to the lowest temperatures studied.

Single crystals of five erbium-chromium sulphides have been grown by chemical vapour transport using iodine as the transporting agent. Single-crystal X-ray diffraction reveals that in Er_3CrS_6, octahedral sites are occupied exclusively by Cr^{3+} cations, leading to one-dimensional CrS_4^{5-} chains of edge-sharing octahedra, whilst in Er_2CrS_4, Er^{3+} and Cr^{2+} cations occupy the available octahedral sites in an ordered manner. By contrast, in $Er_6Cr_2S_{11}$, Er_4CrS_7 and $Er_8Cr_3S_{15}$, Er^{3+} and Cr^{2+} ions are disordered over the octahedral sites. In Er_2CrS_4, $Er_6Cr_2S_{11}$, Er_4CrS_7 and $Er_8Cr_3S_{15}$, the network of octahedra generates an anionic framework constructed from M_2S_5 slabs of varying thickness, linked by one-dimensional octahedral chains. This suggests that these four phases belong to a series in which the anionic framework may be described by the general formula $[M_{2n+1}S_{4n+3}]^{x-}$, with charge balancing provided by Er^{3+} cations located in sites of high-coordination number within one-dimensional channels defined by the framework. Er_4CrS_7, $Er_6Cr_2S_{11}$, $Er_8Cr_3S_{15}$

and Er_2CrS_4 may thus be considered as the n = 1, 2, 3 and ∞ members of this series. Whilst Er_4CrS_7 is paramagnetic, successive magnetic transitions associated with ordering of the chromium and erbium sub-lattices are observed on cooling Er_3CrS_6 (T_C(Cr) = 30 K; T_C(Er) = 11 K) and Er_2CrS_4 (T_N(Cr) = 42 K, T_N(Er) = 10 K) whereas $Er_6Cr_2S_{11}$ exhibits ordering of the chromium sub-lattice only (T_N = 11.4 K). These four materials have been studied using neutron diffraction which allowed magnetic ordering to be examined.

For Panagiotis

Acknowledgments

First of all, I would like to thank my supervisor, Professor Anthony V. Powell for his help, patience and support ensured the success in completing the thesis.

I am also grateful to the late Professor Maria Kurzawa and ever-present Dr. Monika Bosacka from the Szczecin University of Technology, Poland for the supervision in oxide chemistry and their friendly attitude.

I wish to acknowledge the kind help of Dr. Paz Vaqueiro and her valuable suggestions.

Dr. Ron Smith and Dr. Steve Hull of the ISIS facility for their help with collection of POLARIS and OSIRIS data.

Dr. Clemens Ritter from ILL for his assistance and advice about D1A and D2B diffractometers.

Thanks to Dr. Javier Sanchez Benitez from Edinburgh University for his help with SQUID measurements and Dr. Rodolfo Sánchez of the Centro Atómico Bariloche, Argentina for magnetic measurements.

I appreciate immensely the friendship and support of the materials group from Heriot Watt University and people from the Department of Inorganic and Analytical Chemistry, Szczecin University of Technology, Poland.

My parents, my brother and his wife who tried to understand what I do and helped everyway they could.

Finally many thanks to my dearest husband who has always been there to encourage me and listen to me.

Table of contents

Appendices and CIF files may be found on the CD attached to the inside back cover.

Appendix 1: Additional data and results relating to Chapter 4: Ordered Defect Thiospinels.

Appendix 2: Additional data and results relating to Chapter 5: Ternary Erbium Chromium Sulphides.

List of Figures

List of Tables

Chapter 1: Introduction

1.1 Background

In recent years there has been an increasing demand for new magnetic materials, semiconductors, catalysts and environmentally friendly pigments which could be used on an industrial scale [1, 2]. This is the reason why a significant research effort has been directed towards finding new materials with attractive properties. For example phases which are formed in the MO – Bi_2O_3 – V_2O_5 system (where M is a divalent cation) are believed to be able to eliminate more expensive and less stable organic pigments [3]. Magnetic materials are also important as they are all around us. Their range of applications is very broad as they play important roles in recording tapes and disks for audio, video, and computer signals [4]. Furthermore, magnetic materials are used in motors, antennae, and speakers. Recent developments in strong magnets enable communication equipment and computers to be miniaturised. Chalcogenides are a group of materials which exhibit interesting magnetic, electric and structural properties [5, 6] and because of the dramatic advances in semiconductors and magnetic materials they have been of great interest.

In this introduction the most important concepts behind this work will be explained and also a brief overview of some of the research undertaken in the selected fields will be given.

1.2 Physical Properties of Materials

In materials science the terms solid, liquid and gaseous are used to describe states of matter. Materials can be also classified in terms of their electronic and magnetic properties. For the former four broad categories can be identified:

- metals;
- insulators;
- semiconductors;
- superconductors.

Taking into account magnetic properties of materials, they can be classified into the following five principle groups:

- diamagnetic;
- paramagnetic;
- antiferromagnetic;
- ferromagnetic;
- ferrimagnetic.

1.2.1 Electron-Transport Properties

Many of the characteristic properties of materials, such as electrical conductivity, optical and magnetic properties, depend directly on the behaviour of the electrons present. The electrical conductivity of a material, σ, is based on the transport of electrons. It is dependent on the number of charge carriers, n, their mobility, μ, and the charge on the carrier, ε [7]:

$$\sigma = n\varepsilon\mu \tag{1}$$

The number of carriers and their mobility may depend on temperature. In metals the number of mobile electrons is high and their mobility decreases with temperature due to electron-phonon collisions [7]. It means, according to the equation 1, that the conductivity of metals decreases with increasing temperature. Different behaviour is observed in semiconductors. They might conduct at high temperatures but their conductivity declines with decreasing temperature (Figure 1). However, they may still conduct at low temperatures. The number of mobile electrons in semiconductors can be increased either by increasing temperature (intrinsic semiconductors) or by doping semiconducting materials with impurities (extrinsic semiconductors) [7]. Conductivity in insulators is also sensitive to both temperature and donors but is very small. The electrical conductivity of the best insulators is *ca.* 10^{-22} ohm^{-1} cm^{-1} and around 10^{10} ohm^{-1} cm^{-1} for pure metals [8].

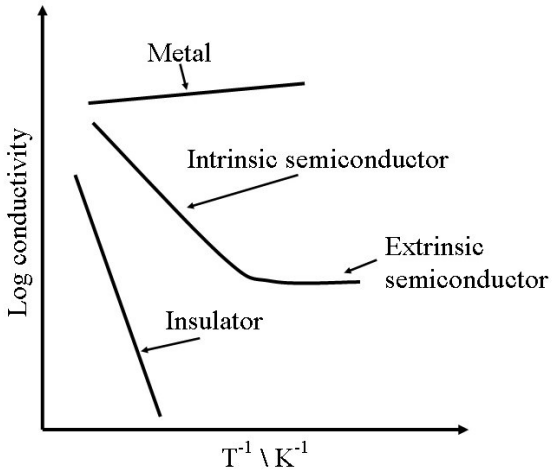

Figure 1: Log conductivity as a function of temperature of metals, semiconductors and insulators [7].

1.2.1.1 Metals

Metals are materials that are good conductors of heat and electricity. The high electrical and thermal conductivity of metals can be understood in terms of the free electron theory of Sommerfeld and the band theory of solids. According to Sommerfeld [9] a metal can be described as a potential well, inside which the loosely held valence electrons are able to move. The energy levels are filled with two electrons per level from the bottom of the well. The highest occupied level at 0 K is called the Fermi level (Figure 2) with a corresponding energy, E_F, called Fermi energy. The energy required to remove the uppermost electrons from the potential well is called the work function, Φ.

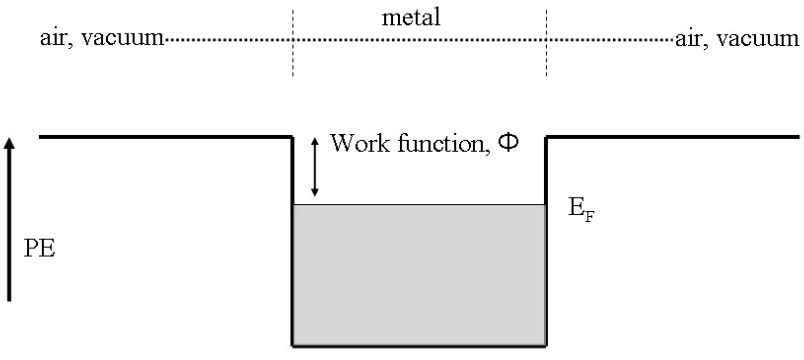

Figure 2: Free electron theory of a metal; electrons in a potential well [7].

The free electron model also allows the density of states, DOS, which is the number of states, *N(E)*, available for electrons per unit volume per unit energy range, within the conduction band to be calculated (Figure 3). *N(E)* depends on the nature and degree of overlap of the orbitals forming the particular energy band. A high value of DOS at a specific energy means that there are many states which could be occupied. When there are no states available for occupation the DOS is zero. Figure 3 shows that at 0 K the levels below E_F are completely filled, and those above E_F are completely empty showing the discontinuity at the Fermi energy.

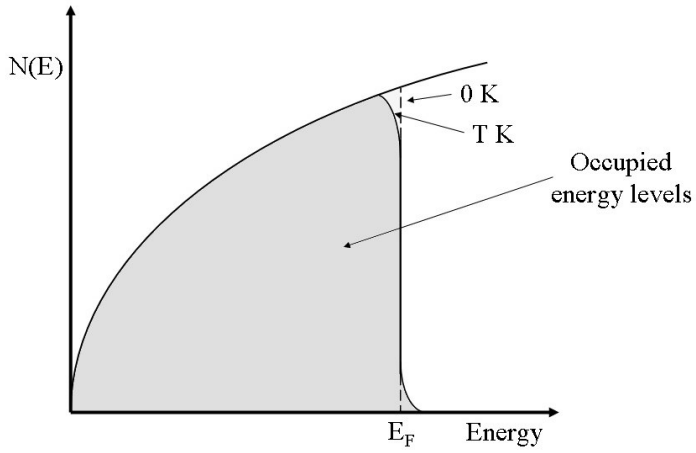

Figure 3: Density of states on the free electron theory [7].

In metals, at temperatures above 0 K, some levels above Fermi energy are occupied and some below are vacant. It is because at higher temperatures some electrons have sufficient thermal energy to be promoted to the empty levels above the E_F. The high electrical conductivity of metals is due to the drift of the electrons that are half occupied states close to E_F. Electrons in singly occupied levels are free to move whilst those in doubly occupied states lower down in the valence band cannot undergo any net migration in a particular direction. Therefore, the promotion of an electron from a full level below E_F to an empty one above E_F gives rise to two mobile electrons.

The free electron theory is useful but is oversimplified. In other theories the potential well is regarded as periodic (Figure 4) and not constant as described in Sommerfeld's theory. The potential energy of the electrons passes through a minimum due to Coulombic attractions at the positions of the positively charged nuclei which are arranged in a regularly repeating manner, and passes through a maximum midway

between adjacent nuclei. An uninterrupted continuum of energy levels does not occur and only certain bands or ranges of energies are permitted for the electrons.

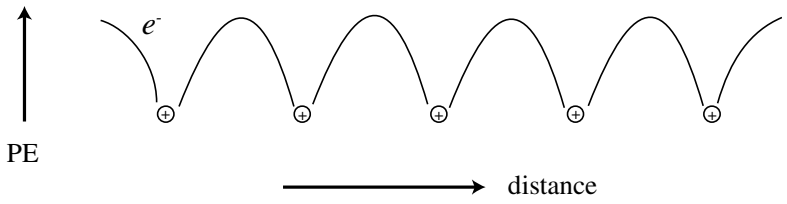

Figure 4: Potential energy of electrons as a function of distance through a solid [7].

In metals, the highest occupied band (valence band) is only part full and in some metals overlaps with a conduction band, as shown in Figure 5.

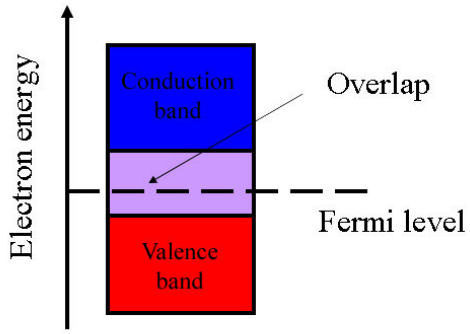

Figure 5: Overlapping band structure of metals.

1.2.1.2 Semiconductors and Insulators

In semiconductors and insulators between the valence band and the conduction band there is a forbidden band gap (Figure 6). The difference between semiconductors and insulators is only the magnitude of the forbidden gap between the valence and the conduction bands. The electrical and optical properties of a non-metallic material depend on the magnitude of this gap. The band gap, E_g, can be express as [10]:

$$E - E_F = E_g / 2 \tag{2}$$

Where E is the energy at the bottom of the conduction band. E-E_F is usually much larger than kT, unless the band gap is very small. For the known value of E_g the number of mobile electrons can be calculated from the following equation [10]:

$$n \propto \exp(-E_g / 2kT) \tag{3}$$

The band gap is larger in insulators (at least several electron-volts wide) and fewer electrons can be found in their conduction band. An ideal insulator has atoms with tightly bonded valence electrons and there are few electrons which can be promoted to the conduction band. Diamond is an example of an excellent insulator with a band gap of *ca.* 6 eV [7, 11]. The band gap in semiconductors is typically in the range of 0.5 to 3.0 eV [7] and electrons can be promoted from the valence to the conduction band. Electrons can be excited to the conduction band due to thermal energy. It means that the conductivity of semiconductors strongly depends on the temperature. In semiconductors, the presence of a small percentage of a doping material can increase conductivity dramatically.

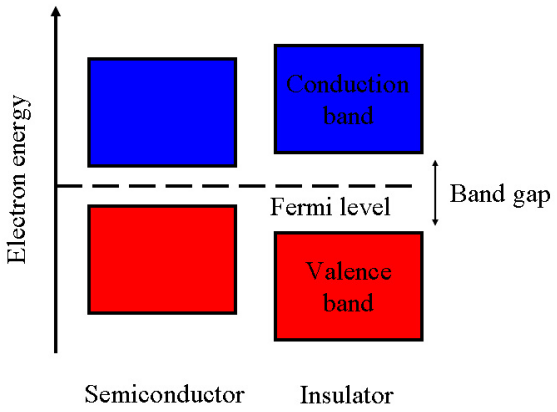

Figure 6: Energy band structure of semiconductors and insulators.

A semiconductor can be doped either with donors or with acceptors. Materials created in this way are called *n*-type and *p*-type semiconductors, respectively. In the first case, by introducing foreign elements into the crystal lattice of the semiconducting material, new energy states within the band gap close to the conduction band are introduced as well and a small amount of energy is required to promote the dopant's electrons to the conduction band. In case of *p*-type semiconductors the new acceptor states in the band

gap close to the valence band are introduced. Electrons from the valence band can move to these new levels leaving behind positively charged holes which conduct through the valence band. By doping semiconducting materials and creating defect states in the band gap it is possible to create devices such as solar cells, diodes, transistors and others [12].

However, there exist many compounds where the predictions of the simple form of band theory appear to break down. This group of materials is called Mott insulators. According to the band theory they are expected to conduct electricity but in fact they turn out to be insulating due to electron-electron interactions which are not taken into account in the conventional band theory. For example, many materials of transition metals and lanthanides have partially filled *d* or *f* orbitals but their electrons are localised and they are not metallic as would be predicted from the simple band theory. The Hubbard model is helpful to understand electron localisation of these materials. There are two basic mechanisms that might cause electron localisation: correlations among the electrons and disorder present in the material. A metal-insulator transition might occur even in samples without disorder, due to electron-electron interactions [13]. It has been proposed [14] that disorder resulting in strong spatial fluctuations in the electrostatic potential caused due to impurities, can drive a metal-insulator transition in a system of non-interacting electrons. Phase transformations can be driven by changing any of the thermodynamic parameters, for instance electron density, temperature or pressure. It is very difficult to achieve the continuous metal-insulator transition and it can take place only at zero temperature. It is because an insulator can carry a small current at non-zero temperatures due to thermal excitation. At non-zero temperatures two cases are possible (Figure 7) [15]:

- there is a line of first-order metal-insulator transitions terminating in the critical point at $T = 0$ (solid line);
- there is a continuous crossover (shaded region) from metallic (resistivity decreases with decreasing temperature) to insulating (resistivity increases) behaviour.

Metal-insulator transitions are observed in many oxide systems. For example, samples of Ti_2O_3, V_2O_3, VO and VO_2 show a temperature-induced transition at the Néel temperature [16]. A large number of studies of the metal-insulator transition have been carried out on oxide systems; by changes of stoichiometry, application of pressure,

and/or substitutions of aliovalent cations. NiO exhibits a pressure-induced transition [8] and samples from the systems $La_{1-x}A_xMO_3$ (A = Ca or Sr and M = V, Mn or Co) and $LaNi_{1-x}M_xO_3$ (M = Mn or Fe) show compositionally-induced metal-insulator transition [8]. There are also a number of sulphides which exhibit metal-insulator transitions. For instance, thiospinel $CuIr_2S_4$ shows a temperature-induced transition from metallic to insulating on cooling with a transition temperature of 230 K [17]. Furthermore, in $Cu(Ir_{1-x}Rh_x)_2S_4$, by doping $CuIr_2S_4$ with Rh, not only is a metal-insulator transition observed but superconductivity as well [17]. The metal-insulator transition has also been observed in other sulphide systems, for instance in $BaCo_{1-x}Ni_xS_{2-y}$ [18].

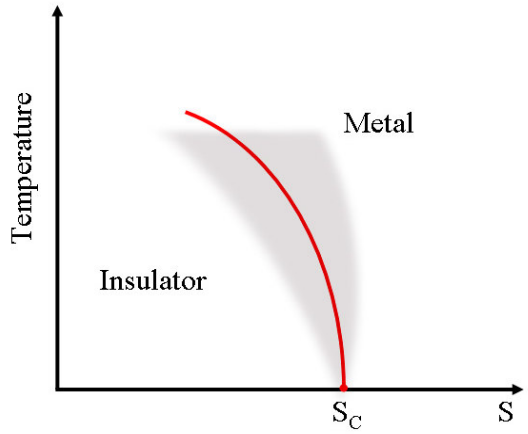

Figure 7: Phase diagram for a metal-insulator transition at the quantum critical point. At $T = 0$, the behaviour is metallic for critical parameter $S > S_C$ and insulating for $S < S_C$. The solid line indicates a line of first-order transitions and the shading shows the crossover region. The abscissa is the control parameter [15].

1.2.1.3 Superconductors

Superconductivity is one of the most challenging problems in solid-state physics. Superconductivity occurs in certain materials at very low temperatures and is characterised by zero electrical resistance to the flow of electrical current. Moreover, these materials expel a magnetic field, provided the field is below the critical field strength, H_c, and show "perfect diamagnetism" (Meissner effect). For superconducting materials the magnetic susceptibility, χ, has the value -1 and a magnetic field is completely expelled. Superconductivity was first discovered in mercury at liquid helium temperatures (4 K) [19]. Since this discovery there have been many attempts to synthesise materials in which this phenomenon occurs at higher temperatures in an

effort to find materials for technological applications. High temperature superconductivity was found in 1986 in a La-Sr-Cu-O phase with superconducting transition temperature, T_c, of about 36 K [20]. Later other cuprates were discovered, for example, Y-Ba-Cu-O compounds (T_c = 80 – 93 K) [21], $HgBa_2CuO_{4+\delta}$ (T_c = 94 K) [22] and materials from the Hg-Ba-Ca-Cu-O system which exhibit a very high T_c above 130 K [23]. Cuprate superconductors usually consist of mixed valence Cu and tend to be layered structures. There are also other oxides which are known to superconduct, for example $LiTi_2O_4$ with a spinel structure and the perovskite-type $BaPb_{1-x}Bi_xO_3$ system [24]. Apart from oxides, there exist a large range of superconductors among metals, alloys and organic compounds. Superconductivity has been also observed in Chevrel phase materials (MMo_6X_8, where M is a metal and X = S, Se or Te) [25]. Some of these materials also possess high critical magnetic size fields [26]. Furthermore, in Chevrel phases the exchange interaction between localised magnetic moments and conduction electrons is weak and allows superconductivity to exist simultaneously with several types of magnetic order on the magnetic sublattices [27, 28]. More recently superconductivity was found in defect thiospinels $GaTa_4Se_8$, $GaNb_4Se_8$ and $GaNb_4S_8$. It was observed [29] that $GaNb_4S_8$ undergoes a transition from the Mott insulating to a superconducting state with T_c up to 4 K at 21 GPa (Figure 8).

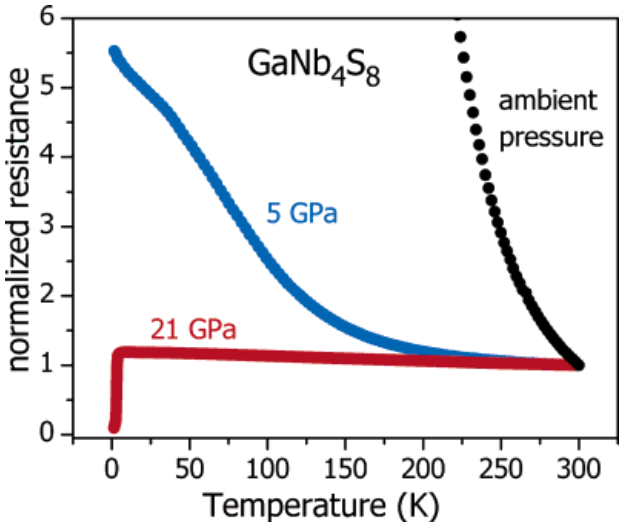

Figure 8: Electrical data of $GaNb_4S_8$ at some selected pressures [29].

Superconductors can be divided into two groups: type I and type II (Figure 9). In type I superconductors with increasing magnetic field, H, or temperature, sudden change from

superconducting to non-superconducting state occurs, while in II type superconductors there is a transition state (vortex state) between these two states. Examples of some materials which belong to the first class are: Hg, Al, Sn, In and the II type superconductors: Nb_3Sn, NbTi and all high-T_c cuprates [7].

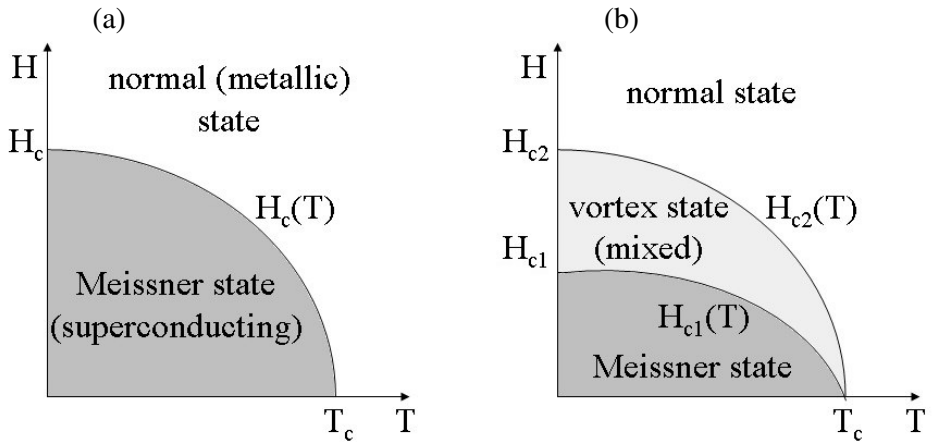

Figure 9: Phase diagram of (a) type I and (b) type II superconductor.

1.2.2 Magnetic Properties

Materials containing unpaired electrons are classified as paramagnetic materials, as opposed to diamagnetic materials which contain no unpaired electrons. Magnetic properties are found in transition metals, lanthanides, and their compounds due to the unpaired *d* and *f* electrons on the metal. Magnetic character of materials is typically analysed relative to its magnetic susceptibility (for more information see Section 2.3.3 in Chapter 2).

1.2.2.1 Magnetic Behaviour of Materials

Magnetic materials can show several different kinds of magnetic effects: paramagnetism, in which the unpaired electrons are randomly arranged, ferromagnetism, in which the unpaired electrons are all aligned, antiferromagnetism and ferrimagnetism, in which the unpaired electrons line up opposite to one another in nearest neighbours (Figure 10). The temperature at which a material orders ferromagnetically is called the Curie temperature, T_C, while the Néel temperature, T_N, is the temperature below which antiferromagnetic order occurs. These temperatures are characteristic of a given material.

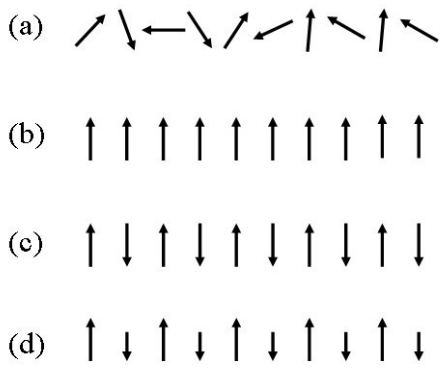

Figure 10: Types of magnetism: (a) paramagnetism, (b) ferromagnetism, (c) antiferromagnetism and (d) ferrimagnetism.

In antiferromagnetic substances some dipoles tend to orientate in one direction, while the other are oppositely directed. When the temperature increases the antiparallel alignment of adjacent magnetic dipoles is increasingly disrupted by thermal fluctuations. The susceptibility increases to the temperature T_N and declines sharply as antiferromagnetism is suppressed and a material becomes paramagnetic.

Ferromagnets are much less common than antiferromagnets. There are two different types of ferromagnetic substances: soft and hard ferromagnets [30]. In the former the magnetisation disappears when the magnetic field is switched off. On the other hand, hard ferromagnets show hysteresis, there being retention of a fraction of the magnetisation when the applied field is reduced to zero.

There exists also a group of magnetic materials which are called ferrimagnetic (Figure 10(d)). In such a material electron spins are orientated antiparallel to one another but, due to an inequality in the number of spins in each orientation, there exists an overall magnetic moment. The temperature below which ferrimagnetic order is established is termed ferrimagnetic Néel temperature. Many oxides containing Fe (III) show ferrimagnetism [30].

The different type of magnetic behaviour may be distinguished by the values of the magnetic susceptibility, χ. Generally the χ value is very small and negative for diamagnetic materials and small but positive for paramagnetic (Table 1). Ferromagnetic substances show values of χ greater than 1 and they are strongly attracted to a magnetic field. Often their susceptibility is very high, even seven or eight orders of magnitude greater than that typical of a paramagnet [30]. For antiferromagnetic substances χ is

positive with values comparable to or somewhat less than for paramagnetic materials.

Table 1: Typical values of magnetic susceptibilities for different materials [30].

Behaviour	Typical χ_{mol} value	Changes of χ with increasing temperature	Field dependence
Diamagnetism	-10^{-3} Z*	none	no
Paramagnetism	1	decreases	no
Ferromagnetism	10^7	decreases below T_C	yes
Antiferromagnetism	≤ 0.1	increases below T_N	yes

1.2.2.2 Spin-Glass and Frustration

Spin frustration is an important feature in magnetism and often leads to spin-glass formation. Frustration is the inability of the system to remain in a single lowest energy state (the ground state). The typical origin of this property is the simultaneous presence of competing interactions and disorder. Since the work of Toulouse [31] on spin frustration, geometrically frustrated magnetic materials have received much attention. Geometrical spin frustration (GSF) arises from the arrangements of spins. The concept of GSF is often discussed [32] by treating spins as simple collinear vectors and considering pair-wise interactions between spins on the building blocks of their spin lattices that have the local spins at each spin site. A simple example is shown in Figure 11. Suppose that spin vectors are collinear. Only two of the three spins can be antiferromagnetically coupled simultaneously. When the first two spins align anti-parallel, the third one is frustrated because its two orientations (up or down) give the same energy and it cannot simultaneously minimise its interactions with both of the other two. Thus the ground state of the spin arrangements is twofold degenerate.

* Z is the atomic number

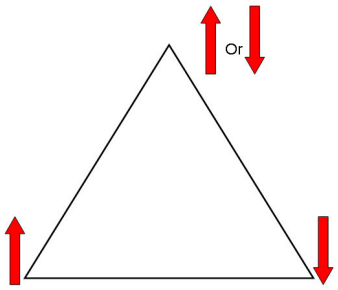

Figure 11: Antiferromagnetically interacting spins in a triangular arrangement.

Spin-glass type materials exhibit a high degree of magnetic frustration. These materials have pockets of aligned spins as shown in Figure 12.

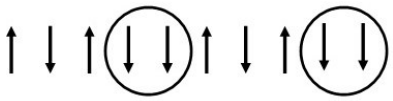

Figure 12: Spin glass-type behaviour in which an antiferromagnetic array is disrupted or frustrated by enforced ferromagnetic coupling (circled).

In materials which show spin-glass behaviour interaction between unpaired electrons leads to a not fully developed antiferromagnetic structure (*i.e.* spin up–spin down arrangement) and a material becomes frustrated by the frequent occurrence of unavoidable spin up–spin up or spin down–spin down ferromagnetic pairs. Antiferromagnetic and ferromagnetic interactions thus coexist and long-range order cannot occur. Due to the couplings between local magnetic moments and magnetic interaction of random sign, the moments become frozen out in random directions below a temperature known as the freezing temperature, T_g [33]. The low temperature state therefore does not possess a global moment. A plot of $1/\chi = f(T)$ shows a peak at T_g. Remanent magnetisations are also found at temperatures below T_g, either thermoremanent obtained after a cooling process from a temperature higher that T_g with an applied field or isothermal acquired at the measuring temperature [33]. The origin of the behaviour can lie in a structural disorder or a disordered magnetic doping in a regular structure.

Spin glass behaviour has been observed in many dilute metallic alloys [33]. Some oxides show also spin glass-type behaviour, for example $(Ti_{1-x}V_x)_2O_3$ [33].

1.2.2.3 Pauli Paramagnetism

Application of a magnetic field induces a marginal spin polarisation of the electrons manifested by a small positive magnetisation, termed Pauli paramagnetism. The effect is illustrated by Figure 13, which shows separate conduction bands for electrons of alternative spin orientation with respect to the applied magnetic field. When a sample is placed in a magnetic field, H, the spins which are parallel to H have slightly lower energy than those which are antiparallel to H. This causes a splitting of the band of energy levels into two half-bands, with spin-up and spin-down, respectively. Some of the spin-up levels at the bottom of the half band have lower energy than those at the bottom of the spin-down half band, giving rise to a net magnetic moment [7]. At the levels which are close to E_F, electrons in the spin-down levels spill over into those in the spin-up levels to have the same energy in two half bands at Fermi energy level. The effect, which is universal in metals, is due to the excess of electrons in the up-spin band. In contrast to Curie paramagnetism, Pauli paramagnetism is independent of temperature because there is an absence of any net unpaired spins in levels near E_F but it depends on field because of the band splitting of levels at the bottom of the conduction band [7]. The magnetic moment in Pauli paramagnets is far smaller that in ferromagnetic materials due to the fact that the splitting occurs spontaneously in the ferromagnetic case due to exchange interactions between neighbouring spins.

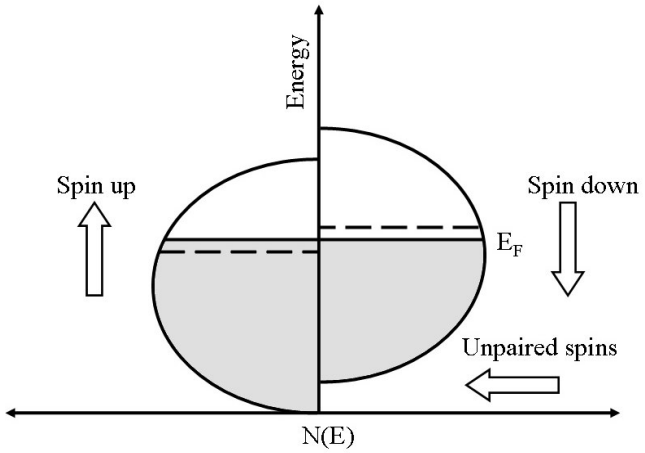

Figure 13: The origin of Pauli paramagnetism [7].

The volume susceptibility associated with Pauli paramagnetism is described by the following equation [30]:

$$\chi = \mu_0 \mu_B^2 N(E_F) \tag{4}$$

where μ_0 is the vacuum permeability ($4\pi \times 10^{-7}$ N A^{-2}) and $\mu_B = 9.274 \times 10^{-24}$ A m^2.

1.2.2.4 Curie Weiss Law

When there are no spontaneous interactions between unpaired electrons the behaviour of a substance in a magnetic field can be described by the Curie law (equation 5) which states that the molar magnetic susceptibility, χ_{mol}, is inversely proportional to the temperature:

$$\chi_{mol} = \frac{C}{T} \tag{5}$$

Where C is the Curie constant and T is temperature. However, paramagnetic materials that obey the Curie law to very low temperature are comparatively rare. In the case of materials in which there are some interactions at low temperatures, a better fit to the high temperature paramagnetic region is obtained using the Curie Weiss law:

$$\chi_{mol} = \frac{C}{T - \theta} \tag{6}$$

Where θ is the Weiss temperature and is a measure of the interactions between the magnetic moments and is characteristic of a substance (See also Sec. 2.3.3 in Chapter 2). Ferromagnetic materials typically show positive values of θ at low temperatures and antiferromagnets, negative values. The Weiss temperature is an indicator of the dominant exchange interactions but it does not necessarily imply long range order. Below Curie (ferromagnets) and Néel (antiferromagnets) temperatures deviations from Curie Weiss behaviour is observed.

1.2.2.5 Percolation threshold

Percolation refers to the process of the formation of long-range connectivity in random systems [34]. It has wide-ranging applications to problems in physics and engineering, including conductivity and magnetism in random systems. To study this phenomenon, one typically models the network by a regular lattice and make it into a random network by independently making sites or bonds occupied with a probability p [35]. At a critical threshold p_c, for a given lattice and percolation type, long-range connectivity first takes place, and this is called the percolation threshold [35]. Finding this threshold exactly is essential to studying the percolation problem on a particular lattice.

Over the last several decades, a tremendous amount of work was done to find exact and approximate values of the percolation thresholds for a variety of systems. There are relatively few lattices where p_c is known exactly, all in two-dimensional lattices. These lattices include bond percolation on the square lattice and site percolation on the triangular lattice (both with $p_c = ½$) [36]. Recently [36] many new thresholds for various classes of lattices have been determined. Table 2 presents the p_c values for three lattices. Values of p_c for other systems might be found in works [37-40].

Table 2: Values of p_c for bond and site percolation on the body-centred cubic (b.c.c.), face-centred cubic (f.c.c.) and simple cubic (s.c.) lattices [41].

System	p_c
b.c.c. (bond)	0.1802875
b.c.c. (site)	0.2459615
f.c.c. (bond)	0.1201635
f.c.c. (site)	0.1992365
s.c. (bond)	0.2488126
s.c. (site)	0.3116080

1.3 Oxide Systems

Work carried out at the Department of Inorganic and Analytical Chemistry, Szczecin University of Technology, Poland focused on oxide systems. An overview of the field of study will be presented in this section.

Numerous studies have been performed on oxides because of their many attractive and useful properties. δ-Bi_2O_3 is known to date to be the best oxide anion conducting material at high temperature [42]. Some oxides are the starting materials for the production of pigments and others are pigments in their own right and produced on an industrial scale. For example zinc oxide is known as a white inorganic pigment and $BiVO_4$ is a commercially available high-performance pigment. The pigments of the $ZnO – Bi_2O_3$ type give intensive yellow hues and they can be used for colouring of paints and plastics [43]. Furthermore, zinc oxide doped with several different metal oxides is widely used as a voltage regulator and surge protector. ZnO-based varistors

are often used to protect electronic circuits [44]. V_2O_5 was reported to be a promising varistor-forming ingredient for ZnO ceramics [45]. In addition, mixed oxides M–V–O, where M = Zn, Pb or Mg are amongst the most effective catalysts for the oxidative dehydrogenation (ODH) of lower alkanes [46]. It has been found [47] that isolated tetrahedral VO_4^{3-} units in $Mg_2V_2O_7$ are active and selective species in the ODH of propane.

The metal oxide systems which consist of bismuth (III) oxide have received a considerable amount of attention over the past decade [48-50]. Oxo-salts of bismuth (III) exhibit interesting properties such as ionic conductivity, they are also yellow pigments and highly selective catalysts for the partial oxidation of propylene and butene [51-53]. For example passing propylene and oxygen over the bismuth catalyst, hexadiene and benzene are produced, whereas passing the same mixture over molybdate catalyst and under the same conditions, acrolein is produced. These compounds are also interesting with respect to their ferroelectric and ferroelastic properties [54]. Since the discovery of oxide ion conductivity in $Bi_4V_2O_{11}$ a number of studies have been performed on the MO – Bi_2O_3 – V_2O_5 systems (where M is divalent cation) with the hope to find improved ion transport materials.

1.3.1 The ZnO – $BiVO_4$ System

The pseudo-binary ZnO – $BiVO_4$ system belongs to the ternary ZnO – V_2O_5 – Bi_2O_3 system. Reference to the literature reveals that the phase relations in the ZnO – $BiVO_4$ system have not been studied. However, it is known that bismuth forms with divalent and pentavalent cations a family of compounds with stoichiometry $BiA_2^{II}M^{V}O_6$ [54-62]. The majority of the compounds from this family adopt closely related crystal structures. They crystallise in the orthorhombic system, with a space group *Pmna* [55, 56, 58, 61, 63], *Cmcm* [57-59], *Cmc2₁* [54], *P2₁/n* [60, 64], *Amma* [61] or *Pnma* [65]. Their structures have been described [54-58, 60, 63-65]. Phase transitions to higher symmetry structures have been detected in $BiMg_2VO_6$, $BiPb_2VO_6$, $BiMg_2PO_6$ and $BiZn_2PO_6$ [58, 61, 66, 67]. These structures contain BiO_2^- chains, MO_4^{3-} tetrahedra and A^{2+} cations (Figure 14) resulting in the general formula $A_2[BiO_2][MO_4]$ [55, 56]. The main differences in the structural details of the individual compounds are a variable orientation of the tetrahedra MO_4 and a different coordination number of the cations M^{2+} that varies with an increase of ionic radius of the cation, assuming the values from 5 to 7 [60].

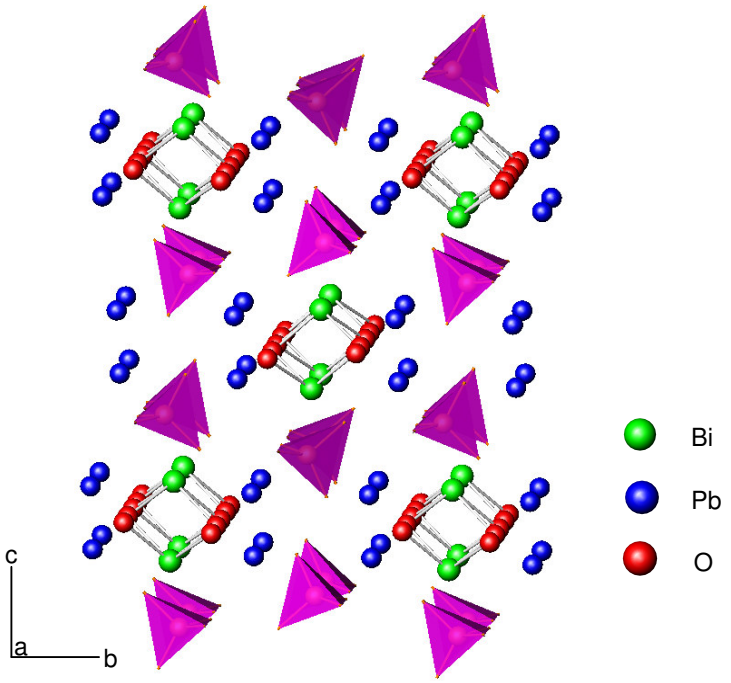

Figure 14: Structure of $BiA_2^{II}M^{V}O_6$, as represented by that of α–Pb_2BiVO_6. Tetrahedra are shaded.

1.3.2 Phase Relations in the PbO – Bi_2O_3 – V_2O_5 System

The $Pb_2V_2O_7$ – $BiVO_4$ and PbO – $BiVO_4$ are pseudo-binary systems in the ternary PbO – Bi_2O_3 – V_2O_5 system. The phase equilibria in the PbO – Bi_2O_3 – V_2O_5 system has been studied [68, 69]. Eleven solid phases in the crystallisation surface of this ternary system were reported [68], with only one quaternary compound. Since then, investigations in this system have led to the discovery of several new quaternary materials [62, 70-73]. These include $(PbO)_n(BiVO_4)$ where n = 1, 2 and 4, $PbBi_6V_4O_{20}$, $Pb_5Bi_{17}V_5O_{43}$ and $PbBi_6V_2O_{15}$.

1.3.2.1 The $Pb_2V_2O_7$ – $BiVO_4$ System

A search of the literature suggests that there exists a series of compounds of stoichiometry $M^{II}{}_2M^{III}V_3O_{11}$ [74-77]. In the structure of these compounds, VO_4 tetrahedra as well as VO_5 bipyramids can be distinguished (Figure 15) [78, 79]. These compounds are particularly interesting because of their good catalytic properties [80].

In the Bi_2O_3 – V_2O_5 – MO systems, where M = Sr or Ba, compounds are formed with the general formula $BiM_2^{II}V_3O_{11}$ [81, 82]. The Sr and Ba analogues are not isostructural. $BiSr_2V_3O_{11}$ crystallises in the triclinic system with the space group $P\bar{1}$

and with unit cell parameters a = 7.0332(6) Å, b = 10.213(2) Å, c = 6.982(2) Å, α = 96.01(2)°, β = 92.87(2)°, γ = 99.16(2)° and Z = 2 [81]. Both the pyrovanadate groups $(V_2O_7)^{4-}$ and the orthovanadate groups $(VO_4)^{3-}$ are isolated in the structure of $BiSr_2V_3O_{11}$. As a result of the substitution of Sr for Ba a compound crystallising in the monoclinic system is formed, despite the fact that it contains the same coordination polyhedra as $BiSr_2V_3O_{11}$. The unit cell parameters of $BiBa_2V_3O_{11}$ are: a = 12.332(4) Å, b = 7.750(4) Å, c = 11.279(4) Å, β = 103.22(3)°, with the space group $P2_1/c$, Z = 4 [82].

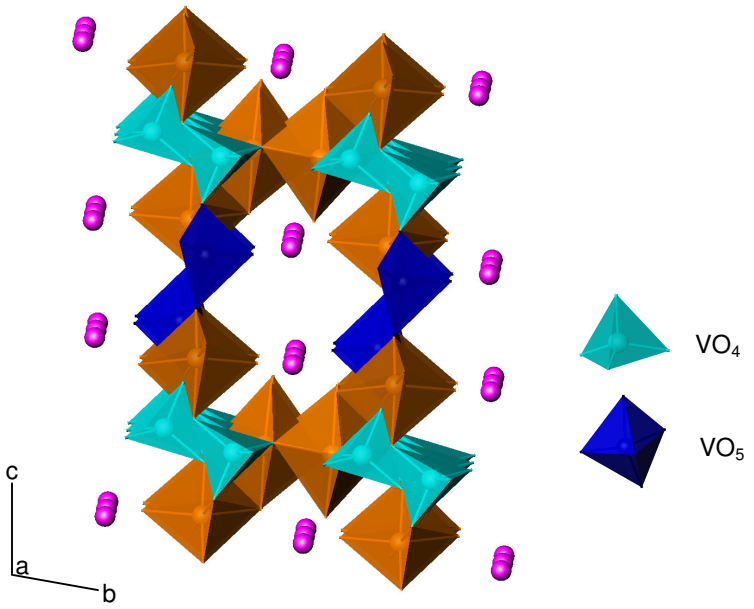

Figure 15: Structure of $M^{II}_2M^{III}V_3O_{11}$, as represented by that of $FeMg_2V_3O_{11}$.

Only one work [69] on the reactivity between lead (II) pyrovanadate (V), $Pb_2V_2O_7$, and bismuth (III) orthovanadate (V), $BiVO_4$, has been reported [69] . It was shown that a compound with the formula $Pb_6Bi_2V_8O_{29}$ was obtained as a result of reaction between $Pb_2V_2O_7$ and $BiVO_4$ at the molar ratio 3:2. This phase melts at 983 K [69]; the way of melting was not described. However, compound which belong to the family $BiM_2^{II}V_3O_{11}$, where M = Pb, has not been reported.

1.3.2.2 The PbO – $BiVO_4$ System

Three compounds exist in the pseudo-binary PbO – $BiVO_4$ system: Pb_2BiVO_6, $PbBiVO_5$, and Pb_4BiVO_8 [62, 70]. However, information about the polymorphic modifications of these is not consistent. Moreover, the phase relations in this system,

over the whole components concentration range up to 1273 K, have not been fully characterised to date.

Pb_2BiVO_6 has several polymorphic modifications labelled α to δ [62], with phase transitions $\alpha \rightarrow \beta$ 688 K, $\beta \rightarrow \delta$ 748 K [83]. The phase transition δ–$Pb_2BiVO_6 \rightarrow$ α–Pb_2BiVO_6 is observed on cooling at 733 K [83]. It has been observed that the cooling process is always accompanied by a direct change from the δ to the α form. The existence of the γ–Pb_2BiVO_6 form was observed in small amounts as a mixture of Pb_4BiVO_8 and the high-temperature form of $PbBiVO_5$ [83]. The transformation γ–$Pb_2BiVO_6 \rightarrow \delta$–$Pb_2BiVO_6$ occurs at 908 K, is relatively slow and is not observed at a fast heating rate [83]. Pb_2BiVO_6 melts congruently at 1053 K [83].

The α–Pb_2BiVO_6 polymorph crystallises in the monoclinic system with the space group $P2_1/n$; a = 7.717(3) Å, b = 5.845(3) Å, c = 29.081(8) Å, β = 94.27(1)° and Z = 8 (Figure 14) [84]. δ–Pb_2BiVO_6 crystallises in the tetragonal system [49, 50, 83]; a = 12.110(2) Å, c = 9.472(8) Å and Z = 8 [83, 85]. Both the β- and γ-Pb_2BiVO_6 forms crystallise in the orthorhombic system [62]. The unit cell parameters for β–Pb_2BiVO_6 and for γ-Pb_2BiVO_6 forms were found only in one work [62]. The existence of γ–Pb_2BiVO_6 form was later re-examined [83] and it was shown to consist of two phases as described previously. The β–Pb_2BiVO_6 modification appears to be metastable [83]. A full structure determination appears to have been reported only for room temperature α and high temperature δ forms [64, 66].

Previous studies indicate that $PbBiVO_5$ exists in two polymorphic forms with a phase transition at 753 K [83]. A low-temperature polymorph $PbBiVO_5$ crystallises in the triclinic system [83]; a = 7.1082(5) Å, b = 7.2802(6) Å, c = 5.6203(1) Å, α = 111.788°, β = 95.207°, γ = 108.717(5)°, Z = 2. A high-temperature polymorph $PbBiVO_5$ crystallises in the monoclinic system; a = 13.635 Å, b = 5.657 Å, c = 7.202 Å, β = 113.82°, Z = 4 [83]. $PbBiVO_5$ melts congruently at 1168 K [70]. The structure of $PbBiVO_5$ (Figure 16) was determined by single crystal X-ray diffraction [86] and consists of 2 Pb and 2 Bi sites which have distorted eight- and six-fold coordination, respectively.

Pb_4BiVO_8, which is also formed in the pseudo-binary PbO – $BiVO_4$ system, occurs only in one polymorphic modification [62]. Pb_4BiVO_8 crystallises in the triclinic system; a = 6.221(2) Å, b = 7.603(5) Å, c = 10.457(4) Å, α = 100.40(3)°, β = 102.18(2)°, γ = 90.03(3)° and Z = 2 [50]. It melts congruently at 1053 K [62]. The crystals of Pb_4BiVO_8 were poor quality and no structure for this compound was determined [62]. However, its lattice parameters indicate that Pb_4BiVO_8 is isostructural

to Pb_4BiPO_8 (Figure 17) [62, 87].

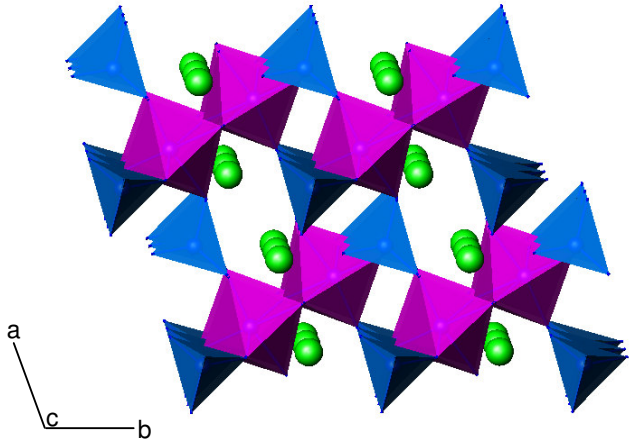

Figure 16: $PbBiVO_5$: spheres for Bi, PbO_6 as octahedra and VO_4 as tetrahedra.

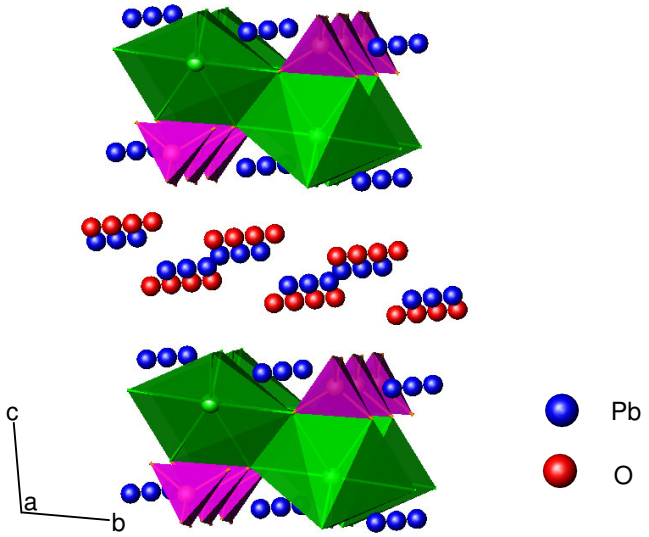

Figure 17: The structure of Pb_4BiPO_8. Octahedra BiO_6 and PO_4 tetrahedra are shaded.

1.4 Sulphide Systems

Following the move to Heriot Watt University in 2006 the focus of the project moved to solid-state sulphide chemistry. The background to this work is described in this section. Sulphides play a very important role in science and industry. Both inorganic and organic sulphides occur in nature and they are an important class of minerals. They occur in large mineral deposits, petroleum and in living organisms. Most major ores of important metals such as copper, lead and silver are sulphides [88]. Because sulphide

minerals are sources of metals they can be considered the most important group of minerals. Furthermore, metal sulphides display interesting electrical, optical and magnetic properties and they are used in various electronic and opto-electronic devices.

The difference between oxygen and sulphide atoms leads to differences in the chemistry of oxides and sulphides. For example, the Pauling electronegativity of sulphide is 2.58, whereas that of oxygen is 3.44. The crystal radius of O^{2-} is 1.4 Å, that of S^{2-} is equal to 1.7 Å [89]. The difference in electric polarisability of sulphide and oxygen is of great structural importance and it can be defined as the value expressing the displacement of the electron cloud relative to the nucleus. Its value is 3.88×10^{-24} cm^3 for O^{2-} and 10.2×10^{-24} cm^3 for S^{2-} [89]. Structural features of certain sulphides (especially that of layer-like structures) are in common with hydroxides, which have low-charge and polarisable OH^- groups [89].

Both, oxides and sulphides have been exploited in important applications. In contrast to oxides, many of the important applications of the sulphides involve their semiconducting properties. All sulphides of main group (*i.e.* non-transition) elements (including Zn, Cd and Hg) are insulators or semiconductors [88]. This is because the valence band is filled and the conduction band empty and they do not overlap. The semiconducting and magnetic properties of metal sulphides makes them particularly attractive and worthy of study.

1.4.1 Ordered Defect Spinels

1.4.1.1 Introduction

Many transition metal chalcogenides of general formula AB_2X_4 adopt a monoclinic Cr_3S_4 structure. It is an ordered defect structure intermediate between NiAs and CdI_2-type structures [90]. An alternative structure for this stoichiometry is the spinel structure [91]. Materials of stoichiometry ACr_2X_4, where *A* is a transition metal and X = O, S, Se, or Te, adopt either the spinel [92] or the NiAs-type structure [93]. The spinel structure is adopted for X = O, while when X = Se or Te a defect NiAs-type structure is favoured [94]. When X = S the type of structure depends on the nature of A cation. Materials adopt the spinel structure when A = Mn, Fe, Co or Cu and the defect NiAs-type structure when A = Ti, V, Cr or Ni [94]. It was also reported that a transition between these two structure types is possible at high temperatures and pressures [94].

1.4.1.2 The Spinel Structure

Spinels (Figure 18) are a class of minerals of general formula $[A]^{tet}[B_2]^{oct}X_4$, with *A* and *B* cations distributed over tetrahedral and octahedral sites in a cubic-close packed array of anions. The spinel structure is described in the high symmetry cubic $Fd\bar{3}m$ space group. In the normal spinel structure *A* cations exclusively occupy 1/8 of the tetrahedral sites and *B* cations occupy 1/2 of the octahedral sites in an ordered fashion [7]. For inverse spinels, half of the *B* cations occupy the tetrahedral sites, and both *A* and *B* cations occupy the octahedral sites, *i.e.* $[B]^{tet}[A,B]^{oct}X_4$. An intermediate cation distribution can also occur, sometimes with a temperature dependence to the distribution. The cation distribution and the degree of inversion, γ, is defined as the proportion of *A* cations in the octahedral sites. In normal spinels $\gamma = 0$ and in inverse spinels $\gamma = 1$. The γ value may vary from 0 to 1. It has been established [95] that $CuCo_2S_4$ and all thiochromites have the normal spinel structure whereas $FeIn_2S_4$ is an inverse thiospinel.

There are several factors which influence γ, including the site preferences of ions in terms of size, covalent bonding effects and crystal field stabilisation energies [7, 96]. The inversion parameter, γ, can be determined from refinement of site occupancy factors based on single-crystal X-ray diffraction data [97]. However, more usually, neutron diffraction is required as the cations are generally neighbouring each other in the periodic table. There are over a hundred known compounds with the spinel structure, mostly oxides. There are also known some sulphides, selenides and tellurides which adopt spinel structure [7]. Examples of compounds with the spinel structure are presented in Table 3.

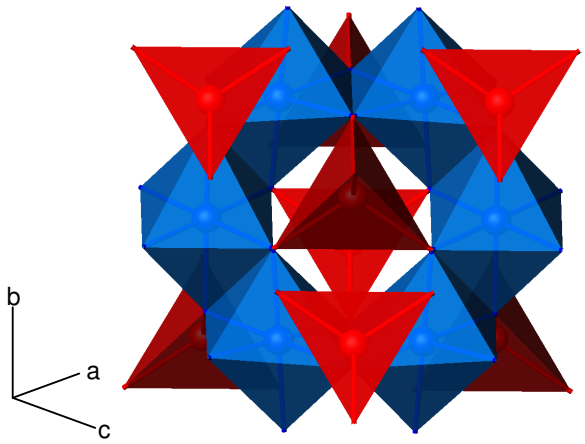

Figure 18: Spinel structure.

Table 3: Selected compounds with the spinel structure [7].

Compound	*a*/Å	Structure	γ
$CuCr_2S_4$	9.629	Normal	0
$MgIn_2S_4$	10.708	Inverse	1
$(Mg_{0.18}Fe_{0.82})(Mg_{0.82}Fe_{1.18})O_4$ = $MgFe_2O_4$ [98]	8.389	Intermediate	0.82

Oxide spinels exhibit very interesting properties which have been the focus of research since 1939 when the work by Verwey on magnetite (Fe_3O_4) was published [99]. For instance, they exhibit good electrochemical performance [100] and superconductivity [101]. Recent reports demonstrate the rich and complex physics that are characteristic of this system [102-104].

The chalcogenide spinels of AB_2X_4 type present attractive structural, electrical and magnetic properties. For instance, $CuIr_2S_4$ exhibits a metal-insulator transition [17], $CuRh_2S_4$ shows a pressure-induced superconductor-insulator transition [105] and the chromium chalcogenide spinels exhibit magnetoresistance [106]. The magnetic behaviour of $ZnCr_2S_4$ is governed by dominant antiferromagnetic interactions but there is also a large group of spinels in which ferromagnetic interactions are found to predominate. For example, $CdCr_2S_4$, $CdCr_2Se_4$, $HgCr_2S_4$ and $HgCr_2Se_4$ have been found to be ferromagnetic [107]. Magnetic properties of these compounds are related to distances between *B* ions [108]. It was shown [109] that the nearest-neighbour *B-B* exchange interactions alone cannot produce any long-range order on the *B* sites and more distant interactions need to be taken into account [107]. Important interactions are long-range interactions between ions *B-X-A-X-B* [107, 110], *B-X-X-B* [111, 112] and sometimes even more distant interactions [113]. The value of the superexchange interaction can be influenced by changes of the bond angles *B-X-B* or *B-X-A* and by changing distances between *B* ions [114, 115]. The magnetic properties of spinels mostly depend on the distances between ions in the unit cell, angles between them and amount of defects [116] and in case of ternary transition-metal chalcogenides containing metallic clusters, strongly depend on the number of valence electrons per cluster and the distance between them [117].

1.4.1.3 Defect Thiospinels

Many compounds of general formula AB_2S_4 adopt a spinel-type structure [92]. Mixed-metal sulphides with the spinel structure are generally stable only at the stoichiometric composition. Cation deficiency is much less common amongst the thiospinels than in the nickel arsenide-type compounds, in which variation in stoichiometry gives rise to a range of vacancy-ordered phases [118, 119]. However, there exists a small family of defective spinel-like materials, in which 50 % cation deficiency associated with the *A*-site gives rise to a superstructure. These materials of general formula $A_{0.5}B_2S_4$ ($\equiv AB_4S_8$) exhibit *A*-site vacancy ordering leading to a structure which consists of heterocubane-like $[B_4S_4]^{n+}$ clusters and $[AS_4]^{n-}$ tetrahedra. These structural units adopt a rocksalt like arrangement in the cubic unit cell observed at room temperature (Figure 19). The cation-deficient spinel-structure was initially characterised from powder X-ray diffraction at room temperature [120] and from single-crystal X-ray diffraction [121]. The space group symmetry is lower than that of spinel. It is found that ordering of the *A* cations over the tetrahedral sites lowers the symmetry of the ideal spinel structure, $Fd\bar{3}m$, to $F\bar{4}3m$, while displacement of the *B* cations results in B_4 clusters with short *B*-*B* distances (*ca.* 2.8 Å) and strong intracluster bonding. This intracluster bonding and distortion of the spinel structure has caused some workers [122, 123] to question whether these compounds should be described as spinels or $[B_4X_4]AX_4$ binary solids.

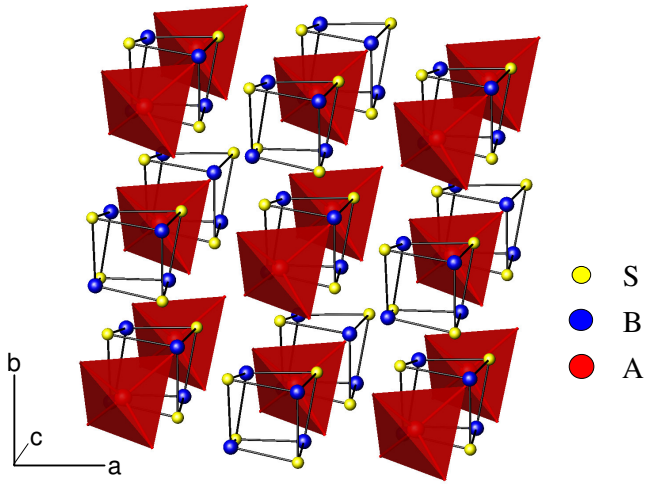

Figure 19: The structure of the ordered defect thiospinels, AB_4S_8, consisting of $[B_4S_4]^{n+}$ cubes and $[AS_4]^{n-}$ tetrahedra. Tetrahedra are shaded.

Following the first report [124] of ferromagnetic semiconducting spinels, $GaMo_4X_8$ (X = S, Se), materials of the stoichiometry AB_4X_8 have been prepared for A = Ga, Ge, Al; B = Mo, V, Nb, Ta and X = S, Se, [S, Te], [Se, Te] [116, 120-122, 124-130] in addition to cation-rich analogues $GaM_xMo_4S_8$ (M = C, Si, Ge) [129]. Cation substitution at the *A*-site has been explored in $Ga_{1-x}Zn_xV_4S_8$ [131, 132] and at the *B*-site in $GaV_{4-x}Mo_xS_8$ [133] and $Ga_xV_{4-y}Cr_yS_8$ [134]. A series of materials, $M[Mo_2Re_2]S_8$ [93, 135, 136], where M = Mg, Fe, Co, Ni, Cu, Zn has also been reported. More recently, the first titanium-containing member of the AB_4X_8 family of compounds was prepared [137].

There have been several attempts to explain theoretically the structures and structural transition to rhombohedral modifications at low temperatures observed in these compounds [122, 123, 138-140]. A lot of effort has been directed at understanding the bonding within the B_4 clusters and explaining the origin of the structural change. Table 4 shows examples of some compounds from the AB_4X_8 family, temperatures of structural transition and lattice parameters of the rhombohedral unit cell.

Table 4: Cubic to rhombohedral distortion of some selected defect spinel-like materials.

Compound	Temperature of phase transition/K	Parameters (*R3m*); *a*/Å, α_{rh}/°
$GaMo_4S_8$ [141]	45	a = 6.8506(2) α_{rh} = 60.533(1)
$GaMo_4Se_8$ [142]	45	a = 7.1537(3) α_{rh} = 60.572(5)
$AlMo_4S_8$ [142]	24	a = 6.8500(3) α_{rh} = 60.374(5)
GaV_4S_8 [123]	38	a = 6.834(1) α_{rh} = 59.66(2)

Powder X-ray diffraction studies [141] of $GaMo_4S_8$ show a low-temperature transition to rhombohedral symmetry, involving a compression along the body diagonal of the cubic unit cell. An analogous distortion is assumed to occur in GaV_4S_8. Recently it was suggested [123], on the basis of Rietveld refinement using medium resolution laboratory powder X-ray diffraction data, that GaV_4S_8 also exhibits a distortion from cubic to rhombohedral symmetry at low temperatures but this distortion is in the opposite sense to that in $GaMo_4S_8$, involving expansion along the body diagonal. By

considering the metal-based orbitals on the B_4 cluster (Figure 20), the opposing nature of the distortion in the vanadium and molybdenum phases was rationalised in terms of the differing crystal field stabilisation energies. In the cubic case, the symmetries of the cluster orbitals at T_d are: a_1, e and t_2. The last is the highest occupied, 3-fold degenerate level. The cluster orbitals require 12 electrons for complete filling. Assuming formal valences for Ga and S, $Ga^{3+}(V^{3.25+})_4(S^{2-})_8$ indicates that only seven valence electrons per V_4 cluster are available for metal-metal bonding in GaV_4S_8 and eleven in $GaMo_4S_8$. In the case of ideal cubic symmetry (α_{rh} = 60°) the 3-fold degenerate highest level in GaV_4S_8 contains one electron. The structural distortion along the C_3 axis of the cube results in the distortion of the B_4 tetrahedron to C_{3v} symmetry. This distortion reduces the symmetry and removes the degeneracy of the t_2-level (T_d) by splitting it into a pair of degenerate levels with e symmetry and one level with a_1 symmetry. As is shown in Figure 20 for α_{rh} < 60°, the a_1 level (C_{3v}) is stabilised and the energy of the e levels increases. For α_{rh} > 60° the a_1 level increases in energy but that of the e levels decreases [123]. Therefore for a 7 electron system there is a net stabilisation for α_{rh} < 60° and for 11 electrons the opposite is true in accord with structural data.

It has been recently reported [133] using high-resolution neutron and synchrotron X-ray diffraction that the phase transition from cubic to rhombohedral in each case is incomplete leading to the coexistence of both phases at low temperature.

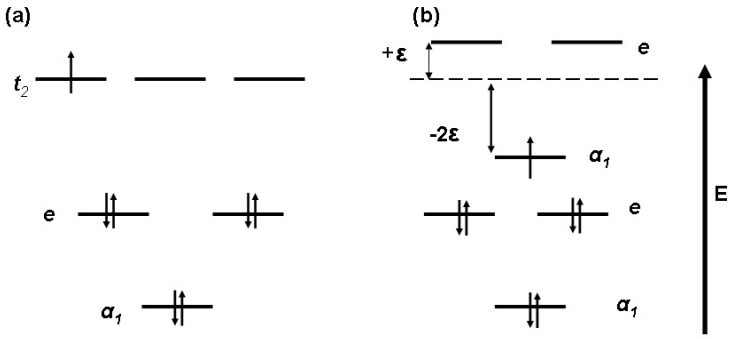

Figure 20: Molecular orbital scheme of the B_4 cluster orbitals in AB_4S_8 (after Pocha *et. al.* [123]): (a) a cluster of tetrahedral symmetry in the cubic structure and (b) a cluster of C_{3v} symmetry for a rhombohedral distortion with α_{rh} < 60°. The energies of the higher-lying e and a_1 orbitals are reversed for α_{rh} > 60°. The orbital filling refers to the composition GaV_4S_8.

The defect thiospinels are Mott insulators [143] in which electrical conduction occurs by inter-cluster hopping of electrons over relatively large distances of 4 Å. Sahoo [144] and Rastogi [145] have shown that GaV_4S_8 exhibits Fermi-glass behaviour, due to the large intercluster distances. Unpaired electrons are thus effectively localised on the cluster with the consequence that at low temperatures, the materials may exhibit cooperative magnetism and many of the defect thiospinels display interesting magnetic properties, which depend on the exchange interaction between the *B* cations. For example, the defect thiospinel GaV_4S_8 is ferromagnetic below T_C = 10 K [123]. $GaMo_4S_8$ shows similar behaviour (T_C = 19.5 K) [141].

It was also demonstrated [133] through the preparation of doped derivatives $GaV_{4-x}Mo_xS_8$ that the occurrence of magnetic order is intimately linked to the presence of a structural distortion at temperature above T_C. *B*-site substitution in $GaV_{4-x}Mo_xS_8$ suppreses both the structural distortion and the magnetic ordering transition and these materials remain paramagnetic to 4.2 K (Figure 21) [133, 146].

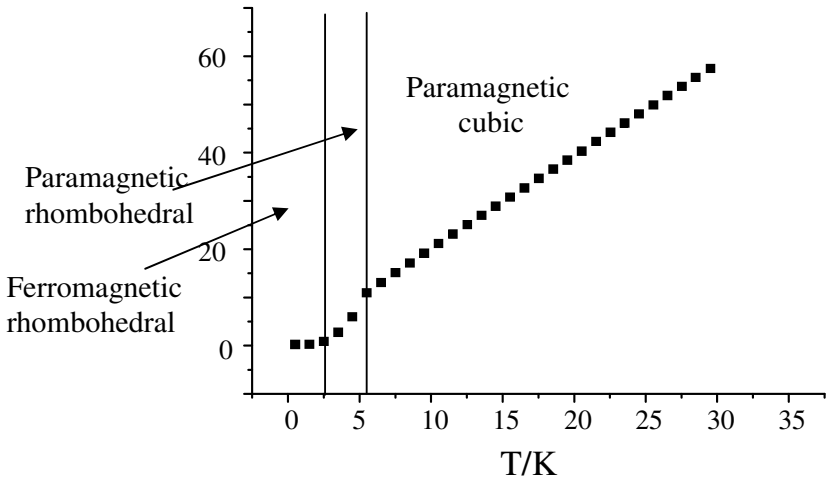

Figure 21: Reciprocal susceptibility for $GaMo_4S_8$ [146].

While GaV_4S_8, with one unpaired electron per V_4 cluster, is ferromagnetic, the properties of GeV_4S_8, which contains 2 unpaired electrons per V_4 cluster, are markedly different. This compound appears to be isotypic to GaV_4S_8 above the Néel temperature [143]. The main difference is the occupation of the cluster molecular orbital with eight instead of seven electrons according to $Ge^{4+}(V^{3+})_4(S^{2-})_8$. GeV_4S_8 is antiferromagnetic (T_N = 13 K) [122]. To date GeV_4S_8 was reported [122] as the only antiferromagnetic AB_4X_8-type compound. Chudo *et al.* [147] have shown that GeV_4S_8 undergoes a

structural transition from cubic to rhombohedral symmetry at 33 K, becoming orthorhombic below the Néel temperature (18 K). However, Bichler *et al*. [148] suggested using low temperature X-ray diffraction that the cubic GeV_4S_8 at room temperature transforms directly to the orthorhombic structure at 30 K. The antiferromagnetic spin structure of GeV_4S_8 has recently been determined by neutron diffraction [143] and described in the magnetic space group P_bmn2_1. The magnetic propagation vector is [½, ½, 0] [143].

$GaTa_4Se_8$, $GaNb_4Se_8$ and $GaNb_4S_8$ are the only superconducting compounds among the defect thiospinels [29]. Pocha *et. al.* [29] observed a sudden drop of the resistance of $GaNb_4S_8$ above 10 GPa with a critical temperature of 2.1 K. T_c increases linearly with increasing pressure (Table 5) [149].

Table 5: Critical temperature for $GaNb_4S_8$, $GaNb_4Se_8$ and $GaTa_4Se_8$ [149].

Material	$T_{c,min}$/K	p/GPa	$T_{c,max}$/K	p/GPa
$GaNb_4S_8$	2.1	10.0	4.0	26
$GaNb_4Se_8$	2.6	12.0	5.8	22
$GaTa_4Se_8$	5.8	11.5	8.1	22

1.4.2 Rare-Earth Transition Metal Sulphides

1.4.2.1 Introduction

There exists only a comparatively small number of examples of rare-earth transition metal chalcogenides reported to date, mostly sulphides, with considerably fewer examples of selenides and tellurides [150]. From the rare-earth transition-metal sulphides known, the majority have incommensurate structures. In many cases, their structures have been inferred solely from comparison of powder X-ray diffraction data with those of known phases and detailed structural investigations, including the nature of any cation ordering have not been carried out. However, chalcogenides containing rare-earth and transition-metal cation are worth of study because of their interesting magnetic and transport properties. The presence of *d*- and *f*-block elements allows three types of electron-electron interaction; *d-d, d-f* and *f-f,* to be simultaneously present. Furthermore, the high and variable coordination number of rare-earth cations offers a degree of structural complexity.

1.4.2.2 Rare-Earth Transition-Metal Sulphides

The Ln_2MS_4 phases are the most extensively characterised rare-earth transition metal chalcogenides. On the basis of powder X-ray diffraction data, three different structure types have been proposed for materials with the stoichiometry Ln_2MS_4 (M = Mg, Cr, Mn, Fe), depending on the identity of the rare-earth cation [151]. For the early lanthanides (Ln = La – Gd), an orthorhombic phase was identified, while rare-earth ions drawn from later in the series (Tb – Tm) generally favour adoption of a Y_2MnS_4-type structure (Figure 22(a)) and a spinel type structure (Figure 22(b)) is also observed for Yb-containing phases. The structure of Er_2CrS_4 [152] consists of $(Er,Cr)_2S_5$ slabs linked through terminal sulphurs. The influence of the Jahn-Teller distortion associated with Cr^{2+} manifests itself in ordering of Er^{3+}/Cr^{2+} within the octahedral chains that make up these slabs, no such ordering being present in the Mn and Fe analogues [153]. Other rare-earth elements which crystallise in the Er_2CrS_4 structure were reported for Ln_2CrS_4, where Ln = Ho – Tm and Y [151, 154]. Their detailed crystal structure were not investigated with exception for Y_2CrS_4 [155]. Recent single-crystal X-ray diffraction studies on "La_2CrS_4" and "La_2FeS_4" indicate greater complexity and reveal that these materials are rhombohedral and better formulated $La_{15.9(2)}Cr_{5.4(2)}S_{32}$ [156] and $La_{52}Fe_{12}S_{90}$ [157], respectively. Single-crystal structural studies on Y_2MnS_4-type materials are confined to "Yb_2MnS_4" [158] and Er_2CrS_4 [152]. In the former this led to its reformulation as $Yb_{2.33}Mn_{0.67}S_4$, whilst an enlarged unit cell was observed in the latter.

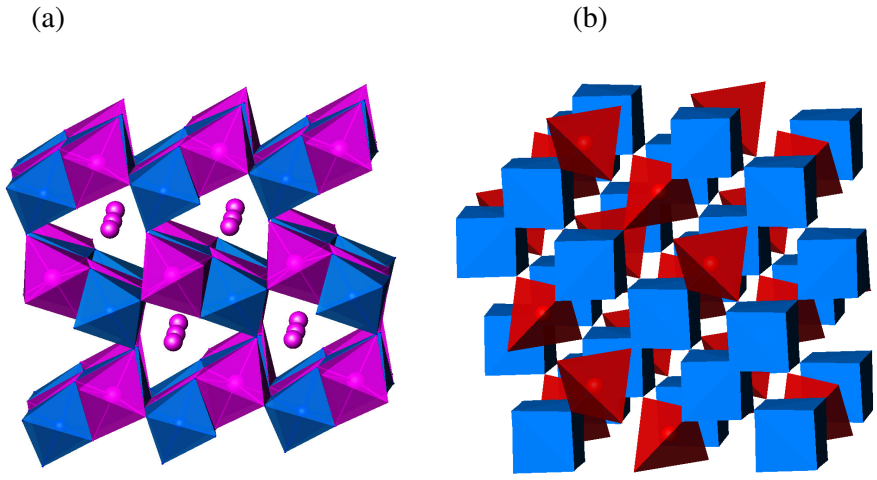

Figure 22: (a) Y_2MnS_4-type structure, represented by Er_2CrS_4 and (b) cubic spinel structure, as represented by that of Er_2CdS_4.

Magnetic susceptibility measurements have been performed on several compounds from the Ln_2MS_4 family. Er_2MnS_4, Er_2MgS_4 and Y_2MnS_4 appear to be paramagnetic down to 4.2 K [159] while Y_2CrS_4 shows an antiferromagnetic transition at 65 K [155].

A family of materials with the stoichiometry Ln_4MS_7, where Ln = Y, Dy, Ho, Er, Tm, Yb and M = Mg, Mn, Cr, Fe, Cd was reported by Adolphe [160-162] who carried out a single crystal study on Y_4FeS_7 [161] and Ho_4FeS_7 [162] and concluded that these two compounds adopt a Y_5S_7-type structure. By comparison of powder X-ray diffraction data, the remaining Ln_4MS_7 phases were considered [162] to be isostructural, with exception of Cd compounds. However, it appears that related materials, initially formulated Ln_4MS_7 (M = Mn, Fe, Co, Ni; Ln = La, Ce, Pr and Nd) [163], are more complex than originally proposed since analysis of single-crystal X-ray diffraction data for "Ce_4FeS_7" leads to a crystallographically-determined composition $Ce_3Fe_{1.94}S_7$ [164]. Aliev *et. al.* [165-167] have reported the existence of Ln_4MS_7 compounds (M = Cd, Zn, Cr, Fe, M, Co, Ni) for all the rare-earth elements. Ln_4VS_7 compounds (Ln = Dy, Ho, Er, Tm) with a Y_5S_7-type structure were also reported [168]. To this structure type belongs also $Mn_{0.4}Er_{4.6}S_7$ [169].

In Ho_4FeS_7 [162] (the structural model for Ln_4MS_7 phases with a Y_5S_7-type structure) individual slabs are separated by single chains, although more detailed structural information has been lacking for these compounds. No detailed structural studies of cation ordering in the Cr (II) materials have been performed. There are also several works which describe magnetic and transport properties of Ln_4MS_7 materials. The magnetic properties were measured [161] for Ln_4FeS_7 and Ln_4MnS_7 (Ln = Er, Y) materials over the temperature range of 77 – 673 K and they were found to be paramagnetic. Physical property measurements of some of the compounds: Ln_4CrS_7 (Ln = La, Ce) and Dy_4MS_7 (M = Cr, Mn, Fe) indicate that these compounds are *p*-type semiconductors [165-167].

Examination by electron microscopy of materials within the MnS - Y_2S_3, MnS - Er_2S_3 [170] and MgS - Yb_2S_3 [171] systems has confirmed the existence of phases of Ln_2MS_4 (Y_2MnS_4-type) and Ln_4MS_7 (Y_5S_7-type), and suggested that other phases with intermediate compositions such as $Ln_6M_2S_{11}$ and $Ln_8M_3S_{15}$ may exist. $Ln_8M_3S_{15}$ phases, where Ln = La, Ce and M = Cr, Mn, Fe are monoclinic of the $La_{32.66}Mn_{11}S_{60}$ type [172].

Whilst a number of rare-earth transition-metal sulphides of general formula $Ln_6M_2S_{11}$ have been reported [170, 173, 174], detailed structural analysis has been

performed only for $Yb_6Fe_2S_{11}$ [175] and $Er_6Cr_2S_{11}$ [176]. $Yb_6Fe_2S_{11}$ in which pairs of M_2X_5 slabs are interleaved by single chains of edge-sharing octahedra [175], shows Yb/Fe disorder, similar to that in Er_2CrS_4. Magnetic properties of $Ln_6Cr_2S_{11}$ (Ln = Gd, Tb, Er, Ho) materials were measured over the temperature range 80 – 100 K and they were found to be paramagnetic [174]. A phase diagram determined for the binary system CrS – Er_2S_3 [174] suggests that there exist only four compounds in this system, *i.e.* Er_2CrS_4, $Er_8Cr_3S_{15}$, $Er_6Cr_2S_{11}$ and Er_4CrS_7.

The synthesis and lattice parameters of two families of rare-earth chromium (III) sulphides, Ln_3CrS_6 (Ln = La – Lu) [177] and $LnCr_3S_6$ (Ln = Y [178], La – Lu [177]), have been reported, [31] but their crystal structure has not been determined and little is known about their physical properties. However, there exist a family of selenides Ln_3CrSe_6 (Ln = Gd, Sm, Tb) [179, 180] which adopt the U_3ScS_6 structure [181]. Powder X-ray diffraction data [177] suggest that remaining La_3CrS_6 (Ln = La – Lu) phases may be isostructural. Measurements of their physical properties are yet to be performed.

1.5 Aim of this Work

There were several broad goals of this project:

1. The aim of the work which was performed at the Department of Inorganic and Analytical Chemistry, Szczecin University of Technology, Poland was to determine the phase relations in three systems, over the whole concentration range of the components:

    - $ZnO – BiVO_4$
    - $Pb_2V_2O_7 – BiVO_4$
    - $PbO – BiVO_4$

and to investigate the existence of new compounds in these systems.

2. To investigate changes in physical properties of mixed metal sulphides induced by progressive chemical substitution or changes in structure.

3. The aim of the work on defect thiospinels was to investigate the changes in the structural, magnetic and transport properties of the *A*-site substituted defect thiospinels, $Ga_{1-x}Ge_xV_4S_8$ ($0 \leq x \leq 1$). The project sought to investigate changes in the magnetic and transport properties of the ferromagnetic semiconductor GaV_4S_8 as the Fermi level is raised by substituting germanium at the gallium site, in the non-stoichiometric series $Ga_{1-x}Ge_xV_4S_8$, leading ultimately to the antiferromagnetic end-member GeV_4S_8.

4. The investigations of complex transition-metal sulphides were extended to rare-earth-containing materials. The objectives of this work were to synthesise a series of erbium-chromium sulphides containing Cr^{2+}:d^4 and Cr^{3+}:d^3 ions, determine their structural properties using single crystal X-ray diffraction and apply powder neutron diffracion and SQUID magnetometry to investigate their magnetic properties.

Chapter 2: Preparation and Characterisation

This chapter describes the reagents and synthetic procedures used to prepare materials, the techniques used to characterise these phases and methods applied to determine magnetic and transport properties of the materials. All of the oxide compounds presented in this work were prepared at the Department of Inorganic and Analytical Chemistry, Szczecin University of Technology, Poland. Sulphides were synthesised in the solid-state chemistry laboratory at Heriot Watt University. Except where otherwise mentioned, all structural and physical property measurements were also performed in this laboratory.

2.1 Materials and General Synthetic Methods

2.1.1 Systems MO – Bi_2O_3 – V_2O_5, where M = Zn or Pb

All of the oxide samples investigated in this thesis can be prepared by standard solid state reaction. This method often requires high temperatures, for which a resistance furnace was used. The basic principle of a solid state reaction is to mix the proper quantities of starting materials whose atoms will diffuse at a sufficiently high temperature. It is very important not only to mix the starting materials but to grind them thoroughly in order to obtain a better diffusion. It is also very common to press the ground powder into a pellet before putting it into the furnace. The process of grinding and pelletization should be repeated several times until a single phase material is obtained. Table 6 lists the oxides used in this study. All materials were used without further purification.

The high–temperature modification of $BiVO_4$ used in the syntheses was obtained as a result of heating an equimolar mixture of Bi_2O_3 and V_2O_5 for 24 hours at each temperature: 873 K, 923 K and 973 K. $Pb_2V_2O_7$ was obtained as a result of heating stoichiometric mixture of PbO and V_2O_5 at temperatures: 723 K (2 h), 823 K (24 h) and 923 K (24 h). Detailed descriptions of syntheses of the samples prepared in this study are presented in Chapter 3.

Table 6: Materials used.

Reagents	Purity (%)	Supplier
ZnO	99+	Ubichem, UK
PbO	99+	Merck, Germany
V_2O_5	99+	Riedel-de Haën, Germany
Bi_2O_3	99+	POCh, Gliwice, Poland

2.1.2 High-Temperature Synthesis of Sulphides

Table 7 presents materials used in the study of high-temperature sulphides.

Table 7: Materials used.

Reagents	Purity (%)	Supplier
Gallium ingot	99.99	Alfa Aeasar
Germanium	99.99	Aldrich
Vanadium	99.50	Alfa Aeasar
Erbium	99.90	Aldrich
Chromium	99.95	Alfa Aesar
Sulphur	99.99	Sigma Aldrich
Iodine	99.90	Fisher

The gallium was stored in a refrigerator because of its low melting point (303 K [7]). The ingot of gallium was rubbed on a filter paper before using it to remove any surface deposit and was then cut into slivers. Vanadium used in the reactions needed to be cleaned to remove a green coating of V_2O_3. The vanadium powder was treated with dilute (2M) HCl, then washed with distilled water, dried on a vacuum line and stored in a desiccator. Germanium, vanadium, erbium, chromium and sulphur were supplied as fine powders. Sulphur needed to be dried. In order to remove water from sulphur, it was loaded into a flask, connected to the vacuum line, evacuated for 8 hours and then kept in a desiccator. Erbium powder is air-sensitive and was stored in an argon glove box.

All metal-sulphides were prepared by standard high-temperature reactions. Pure elements were weighed in appropriate portions and homogenised by grinding. The mixtures were loaded into silica tubes and sealed under vacuum ($< 10^{-4}$ Torr).

Syntheses of gallium germanium vanadium sulphides required 2 firings, whilst only one firing was needed in case of syntheses of erbium chromium sulphides. After each firing the materials produced were ground and analysed using powder X–ray diffraction. The details of syntheses of the series of sulphides $Ga_{1-x}Ge_xV_4S_8$ ($0 \leq x \leq 1$) and erbium chromium sulphides are described in Chapter 4 and 5, respectively.

2.1.3 Crystal Growth

The crystals of erbium chromium sulphides were grown using a vapour phase transport technique. Chemical transport can take place when the reaction 7 is reversible. Solid material *A* reacts with gas *B* forming gaseous material *AB* [182].

$$A_s + B_g = AB_g \tag{7}$$

In this work iodine was used as the transporting agent. Iodine reversibly converts non-volatile solid samples into volatile species. It migrates throughout a sealed, evacuated silica tube heated in a tube furnace, where a temperature gradient is used. The volatile species revert to the solid and the transporting agent is released. In principle, there is no upper limit for the amount of transporting agent. However, small amounts of the agent are sufficient to transport big amounts of the solid, because the agent set free during crystallisation diffuses back to pick up more solid [183]. The transport occurs from hot to cold end for endothermic reactions and from cold to hot end for exothermic reactions. Transport of metal chalcogenides with iodine as a transporting agent occurs always from hot to cold regions (Figure 23) [184].

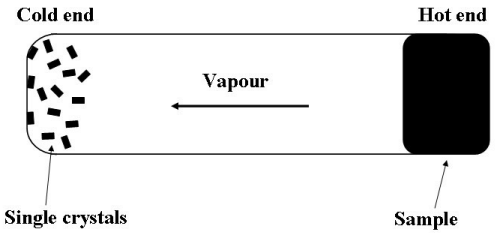

Figure 23: Scheme of the crystal growth by vapour transport technique.

The vapour phase transport technique requires the two ends of the tube be maintained at different temperatures. For this purpose the Lenton three-zone furnace, type PTF 12/50/300E was used. Detailed descriptions of synthesis of the crystals of erbium chromium sulphides samples are presented in Chapter 5.

2.2 Characterisation Methods

2.2.1 Powder X-ray Diffraction

Powder X-ray diffraction was employed for phase identification and to monitor the progress of reactions of powder samples. Air stable materials were finely ground and mounted in open aluminium or plastic sample holders. Aluminium holders were used for the $Ga_{1-x}Ge_xV_4S_8$ samples and PMMA holders for the rest of the materials prepared. Gas-tight holders were used for air-sensitive materials. Erbium chromium sulphide samples were ground and mounted in an argon glove box. During this study three different powder X-ray diffractometers were used.

The identification of individual phases was carried out by comparing with the Inorganic Crystal Structure Database and the Cambridge Structural Database (ICSD) [185] and powder diffraction file PDF-2 [186]. The powder diffraction patterns of sulphides were analysed by the Rietveld method [187, 188] using the refinement program GSAS [189] with input through the EXPGUI interface [190]. Detailed results of XRD analysis for prepared samples can be found in later chapters.

2.2.1.1 Powder X-ray Diffractometer DRON-3

The powder diffraction patterns of the samples from the $ZnO – Bi_2O_3 – V_2O_5$ and $PbO – Bi_2O_3 – V_2O_5$ systems were obtained in Poland with the use of the diffractometer DRON-3 (Bourevestnik, Sankt Petersburg, Russia) operating with Co-K_α radiation (λ = 1.7890 Å) and using an Fe filter. Scans were performed over the angular range $12 \leq 2\theta/° \leq 52$, counting for 1 s at 0.02° in 2 θ.

2.2.1.2 Philips PA2000 Diffractometer

Powder X-ray diffraction data of gallium germanium vanadium sulphides were collected at room temperature with a Philips PA2000 diffractometer using nickel-filtered Cu-K_α radiation (λ = 1.5418 Å). Data were collected over the angular range $5 \leq 2\theta /° \leq 80$ by counting for 1 s at each 0.05° increment in 2θ. Scans of the final products for subsequent structure refinement were run by increasing the counting time up to 5 s and decreasing the step size to 0.02°.

2.2.1.3 Bruker D8 Advance X-ray Diffractometer

To examine the erbium chromium sulphide materials and selected samples from $Ga_{1-x}Ge_xV_4S_8$ series the D8 Advance Bruker diffractometer fitted with a Bruker LynxEye linear detector was employed. The D8 diffractometer is operating with germanium-monochromated Cu-$K_{\alpha 1}$ radiation (λ = 1.54056 Å). Data were collected in step-scan mode over the angular range $10 \leq 2\theta/° \leq 120$ in 0.014° increments, counting for 2.4 s at each step.

2.2.2 Single Crystal X-ray Diffraction

Crystals of erbium chromium sulphides were characterised by single crystal X-ray diffraction using a Bruker X8-APEX 2 diffractometer [191] with graphite-monochromated Mo-K_α radiation (λ = 0.71073 Å). Data were processed using Bruker APEX2 software [192] suite incorporating COSMO and SAINT data collection strategies and data reduction, respectively.

For each material a single crystal with a regular shape was handpicked under an optical microscope from the bulk of the product, mounted on a glass fibre and loaded onto a goniometer head. The crystal was optically aligned within the X-ray beam using the video camera, which is interfaced to the computer and is operated through the VIDEO program. Typically a number of crystals were tested for quality (intensity and shape of the spots) and the best crystal was selected for subsequent data collection. The crystal's dimensions were measured using video camera. Data were collected at room temperature. The unit cell for the crystal was determined by collecting a series of three runs, for 6° Ω sweeps at Φ angles of 0, 120 and 240° and constant 2θ and χ angles, with twelve frames per run at 10 s capture. The reflections were harvested and indexed. The crystal was considered to be of a good enough quality for collecting data when more than 75 % of the spots were fitted by the assigned unit cell, and the RMS angle was lower than 0.25. A unit cell data collection strategy was then determined for a resolution of 0.7 Å and 10 s collection per frame. Collections were typically 6 – 8 hours long and collected at least 99 % of the data.

The measured intensity, *I(hkl)*, is affected by various factors for which corrections must be applied. The measured intensity was corrected to the observed structure amplitude, $|F_o|$, through the reduction process using the APEX2 software [192]. The reduction includes corrections associated with the data collection process, which are geometrical in nature. There are also other corrections which are needed, *i.e.*

corrections which take into account the fact that reflected radiation is partially polarised, corrections for changes in the incident X-ray beam intensity or in the scattering power of the crystal during the experiment (crystal decay) and for absorption effects. The various corrections were applied using the program SADABS [193]. The result of this process is a list of reflections as *h, k, l,* $|F_o|$, $\sigma(F_o)$, where *h, k, l* are Miller indices, $|F_o|$ is observed structure amplitude and $\sigma(F_o)$ is the standard uncertainty. The space group was determined using the APEX routine, XPREP, which compares the intensities that are equivalent by symmetry, and considers the special subsets of reflections with zero intensity.

The intensities of the diffraction pattern and the atomic coordinates are related by a Fourier transform [194]. The electron density, $\rho(xyz)$, is the reverse Fourier transform of the diffraction pattern

$$\rho(xyz) = \frac{1}{V}\sum_{h,k,l}|F(hkl)|\exp[i\Phi(hkl)]\exp[-2i\pi(hx+ky+lz)] \qquad (8)$$

The summation is performed for all the reflections in the diffraction pattern. It must be carried out for many various coordinates *x, y, z* to obtain an electron density map and hence locate the atoms in the unit cell where the electron density is the highest. The amplitudes $|F(hkl)|$ were measured and the exponential term was calculated for the contribution of each reflection *hkl* to each position *xyz*. The structure was solved by direct methods using the program SIR92 [195] to locate the heavy atoms. Direct methods involve selecting the strongest reflections which contribute the most to the Fourier transform. Probable relationships among the phases were calculated, and afterwards tried with different possible phases to see how well the probability relationships were satisfied. The model was refined using the CRYSTALS program suite [196]. From the best combination of phases a Fourier difference map was created. A Chebyshev polynomial was applied as a weighting scheme [197].

The quality of agreement between observed and calculated diffraction patterns (between the $|F_o|$ and $|F_c|$ amplitudes values) can be expressed by *R*-factor, (equation 9). For a correct crystal structure, *R*-factor is around 0.02 – 0.07.

$$R = \frac{\Sigma\big||F_o|-|F_c|\big|}{\Sigma|F_o|} \qquad (9)$$

2.2.3 Differential Thermal Analysis (DTA)

The DTA investigations of the samples from the ZnO – Bi_2O_3 – V_2O_5 and PbO – Bi_2O_3 – V_2O_5 systems, were carried out at the Szczecin University of Technology, Poland by means of a derivatograph of F.Paulik-J.Paulik-L.Erdey type (MOM, Budapest, Hungary). All measurements were conducted in an atmosphere of air, in the temperature range 293 – 1273 K at a heating rate of 10 K min^{-1}. The samples of 0.5 – 1 g weight subjected to the measurements were placed in quartz crucibles.

In differential thermal analysis technique the difference in temperature between the sample and a reference is recorded while heating. Al_2O_3 was used as a reference. In all the investigated samples negative peaks on heating were observed. It means that the temperature of the sample lags behind the temperature of the reference (endothermic thermal process).

2.2.4 Thermogravimetric Analysis (TGA)

Measurements of changes in sample mass of mixed–metal sulphides with temperature were performed on a DuPont Instruments 951 Thermogravimetric Analyzer. The sulphur content of the $Ga_{1-x}Ge_xV_4S_8$ samples was determined thermogravimetriacally by oxidation. The weight loss on conversion to the appropriate oxides is related directly to the sulphur content. Bulk samples of 10 – 20 mg were loaded into a quartz crucible suspended from the balance arm by a platinum wire. Measurements were performed in a flow of dry oxygen with a rate of 60 cm^3 min^{-1}. All samples were heated to 1273 K at 5 K min^{-1}. The maximum temperature was maintained for 60 minutes to ensure complete conversion to oxides.

2.3 Studies of Physical Properties

2.3.1 Electron Transport Measurements

The electrical resistance of the samples over the temperature range $77 \leq T/K \leq 300$ was determined using a standard four-probe DC technique. The samples were pressed into pellets under 10 tons of pressure using a 13 mm diameter Specac die and sealed into evacuated ($< 10^{-4}$ Torr) silica tubes. All the pellets were annealed at the temperature of the final firing to improve the mechanical robustness of the pellets and reduce grain boundary effects. A bar-shaped ingot (*ca.* $6 \times 3 \times 1$ mm) was cut from a sintered pellet

and four 50 μm silver wires (GoodFellow, 99.5 %) were attached, using conductive silver paint (RS components). The pellet was connected to an 8 pin DIL socket by silver paint as shown in Figure 24(a). The DIL socket was mounted on a sample stick (Figure 24(b)) to provide connections to an HP34401A multimeter. The sample stick was placed in an Oxford Instruments CF1200 cryostat connected to an ITC502 temperature controller. Liquid nitrogen was used as a coolant. Data were collected under computer control using a program written by Dr. Paz Vaqueiro of this department. The experimental setup for the electrical resistance measurements is shown schematically in Figure 25.

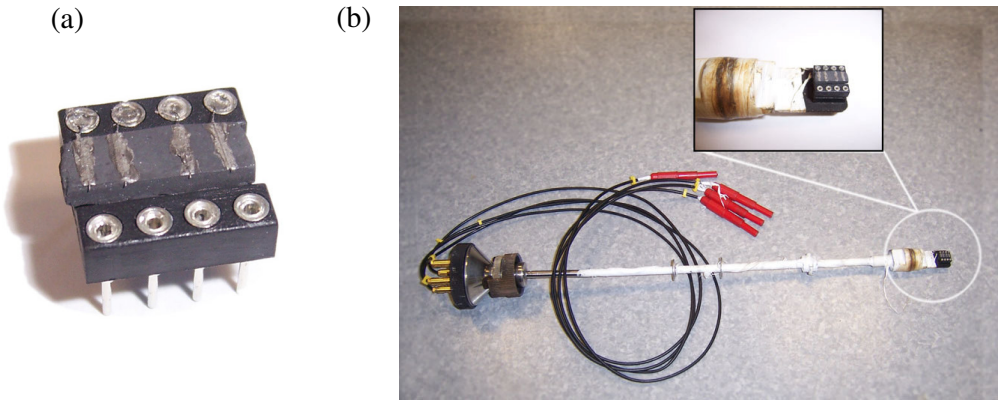

Figure 24: Sample (a) connected to the 8 pin DIL socket and (b) mounted on a sample stick.

In the four-probe DC technique a known current, *I*, is passed through a bar of the sample by two outer leads (A and D in Figure 26), while the voltage drop, *V*, across the sample is measured using two inner leads (B and C in Figure 26). This measures the resistance, *R*, of the sample while largely eliminating resistances arising from leads and contacts.

The resistivity, ρ, of the sample is obtained by first measuring its resistance, *R*, and then converting it to resistivity by taking into account the dimensions of the pellet

$$\rho = R \times A/d \qquad (10)$$

Where *A* is the cross-sectional area of the pellet ($A = a \times b$ in Figure 26) and *d* is the distance between the inner contacts through which the potential difference is measured. Values *A* and *d* are different for every pellet and they were measured using a micrometer. The resistance of a sample increases with its length and decreases with its

cross-sectional area. The electrical conductivity, σ, is the inverse of the resistivity and is equal to the number of charge carriers, n, their mobility, μ, and the charge on the carrier, ε_o

$$\sigma = n\varepsilon_o\mu \tag{11}$$

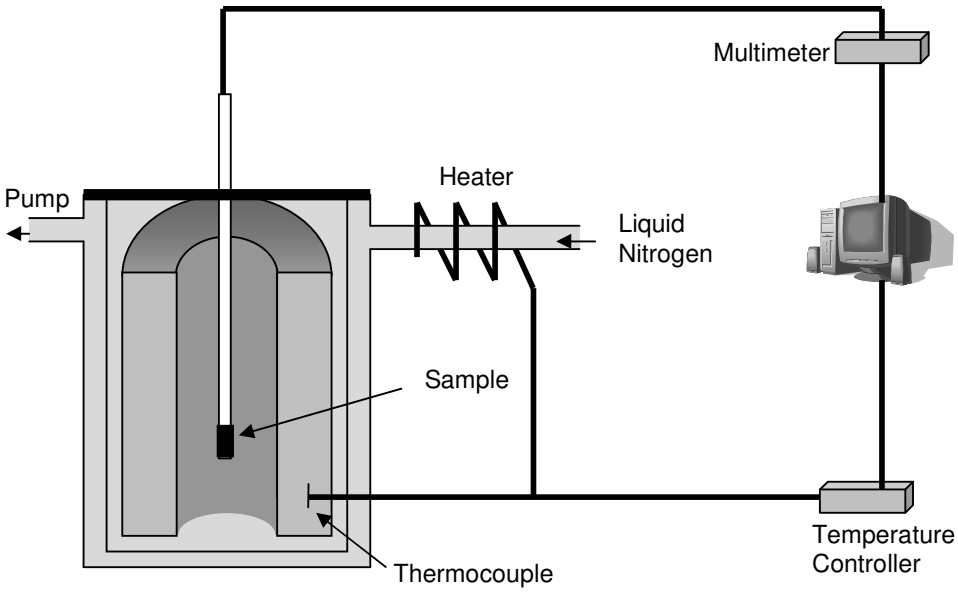

Figure 25: Experimental setup for electrical resistivity measurements.

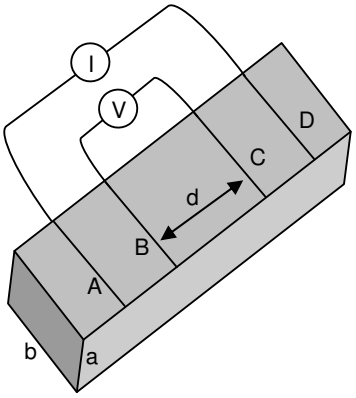

Figure 26: Schematic diagram of the four-probe technique.

2.3.2 Seebeck Measurements

Measurements of the Seebeck coefficient over the temperature range $100 \leq T/K \leq 300$ were made on the ingots (*ca.* $8 \times 4 \times 1$ mm) cut from a sintered pellets which were prepared in the manner described in the previous paragraph. The ingot was then mounted on a copper holder using Apiezon® Type N grease. A small amount of copper powder (Alfa Aesar, 99.5 %) was added to the grease to ensure good thermal and electrical contact between the sample and the holder. The copper holder incorporates a small heater (120 Ω strain gauge) located close to one end of the sample and is attached to the hot stage of a closed-cycle refrigerator (DE-202, Advanced Research Systems), controlled by a Lakeshore LS-331 temperature controller. Two 50 μm copper wires (GoodFellow, 99.5 %) were attached to the ends of the sample using high-temperature silver conductive coating (Electrodag® 503) and connections made to a Keithley 2182A nanovoltmeter. Two Au: 0.07 % Fe vs. chromel thermocouples were placed close to the sample at the hot and cold ends, and connected to a second Lakeshore LS-331 temperature controller. The measurements were carried out under computer control using a Labview program written by Dr. Paz Vaqueiro of this department.

The Seebeck coefficient at a given temperature was determined by applying a temperature gradient, ΔT, across the sample and measuring the corresponding thermal voltage, ΔV. The slope of the line, $\Delta V/\Delta T$, was used to determine the Seebeck coefficient. The data were corrected for the contribution from the copper wires [198].

A schematic diagram of the apparatus used for Seebeck coefficient measurements is presented in Figure 27. A bar-shaped sample is held between metal blocks *A* and *B*. The heater on one block (*B* in Figure 27) produces a temperature gradient in the sample. One junction is raised to a temperature slightly above the temperature *T* at which the Seebeck coefficient is to be measured. Temperatures at the two ends of the pellet are measured by thermocouples which are in good thermal and electrical contact with the sample.

The temperature gradient between hot and cold ends causes the diffusion of electrons. The electrons in the hot end are more energetic and they move towards the cold end leaving the positive ions in the hot region until a potential difference ΔV that prevents further diffusion is built up [199]. The electrons are accumulated in the cold region as shown in Figure 28. A voltage thus develops between hot and cold ends. The Fermi energy in the hot region is slightly lowered by the increase in temperature. However, the average energy per electron is greater in this region. The Seebeck effect, describes the electrical voltage difference ΔV across the bar of isolated conducting

sample due to a temperature difference ΔT [199]

$$S = dV/dT \tag{12}$$

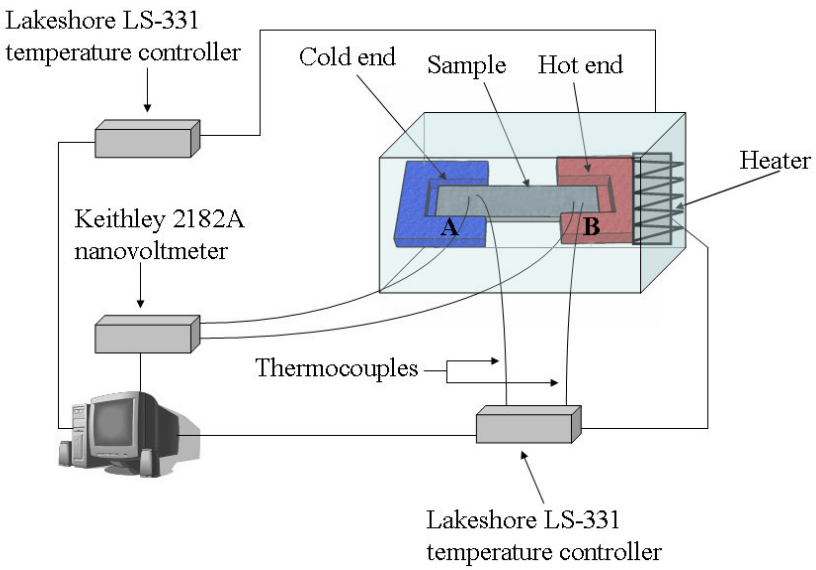

Figure 27: Schematic diagram of the apparatus used for Seebeck coefficient measurements.

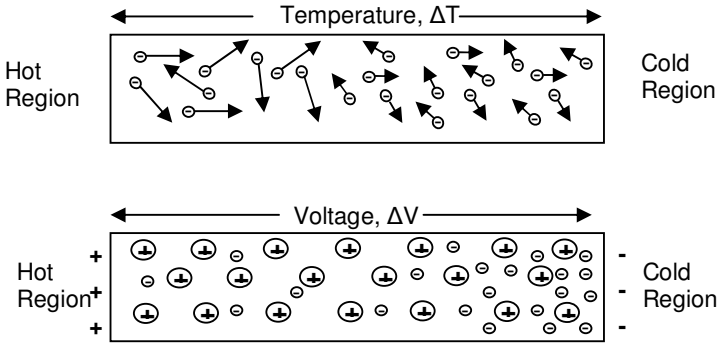

Figure 28: The Seebeck effect.

The change in entropy of the electrons in crossing the junction is π_{AB}/T, where π_{AB} is the Peltier coefficient [200]. The third law of thermodynamics requires the entropy change to approach zero when the absolute temperature approaches zero. It means that the Seebeck coefficient must approach zero. In actual materials it appears that the Seebeck coefficient approaches zero as the temperature approaches absolute

zero [201]. However, π_{AB}/T is the difference in the entropy of transport of the electrons and not the difference in their entropy. These entropies can be appreciably different from each other. According to Wood [200] there is a relationship between Peltier (π_{AB}) and Seebeck (S_{AB}) effects

$$\pi_{AB} = S_{AB}T \tag{13}$$

It means that Seebeck coefficient is equal to π_{AB}/T.

The Seebeck coefficient can be negative and this indicates that the material is *n*-type in which conduction is dominated by electrons. Hole-type conduction is indicated by a positive Seebeck coefficient. In these materials holes diffuse from the hot to the cold end. It means that the cold end is positive with respect to the hot end and material is called *p*-type. If charge carriers of both types are present the resulting Seebeck coefficient is a sum of their relative contributions (S_n and S_p) weighted by their contributions to the electrical conductivities (σ_n and σ_p) [200]

$$S = \frac{S_n\sigma_n + S_p\sigma_p}{\sigma_n + \sigma_p} \tag{14}$$

The Seebeck coefficient is usually expressed in μV K^{-1}.

2.3.3 Magnetic Susceptibility Measurements

When a substance is subjected to a magnetic field, $\boldsymbol{H}$ [A m^{-1}], the magnetisation of that substance, $\boldsymbol{M}$ [A m^{-1}], is defined as the magnetic dipole moment per unit volume [30]. Magnetisation is related to a magnetic field by the magnetic susceptibility, χ, which is the magnetisation induced by unit applied magnetic field

$$\boldsymbol{M} = \mu_o^{-1}\chi\boldsymbol{B} \tag{15}$$

where μ_o is the vacuum permeability. In practice more often the molar susceptibility, χ_{mol} [m^3 mol^{-1}], is used which is the susceptibility per mole of the substance

$$\chi_{mol} = \frac{\chi M_r}{10^3\rho} \tag{16}$$

where M_r [g mol^{-1}] is the relative molecular mass of the substance and ρ [g m^{-3}] is the density*.

Magnetic properties are often expressed in terms of the magnetic moment, μ, because this is related directly to the number of unpaired electrons. The total magnetic moment of a metal ion is due to a combination of the spin moments and the orbital moments of the electrons.

Magnetic moments are related to the electronic configuration via the quantum numbers, ***S***, ***L*** and ***J***. Electrons possess a total spin, ***S***, and orbital angular momentum, ***L***. The vector sum of the spin and orbital angular moments of an electron is defined as the total angular momentum, expressed by the quantum number, ***J***, which is related to the total magnetic moment, μ, by equation 18.

$$\boldsymbol{J} = \boldsymbol{S} + \boldsymbol{L} \tag{17}$$

$$\mu = g_J \sqrt{J(J+1)} \tag{18}$$

g_J is the "Landé g-factor" and is defined by following equation

$$g_J = \frac{3J(J+1) + S(S+1) - L(L+1)}{2J(J+1)} \tag{19}$$

For transition-metal ions, $g_J = 2$, whereas take the values between 1–2 for rare-earth ions. μ from the equation 18 can also be described by following equation

$$\mu = g_J J \mu_B B_J\left(\frac{g_J J \mu_B \mu_0 H}{kT}\right) \tag{20}$$

where J is the exchange constant, k is Boltzmann constant, μ_B is Bohr magneton, μ_0 is the permeability of the free space and B_J is the Brillouin function given by equation 21.

$$B_J = \left(\frac{1}{J}\right)\left[(J+0.5)\coth(J+0.5)x - 0.5\coth\left(x/2\right)\right] \tag{21}$$

$$x = \left(\frac{g_J J \mu_B \mu_0 H}{kT}\right) \tag{22}$$

* Susceptibility data quoted in cgs/-emu terms, e.g. in cm^3 mol^{-1}, can be translated into SI quantities (m^3 mol^{-1}) through multiplication by $4\pi \times 10^{-6}$.

At high fields and low temperatures $x >> 1$ and $B_J(x) \rightarrow 1$ and the equation 20 is reduced

$$\mu = g_J J \mu_B \tag{23}$$

For transition metal ions, it is frequently assumed that the spin-orbit coupling is $<< kT$, and that the thermal energy is sufficient to populate all levels of the lowest lying multiplet to an effectively equal extent. The best agreement with the experimentally observed moments is obtained from the spin-only formula (equation 24), where the orbital contribution is zero ($L \approx 0$) and hence $J = S$ and $g_J = 2$.

$$\mu_{so} = 2\sqrt{S(S+1)} \tag{24}$$

$g_J = 2$ for the first row transitions metal ions. Later transition metals exhibit spin-orbit coupling and the situation becomes more complicated.

The magnetic moment is measured in Bohr magnetons (μ_B) and for a single electron gives a value $\mu_{so} = 1.73\ \mu_B$, where the Bohr magneton is defined by following equation:

$$1\mu_B = \frac{eh}{4\pi mc} \tag{25}$$

where e is the electron charge, h is Planck's constant, m the electron mass and c the velocity of light.

Magnetic data for erbium chromium sulphides were collected in the Centro Atómico Bariloche in Argentina by Dr. R.D. Sánchez. Magnetic measurements over the temperature range $90 \leq T/K \leq 300$ were performed using a LakeShore 7300 series vibrating-sample magnetometer (VSM), with magnetic field up to 10,000 G. Samples were contained in Lucite® capsules (previously turned and magnetically tested) and measurements were conducted in an applied field of 1000 G, after cooling in zero applied field (zfc). The magnetisation data as a function of temperature, under zero field cooling (zfc) and field cooling (fc) conditions, were collected in a commercial superconducting quantum interference device (Quantum Design MPMS-5S) between 4 and 300 K and at $H = 1000$ G.

The magnetic properties of the $Ga_{1-x}Ge_xV_4S_8$ ($0 \leq x \leq 1$) materials and of Er_2CrS_4 were measured using a Quantum Design Magnetic Property Measurement System (MPMS®) SQUID susceptometer (Superconducting Quantum Interference Device). A SQUID is a very sensitive detector for measuring magnetic responses from

a sample. Utilizing the Josephson junction based on the quantum tunnelling effect allows the SQUID detector to sense magnetic fields as low as 10^{-14} T. The MPMS® does not measure the magnetic response from the sample directly. It works by accurately measuring the changes in magnetic flux density produced by a sample as it moves through a series of detection coils which are located at the midpoint of the superconducting solenoid (Figure 29). The detection coils are inductively coupled to the input of a SQUID detector which is located in a magnetic shield below the detection coils. The magnetic field applied to the sample is produced by the superconducting magnet. When the sample moves through the detection coils, its magnetic moment causes a change in magnetic flux which induces an electric current in the detection coils. The current is then detected by the SQUID detector. The magnetic moment of the sample is determined by measuring the output voltage of the SQUID detector by fitting a function to the voltage response and extracting the moment.

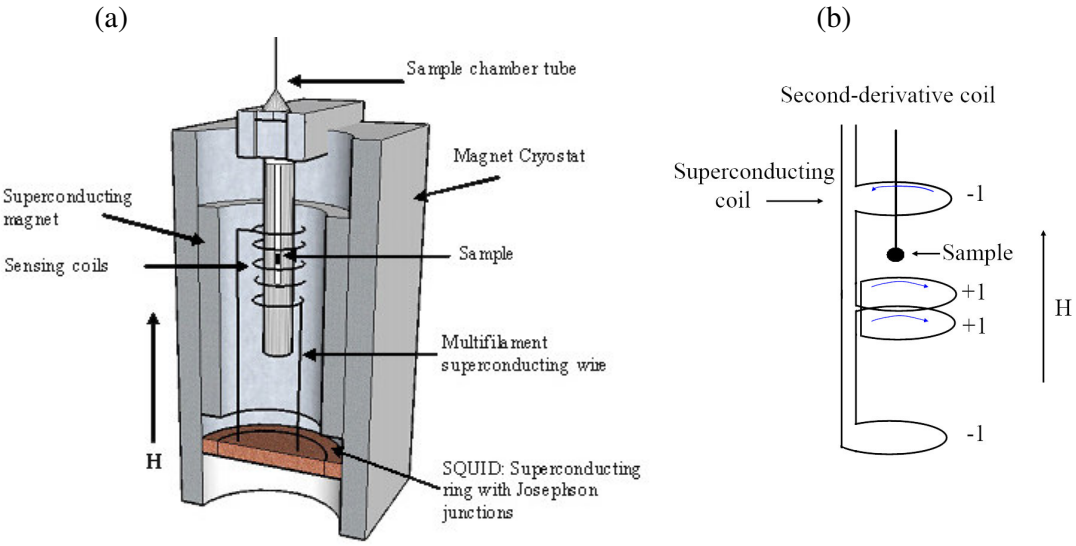

Figure 29: Schematic diagram of a SQUID magnetometer: (a) the location and (b) the configuration of the second-order gradiometer superconducting detection coil.

SQUID measurements were carried out at the University of Edinburgh. Samples of *ca.* 50 mg were weighed and loaded at room temperature into gelatine capsules of known weight. The capsule was positioned nearly in the middle of a transparent plastic drinking straw (typical diamagnetic contribution: 10^{-5} emu in 1 T). A few holes in the upper end of the straw were punctured to let air out during the sample chamber evacuation. The straw was attached to the end of the sample stick and placed in the

sample transport. The sample was first centred in the second-order gradiometer pickup coil in order to get a uniform magnetisation of the sample. The centering of the sample was performed via GPIB connection using the Graphical User Interface (GUI) software, MultiVu®. The external magnetic field and temperature were controlled using the same software. The MultiVu® software also provides control of measurements, for example field-cooled and zero-field cooled measurements through a series of commands. Data were collected over the temperature range $5 \leq T/K \leq 310$, both after cooling in zero applied field (zfc) and after cooling in the measuring field (fc) of 1000 G. Data were collected in 1 K steps at low temperatures, increasing gradually to 10 K steps in the range of 100 – 310 K. Measurement of the magnetisation as a function of field was performed for Er_2CrS_4 at 5 K by collecting data between 0 G and 10,000 G in 500 G steps.

The SQUID output is expressed as raw magnetisation, M_{raw} (emu). The gelatin capsule has a diamagnetic signal (negative signal) and the data were corrected for the diamagnetic contribution of the capsule

$$M_{cap} = -3.188 \times 10^{-10} \times \text{mass of capsule (mg)} \times \text{field (G)} \tag{26}$$

The molar susceptibility, χ_{mol}, can be calculated using the formula

$$\chi_{mol} = \frac{M_{corr}}{nH} \tag{27}$$

where H is the external field, n is the number of mols of the sample and M_{corr} is a corrected magnetisation

$$M_{corr} = M_{raw} - M_{cap} \tag{28}$$

χ_{mol} was corrected for the diamagnetic contribution from the ions within the formula unit.

For the materials which exhibit Curie-Weiss behaviour, the temperature dependence of the susceptibility is given by following equation

$$\chi_{mol} = \frac{C}{T - \theta} \tag{29}$$

where C is the Curie constant and θ is the Weiss temperature. θ is a measure of the interactions between the magnetic moments and is characteristic of a substance. It is typically positive for materials that order ferromagnetically at low temperatures and negative for antiferromagnetic materials. The Weiss temperature is an indicator of the dominant exchange interactions. When a material obeys the Curie-Weiss law, a plot of $1/\chi_{mol}$ against temperature is a straight line. The slope of the line is the Curie constant, and the intercept is Weiss constant

$$\frac{1}{\chi_{mol}} = \frac{1}{C}T - \frac{\theta}{C} \tag{30}$$

The Curie constant is related to the effective magnetic moment by the formula

$$\mu_{eff} = \sqrt{\frac{8C}{n}} \tag{31}$$

where n is the number of magnetic ions. When there are more than one type of magnetic ions present the Curie constant in the above equation can be calculated using formula

$$C_{th} = \frac{1}{8}\mu_1^2 + \frac{1}{8}\mu_2^2 + ... + \frac{1}{8}\mu_n^2 \tag{32}$$

where μ_1, μ_2, …, μ_n are spin-only magnetic moment values of magnetic ions present in the sample.

The measurements of magnetisation as a function of field at low temperatures allow the calculation of the saturated magnetic moment per magnetic centres in the sample, μ_{sat}

$$\mu_{sat} = \frac{M_{corr}}{anN_A\mu_B} \tag{33}$$

where a is the number of magnetic centres in the formula unit, N_A is Avogadro number and μ_B is the Bohr magneton. In case of first row transition metal ions ($J = S$), the theoretical magnetic saturated moment approaches a maximum of $2S$ in the ferromagnets. In the ferrimagnets different values of μ_{sat} occur.

2.4 Neutron scattering

2.4.1 Introduction

Neutron measurements on $Ga_{1-x}Ge_xV_4S_8$ samples were performed at the Institut Laue-Langevin (ILL), Grenoble, France. Investigations on erbium chromium sulphides materials were carried out at the ISIS facility, Rutherford Appleton Laboratory, UK.

Neutron scattering on gases, liquids and solid matter is a very powerful tool for the study of materials from many points of view. Neutron diffraction is a very useful technique for investigating the structure of crystalline materials and can provide information about magnetic ordering, that is not attainable using other techniques. The neutron is electrically neutral with a mass 1,839 times bigger than that of electron and a lifetime of about 1,000 seconds as a free particle [7]. The thermal neutron exhibits features, such as absence of electrical charge, wavelength comparable to that of interatomic distances and a magnetic moment. The scattering powers of atoms towards neutrons are quite different from those towards X-rays. In X-ray diffraction, the scattering power of an atom is related to its atomic number. Neutrons interact with unpaired electrons and are diffracted by both atomic nuclei and unpaired electrons. Light atoms diffract X-rays very weakly but may be strong scatterers of neutrons (Figure 30). Neutron diffraction provides discrimination between atoms which have similar X-ray scattering powers, like for example Mn and Fe. Neutrons give a continuous spectrum of radiation, without the intense characteristic peaks which are observed in X-ray diffraction patterns. The neutron wavelength, λ, used for diffraction, is of the order 0.5 to 3 Å and is related to the neutron mass by the Broglie relation. It depends on velocity, v:

$$\lambda = \frac{h}{mv} \tag{34}$$

where h is Planck's constant and m is the mass of the neutron.

The relationship between wavelength and diffraction angle is given by Bragg's law (equation 35). Figure 31 presents a graphical representation of Bragg's law.

$$n\lambda = 2d \sin\theta \tag{35}$$

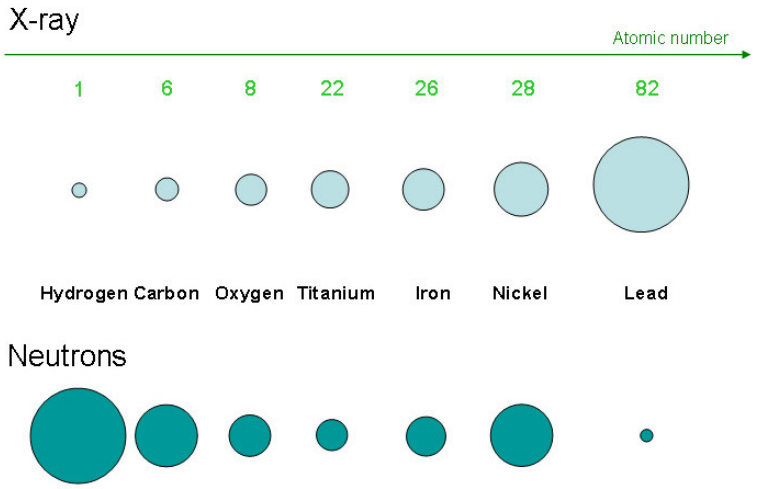

Figure 30: Comparison of neutron and X-ray scattering cross-sections of the same set of elements.

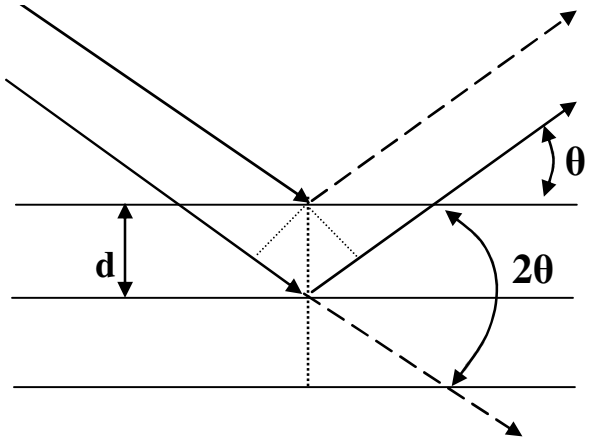

Figure 31: A graphical representation of Bragg's law.

During the neutron measurement at a reactor source, such as ILL, λ is constant and the diffraction angle, θ, is changing. In pulsed neutron sources with time-of-flight (TOF) analysis a "white" source with a range of λ is used with a fixed angle.

2.4.1.1 Magnetic Neutron Scattering

Neutron diffraction is often used to study magnetic structures of materials. Neutrons are not scattered by electrical charges within matter and have spin ½, which is directed opposite to the angular momentum and have magnetic dipole moment of μ_n = -1.913 μ_N

(with the nuclear magneton $\mu_N = 5.051\times10^{-27}$ J T^{-1}). However, they are scattered by the spin of unpaired electrons in the sample if they exist. When a material reveals long-range magnetic order in neutron analysis, magnetic Bragg peaks in neutron diffraction pattern at low temperatures are observed. This is because the long-range magnetically ordered unpaired electrons cause the neutrons to be scattered coherently, similar to the scattering of neutrons by the nuclei of the atoms. Magnetic and nuclear interaction strengths are often of the same order of magnitude, such that magnetic and structural properties of the sample can be examined simultaneously.

In this study, the Rietveld refinement technique [187] was used to refine the magnetic structure model using GSAS software [189].

2.4.2 Measurements at ILL

High-resolution powder neutron diffraction data were collected on the D2B and D1A diffractometers at the high-flux reactor, located at the Institut Laue-Langevin (ILL), Grenoble in France (Figure 32).

2.4.2.1 The High-flux Reactor at ILL [202]

The reactor at the Institut Laue-Langevin, Grenoble produces 1.5×10^{15} neutrons per second per cm^2, with a thermal power 58.3 MW. The 2.5 m diameter tank contains the single fuel element placed in its centre and the heavy water moderator which partly reflects thermalised neutrons back towards the fuel element. Heavy water circulates and passes through heat exchangers. The reflector tank is surrounded by a light water swimming pool encased in concrete. The essential features for the high-flux reactor at the ILL are listed in Table 8.

Table 8: Characteristics of the high-flux reactor at the ILL, Grenoble [202].

Thermal power	**58.3 MW**
Max. unperturbed thermal flux in the reflector	1.5×10^{15} neutrons cm^{-2} s^{-1}
Max. perturbed thermal flux at the beam tubes	1.2×10^{15} neutrons cm^{-2} s^{-1}
Reactor cycle	50 days
Average consumption of ^{235}U	36 %

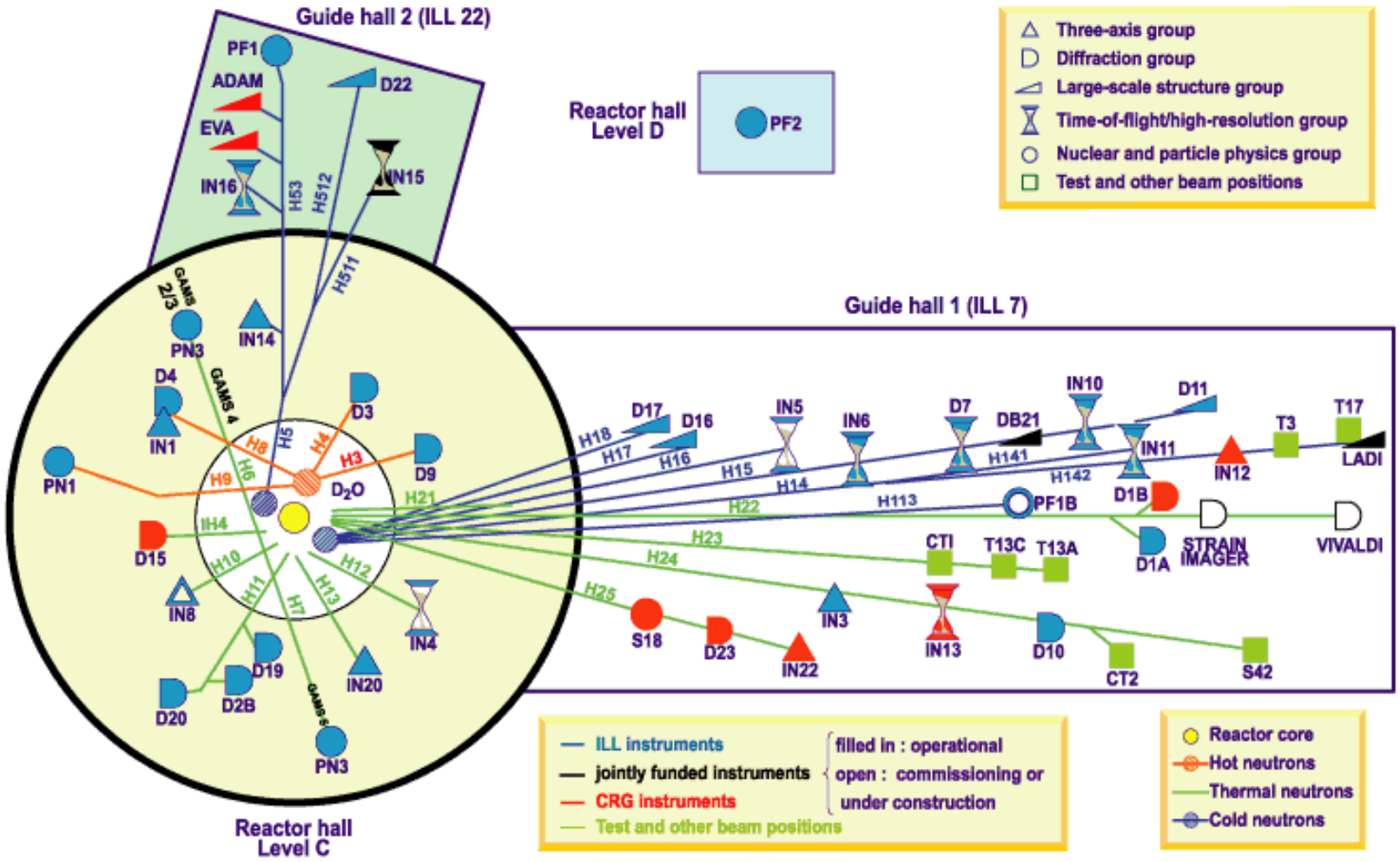

Figure 32: Experimental facilities at the ILL, Grenoble, France [202].

2.4.2.2 The D2B Diffractometer

The D2B instrument is a very high-resolution powder diffractometer (Figure 33) located at the Institut Laue-Langevin, Grenoble, France. It is used mostly for work on magnetism with high resolution and high intensity. The D2B diffractometer is characterised by a very high take-off angle (135°). The D2B detector bank was recently replaced by a new pseudo-2D detector (Figure 33(b)), improving both signal and background. It also allows collecting data on small samples as 0.2 – 0.5 g with high resolution in a few hours or samples of a few grams in a few minutes. There are 128 detectors spaced at 1.25° intervals. In D2B diffractometer it is possible to use wavelengths as short as 1.05 Å. The optimum wavelength for D2B is 1.594 Å which can be quickly changed under computer control, since they are all obtained by a simple rotation within the Ge [*hkl*] plane. A large graphite filter can be switched in to provide a very clean beam at 2.4 Å, and a cold Be-filter can be used for longer wavelengths. The instrument data for D2B diffractometer are listed in Table 9.

(a) (b)

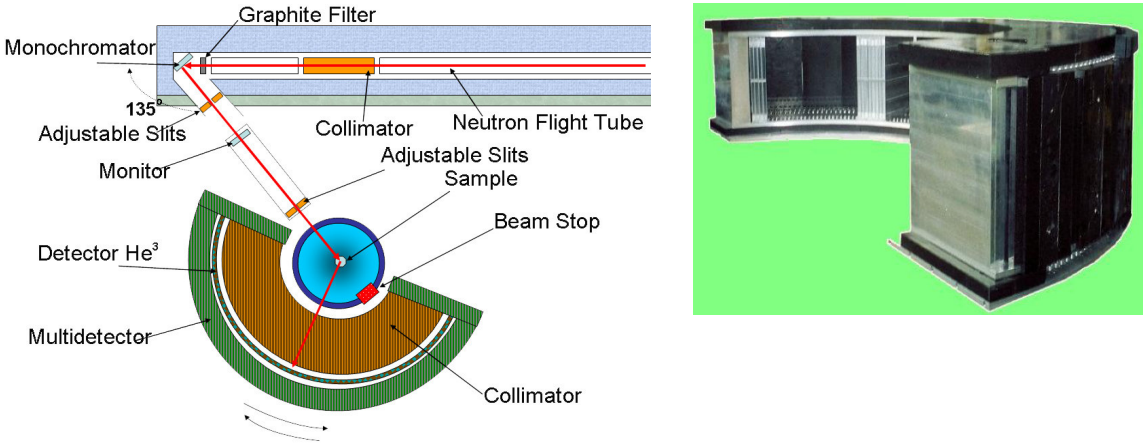

Figure 33: High-resolution (a) two-axis diffractometer D2B, adopted from [202] and (b) 2-D detector [203].

Table 9: Instrument data for D2B diffractometer [202].

Monochromator	
28 Ge [115] crystals of $1 \times 5 \times 1$ cm^3	
Take-off-angle	135°
Ge [*hkl*]	wavelength λ/Å
335	1.594 (optimum λ)
flux at sample λ = 1.594 Å	10^6 high resolution 10^7 high intensity
Sample	
Beam size at sample	2×5 cm^2
Angular range	$5° < 2\theta < 165°$
Detectors	
128 ^{3}He counting tubes	
Background without sample	0.1 Hz

2.4.2.3 The D1A Diffractometer

D1A is a high-resolution two-axis diffractometer with a high take-off angle (Figure 34). The instrument is able to provide high resolution at long wavelengths, with shorter wavelength contamination eliminated by the guide tube. The wavelengths used in D1A range from 1.39 Å to 2.99 Å and can be easily changed by rotation of the focusing monochromator. The optimum wavelength for the D1A diffractometer is 1.911 Å. The D1A diffractometer is particularly suited to magnetic structures. Complete scans on the D1A instrument take 2 to 10 hours. D1A gives excellent results with the Rietveld refinement due to its nearly perfect Gaussian peak shape for 2θ between 30° and 150°. Crystal structures with low-symmetry unit cells and cell values up to *ca.* 1000 Å may be satisfactorily refined using D1A. Table 10 lists the instrument data for D1A and Table 11 compares the D2B and D1A diffractometers.

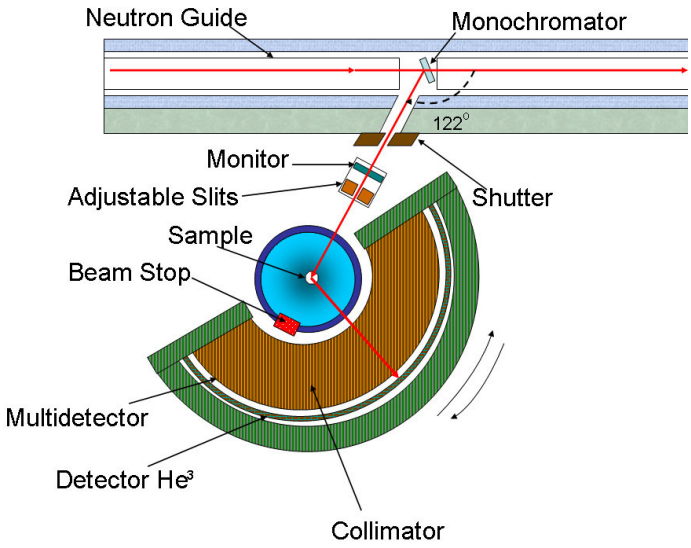

Figure 34: High-resolution two-axis diffractometer D1A, adopted from [202].

Table 10: Instrument data for D1A diffractometer [202].

Monochromator	
30 Ge crystals, 30 mm high	
Take-off-angle	122°
Ge [*hkl*]	wavelength λ/Å
115	1.911 (optimum λ)
Flux at sample	2×10^6 ncm^{-2} s^{-1}
Sample	
Beam size at sample	2 × 30 mm < SUP > 2 < SUP >
Angular range	$6^\circ < 2\theta < 160^\circ$
Detectors	
25 ^{3}He counters at 5 atm	
Efficiency	90 % at 1.5 Å
Background without sample	0.04 Hz

2.4.2.4 Experiments at ILL

High-resolution powder neutron diffraction data were collected at several temperatures over the angular range $0 \leq 2\theta/° \leq 158$ at a neutron wavelength of 1.59432 Å on the D2B diffractometer at the high-flux reactor, at the Institut Laue-Langevin. Up to 3 g of sample were contained in a thin-walled vanadium can, mounted in a standard ILL

cryostat. A complete diffraction pattern was obtained after about 25 steps of 0.05° in 2θ. Such scans take typically 30 minutes. Repetition and summation of such scans was used to improve statistics. Data were collected over a period of *ca.* 6 – 8 hours, depending on the size of the sample. Smaller samples needed longer data collection time. Additional low temperature data at 48, 38, 28, 18 and 2 K were collected for $Ga_{0.25}Ge_{0.75}V_4S_8$ using the high-resolution D1A diffractometer (λ = 1.9090 Å) also at ILL, over the angular range $0 \leq 2\theta/° \leq 158$.

Table 11: Comparison of D1A and D2B diffractometers [202].

	D1A		D2B	
λ/Å	1.9	3.0	1.6	2.4
d_{min}/Å	1	1.5	0.8	1.2
d_{max}/Å	27	42	22	34
Time/dataset	5 h	4 h	1 h	2 h
Resolution $\Delta d/d \times 10^{-3}$	2		0.5 – 1.5[†]	

2.4.3 Measurements at ISIS

Powder neutron diffraction data on erbium chromium sulphide samples were collected on the POLARIS and OSIRIS diffractometers at the ISIS facility, CCLRC Rutherford Appleton Laboratory, UK (Figure 35).

2.4.3.1 The Production of Neutrons at ISIS [204]

Neutrons at ISIS are obtained by the spallation process using intense pulses of high energy protons produced by accelerator. Proton acceleration at ISIS begins with the ion source, which produces H ions from hydrogen/caesium plasma. The H then are speeded up to 70 MeV by a linear accelerator and passed through a 3 μm thick aluminium oxide stripping foil which strips H electrons. The protons produced are directed into a synchrotron which traps the beam into two bunches and accelerates them to 800 MeV. They are then directed towards a heavy metal target. Neutrons are produced when the

[†] high resolution and high intensity mode

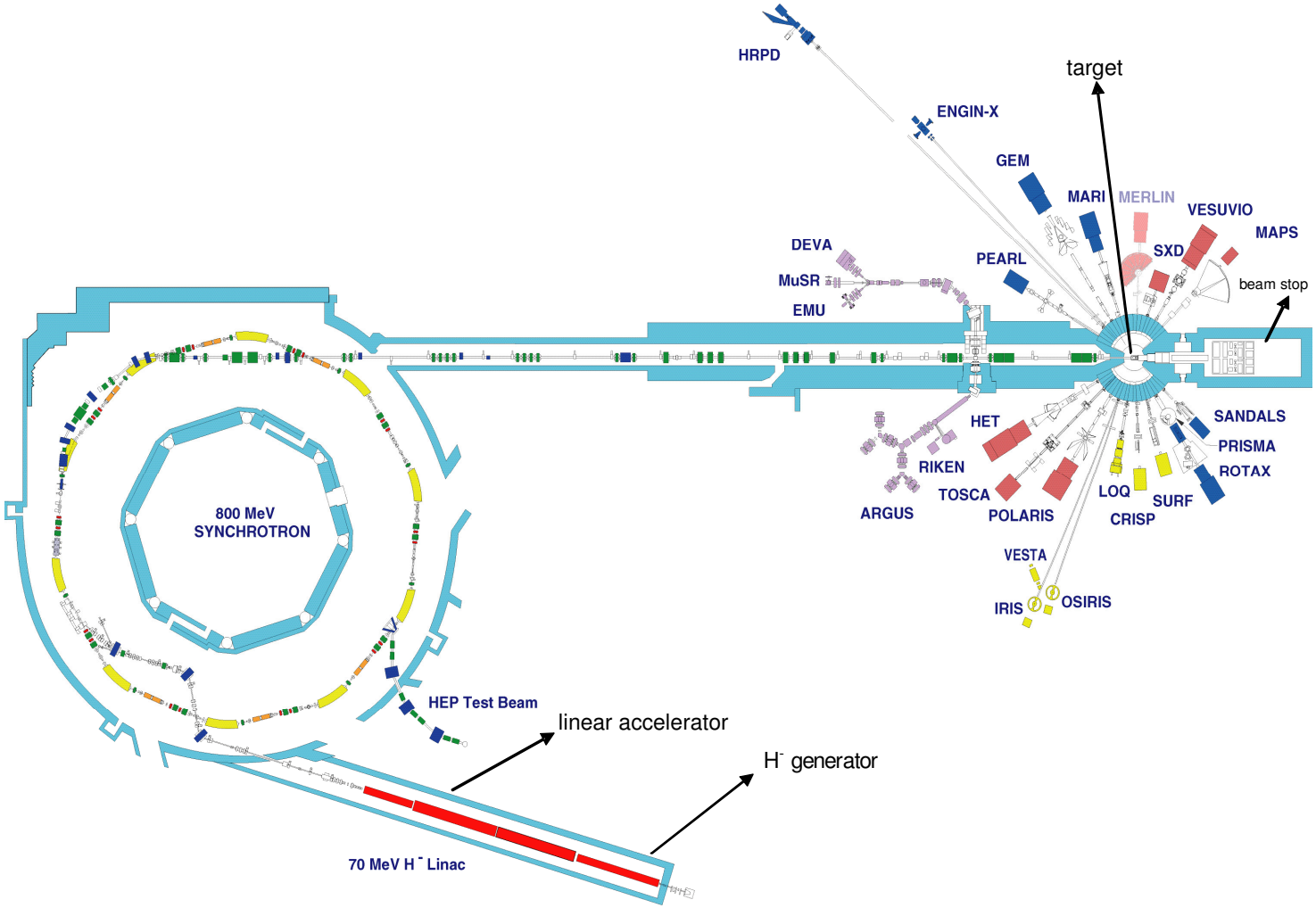

Figure 35: Experimental facilities at ISIS [205].

160 kW proton beam from the accelerator bombards a metal target. The target is made from a series of thick tungsten plates, covered with tantalum to prevent corrosion. Collision with the target causes a decay process that produces 15 neutrons per collision. Neutrons are then slowed down by moderators around the target and directed to neutron instruments at ISIS (Figure 35). The moderators are surrounded by a beryllium reflector which scatters neutrons back into the moderators and doubles the useful flux of neutrons. There are four moderators at ISIS. Two moderators use water at room temperature, one uses liquid methane at 100 K and the fourth liquid hydrogen at 20 K. The different temperatures result in different energy neutron beams.

2.4.3.2 The OSIRIS Diffractometer at ISIS

OSIRIS is a long wavelength diffractometer and backscattering crystal-analyser spectrometer located at the ISIS facility. With regard to spectroscopy, it is an inverted geometry instrument such that neutrons scattered by the sample are energy analysed by means of Bragg scattering from large-area crystal-analyser array. In common with the POLARIS instrument at a pulsed neutron-source, the time-of-flight (TOF) technique is used for data analysis. Instrument data for OSIRIS are listed in Table 12.

Table 12: Instrument data for OSIRIS.

Diffractometer specifications	
Angular range	$150 \leq 2\theta/° \leq 171$
Resolution	$2.5 \times 10^{-3} < \Delta d/d < 6 \times 10^{-3}$
d-spacings range/Å	0.8 - ~ 20

The instrument views a liquid hydrogen moderator cooled to 25 K and consequently has access to a large flux of long-wavelength cold neutrons. OSIRIS has two coupled spectrometer components: the primary component (beam transport) and the secondary spectrometer (Figure 36 and Figure 37).

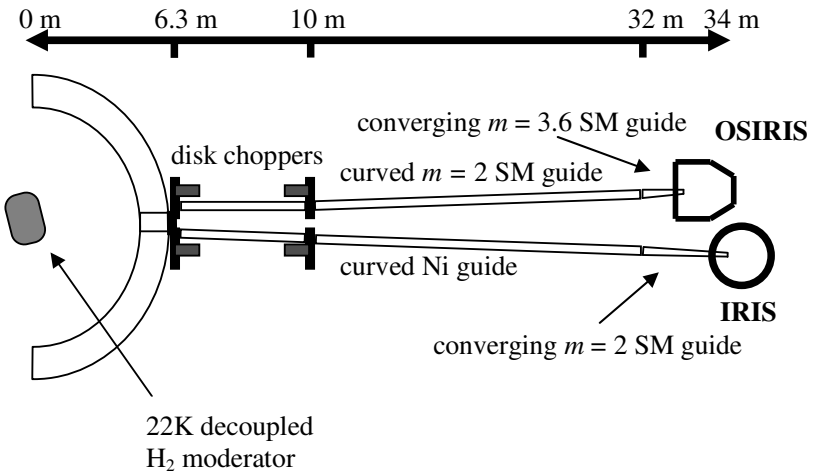

Figure 36: The OSIRIS primary spectrometer [26].

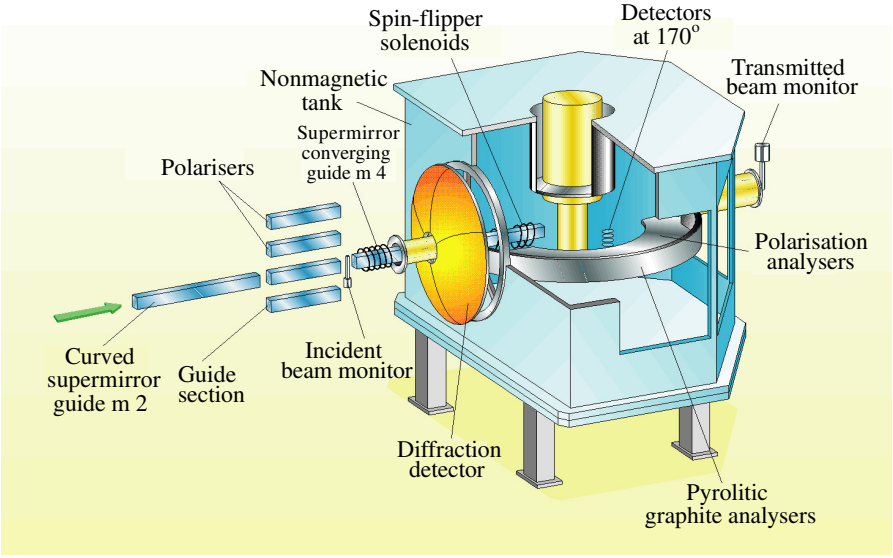

Figure 37: The OSIRIS secondary spectrometer [206].

Neutron beam transport, from moderator to sample position, is achieved using a curved neutron guide. Due to the curvature of the guide no neutron with a wavelength less than approx 1.5 Å is transported. While the majority of the guide section consists of accurately aligned, nickel-titanium coated (m = 2), super mirror sections (1 m long, 65 mm high by 43 mm wide), a 1.5 m-long converging m = 3.6 guide piece terminates the end. This tapered component helps focus the beam at the sample position (44 mm (high) by 22 mm (wide)) but also serves to increase flux. The incident neutron flux at the sample position is approximately 2.7×10^7 ncm^{-2} s^{-1} (white beam at full ISIS

intensity) with the wavelength intensity distribution at the sample position (up to 12 Å). However, the flux at longer wavelengths (> 12 Å) is still sufficient to detect Bragg peaks with *d*-spacing close to 17.5 Å (corresponding to ~ 35 Å neutrons) without significant frame overlap.

The incident beam monitor is placed immediately after the Polariser Interchanger. There is also a transmitted beam monitor in the tube after the sample bin. Both are glass bead monitors. There are five beads horizontally and six vertically and the active component is ^{6}Lithium. The monitor efficiencies are wavelength-dependent, but always less than 1 % over the range of wavelengths accessible on OSIRIS.

The diffraction detector bank on OSIRIS is used for either simultaneous measurement of structure vs. quasi/in-elastic information or purely crystallographic determination during a diffraction experiment. Scattered neutrons reach the diffraction detectors directly and time-of-flight analysis is used to determine the *d*-spacing of the observed Bragg reflections.

2.4.3.3 POLARIS Diffractometer at ISIS

POLARIS (Figure 38) is a medium resolution, high intensity time-of-flight powder diffractometer located at the ISIS facility. Using POLARIS it is possible to perform experiments on small size samples (as little as ~ 1 mm^3) and with short counting time (with data collection times down to ~5 minutes). It is because of intense neutron flux on this instrument, combined with a large detector solid angle. POLARIS receives neutrons from the ambient temperature water moderator. Wavelengths used on this instrument are in the range $0.1 \leq \lambda/\text{Å} \leq 6.0$. Neutrons are detected in four discrete resolution focused banks: low and very low angle, 90° and backscattering. Table 13 lists the detector bank details.

2.4.3.4 Experiments at ISIS

During the experimental work at ISIS, data were collected on *ca.* 1.5 g of sample loaded into a vanadium sample can. The can was attached to a sample stick and loaded to a cryostat, placed in the sample chamber. For data collection at room temperature on POLARIS, the can was attached to a sample stick so that the centre of the sample was 314 mm from the lower face of the aluminium plate on the stick. In this case the sample stick was placed directly into the sample chamber. Variable temperature studies were

performed on Er_3CrS_6, Er_2CrS_4, $Er_6Cr_2S_{11}$ and Er_4CrS_7 samples. Initial data manipulation and reduction was carried out using GENIE spectrum manipulation software [207].

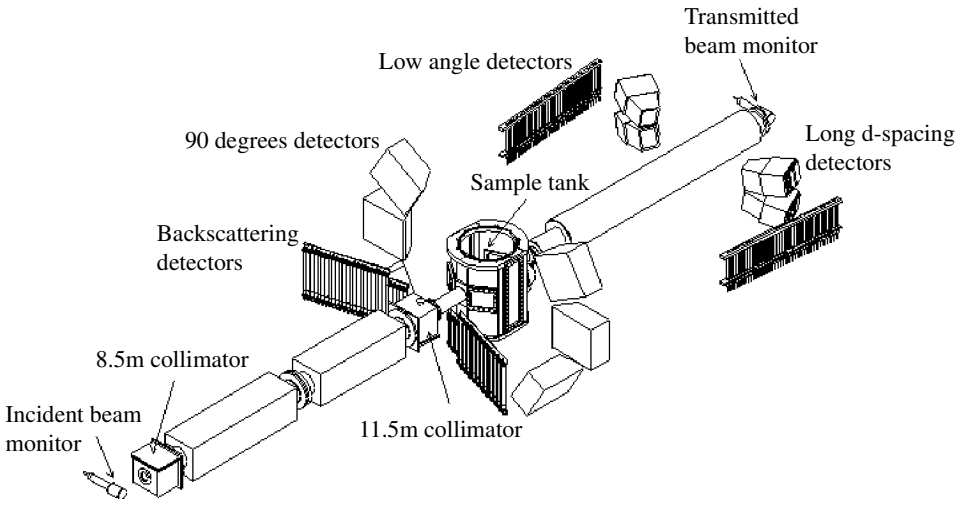

Figure 38: POLARIS instrument [208].

Table 13: POLARIS detector bank details [208].

Bank	**Low angle (A)**	**Very low angle (B)**	**90° (E)**	**Backscattering (C)**
Detector type	^{3}He gas tubes (½")	ZnS scintillator	ZnS scintillator	^{3}He gas tubes (1")
No. of detectors	2 × 40 = 80	4 × 20 = 80	6 × 36 = 216	2 × 29 = 58
2θ range	$28 \leq 2\theta/° \leq 42$	$13 \leq 2\theta/° \leq 15$	$83 \leq 2\theta/° \leq 97$	$130 \leq 2\theta/° \leq 160$
Resolution, $\Delta d/d$	~ 1×10^{-2}	~ 3×10^{-2}	~ 7×10^{-3}	~ 5×10^{-3}
d – range/Å	0.5 – 8.3	0.5 – 21.6	0.3 – 4.0	0.2 – 3.2

2.5 Structure Refinement by the Rietveld Method

The structures of all the compounds from a series of sulphides $Ga_{1-x}Ge_xV_4S_8$ ($0 \leq x \leq 1$) and erbium chromium sulphides were refined by the Rietveld method [187, 188, 209], using the General Structure Analysis System GSAS suit of programs [189] with input through the EXPGUI interface [190]. Rietveld refinement was used for the processing and analysis of powder diffraction data obtained with X-rays or neutrons. The goal of Rietveld analysis is to refine a structural model to the diffraction data. The intensities of Bragg peaks in a diffraction pattern were calculated within the constraints imposed by a crystallographic space group. In the Rietveld method no effort is made to assign observed intensity to a particular Bragg peak or to resolve overlapped peaks. Therefore a good starting model for the structure refinement is needed. This method is not a structure determination method. It is also very important to obtain good quality data. The quality of the data can be improved by ensuring the crystallites are randomly ordered, reasonably sized and have a narrow particle size distribution. In the Rietveld method the entire diffraction profile is modelled and compared with the observed profile point by point. The parameters of the structural model were refined using the least-square method until the best-fit between theoretical line profile and the measured profile was achieved. The weighted difference between the observed and calculated diffraction patterns (Rietveld residual), S_y, is the sum of overall data points, ideally $S_y = 0$.

$$S_y = \sum_i w_i (y_{iobs} - y_{ical})^2 \tag{36}$$

w_i is a weighting factor ($w_i = 1/y_{iobs}$), y_{iobs} and y_{ical} are the observed and calculated intensities at the i^{th} step, respectively. y_{ical} is a combination of many factors and it is given by following equation

$$y_{ical} = s\sum_K L_K |F_K|^2 \varphi(2\theta_i - 2\theta_K) P_K A + y_{bi} \tag{37}$$

where:

s is the scale factor;

K represents Miller indices $h, k, l,$ for a given reflection;

L_K are Lorentz, polarisation and multiplicity factors;

φ is the reflection profile function;

P_K is preferred orientation function;

A is an absorption factor and it differs with instrument geometry;

F_K is the structure factor for the K^{th} reflection;

y_{bi} is the background intensity at point i.

$|F_K|$ depends on the positions of each atom j within the unit cell

$$F_K = \sum_j N_j f_j \exp[2\pi i(hx_j + ky_j + lz_j)]\exp(-M_j) \tag{38}$$

where h, k, l are Miller indices, N_j is the site occupancy factor for the j^{th} atom site, x_j, y_j, z_j are the coordinates for atom j, and f_j is the scattering power of the j^{th} atom. $exp(-M_j)$ describes the thermal displacement of the scattering centre

$$M_j = 8\pi^2 \overline{u}_s^2 \sin^2\theta / \lambda^2 \tag{39}$$

$\overline{u}_s^2$ in the above equation is the root-mean-square of the thermal motion of the j^{th} atom parallel to the diffraction vector.

The least squares minimisation procedure results in a set of equations involving derivatives of the calculated intensities, y_{ical}, with respect to every adjustable parameter. The solution is found in an iterative procedure

$$\Delta x_k = \sum M_{jk}^{-1} \frac{\partial S_y}{\partial x_k} \tag{40}$$

Δx_k is the shift and x_k is the adjustable parameter. M_{jk}^{-1} is given by following equation

$$M_{jk}^{-1} = -\sum_i 2w_i \left[(y_i - y_{ical}) \frac{\partial^2 y_{ical}}{\partial x_j \partial x_k} - \left(\frac{\partial y_{ical}}{\partial x_j} \right) \left(\frac{\partial y_{ical}}{\partial x_k} \right) \right] \tag{41}$$

To improve the model, the calculated shifts are applied to the initial parameters and then the process is repeated.

Typically in the first step of the Rietveld refinement the background and scale factor are refined and then the structural parameters (*i.e.* unit cell, atom positions and thermal parameters) for all phases present in the sample, followed by a variety of instrumental and sample parameters that describe the experimental and sample

conditions (peak shape, preferred orientation, etc.). There are seven background functions available in GSAS [189]. Each function has a maximum of 36 coefficients. Usually refining far fewer coefficients is sufficient to get a good fit of the background to the diffraction pattern. In this work, for the majority of the refinements, a simple linear interpolation was used. This function fits the background using the equation

$$y_{bi} = B_j\left(T_{j+1} - T\right) + B_{j+1}\left(T - T_j\right) \tag{42}$$

for $T_j \leq T \leq T_{j+1}$

The B_j are adjustable parameters in the least squares but the T_j locations are fixed. The shape of the diffraction peaks is the convolution of sample effects (for example broadening of the peaks due to the particle size) and instrumental effects. There are several contributions to the instrumental profile due to the instrumental arrangements, for instance: radiation source, wavelength distribution within the beam. The profile has Gaussian, *G*, and Lorentzian, *L*, contribution, given by equations 43 and 44, respectively [210]

$$G = \frac{\sqrt{4\ln 2}}{H_k\sqrt{\pi}}\exp\left(\frac{-4\left(2\theta_i - 2\theta_k\right)^2 \ln 2}{H_k^2}\right) \tag{43}$$

$$L = \frac{2}{\pi H_k}\left(\frac{1}{1 + 4\dfrac{\left(2\theta_i - 2\theta_k\right)^2}{H_k^2}}\right) \tag{44}$$

In this work a pseudo-Voigt function [210], *pV*, was used to model peak shapes in both X-ray and neutron data. This function is the result of the analytical convolution of Gaussian, and Lorentzian functions

$$pV = \eta L + (1 - \eta)G \tag{45}$$

where η is given by equation

$$\eta = NA + NB \times (2\theta) \tag{46}$$

NA and *NB* are refinable parameters.

All peakshape functions take into account dependence of halfwidth of Bragg peaks, *H*, or full-width-at-half-maximum (Figure 39) [210]. H_k in equations 43 and 44 is the *FWHM* of the k^{th} Bragg reflection. For the Gaussian function, the full-width-at-half-maximum shows angular dependence expressed by the Caglioti function

$$H^2 = U\tan^2\theta + V\tan\theta + W \tag{47}$$

U, V, W in above equation are refinable parameters.

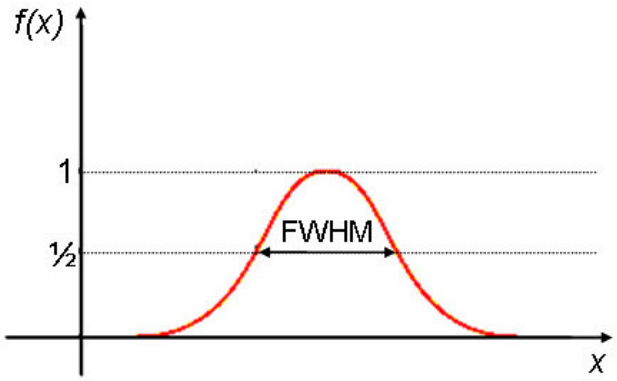

Figure 39: A full-width-at-half-maximum (FWHM).

The refinable parameters are progressively refined until the residual, S_y, in equation 36, is minimised. There are several "best fit" parameters [211] which describe the quality of agreement between observed and calculated profiles, given by equations 48 - 51. The weighted profile residual, R_{wp}, (equation 48), is commonly used. It is the most meaningful from a mathematical point of view as the numerator is the residual, S_y, being minimised. R_{wp} is the best function to reflect the progress of the refinement.

R-weighted profile:

$$R_{wp} = \sqrt{\frac{\sum_{i=1}^{N} w_i (y_{iobs} - y_{ical})^2}{\sum_{i=1}^{N} w_i y_{iobs}^2}} \tag{48}$$

R-profile:

$$R_p = \sqrt{\frac{\sum \left| y_{iobs} - y_{ical} \right|}{\sum y_{iobs}}} \tag{49}$$

Expected *R*-factor:

$$R_e = \sqrt{\frac{(N-P)}{\sum_{i=1}^{N} w_i y_{iobs}^2}} \tag{50}$$

Where N is the number of profile points and P is the number of refined parameters. A very useful measure of the quality of the refinement is quantity χ^2 (equation 51), which is the square of the ratio of R_{wp} and R_e

$$\chi^2 = \frac{\sum_{i=1}^{N} w_i (y_{iobs} - y_{ical})^2}{N-P} = \left(\frac{R_{wp}}{R_e} \right)^2 \tag{51}$$

However, the value of χ^2 can be distorted by statistical errors and a well fitted background may artificially lower the value.

Chapter 3: Phase Relations in the ZnO – Bi_2O_3 – V_2O_5 and PbO – Bi_2O_3 – V_2O_5 Systems

3.1 Introduction

The knowledge of phase diagrams is essential to understand, control and improve the stability of materials [212]. Phase diagrams also provide basic information with regard to preparation of new types of materials. The experimental determination of phase diagrams generally includes two stages: the preparation of samples and the measurement of phase relation parameters under conditions as close to the equilibrium state as possible. The phase diagrams show the phase relations against the temperature (composition coordinates). Phase diagrams supply information without which it would be difficult to understand relations between properties, composition and structure. This is why they are needed not only for research but also for industrial purposes.

This chapter presents the results and discussion of a study into three pseudo-binary bismuth vanadate oxide systems: ZnO – $BiVO_4$, PbO – $BiVO_4$ and $Pb_2V_2O_7$ – $BiVO_4$. The first belongs to the ternary system ZnO – Bi_2O_3 – V_2O_5 and the other two are from the PbO – Bi_2O_3 – V_2O_5 system. Particular attention was focused on checking whether new compounds belonging to the $BiA_2M^VO_6$ and $BiM_2^{III}V_3O_{11}$ families are formed in the investigated systems, where A is divalent; M^V and M^{III} are pentavalent and trivalent cations, respectively. The phase relations in these systems were examined and the phase equilibria were established over the whole components concentration range up to 1273 K.

Work presented in this chapter was performed at the Department of Inorganic and Analytical Chemistry, Szczecin University of Technology, Poland (10.2003 – 01.2006) under the supervision of the late Professor Maria Kurzawa.

3.2 The ZnO – $BiVO_4$ System: Synthesis and Properties of a New Bismuth Vanadate $BiZn_2VO_6$

3.2.1 Introduction

It is known that bismuth forms with divalent and pentavalent elements a great family of compounds with their general formula BiA_2MO_6, where A is divalent cation, and M is

pentavalent cation. This family comprises: arsenates (A = Ca, Cd, Cu, Mg, Mn, Pb) [55-57], phosphates (A = Ca, Cd, Cu, Mg, Mn, Pb, Zn) [55, 57, 58] and vanadates (A = Ca, Cd, Cu, Mg, Mn, Pb) [54, 55, 59-62]. Almost all the above-mentioned compounds were obtained in an atmosphere of air, only the synthesis of $BiMn_2MO_6$ (M = As, P, V) was conducted in an inert atmosphere [55].

The aim of this work was to determine the phase relations in the system ZnO – $BiVO_4$ and to check whether a compound belonging to the family BiA_2MO_6 is formed in the investigated system.

The components of the system ZnO – $BiVO_4$ are well known. ZnO crystallises in the hexagonal system with a space group $P6_3mc$. Its unit cell parameters are: $a = b =$ 3.250 Å, c = 5.207 Å [213]. Zinc oxide does not form any polymorphic modifications at ambient pressure [213].

Bismuth (III) orthovanadate (V), $BiVO_4$, occurs in nature as a mineral named pucherite, crystallising in the orthorhombic system [28]. This polymorph has never been obtained in laboratory conditions. As a result of the synthesis of this compound, conducted under laboratory conditions at low temperatures, a tetragonal polymorph of $BiVO_4$ is obtained, possessing a zircon-type structure [214, 215]. This polymorphic modification of $BiVO_4$ undergoes at 623 – 723 K an irreversible transformation to a monoclinic polymorph with a fergusonite-type structure [214, 215]. The monoclinic modification is formed at high temperatures, above 873 K [216]. At 528 K, monoclinic $BiVO_4$ undergoes a reversible second-order phase transition to the tetragonal scheelite-type structure [214, 215]. Above 528 K $BiVO_4$ has an ideal scheelite structure. At temperatures higher than 673 K the zircon form of $BiVO_4$ transforms irreversibly into the monoclinic form [28, 215, 217]. Bismuth (III) orthovanadate (V) melts congruently at 1213 K [214]. The high–temperature modification of $BiVO_4$ (scheelite) crystallises in the tetragonal system with the space group $I4_1/a$. Its cell parameters are: $a =$ 7.307(0) Å, c = 6.466(3) Å [215].

3.2.2 Synthesis

All materials used in this study were supplied as fine powders and they are listed in Table 6 in Chapter 2 of this thesis. The work was begun with an attempt to synthesise the compound $BiZn_2VO_6$. For this purpose a sample was prepared at the composition 33.33 mol % $BiVO_4$ and 66.67 mol % ZnO. The stoichiometric mixture of the reactants was thoroughly ground, pressed into pellets, placed in the porcelain crucible and heated

in air in a resistance furnace. Synthesis required three successive firings, all of 12 hours duration at 873 K, 923 K and 973 K. At the completion of the heating period, products were cooled down to room temperature at the natural rate of the furnace (*ca.* 5 K min^{-1}). After each firing the pellets were ground and characterised by powder X-ray diffraction and differential thermal analysis (DTA).

Twelve extra samples were prepared to check the phase relations in the ZnO – $BiVO_4$ system. All samples were synthesised in the same manner as the $BiZn_2VO_6$ compound. In order to determine the kind of phases co-existing with liquid, some selected samples were additionally heated at temperatures above the solidus line, *i.e.* 1053, 1093, 1113, 1123 and 1143 K for 2 hours. These samples were rapidly cooled to ambient temperature by removing them from the hot furnace and placing them in a refrigerator.

3.2.3 Results and Discussion

All products were characterised using powder X-ray diffraction. In the powder diffraction pattern of the $BiZn_2VO_6$ sample, recorded after the final firing, no lines characteristic for any known phases belonging to the ternary system ZnO – Bi_2O_3 – V_2O_5 were observed. This diffractogram did not show any similarity to the diffractograms of other known BiA_2MO_6-type phases (where A is divalent cation and M is pentavalent cation, of As, P and V) [54, 55, 59-61]. Figure 40 presents the powder diffraction pattern of the initial 33.33 mol % $BiVO_4$; 66.67 mol % ZnO mixture and of the product obtained. It can be concluded that a new compound was obtained with its formula $BiZn_2VO_6$, according to the following reaction

$$2\ ZnO_{(s)} + BiVO_{4(s)} = BiZn_2VO_{6(s)} \qquad (52)$$

However, this compound is not isostructural with other compounds of the type BiA_2MO_6 described in the literature [54, 55, 59-61].

The $BiZn_2VO_6$ material was also synthesised from the oxides ZnO, Bi_2O_3 and V_2O_5 mixed at the stoichiometric quantities. The mixture of oxides was heated analogously to the mixture of ZnO with $BiVO_4$. The powder X-ray diffractogram recorded after the last firing of this sample revealed a set of diffraction lines with both their positions and intensities being similar with those recorded in the diffractogram of

$BiZn_2VO_6$ obtained from $BiVO_4$ and ZnO. It can be concluded that $BiZn_2VO_6$ can also be obtained as the result of a reaction occurring in accordance with the following equation

$$4\ ZnO_{(s)} + Bi_2O_{3(s)} + V_2O_{5(s)} = 2\ BiZn_2VO_{6(s)} \qquad (53)$$

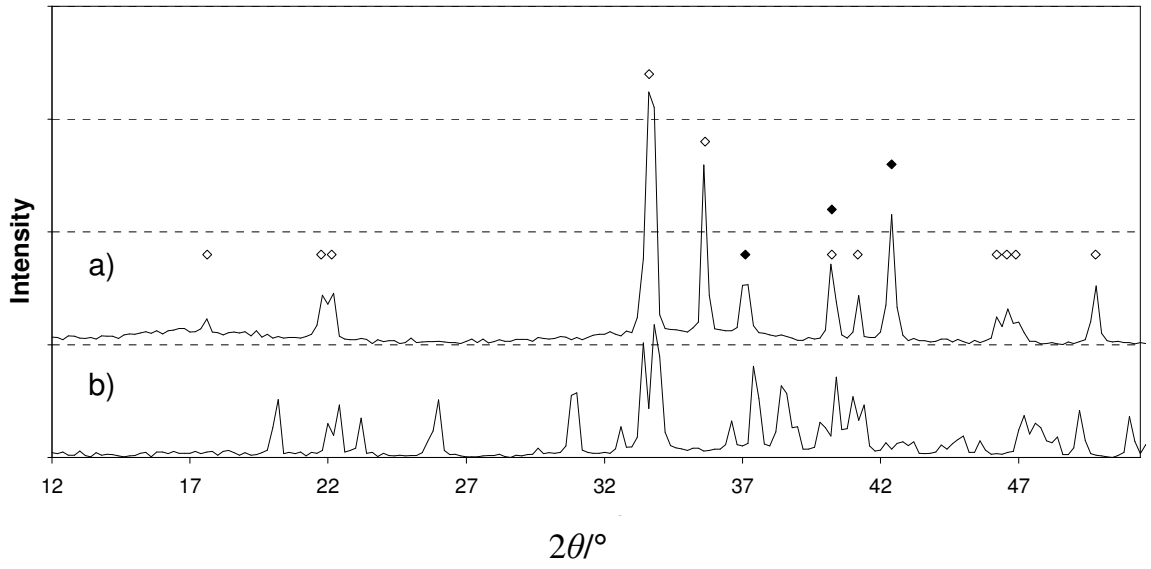

Figure 40: Powder diffraction patterns of: (a) 2:1 ZnO and $BiVO_4$ mixture, where ◇ - ZnO, ◆ - $BiVO_4$ and (b) of $BiZn_2VO_6$.

The $BiZn_2VO_6$ compound is yellow and melts incongruently at 1078 ± 5 K with a separation of solid ZnO. The DTA curve of $BiZn_2VO_6$ is presented in Figure 41.

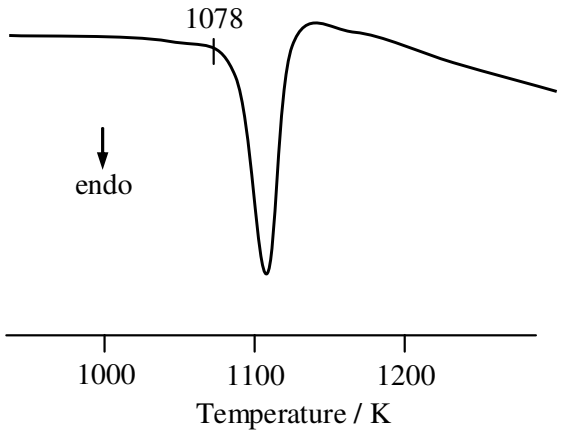

Figure 41: DTA curve of $BiZn_2VO_6$.

The powder X-ray diffraction pattern of the $BiZn_2VO_6$ sample was indexed on a triclinic unit cell and the results are presented in Table 14. The triclinic unit cell parameters of $BiZn_2VO_6$ are: a = 6.879(5) Å, b = 5.725(3) Å, c = 8.903(3) Å, α = 91.0(1)°, β = 130.1(2)°, γ = 99.5(2)°, Z = 2. The program POWDER [218], belonging to the crystallographic programs package X-Ray System 70, was used to index the powder X-ray diffraction pattern of the new material and to calculate unit cell parameters. Exact positions of the diffraction lines were determined by the internal standard method. The internal standard used was KCl (space group *Fm3m*, a = 6.293 Å). The X-ray calculated density amounts to d_{rtg} = 6.20 g cm^{-3} and the pycnometric density d = 6.10 ± 0.05 g cm^{-3}. The density of $BiZn_2VO_6$ was determined by the method described in the work [219].

Further investigations were aimed at establishing the phase equilibria over the whole components concentration range of the system ZnO – $BiVO_4$. Table 15 lists the composition of the samples prepared and the phases identified in individual samples after the final firing.

The results of this study prove that ZnO and $BiVO_4$ are not inert towards each other in the solid state. In the concentration range up to 33.33 mol % $BiVO_4$ the phases remaining at equilibrium are $BiZn_2VO_6$ and ZnO, while at the content of $BiVO_4$ equal to 33.33 mol % the components of the system react with each other forming a new compound $BiZn_2VO_6$; and in the concentration range of $BiVO_4$ above 33.33 mol % the phases remaining at equilibrium are $BiZn_2VO_6$ and $BiVO_4$.

Table 14: Results of indexing the powder diffraction pattern of $BiZn_2VO_6$.

No.	d_{exp} [Å]	d_{cal} [Å]	*h k l*	I/I_0 [%]
1	6.714	6.719	0 0 1	6.6
2	5.679	5.569	0 1 0	3.2
3	5.116	5.115	1 0 0	83.4
4	4.682	4.681	$0\ 1\ \bar{1}$	32.6
5	4.616	4.614	$1\ \bar{1}\ \bar{1}$	57.0
6	4.451	4.451	$1\ 0\ \bar{2}$	30.0
7	4.021	4.022	$1\ 1\ \bar{1}$	32.8
8	3.976	3.976	0 1 1	47.5
9	3.507	3.506	$1\ 1\ \bar{2}$	7.1
10	3.444	3.448	$1\ \bar{1}\ \bar{2}$	4.1
11	3.358	3.356	0 0 2	100
		3.359	$2\ 0\ \bar{2}$	
12	3.186	3.184	1 0 1	21.1
		3.186	$2\ 0\ \bar{1}$	
13	3.110	3.110	$0\ 1\ \bar{2}$	76.3
14	3.070	3.070	$1\ \bar{1}\ 1$	92.5
		3.072	$2\ \bar{1}\ \bar{2}$	
15	2.851	2.849	$1\ 0\ \bar{3}$	20.9
16	2.785	2.784	0 2 0	83.9
17	2.714	2.714	$2\ 1\ \bar{2}$	62.1
18	2.686	2.685	0 1 2	26.1
19	2.624	2.624	$1\ 1\ \bar{3}$	26.8
20	2.589	2.588	$2\ \bar{1}\ \bar{3}$	44.3
21	2.558	2.558	2 0 0	28.4

Table 15: Composition of samples and phases detected in equilibrium samples in the $ZnO - BiVO_4$ system.

No.	Composition of initial mixtures in terms of the system components [mol %]		Composition of equilibrium samples
	ZnO	**$BiVO_4$**	
1	10.00	90.00	$BiZn_2VO_6 + BiVO_4$
2	20.00	80.00	
3	30.00	70.00	
4	40.00	60.00	
5	50.00	50.00	
6	60.00	40.00	
7	65.00	35.00	
8	66.67	33.33	**$BiZn_2VO_6$**
9	70.00	30.00	$BiZn_2VO_6 + ZnO$
10	75.00	25.00	
11	80.00	20.00	
12	85.00	15.00	
13	90.00	10.00	

Figure 42 presents the DTA curves of some selected samples belonging to the investigated system and having attained an equilibrium state. In the DTA curves of equilibrium samples containing in their initial mixtures up to 33.33 mol % $BiVO_4$ one endothermic event was recorded, caused by melting $BiZn_2VO_6$ at 1078 ± 5 K (Figure 42(a)). The DTA curves of the samples with $BiVO_4$ concentration from 35.00 to 60.00 mol % contained two endothermic effects with onset temperatures of 1033 ± 5 K and 1078 ± 5 K, respectively (Figure 42(b)). The first of these effects, recorded also in DTA curves of samples containing in their initial mixtures 60 or more mol % $BiVO_4$, appears to be associated with melting of the eutectic mixture of $BiZn_2VO_6$ and $BiVO_4$. This event occurs as the only one in the DTA curve of the sample containing 60 mol % $BiVO_4$ and its intensity was the biggest (Figure 42(c)); hence the composition of the eutectic mixture was determined to be *ca.* 33 mol % $BiZn_2VO_6$ and *ca.* 67 mol % $BiVO_4$. This is equivalent to 60 mol % $BiVO_4$ and 40 mol % ZnO. The other feature

recorded in the DTA curves of these samples is due to the melting of $BiZn_2VO_6$. In DTA curves of samples containing in their initial mixtures above 60 mol % $BiVO_4$, two thermal events were also recorded (Figure 42(d)), where the first one with its onset temperature equal to 1033 ± 5 K was considered to be due to melting of the eutectic mixture of $BiZn_2VO_6$ and $BiVO_4$, while the second with its onset temperature varying from 1123 to 1183 K is assigned to the melting of the mixture $BiVO_{4(s)}$ + liquid. Differential thermal analysis (DTA) indicated the melting point of $BiVO_4$ to be *ca.* 1208 ± 5 K, which is in good agreement with literature information (1213 K) [28, 214]. $BiVO_4$ melts congruently (Figure 43).

On the basis of the data presented in Table 15, the DTA curves of equilibrium samples (Figure 42) as well as the results of powder X-ray diffraction analysis of samples heated additionally at temperatures above the solidus line and next "frozen", a diagram of phase equilibria has been determined for the system ZnO – $BiVO_4$ over the whole components concentration range (Figure 44). The solid lines were drawn on the basis of DTA curves and powder X-ray diffraction analysis of individual equilibrium samples, the dashed lines on the base only of XRD analysis of samples heated additionally and rapidly cooled to ambient temperature. The temperatures of the solidus line were determined on the basis of the onset temperatures of the first endothermic events recorded in DTA curves of the investigated samples. The liquidus curves, on the other hand, were determined by reading the maxima of the features recorded as the last ones in DTA curves.

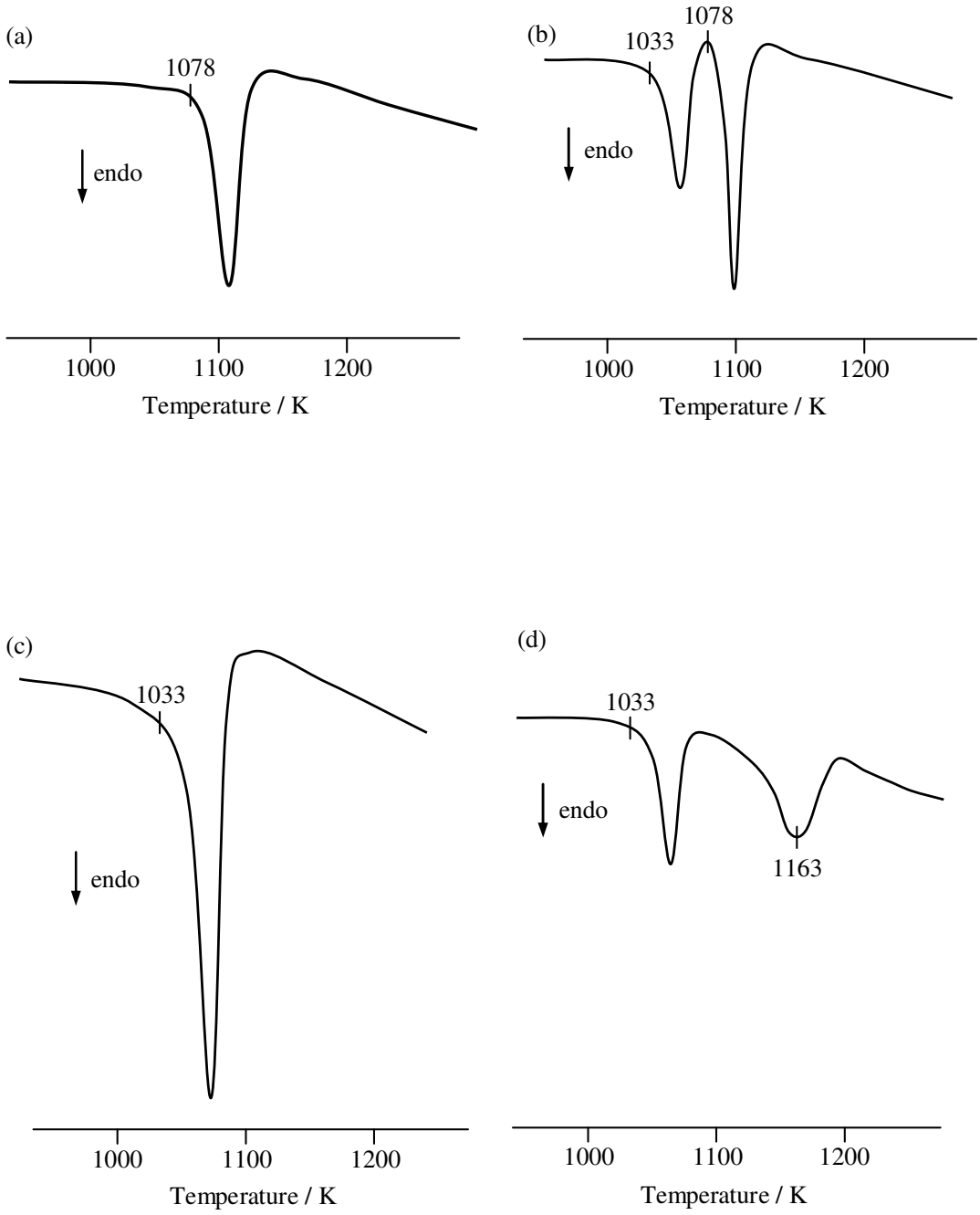

Figure 42: DTA curves of selected samples in the ZnO – $BiVO_4$ system: (a) 30 mol % $BiVO_4$, (b) 40 mol % $BiVO_4$, (c) 60 mol % $BiVO_4$ and (d) 80 mol % $BiVO_4$.

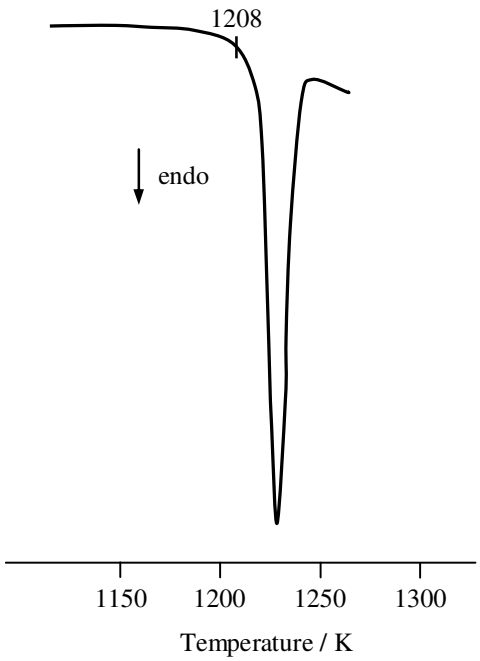

Figure 43: DTA curve of $BiVO_4$.

The diagram of phase equilibria presented in Figure 44 implies that only one compound exists in the system ZnO – $BiVO_4$ with the formula $BiZn_2VO_6$. This compound melts incongruently at 1078 ± 5 K with a deposition of ZnO crystals. This was corroborated by powder X-ray diffraction analysis results of a preparation of $BiZn_2VO_6$ heated additionally at 1123 K for 3 hours and next rapidly cooled to room temperature. Bismuth (III) orthovanadate (V) forms with $BiZn_2VO_6$ an eutectic melting at 1033 ± 5 K. Above the eutectic temperature, $BiZn_2VO_6$ and $BiVO_4$ remain at equilibrium with liquid in the components concentration range above 33.33 mol % $BiVO_4$. $BiZn_2VO_6$ and ZnO co-exist at equilibrium up to the temperature of the solidus line that is determined by the temperature of incongruent melting $BiZn_2VO_6$, *i.e.* 1078 K. Above this temperature the phase remaining at equilibrium with liquid is zinc oxide.

The results of this study were published in Thermochimica Acta [220].

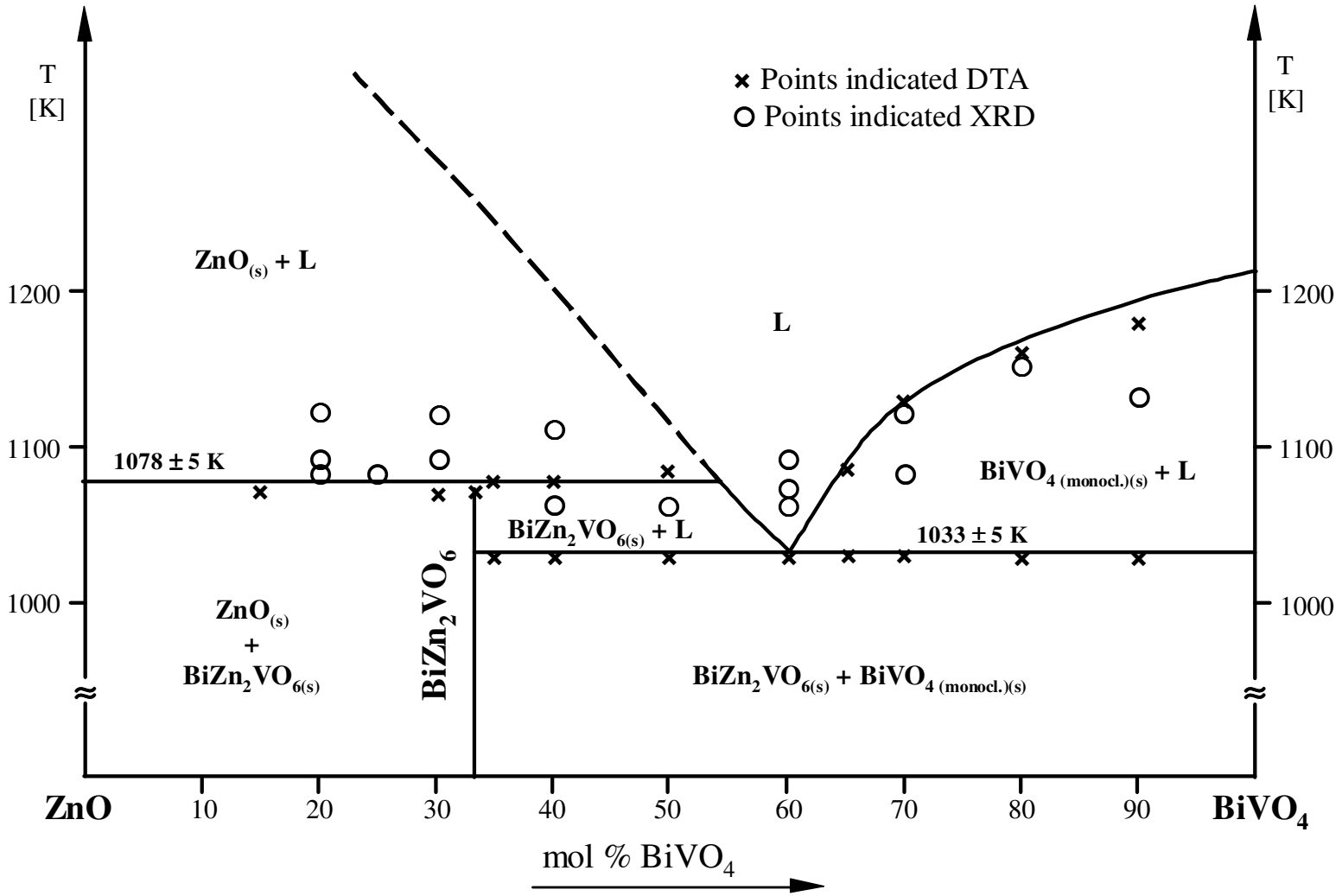

Figure 44: Diagram of phase equilibria of the system ZnO – $BiVO_4$, determined from powder X-ray diffraction and DTA measurements.

3.3 The $Pb_2V_2O_7$ – $BiVO_4$ System: Synthesis and Characterisation of a New Bismuth Lead Vanadate $Pb_2BiV_3O_{11}$

3.3.1 Introduction

There exists a series of new compounds of the general formula $M^{II}_2M^{III}V_3O_{11}$ in the ternary system of metal oxides $M^{II}O$ – V_2O_5 – $M^{III}_2O_3$, where M^{II} = Co, Mg, Ni, Zn and M^{III} = Fe, Cr, In [74-77]. Also, compounds of $M^{II}_3Fe_4V_6O_{24}$ type are formed in the $M^{II}O$ - V_2O_5 – Fe_2O_3 systems [78, 79]. These compounds are interesting due to their catalytic properties [80]. A search of the literature showed that in the systems Bi_2O_3 – V_2O_5 – MO, where M = Sr, Ba compounds with general formula $BiM_2^{II}V_3O_{11}$ are formed [81, 82].

The aim of this work was to determine the phase relations in the system $Pb_2V_2O_7$ – $BiVO_4$ and to investigate whether a compound belonging to the family $BiM_2^{II}V_3O_{11}$ is formed in this pseudo-binary system. Research on the PbO – Bi_2O_3 – V_2O_5 system is motivated by the fact that many of these tetrahedral anion compounds display interesting properties due to presence of Bi and Pb lone-pair electrons [50]. It is particularly interesting that these compounds exhibit anion transport behaviour [50].

The components of the $Pb_2V_2O_7$ – $BiVO_4$ system are well known. $Pb_2V_2O_7$, is one of five compounds belonging to the system PbO – V_2O_5. This compound does not form polymorphic modifications. $Pb_2V_2O_7$ melts congruently at 1013 K [221]. Lead (II) pyrovanadate (V) crystallises in the monoclinic system with the space group $P2_1/c$, Z = 4 with unit cell parameters: a = 7.1027 Å, b = 7.1607 Å, c = 13.368 Å, β = 105.935° [221]. $BiVO_4$, the other end-member phase from the investigated system was described in Section 3.2.1.

3.3.2 Synthesis

A bulk sample of a new bismuth lead vanadate, $Pb_2BiV_3O_{11}$, was prepared by a standard solid-state reaction from a stoichiometric mixture of $Pb_2V_2O_7$ and $BiVO_4$, both synthesised in the manner described in Paragraph 2.1.1 in Chapter 2. The $Pb_2BiV_3O_{11}$ compound was also obtained by heating a mixture of the oxides PbO, Bi_2O_3 and V_2O_5 at the molar ratio 4:1:3 for 24 hours at each temperature: 773 K and 873 K. The materials used for the syntheses are listed in Table 6, Chapter 2.

Sixteen samples were prepared from the system $Pb_2V_2O_7$ – $BiVO_4$. The reagents were weighed in appropriate amounts, homogenised by grinding, pressed into pellets and heated in an air atmosphere in the furnace. The oxide mixtures were pretreated for 24 hours at 873 K, reground and heated for the next 24 hours at 923 K. The samples were furnace-cooled and analysed by powder X-ray diffraction and differential thermal analysis. The phases remaining at equilibrium were determined on the basis of the results of powder X-ray diffraction analysis of samples heated additionally for 2 – 4 hours at selected temperatures and rapidly cooled to ambient temperature.

Powder X-ray diffraction and DTA examinations were performed using the instruments and conditions which are described in Chapter 2 of this thesis. The weight of samples for differential thermal analysis was *ca.* 0.5 g. The density and the unit cell parameters of $Pb_2BiV_3O_{11}$ were obtained as described in the Paragraph 3.2.3.

3.3.3 Results and Discussion

The first stage of this work was an attempt to synthesise the new compound $Pb_2BiV_3O_{11}$. For this purpose a sample of the composition 50 mol % $Pb_2V_2O_7$ and 50 mol % $BiVO_4$ was weighed and prepared by conventional method at temperatures: 873 K (24 h) and 923 K (24 h). In the powder diffraction pattern of this sample, recorded after the final firing, no lines were observed characteristic of any known phases belonging to the ternary system PbO – V_2O_5 – Bi_2O_3. Figure 45 presents the powder diffraction pattern of the investigated reaction product and that of the initial mixture. The results of the XRD examinations revealed that a compound with the formula $Pb_2BiV_3O_{11}$ was obtained as a result of the reaction between $Pb_2V_2O_7$ and $BiVO_4$ at the molar ratio 1:1 according to the reaction

$$Pb_2V_2O_{7(s)} + BiVO_{4(s)} = Pb_2BiV_3O_{11(s)} \quad (54)$$

A material of composition $Pb_2BiV_3O_{11}$ was also synthesised by heating a mixture of the oxides PbO, Bi_2O_3 and V_2O_5 at the molar ratio 4:1:3 at temperatures: 773 K (24 h) and 873 K (24 h). After the first firing, the diffractogram of this mixture revealed a set of diffraction lines characteristic of the starting materials and a set of lines identical with those recorded in the diffractogram of $Pb_2BiV_3O_{11}$ obtained from $BiVO_4$ and $Pb_2V_2O_7$. Only the latter lines were observed in the diffractogram recorded after the final firing. It was

concluded that $Pb_2BiV_3O_{11}$ could also be obtained as a result of a following reaction

$$4PbO_{(s)} + Bi_2O_{3(s)} + 3V_2O_{5(s)} = 2\ Pb_2BiV_3O_{11(s)} \qquad (55)$$

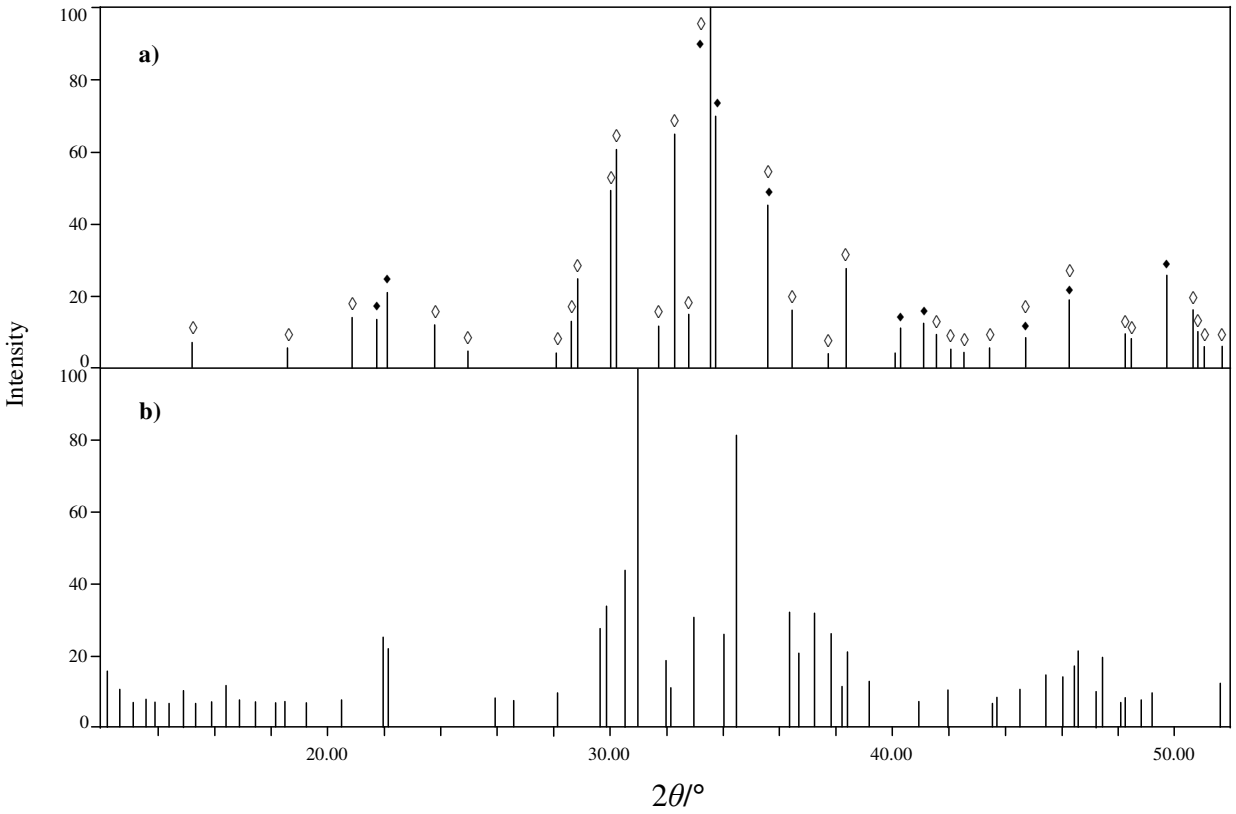

Figure 45: Powder X-ray diffraction patterns of: (a) $Pb_2V_2O_7$ + $BiVO_4$ mixture, where ◇ - $Pb_2V_2O_7$, ◆ - $BiVO_4$ and (b) $Pb_2BiV_3O_{11}$.

$Pb_2BiV_3O_{11}$ is a yellow solid and melts congruently at 998 K. The DTA curve of $Pb_2BiV_3O_{11}$ is presented in Figure 46.

The powder X-ray diffraction pattern of $Pb_2BiV_3O_{11}$ can be indexed on the basis of a triclinic unit cell, a = 7.10076(4) Å, b = 14.1975(3) Å, c = 14.2972(5) Å, α = 134.6(3)°, β = 97.3(2)°, γ = 89.6(2)°, Z = 4. The assignment of peaks is presented in Table 16. The X-ray calculated density is equal to d_{rtg} = 6.25 g cm^{-3} and the pycnometric density d = 6.27 ± 0.05 g cm^{-3}.

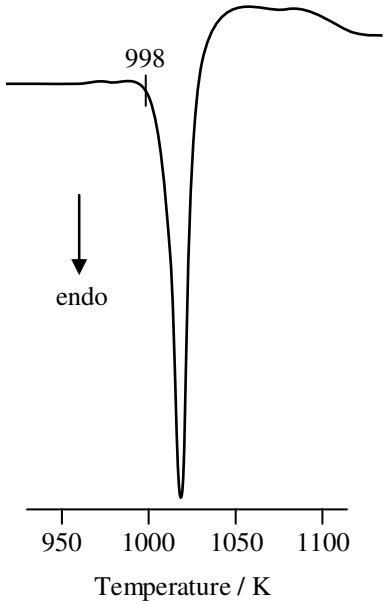

Figure 46: DTA curve of $Pb_2BiV_3O_{11}$.

Fifteen additional samples were prepared from the investigated system to check whether only one compound can be obtained in the reaction between $BiVO_4$ and $Pb_2V_2O_7$. Table 17 presents the initial composition of the samples and the phases detected after the last firing. The results show that only one compound is formed in the system $Pb_2V_2O_7$ – $BiVO_4$ (Table 17).

The sample of the composition 60 mol % $Pb_2V_2O_7$ and 40 mol % $BiVO_4$ (no.12 in Table 17) corresponds to the composition of the compound $Pb_6Bi_2V_8O_{29}$ which was reported in earlier work [69]. In the diffraction pattern of that sample only lines characteristic for $Pb_2V_2O_7$ and $Pb_2BiV_3O_{11}$ have been observed.

Figure 47 shows a calculated phase diagram of the system $Pb_2V_2O_7$ – $BiVO_4$. The diagram implies that $Pb_2V_2O_7$ – $BiVO_4$ is a genuine quasibinary system with one compound melting congruently. The eutectic composition of 25 mol % $BiVO_4$ and 75 mol % $Pb_2V_2O_7$ was found to melt at 973 K. Another eutectic composition of *ca.* 56 mol % $BiVO_4$ and 44 mol % $Pb_2V_2O_7$ melts at 983 K. Powder X-ray diffraction analysis after the last firing of the samples containing in the initial mixtures less than 50 mol % $Pb_2V_2O_7$ shows that the phases in equilibrium are $Pb_2BiV_3O_{11}$ and $BiVO_4$. The analysis of samples in the concentration range above 50 mol % $Pb_2V_2O_7$, indicated equilibrium phases $Pb_2V_2O_7$ and $Pb_2BiV_3O_{11}$.

Table 16: Results of indexing the X-ray powder diffraction pattern of $Pb_2BiV_3O_{11}$.

No.	d_{exp}[Å]	d_{cal} [Å]	*h k l*	I/I_0 [%]
1	10.048	10.038	0 0 1	1.3
2	7.003	6.996	1 0 0	1.7
3	6.268	6.265	1 0 $\bar{1}$	4.3
4	6.051	6.082	1 $\bar{1}$ 0	1.7
5	5.448	5.452	1 1 0	1.5
6	5.347	5.327	1 0 1	2.8
7	5.028	5.024	0 2 0	2.6
8	4.730	4.725	0 3 $\bar{2}$	7.3
9	4.681	4.658	1 $\bar{1}$ $\bar{1}$	11.5
10	4.627	4.619	1 $\bar{2}$ 2	6.3
11	4.455	4.455	1 0 $\bar{2}$	3.5
12	4.385	4.369	0 3 $\bar{3}$	3.4
13	4.311	4.326	1 $\bar{2}$ 0	1.2
14	3.999	4.001	1 1 1	3.3
15	3.875	3873	1 2 0	3.0
16	3.826	3.832	1 3 $\bar{3}$	1.4
17	3.685	3.692	1 $\bar{2}$ 3	2.8
18	3.537	3.539	0 3 $\bar{4}$	8.3
19	3.500	3.498	2 0 0	10.0
20	3.480	3.481	1 3 $\bar{1}$	9.2
21	3.405	3.400	1 $\bar{2}$ $\bar{1}$	14.1
22	3.353	3.346	0 0 3	100.0
23	3.251	3.242	1 0 $\bar{3}$	5.1
24	3.180	3.175	2 $\bar{1}$ $\bar{1}$	6.3
25	3.157	3.165	2 $\bar{2}$ 1	16.1
26	3.132	3.132	2 0 $\bar{2}$	9.8
27	3.100	3.115	1 $\bar{4}$ 2	4.5

Table 17: Composition of samples prepared for research and phases detected in equilibrium samples in the $Pb_2V_2O_7$ – $BiVO_4$ system.

No.	Composition of initial mixtures in terms of the system components [mol %]		Composition of equilibrium samples
	$Pb_2V_2O_7$	**$BiVO_4$**	
1	5.00	95.00	$Pb_2BiV_3O_{11}$ + $BiVO_4$
2	10.00	90.00	
3	12.00	88.00	
4	16.00	84.00	
5	20.00	80.00	
6	25.00	75.00	
7	30.00	70.00	
8	35.00	65.00	
9	40.00	60.00	
10	46.00	54.00	
11	50.00	50.00	**$Pb_2BiV_3O_{11}$**
12	60.00	40.00	$Pb_2V_2O_7$ + $Pb_2BiV_3O_{11}$
13	66.67	33.33	
14	75.00	25.00	
15	80.00	20.00	
16	90.00	10.00	

The existence of the new $Pb_2BiV_3O_{11}$ compound and results of the studies into $Pb_2V_2O_7$ – $BiVO_4$ system were reported in Journal of Phase Equilibria and Diffusion [222].

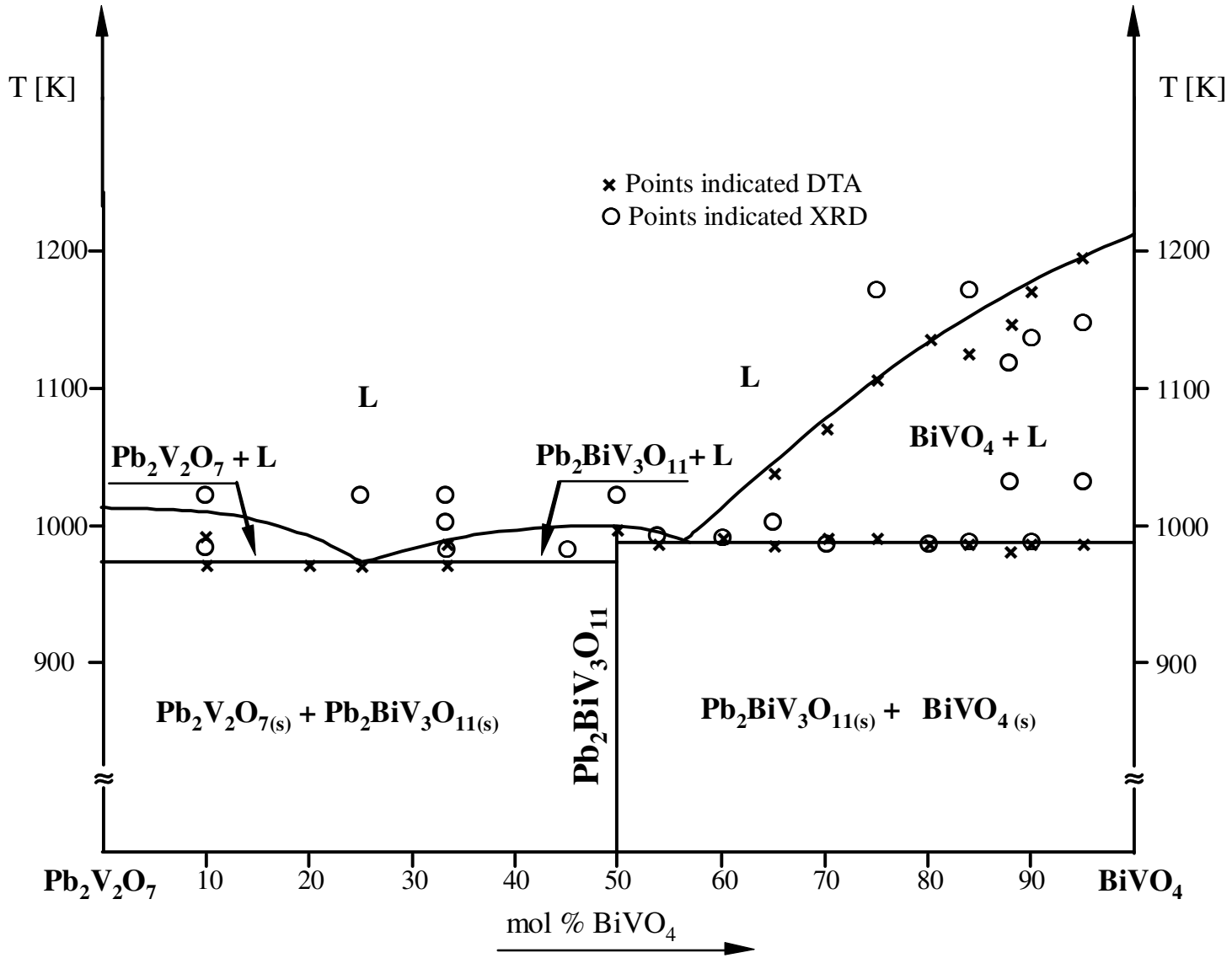

Figure 47: Diagram of phase equilibria of the system $Pb_2V_2O_7$ – $BiVO_4$ determined from powder X-ray diffraction and DTA measurements.

3.4 The PbO – $BiVO_4$ System

3.4.1 Introduction

The ternary system PbO – Bi_2O_3 – V_2O_5 has been under intensive study due to the fact that phases which exist in this three-component system display good ionic transport properties, which are better than some of the more traditional phases used in these applications [50]. The pseudo-binary PbO – $BiVO_4$ system belongs to the ternary system PbO – Bi_2O_3 – V_2O_5. Reference to the literature reveals that there exist three phases in this system: $PbBiVO_5$, Pb_2BiVO_6 and Pb_4BiVO_8 [62, 70]. These structures are well known [62, 70, 83, 84]. However, there is no consistency in the literature with regards to the polymorphic modifications and temperatures at which they are stable. Also, the phase relations in the system PbO – $BiVO_4$, over the whole components concentration range up to 1273 K, have not been fully characterised. The aim of this work was to determine the phase relations in this system and verify their thermal properties.

3.4.2 Synthesis

The reagents used for the syntheses are listed in Table 6, Chapter 2. For the research on the phase relations in the system PbO – $BiVO_4$, 19 samples were prepared in a similar manner to that described in Section 3.2.2. The temperatures of the sample preparation are summarised in Table 18. After each firing the pellets were cooled rapidly to room temperature by removing them from the hot furnace.

To verify the thermal properties of $PbBiVO_5$, Pb_2BiVO_6 and Pb_4BiVO_8 the measurements were carried out using a UVD-2000 high-temperature chamber (Bourevestnik, Sankt Petersburg, Russia) located on an HZG4/A2 XRD diffractometer (Carl Zeiss, Jena, Germany). The powder X-ray investigations were carried out for all samples and the identification of individual phases was based on the comparison of experimental diffraction patterns with the data contained in the PDF cards [223] and literature works [62, 70, 83, 84].

The DTA measurements were performed on the samples of *ca.* 0.5 g under the conditions described in Chapter 2. The accuracy of reading the temperature of thermal effects on the DTA curves, as evaluated on the base of repetitions, is *ca.* ± 5 K.

3.4.3 Results and Discussion

The work was begun with the aim to verify the literature information [49, 50, 62, 70] about thermal properties of the compounds $PbBiVO_5$, Pb_2BiVO_6 and Pb_4BiVO_8 which are formed in the PbO – $BiVO_4$ system. Figure 48 presents DTA curves of the established bismuth (III) lead (II) vanadates (V). In the DTA curves of $PbBiVO_5$ and Pb_4BiVO_8 one endothermic feature was recorded (Figure 48(a) and Figure 48(b)). The measurements were repeated with slower heating rates of 5 and 2.5 K min^{-1}. In the DTA curves still only one endothermic effect was observed. To confirm that $PbBiVO_5$ and Pb_4BiVO_8 do not have polymorphic modifications powder diffraction measurements were carried out using XRD diffractometer equipped with a high-temperature chamber. The experiments confirmed that under normal pressure Pb_4BiVO_8 exists only in one polymorphic modification. The results of the measurements in the high-temperature chamber for $PbBiVO_5$ show that at 753 ± 5 K one polymorphic transformation occurs, which is not observed in DTA curve. The temperature of the phase transition is in agreement with literature information [62].

The DTA curve of Pb_2BiVO_6 contains three endothermic peaks with onset temperatures of 703, 748 and 1033 K, respectively (Figure 48(c)). The onset temperatures of the two first thermal events are similar to the temperatures at which polymorphic modifications occur. This suggests that Pb_2BiVO_6 has three polymorphic forms. The existence of the polymorphic forms of Pb_2BiVO_6 was confirmed by heating the samples above the modification temperatures for three hours and rapidly cooled to ambient temperature. The temperatures at which the phase changes of Pb_2BiVO_6 occur were confirmed using high – temperature X-ray diffraction.

Table 18: Composition of initial mixtures, conditions of preparation and powder X-ray diffraction results for samples in the PbO – $BiVO_4$ system after the final firing.

No.	Composition of initial mixtures [mol %]		Conditions of preparation[‡]	Phases detected
	PbO	**$BiVO_4$**		
1.	2.50	97.50		
2.	5.00	95.00		
3.	10.00	90.00		
4.	15.00	85.00		$PbBiVO_5$ + $BiVO_4$
5.	17.50	82.50		
6.	20.00	80.00		
7.	30.00	70.00		
8.	40.00	60.00		
9.	50.00	50.00		**$PbBiVO_5$**
10.	60.00	40.00		
11.	65.00	35.00		Pb_2BiVO_6 + $PbBiVO_5$
12.	64.00	36.00		
13.	66.67	33.33		**Pb_2BiVO_6**
14.	70.00	30.00		Pb_4BiVO_8 + Pb_2BiVO_6
15.	75.00	25.00		
16.	80.00	20.00		**Pb_4BiVO_8**
17.	82.50	17.50	873 K (24 h) + 923 K (24 h)	PbO + Pb_4BiVO_8
18.	90.00	10.00		
19.	95.00	5.00		

[‡] All the samples required three successive firings, all of 24 hours duration at 872, 923 and 973 K, unless stated otherwise.

Figure 49 presents the DTA curves of selected samples that belong to the investigated system at equilibrium. In the DTA curve of the sample containing in the initial mixture 30 mol % PbO one endothermic event was recorded at 1048 ± 5 K (Figure 49(a)). A similar feature was observed in DTA curves of the samples with PbO concentrations from 10 to 50 mol %. This feature occurs as the only one in the DTA curve of the sample containing 30 mol % PbO and is the most intense; hence the composition of the eutectic mixture (E_1) was determined to be about 30 mol % PbO and 70 mol % $BiVO_4$. The composition of other eutectic mixtures, 64 mol % (E_2), 75 mol % (E_3) and 82.5 mol % PbO (E_4), were determined in the same way. The DTA curves of the samples with PbO concentration from 50 to 64 mol % PbO contained two endothermic peaks (Figure 49(b)); the first one with an onset temperature of 1028 ± 5 K. This feature is associated with melting of the eutectic mixture of 64 mol % PbO and 35 mol % $BiVO_4$. In DTA curves of the samples containing in their initial mixtures from 75 to 80 mol % and from 75 to 66.67 mol % PbO, with constant heating rate 10 K min^{-1}, three endothermic events were detected (Figure 49(c)). The first of these with an onset temperature between 723 and 748 K is considered to be due to polymorphic modification of Pb_2BiVO_6. This peak is split into two small endotherms while decreasing the heating rate to 2.5 K min^{-1}. The DTA curves of the samples with PbO concentration from 80 to 82.5 mol % and above 82.5 mol % show two endotherms, the first of them with the onset temperature 953 ± 5 K (Figure 49(d)) is believed to be due to melting of the eutectic mixture: 82.5 mol % PbO and 17.5 mol % $BiVO_4$.

Table 18 presents the contents of initial mixtures, the conditions of preparation and the results of powder X-ray diffraction analysis of all samples in equilibrium detected after the final firing.

Figure 50 presents a diagram of predicted phase equilibria of the system PbO – $BiVO_4$ over the whole components concentration range up to 1273 K. This diagram has been determined on the basis of the results of XRD analysis (Table 18) and the DTA curves of equilibrium samples. The temperatures of the solidus line were determined on the basis of the onset temperatures of first endotherms, which were not due to the polymorphic modifications, recorded in DTA curves of the investigated samples. The liquidus curves were determined by reading the temperatures of the endotherms recorded as the last ones in DTA curves.

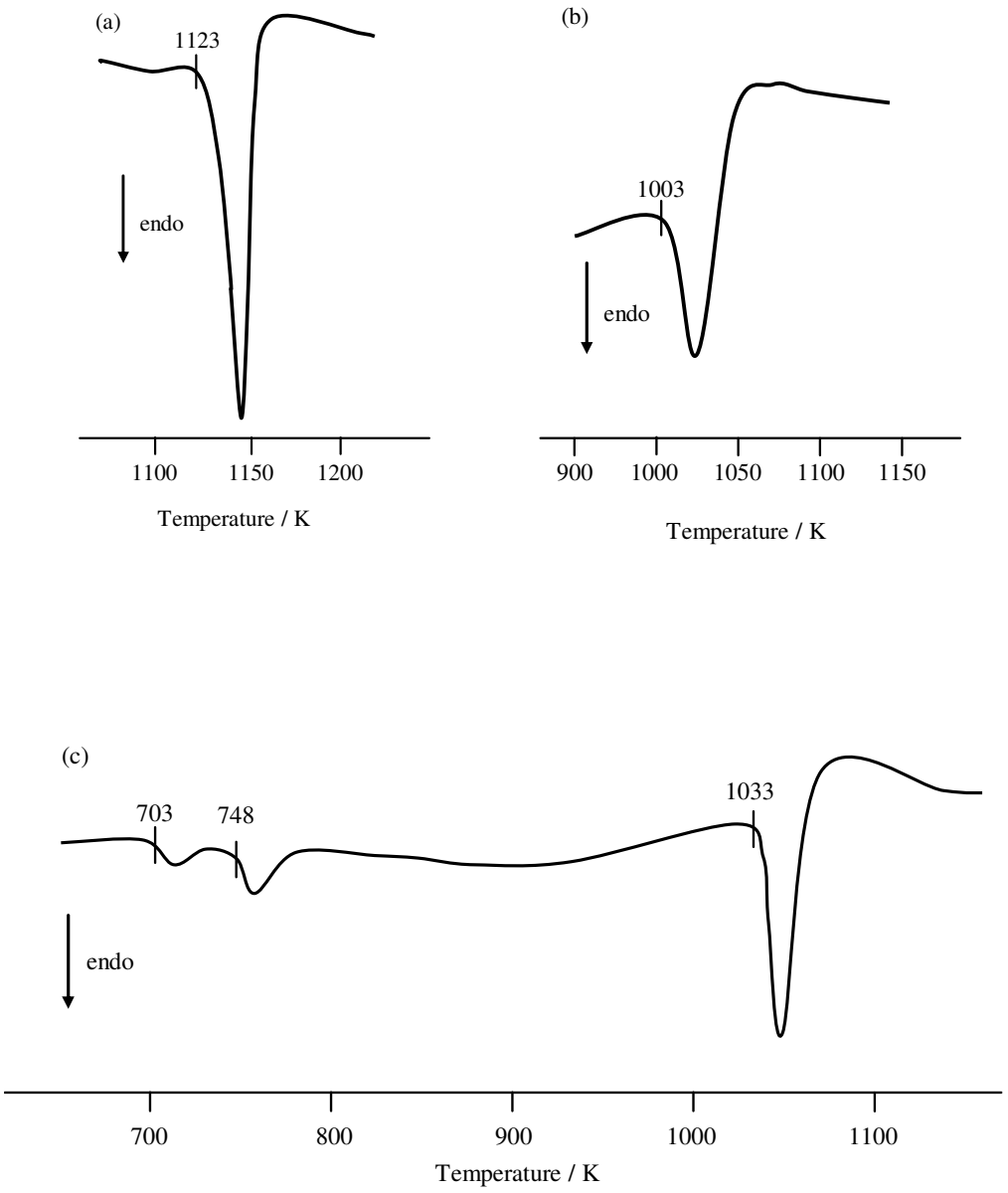

Figure 48: DTA curves of the phases existed in the system PbO – $BiVO_4$: (a) $PbBiVO_5$, (b) Pb_4BiVO_8 and (c) Pb_2BiVO_6.

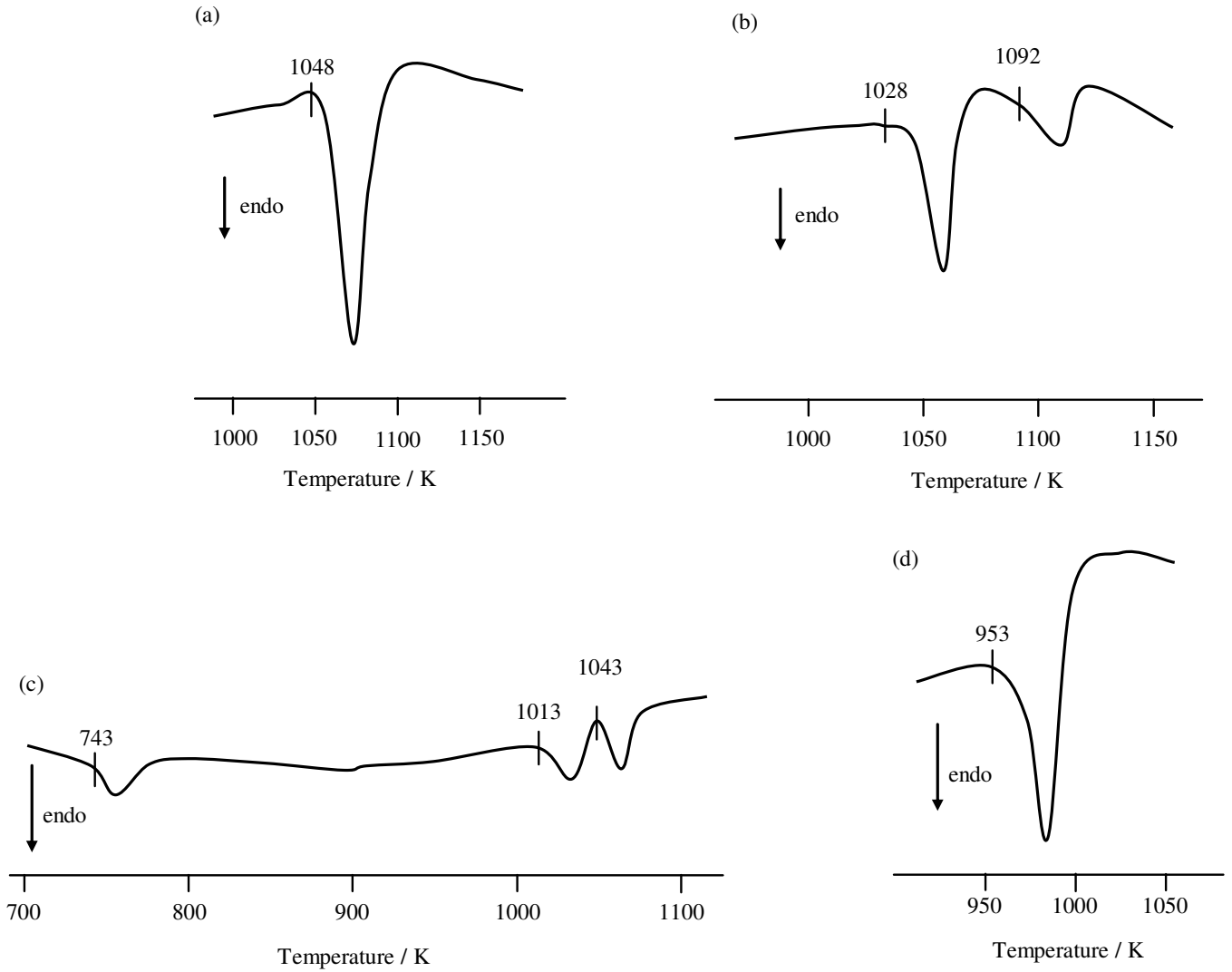

Figure 49: DTA curves of selected samples of the PbO – $BiVO_4$ system: (a) 30 mol % PbO + 70 mol % $BiVO_4$, (b) 60 mol % PbO + 40 mol % $BiVO_4$, (c) 70 mol % PbO + 30 mol % $BiVO_4$ and (d) 82.5 mol % PbO + 17.5 mol % $BiVO_4$.

The ranges over which solid-state phases co–exist with liquid were determined on the basis of DTA curves of the samples at equilibrium and the kind of phases on the basis of XRD analysis of some samples heated additionally for two hours and then rapidly cooled to ambient temperature. The composition of the samples and the temperature at which some samples were "frozen" are marked in the phase diagram. The phase diagram (Figure 50) shows that in the system PbO – $BiVO_4$ there exist three compounds: $PbBiVO_5$, Pb_2BiVO_6 and Pb_4BiVO_8. They all melt congruently.

Reading the temperature of the maximum of the second endothermic feature in DTA curves of the samples containing in the initial mixture above 90 mol % PbO was impossible. The liquidus curve in the Figure 50 for the concentration of PbO above 82.50 mol % is thus marked as dashed line. The compositions of the samples above the solidus curve were determined on the basis of the samples melted above this curve. The point where the liquidus curve crosses the *y* (temperature) axis is equal to the melting temperature of PbO [218]. Figure 51 presents the powder X-ray diffraction patterns of the sample containing in the initial mixture 95 mol % PbO, before melting and after melting at 988 K (above the solidus curve) and at 1223 K (above the liquidus curve). Powder X-ray diffraction pattern of the sample containing in the initial mixture 95 mol % PbO, melted at 988 K, (Figure 51(b)) consists of lines characteristic of the Pb_4BiVO_8 compound. This compound crystallised from the liquid (Pb_4BiVO_8 melts congruently).

The results of the studies into the PbO – $BiVO_4$ system were presented at the European Conference in Krakow, Poland [224] and submitted to Central European Journal of Chemistry.

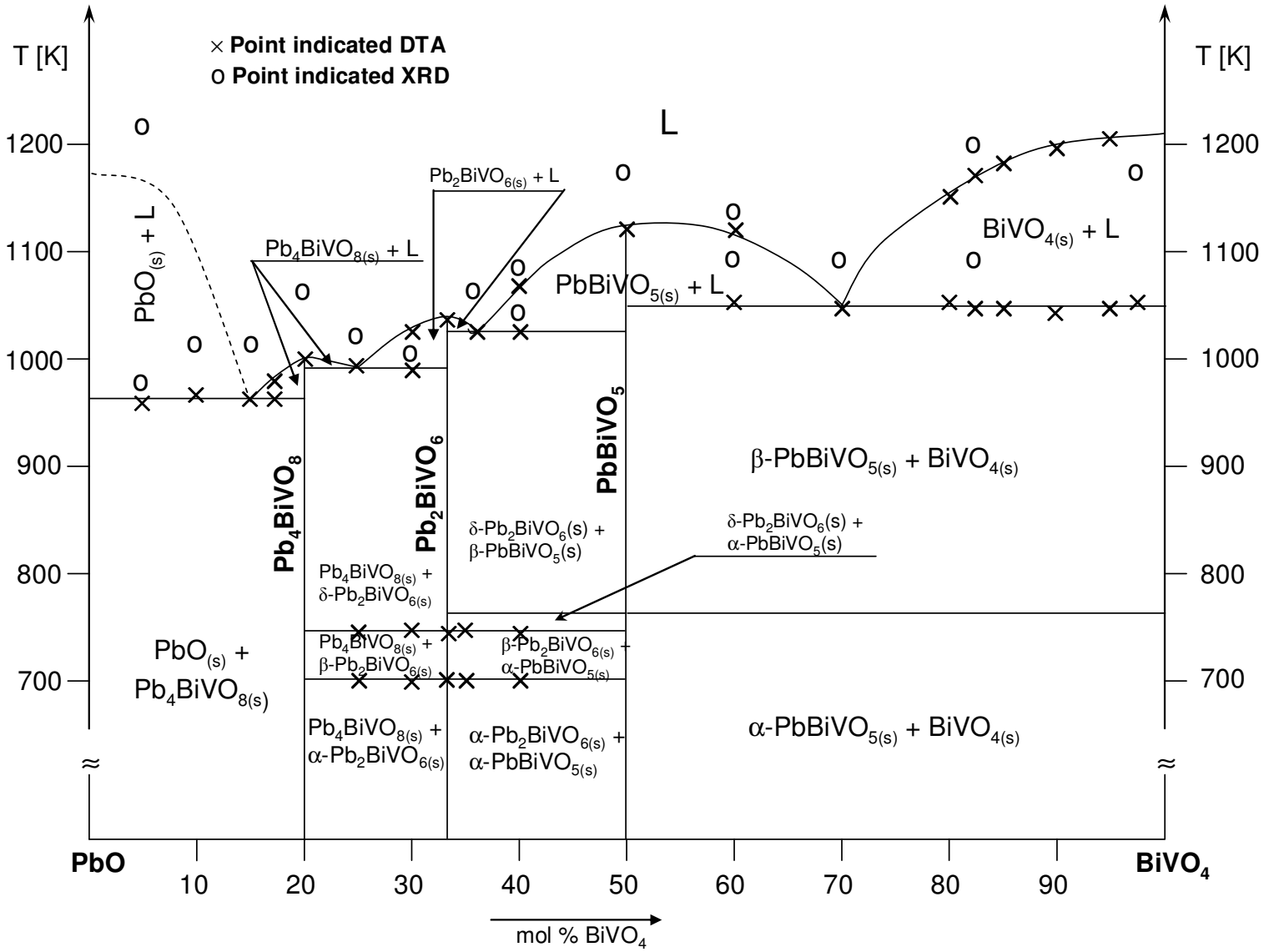

Figure 50: Phase diagram of PbO – $BiVO_4$ system determined by a combination of powder X-ray diffraction and DTA measurements.

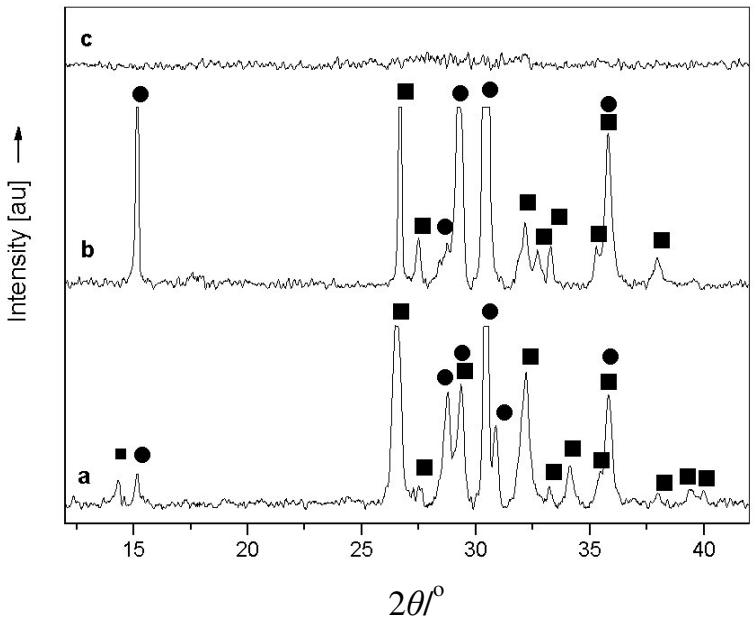

Figure 51: Powder diffraction patterns of (a) a sample at the composition 95 mol % PbO, before melting, (b) after melting at 988 K and (c) after melting at 1223 K, ■ - Pb_4BiVO_8, ● - PbO.

Chapter 4: Ordered Defect Thiospinels

4.1 Introduction

This chapter presents the results into a study of *A*-site substituted defect thiospinels. A new series of mixed-metal sulphides was synthesised, through progressive substitution of gallium by germanium in the $Ga_{1-x}Ge_xV_4S_8$ ($0 \leq x \leq 1$) series to investigate the effect on the physical properties of varying the electron count in the vanadium-sulphur cluster orbitals. The physical properties of the mixed metal sulphides were studied in detail and are found to be very different to properties of the end members of the series. Both transport and magnetic properties show a marked dependence on the *A*-site composition.

4.2 Synthesis

A series of materials of general formula $Ga_{1-x}Ge_xV_4S_8$ ($0 \leq x \leq 1$) was prepared by high-temperature reaction. Stoichiometric quantities of high-purity germanium, vanadium and sulphur powders were ground in an agate mortar and then loaded into a silica tube, to which was added the required quantity of slivers of gallium cut from an ingot. The silica tubes were evacuated to $\leq 10^{-4}$ Torr before being sealed. For the preparation of quaternary phases, reaction mixtures were fired for 24 hours at 873 K and reground prior to firing for a further 2 days at the same temperature. An analogous procedure was used for the synthesis of the ternary compounds, with the reaction temperature being raised to 1003 K and 1023 K for GeV_4S_8 and GaV_4S_8 respectively. To avoid the formation of V_3S_4 *ca.* 5 mg of iodine was added to all the samples. The addition of iodine required the reacting mixtures to be cooled using liquid nitrogen whilst evacuating the tubes prior to sealing. In all cases the reaction mixtures were placed directly into the furnace held at the appropriate temperature. At the completion of the heating period, products were cooled to room temperature at the natural rate of the furnace (*ca.* 5 K min^{-1}). The tubes were opened and the contents were finely ground in an agate mortar. Reaction progress was monitored by powder X-ray diffraction. Prior to the second firing all the materials were pressed into pellets under 10 tons of pressure using a 13 mm diameter Specac die and sealed into a silica tube and refired. The tubes were placed in a furnace and heated up to the required temperature. All products were

fine, loose, dark grey powders.

The purity of the vanadium powder was found to be highly sensitive to obtain single-phase materials. The amount of the sample was limited to 3 g in order to avoid explosion of the tube. All the tubes containing more than 3 g of reactants exploded in the furnace whilst heating. It was also found to be very important that the tube was placed in a hot furnace at the ultimate reaction temperature which varied with the material. When the reactants were placed in the "cold" furnace and then heated up to the reaction temperature V_3S_4 was formed.

4.3 Results

4.3.1 Characterisation

All materials prepared were initially examined using powder X-ray diffraction. Powder X-ray diffraction data throughout the composition range $0 \leq x \leq 1$ can be indexed on the basis of a face-centred cubic unit cell, indicating solid-solution behaviour. Patterns of selected samples from the $Ga_{1-x}Ge_xV_4S_8$ series are presented in Figure 52.

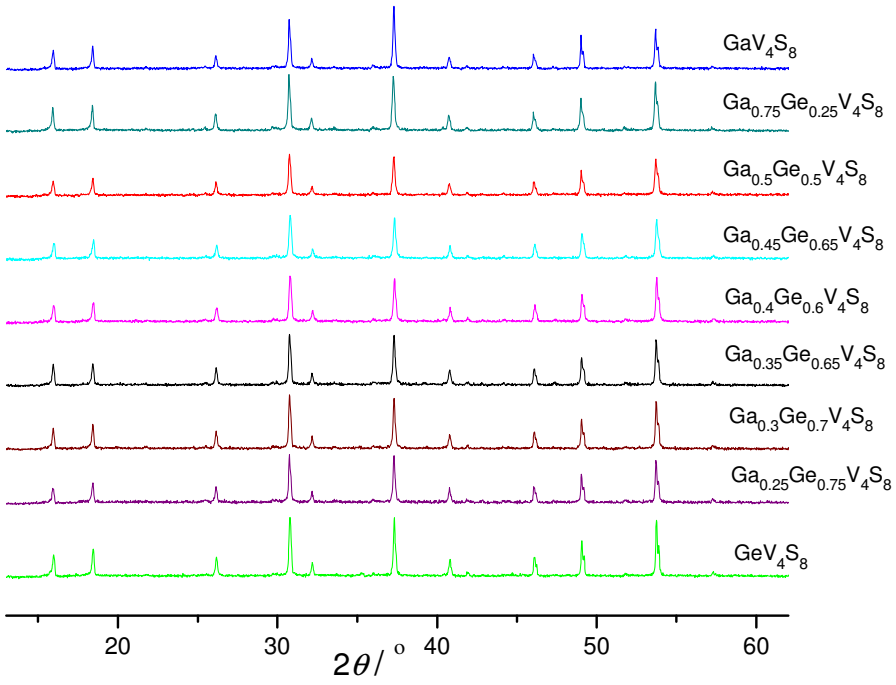

Figure 52: Powder X-ray diffraction data for $Ga_{1-x}Ge_xV_4S_8$ ($0 \leq x \leq 1$).

Powder X-ray diffraction demonstrates that mixed-metal sulphide samples are single phase materials and not simple mixtures of GaV_4S_8 and GeV_4S_8 (Figure 53). The lattice

parameters from powder X-ray diffraction data were obtained from Rietveld refinement with GSAS [189] using the graphical user interface EXPGUI [190]. The refined lattice parameters (Table 19) of the end-member phases are in excellent agreement with those reported previously [122, 123], while the compositional variation of the lattice parameters obtained from Rietveld refinement using powder X-ray diffraction data reveal that the unit cell volume decreases with increasing levels of germanium substitution (Figure 54).

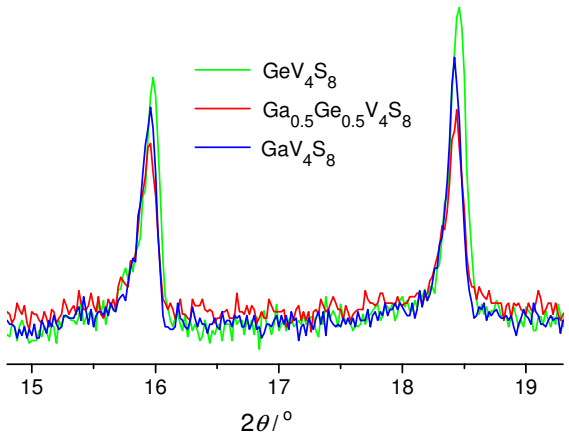

Figure 53: Expansion of a region of the powder X-ray diffraction pattern of GeV_4S_8, $Ga_{0.5}Ge_{0.5}V_4S_8$ and GaV_4S_8 showing that the $Ga_{0.5}Ge_{0.5}V_4S_8$ peaks are distinct from those of end members of the series and not a mixture of both.

Table 19: Refined lattice parameters for $Ga_{1-x}Ge_xV_4S_8$ phases.

***x* in $Ga_{1-x}Ge_xV_4S_8$**	***a*/Å**
1.0	9.65524(4)
0.9	9.65577(2)
0.85	9.65584(1)
0.75	9.65644(1)
0.65	9.65815(2)
0.3	9.65958(4)
0.0	9.66027(2)

The sulphur content of the $Ga_{1-x}Ge_xV_4S_8$ phases was determined using TGA. Thermogravimetric analysis of GaV_4S_8 under oxygen flow (Figure 55) reveals a weight loss of 16.31 % at T_1 = 676 K, associated with conversion to $Ga_2O_3 + V_6O_{13}$, followed by a weight gain of 2.71 % due to oxidation to V_2O_5. For the other end-member GeV_4S_8 a weight loss of 13.54 % at T_1 = 678 K (Figure 56) arising from conversion to

GeO_2 + V_6O_{13} is followed by a weight gain of 1.92 %, which occurs at temperature of about 873 K as a result of oxidation to V_2O_5.

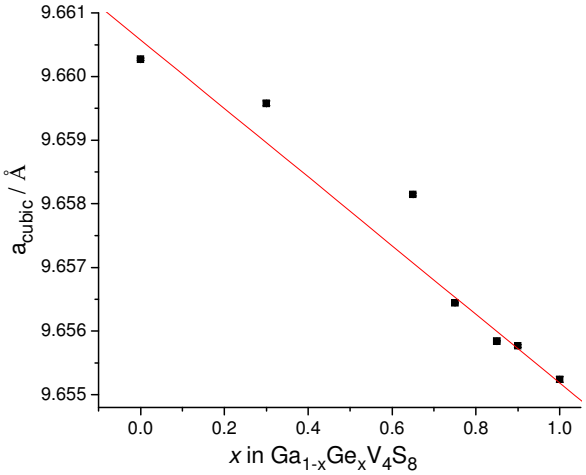

Figure 54: Cubic unit cell parameter at room temperature as a function of composition. Errors are marked but typically smaller than the points. The solid line is a guide for the eye.

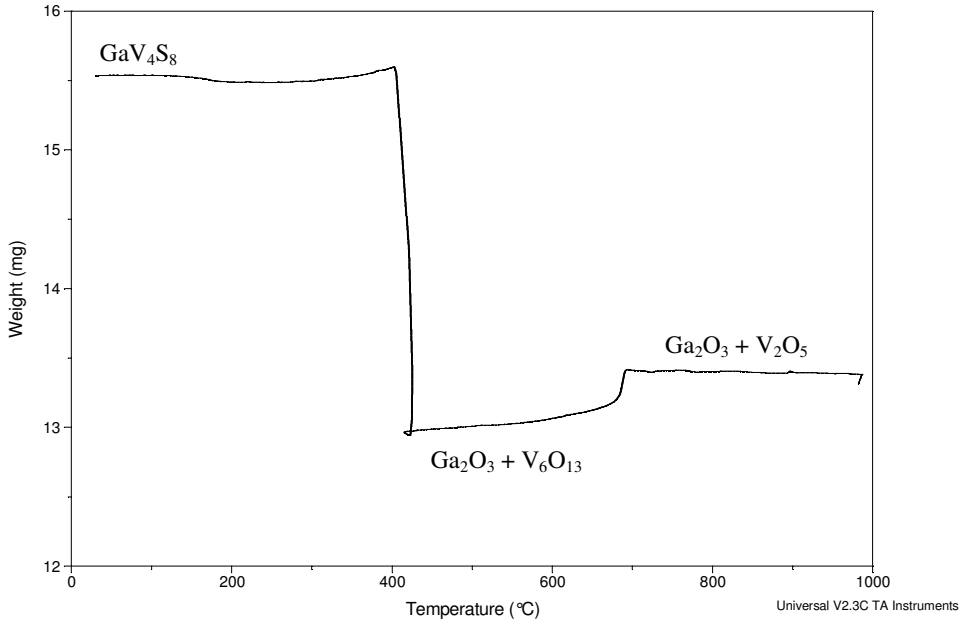

Figure 55: Thermogravimetric analysis data for GaV_4S_8.

Powder X-ray diffraction patterns recorded on the residues of thermogravimetric analysis (Figure 57) prove that the species formed upon the oxidation are GeO_2 and/or Ga_2O_3 and V_6O_{13} (which subsequently oxidises to V_2O_5). All the measurements were repeated several times and the average value of weight loss was taken to calculate the sulphur content. In case of GeV_4S_8 phase a small weight loss below the oxidation

temperature is observed and it might be due to moisture present in the sample.

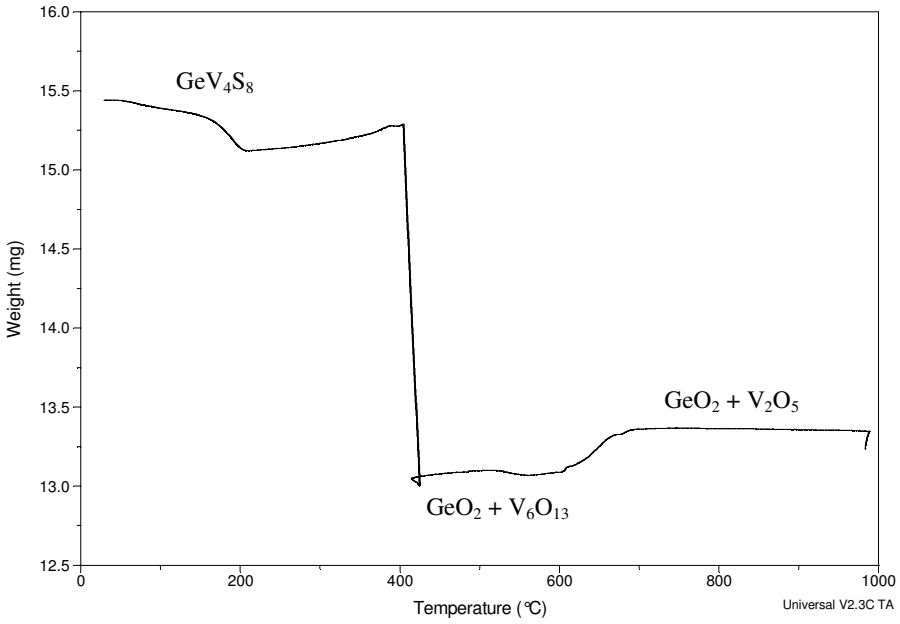

Figure 56: Thermogravimetric analysis data for GeV_4S_8.

Thermogravimetric data for the intermediate compositions show two distinct weight changes due to, in order of increasing temperature, conversion to oxides and oxidation of V_6O_{13} to V_2O_5. The representative TGA curve of a quaternary phase is presented in Figure 58[§]. Initial conversion of quaternary phases to a mixture of oxides requires a higher temperature than that for either of the end-member phases. The initial step (at temperature T_1) involving conversion to the mixture of oxides was used to determine the sulphur contents shown in Table 20, where thermogravimetric data are summarised. All materials show an appreciable sulphur deficiency. The sulphur contents show significant deviations from those expected from the nominal stoichiometries (Table 20). The sulphur deficiency has a marked influence on the number of electrons available to the cluster. On going from GaV_4S_8 to GeV_4S_8 the number of electrons per cluster increases. At the nominal end-member compositions there are 7 and 8 *d*-electrons per V_4 cluster, respectively. The actual number of electrons is higher (Table 20). In particular, on germanium substitution, the number of cluster electrons quickly exceeds the eight electrons expected for complete substitution, attaining a value of 8.9 e^-/cluster at GeV_4S_8.

[§] A full set of thermogravimetric analysis data is provided in Appendix 4.1.

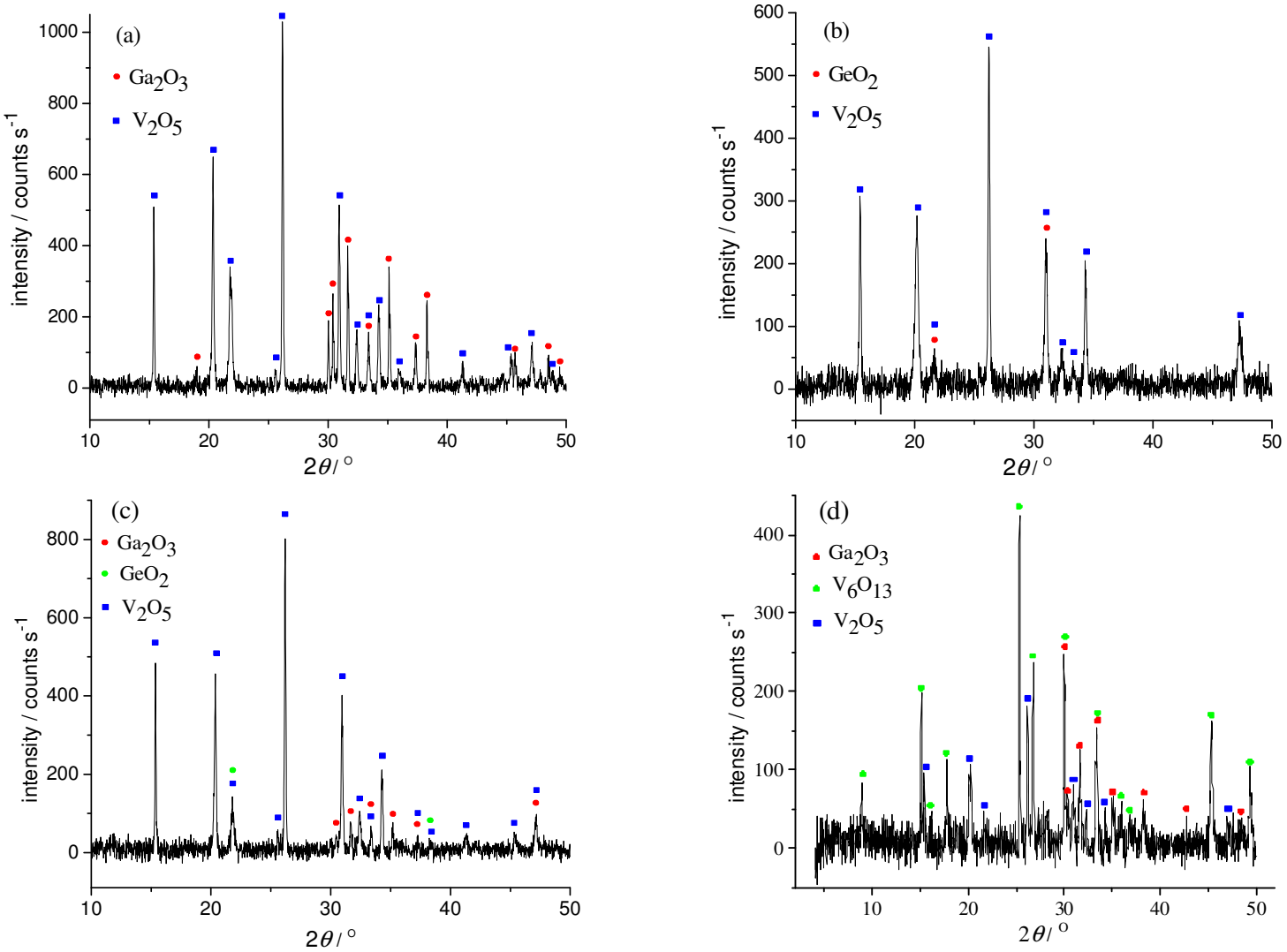

Figure 57: Powder X-ray diffraction patterns of (a) GaV_4S_8, (b) GeV_4S_8, (c) $Ga_{0.25}Ge_{0.75}V_4S_8$ heated to 1273 K in O_2 and (d) GaV_4S_8 heated to 773 K

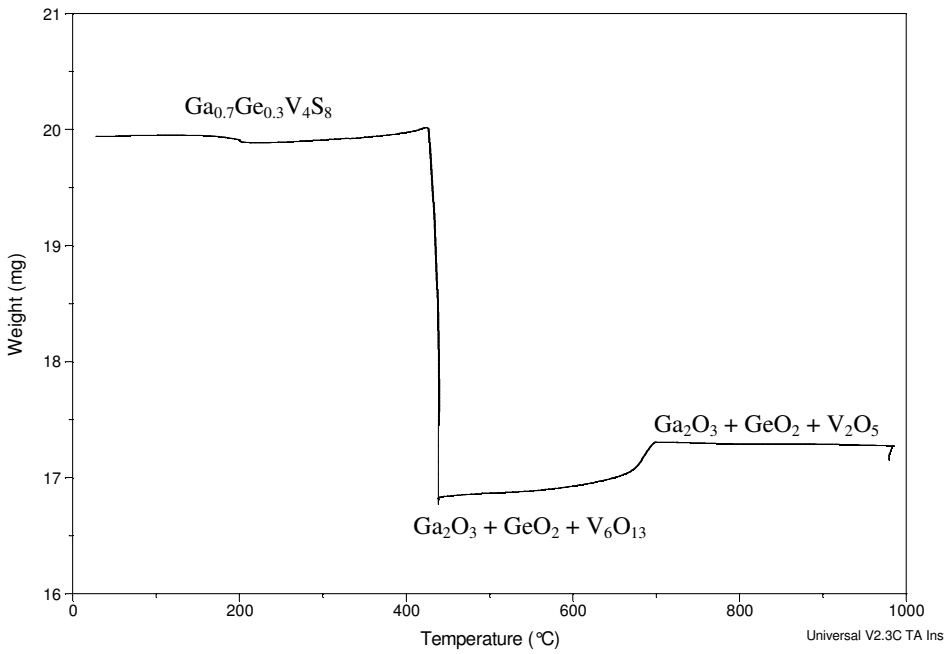

Figure 58: Thermogravimetric analysis data for $Ga_{0.7}Ge_{0.3}V_4S_8$.

Table 20: Results of thermogravimetric analysis on samples from the $Ga_{1-x}Ge_xV_4S_8$ ($0 \leq x \leq 1$) family of materials.

Nominal composition	**GaV_4S_8**	**$Ga_{0.9}Ge_{0.1}V_4S_8$**	**$Ga_{0.75}Ge_{0.25}V_4S_8$**	**$Ga_{0.7}Ge_{0.3}V_4S_8$**	**$Ga_{0.5}Ge_{0.5}V_4S_8$**	**$Ga_{0.45}Ge_{0.55}V_4S_8$**
T_1* / K	676	672	674	698	674	706
Theoretical weight loss at T_1 / %	17.71	17.42	17.18	17.10	16.78	16.70
Actual weight loss at T_1 / %	16.31	16.25	16.06	15.05	14.03	13.57
Weight gain at ~ 943 K / %	2.71	2.97	2.36	2.33	1.86	1.93
Experimentally determined composition**	$GaV_4S_{7.75(4)}$	$Ga_{0.9}Ge_{0.1}V_4S_{7.77(4)}$	$Ga_{0.75}Ge_{0.25}V_4S_{7.78(4)}$	$Ga_{0.7}Ge_{0.3}V_4S_{7.60(3)}$	$Ga_{0.5}Ge_{0.5}V_4S_{7.47(4)}$	$Ga_{0.45}Ge_{0.55}V_4S_{7.40(3)}$
Number of *d*-electrons per V_4 cluster***	7.5	7.56	7.69	8.1	8.56	8.75
Nominal number of *d*-electrons per V_4 cluster	7	7.1	7.25	7.3	7.5	7.55

* Initial oxidation temperature.
** Normalised to a Ga / Ge content of 1 mol / formula unit.
*** For experimentally determined composition.

Table 20: continued

Nominal composition	**$Ga_{0.4}Ge_{0.6}V_4S_8$**	**$Ga_{0.35}Ge_{0.65}V_4S_8$**	**$Ga_{0.3}Ge_{0.7}V_4S_8$**	**$Ga_{0.25}Ge_{0.75}V_4S_8$**	**$Ga_{0.1}Ge_{0.9}V_4S_8$**	**GeV_4S_8**
T_1* / K	679	685	712	716	702	678
Theoretical weight loss at T_1 / %	16.62	16.54	16.46	16.38	16.14	15.98
Actual weight loss at T_1 / %	13.50	13.52	13.87	13.68	14.18	13.54
Weight gain at ~ 943 K / %	1.65	2.01	1.77	1.97	2.04	1.92
Experimentally determined composition**	$Ga_{0.4}Ge_{0.6}V_4S_{7.40(2)}$	$Ga_{0.35}Ge_{0.65}V_4S_{7.42(6)}$	$Ga_{0.3}Ge_{0.7}V_4S_{7.50(4)}$	$Ga_{0.25}Ge_{0.75}V_4S_{7.48(4)}$	$Ga_{0.1}Ge_{0.9}V_4S_{7.62(2)}$	$GeV_4S_{7.53(4)}$
Number of *d*-electrons per V_4 cluster***	8.8	8.81	8.7	8.79	8.66	8.94
Nominal number of *d*-electrons per V_4 cluster	7.6	7.65	7.7	7.75	7.9	8

* Initial oxidation temperature.
** Normalised to a Ga / Ge content of 1 mol / formula unit.
*** For experimentally determined composition.

4.3.2 Structural Studies of Defect Thiospinels at Room Temperature

All $Ga_{1-x}Ge_xV_4S_8$ materials were examined by powder X-ray diffraction at room temperature. Additionally, room temperature neutron diffraction data were collected on selected samples (x = 0.9, 0.85, 0.65, 0.3 and at 200 K for x = 0.75) using the high resolution D2B diffractometer at ILL. The initial structural model, for Rietveld refinement of the structure of the end-member phase GaV_4S_8, was that of Pocha *et al.* [123], described in the space group $F\bar{4}3m$, whilst for GeV_4S_8 the atomic coordinates of Johrendt [122] were used for the initial structural model. The structural model for the quaternary phases was obtained by progressively introducing germanium in place of gallium at the *A*-cation site to maintain the correct stoichiometry. Powder X-ray and neutron diffraction data collected at room temperature were used simultaneously in Rietveld analysis in order to confirm that germanium is incorporated exclusively at the *A*-cation (4(*a*)) site initially occupied by gallium alone. In the region d = 2.1 – 2.2 Å in the neutron data collected at room temperature weak reflection due to vanadium (d_{110} = 2.14 Å) originating from the sample can was observed. The background of the neutron data was modelled using a cosine Fourier series whilst a linear interpolation function was used to fit the background of the X-ray data. Following initial refinement of scale factors, background terms, X-ray zero-point, positional, lattice parameters and thermal parameters were introduced as variables into the refinement. In all cases, the thermal parameters for Ga and Ge were constrained to be equal and also a single thermal parameter was used for both the vanadium and sulphide ions. In case of end member phases it was found to be necessary to constrain the thermal parameters of all atoms to the same value in order to produce a stable refinement. A pseudo-Voigt peak shape was used for both X-ray and neutron data, with the coefficients introduced as refinable parameters. The site occupancy factors were refined using neutron diffraction data and they were allowed to vary with the constraint that the overall stoichiometry was maintained. The refined site occupancy factors result in a Ga:Ge ratio in excellent agreement with the values of the initial reaction mixtures. Attempts to locate the sulphur vacancies by Rietveld analysis were unsuccessful suggesting they are disordered over the available sites. The final cycles of refinement produced residuals in the range 4.58 – 5.12 % (X-ray) and 3.25 – 4.81 (neutron). Observed, calculated and difference profiles from the simultaneous X-ray/neutron refinement are presented in Figure 59 - Figure 63. Corresponding profiles for the remaining compositions, obtained using X-ray diffraction data alone are provided in Appendix 4.2. Refined structural

parameters obtained from refinement against X-ray and neutron diffraction data simultaneously are given in Table 21, whilst significant bond distances and angles appear in Table 22. The refined parameters for those obtained from powder X-ray diffraction data alone are presented in Table 23 and Table 24.

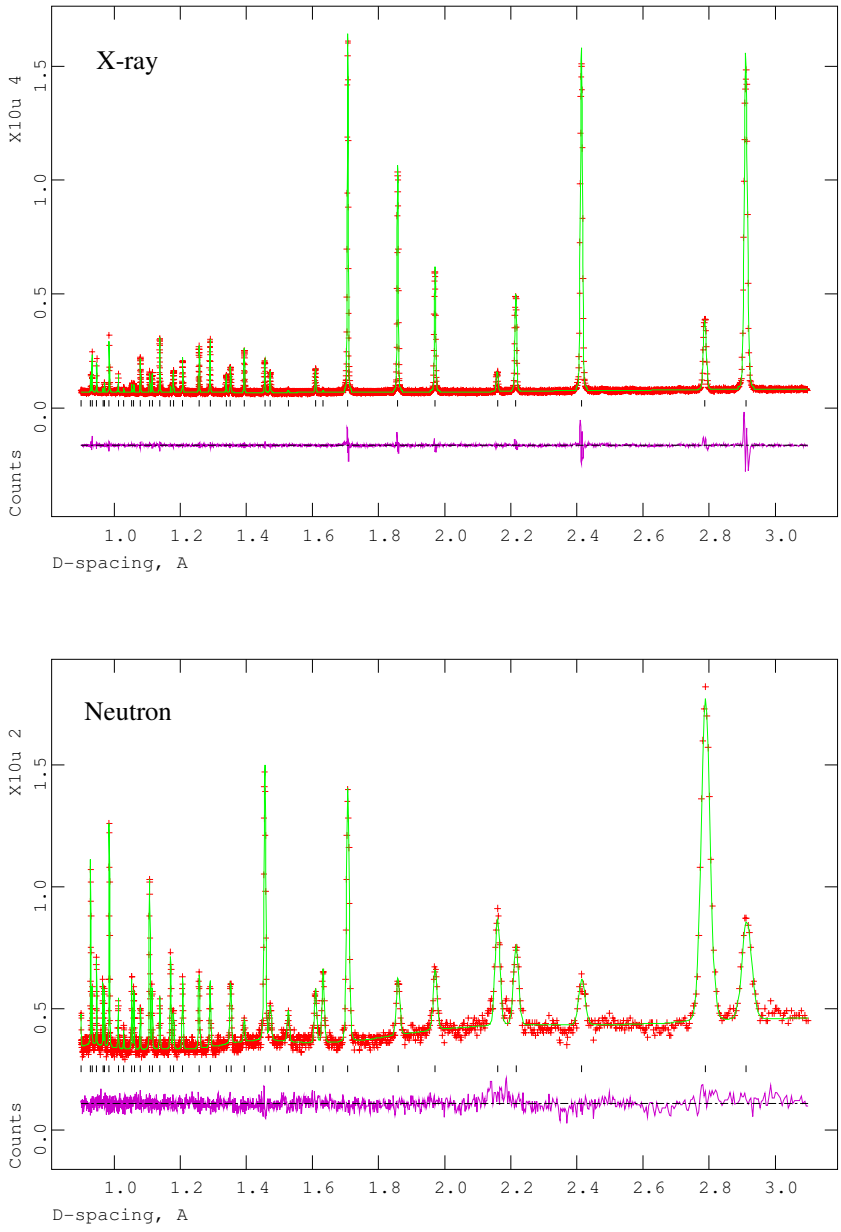

Figure 59: Final observed (crosses), calculated (upper full line) and difference (lower full line) profiles for nominal composition $Ga_{0.1}Ge_{0.9}V_4S_8$ at 298 K (X-ray data: upper plot, neutron data: lower plot). Reflection positions are marked.

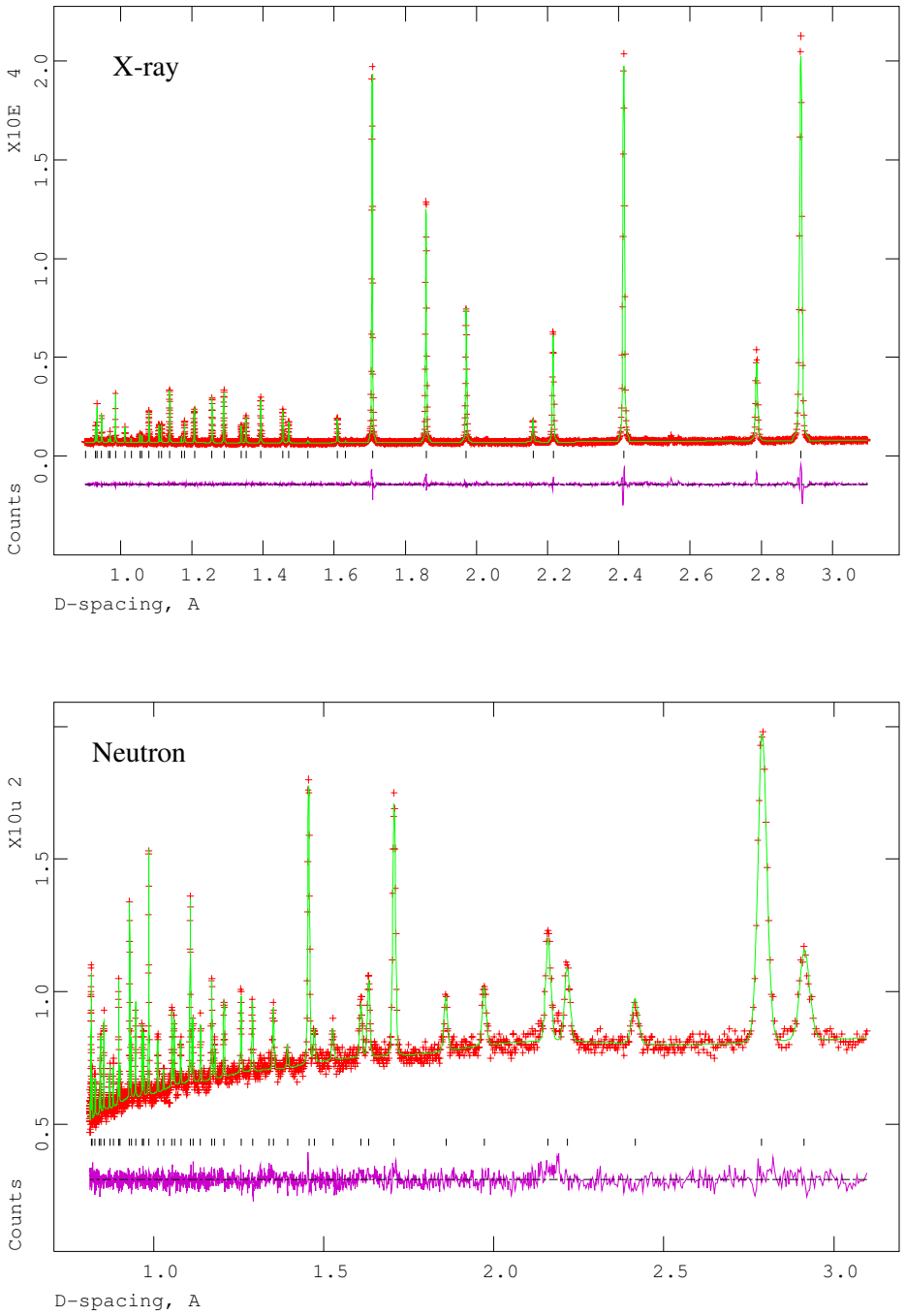

Figure 60: Final observed (crosses), calculated (upper full line) and difference (lower full line) profiles for nominal composition $Ga_{0.15}Ge_{0.85}V_4S_8$ at 298 K (X-ray data: upper plot, neutron data: lower plot). Reflection positions are marked.

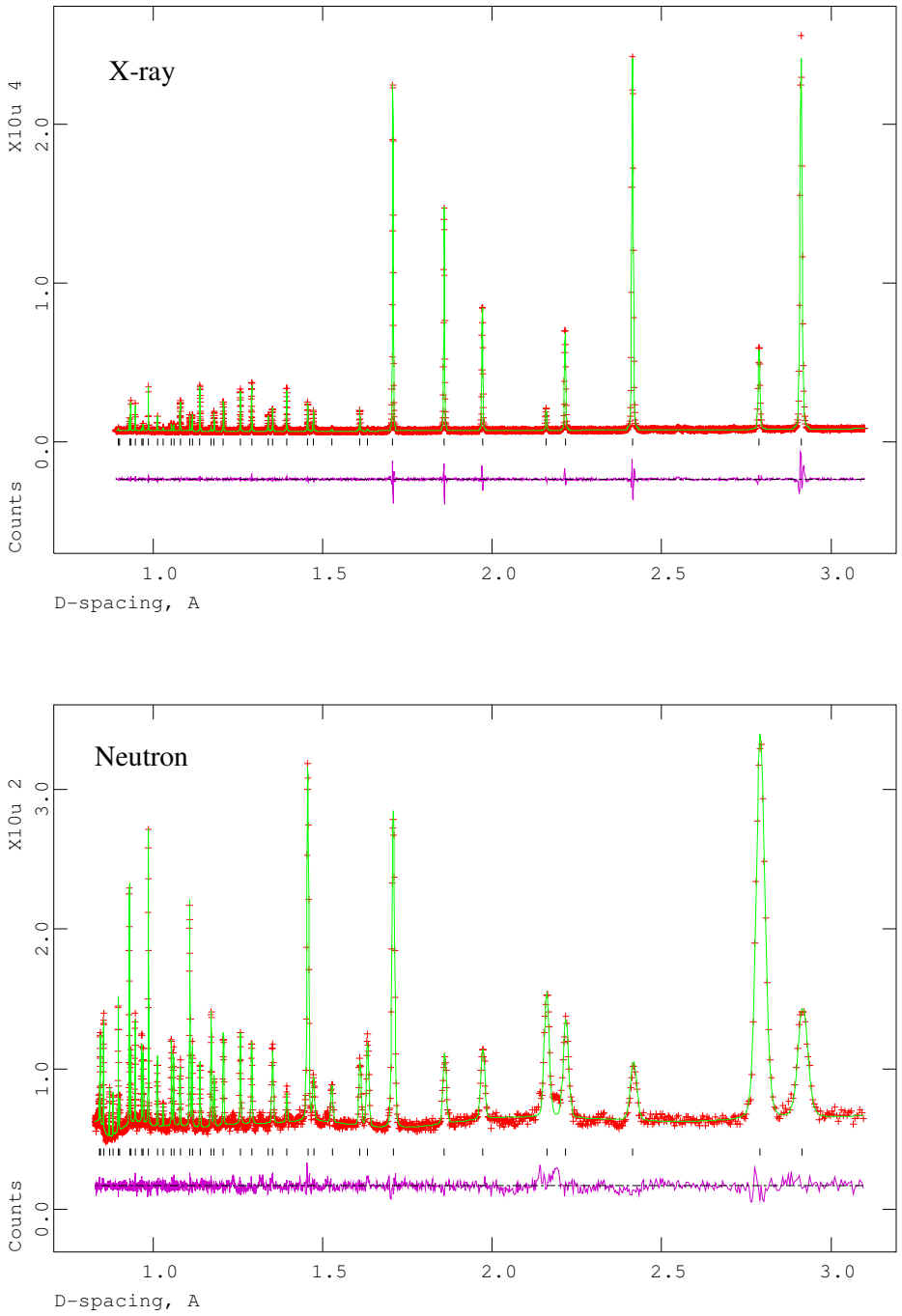

Figure 61: Final observed (crosses), calculated (upper full line) and difference (lower full line) profiles for nominal composition $Ga_{0.35}Ge_{0.65}V_4S_8$ at 298 K (X-ray data: upper plot, neutron data: lower plot). Reflection positions are marked.

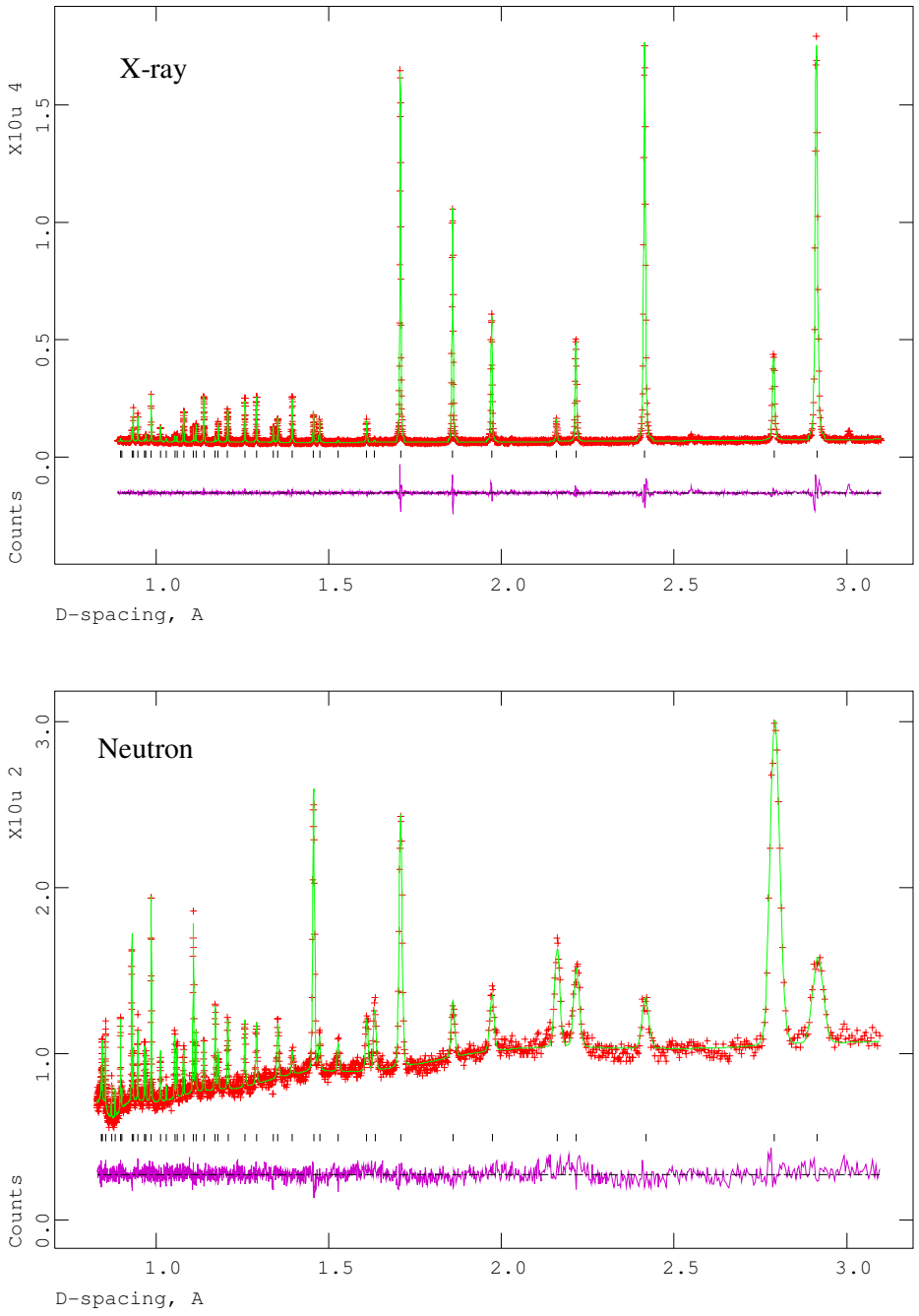

Figure 62: Final observed (crosses), calculated (upper full line) and difference (lower full line) profiles for nominal composition $Ga_{0.7}Ge_{0.3}V_4S_8$ at 298 K (X-ray data: upper plot, neutron data: lower plot). Reflection positions are marked.

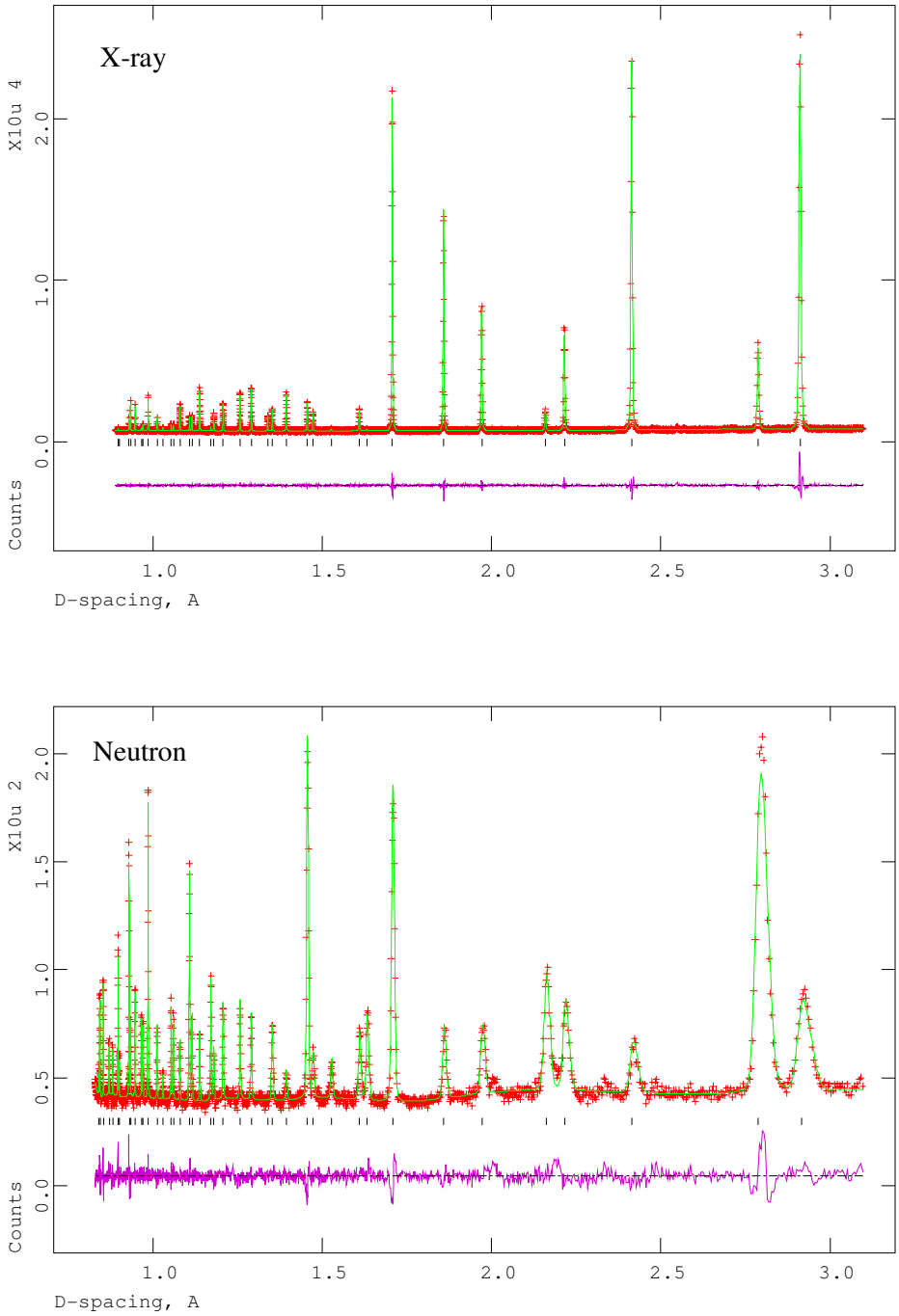

Figure 63: Final observed (crosses), calculated (upper full line) and difference (lower full line) profiles for nominal composition $Ga_{0.25}Ge_{0.75}V_4S_8$ at 298 K (X-ray) and 200 K (neutron). Reflection positions are marked.

Table 21: Final refined parameters from simultaneous X-ray/neutron refinement for $Ga_{1-x}Ge_xV_4S_8$ materials described in the space group $F\bar{4}3m$ [*].

***x* in $Ga_{1-x}Ge_xV_4S_8$**		**0.9**	**0.85**	**0.75**	**0.65**	**0.3**
T/K		298	298	200	298	298
a/Å		9.65550(2)	9.65565(1)	9.65640(1)	9.65803(1)	9.65958(2)
Ga/Ge	SOF(Ga)	0.08(5)	0.18(5)	0.31(3)	0.39(3)	0.66(4)
	SOF(Ge)	0.92(5)	0.82(5)	0.69(3)	0.61(3)	0.34(4)
	B/Å^2	0.41(3)	0.18(3)	0.32(2)	0.47(2)	0.38(3)
	x	0	0	0	0	0
V	B/Å^2	0.49(1)	0.34(1)	0.44(1)	0.50(1)	0.40(1)
	x	0.60414(5)	0.60439(5)	0.60435(6)	0.60466(5)	0.60533(5)
S(1)	B/Å^2	0.49(1)	0.34(1)	0.44(1)	0.50(1)	0.40(1)
	x	0.36988(8)	0.36916(8)	0.37086(8)	0.37089(7)	0.37125(8)
S(2)	B/Å^2	0.49(1)	0.34(1)	0.44(1)	0.50(1)	0.40(1)
	x	0.86518(8)	0.86545(8)	0.86452(8)	0.86437(7)	0.86392(9)
R_{wp}/% (neutron) R_{wp}/% (X-ray)		4.63 4.97	3.25 4.58	4.81 4.64	3.81 5.12	3.59 4.67
χ^2		2.11	1.79	2.28	2.33	1.80

[*] Ga and Ge on 4(*a*) (0, 0, 0) site; V, S(1) and S(2) on 16(*e*) (*x,x,x*) site.

Table 22: Bond distances (Å) and bond angles (^{o}) from simultaneous X-ray/neutron refinement for $Ga_{1-x}Ge_xV_4S_8$ materials ($F\bar{4}3m$).

***x* in $Ga_{1-x}Ge_xV_4S_8$**	**0.9**	**0.85**	**0.75**	**0.65**	**0.3**
T/K	298	298	200	298	298
M-S(2)	2.255(1) × 4	2.250(1) × 4	2.266(1) × 4	2.269(1) × 4	2.277(1) × 4
V-S(1)	2.290(1) × 3	2.300(1) × 3	2.280(1) × 3	2.282(1) × 3	2.284(1) × 3
V-S(2)	2.555(1) × 3	2.554(1) × 3	2.548(1) × 3	2.544(1) × 3	2.533(1) × 3
V-V within the V_4 clusters	2.844(2) × 6	2.851(1) × 6	2.850(2) × 6	2.859(2) × 6	2.878(2) × 6
V-V between clusters	3.983(2)	3.977(1)	3.905(2)	3.970(2)	3.952(2)
S(2)-M-S(2)	109.471(0) × 6	109.471(0) × 6	109.471(0) × 6	109.471(0) × 6	109.471(0) × 6
S(1)-V-S(1)	102.1(4) × 3	101.8(5) × 3	101.6(3) × 3	101.19(4) × 3	100.74(4) × 3
S(1)-V-S(2)	89.54(3) × 6	89.45(3) × 6	90.04(3) × 6	90.12(3) × 6	90.39(3) × 6
S(2)-V-S(2)	75.98(5) × 3	76.23(4) × 3	75.72(5) × 3	75.77(4) × 3	75.82(5) × 3

Table 23: Refined structural parameters from powder X-ray diffraction data for $Ga_{1-x}Ge_xV_4S_8$ phases ($F\bar{4}3m$)*.

***x* in $Ga_{1-x}Ge_xV_4S_8$**		**1.0**	**0.9**	**0.85**	**0.75**	**0.65**	**0.3**	**0.0**
Ga	B/Å^2	1.66(3)	0.59(2)	0.33(3)	0.40(3)	0.54(4)	0.39(4)	0.13(2)
	x	-	0	0	0	0	0	0
Ge	B/Å^2	1.66(3)	0.59(2)	0.33(3)	0.40(3)	0.54(4)	0.39(4)	0.13(2)
	x	0	0	0	0	0	0	-
V	B/Å^2	1.66(3)	0.59(2)	0.36(2)	0.45(1)	0.51(2)	0.37(2)	0.13(2)
	x	0.60370(9)	0.60415(7)	0.60429(5)	0.60441(5)	0.60477(7)	0.60527(5)	0.60602(7)
S(1)	B/Å^2	1.66(3)	0.59(2)	0.36(2)	0.45(1)	0.51(2)	0.37(2)	0.13(2)
	x	0.37051(15)	0.37144(10)	0.37083(8)	0.37137(8)	0.37105(11)	0.37148(8)	0.36996(11)
S(2)	B/Å^2	1.66(3)	0.59(2)	0.36(2)	0.45(1)	0.51(2)	0.37(2)	0.13(2)
	x	0.86520(14)	0.86396(10)	0.86423(8)	0.86402(8)	0.86393(10)	0.86380(8)	0.86459(10)
R_{wp}/%		6.02	5.75	4.45	4.57	6.23	4.55	5.55

* Ga and Ge on 4(*a*) (0, 0, 0) site; V, S(1) and S(2) on 16(*e*) (*x,x,x*) site.

Table 24: Bond distances (Å) and bond angles (^{o}) from powder X-ray diffraction refinement for $Ga_{1-x}Ge_xV_4S_8$ phases ($F\bar{4}3m$).

***x* in $Ga_{1-x}Ge_xV_4S_8$**	**1.0**	**0.9**	**0.85**	**0.75**	**0.65**	**0.3**	**0.0**
M-S(2)	2.254(2) × 4	2.275(2) × 4	2.271(1) × 4	2.274(1)× 4	2.276(2) × 4	2.279(1) × 4	2.266(2) × 4
V-S(1)	2.279(2) × 3	2.272(1) × 3	2.280(1) × 3	2.274(1) × 3	2.281(1) × 3	2.281(1) × 3	2.304(1) × 3
V-S(2)	2.560(2) × 3	2.546(1) × 3	2.546(1) × 3	2.544(1) × 3	2.539(1) × 3	2.533(1) × 3	2.530(1) × 3
V-V within the V_4 clusters	2.832(3) × 6	2.844(2) × 6	2.848(2) × 6	2.852(1) × 6	2.862(2) × 6	2.876(2) × 6	2.897(2) × 6
V-V between clusters	3.995(3)	3.983(2)	3.979(1)	3.976(1)	3.967(2)	3.954(2)	3.934(2)
S(2)-M-S(2)	109.471(0) × 6	109.471(0) × 6	109.471(0) × 6	109.471(0) × 6	109.471(0) × 6	109.471(0) × 6	109.471(0) × 6
S(1)-V-S(1)	101.77(7) × 3	101.21(5) × 3	101.38(4) × 3	101.12(4) × 3	101.08(5) × 3	100.68(4) × 3	100.91(5) × 3
S(1)-V-S(2)	89.73(6) × 6	90.28(4) × 6	90.091(31) × 6	90.280(31) × 6	90.27(4) × 6	90.463(32) × 6	90.02(4) × 6
S(2)-V-S(2)	75.81(8) × 3	75.35(6) × 3	75.55(5) × 3	75.49(5) × 3	75.59(6) × 3	75.73(5) × 3	76.46(6) × 3

4.3.3 Physical Property Measurements

4.3.3.1 Magnetic Properties of $Ga_{1-x}Ge_xV_4S_8$

The magnetic behaviour of the defect thiospinels was studied using SQUID magnetometry as described in Chapter 2. Data were collected on seven samples as a function of temperature in an applied field of 1000 G under both field-cooled (fc) and zero-field-cooled (zfc) conditions. Data for $Ga_{0.5}Ge_{0.5}V_4S_8$ were collected only under field-cooled conditions owning to time constraints. Zero-field-cooled and field-cooled magnetic susceptibility data for all materials (Figure 64) overlie each other over the entire temperature range studied. Reciprocal magnetic data for the end member phases [146] down to 45 K are well described by a modified Curie-Weiss expression, incorporating a temperature-independent term. Low-temperature anomalies at 40 K and at 9 K in GaV_4S_8 are associated respectively with a rhombohedral distortion and ferromagnetic ordering and that at 13 K in GeV_4S_8 with antiferromagnetic ordering. Data for the mixed $Ga_{1-x}Ge_xV_4S_8$ ($0 < x < 1$) phases follow Curie-Weiss behaviour over a wide range of temperatures, with deviations being observed only at low temperatures. Magnetic parameters derived from the linear fits to reciprocal susceptibility data are presented in Table 25. The effective magnetic moment, μ_{eff}, of GaV_4S_8 is *ca.* 1.6 μ_B per vanadium-sulphur cluster. This is close to the value for a single unpaired electron, which the molecular orbital treatment of Pocha *et al.* would predict [123] for $V_4S_4^{5+}$. Substitution of Ga^{3+} with Ge^{4+} causes reduction of the cluster which would be expected to increase μ_{eff}. Whilst the magnetic susceptibility data reveal that μ_{eff} does indeed increase with increasing germanium content, the observed moments are slightly higher than predicted on the basis of the changing occupation of the cluster orbitals. This would appear to be related to the increased electron count arising from the sulphur non-stoichiometry. For instance, the expected value of $\mu_{eff} = 2.29$ for $Ga_{0.5}Ge_{0.5}V_4S_8$ rises to 3.4 μ_B when sulphur deficiency is taken into account. The latter compares favourably with the experimentally-determined value of $\mu_{eff} = 2.97$ μ_B, allowing for the expected reduction from the spin-only moment due to an orbital contribution. The observation of moderately large, negative Weiss constants for all non-stoichiometric materials, suggests that the dominant exchange interactions are antiferromagnetic in origin.

Depending on composition, two distinct types of low-temperature magnetic behaviour are observed. For all samples with $x \leq 0.7$, the reciprocal susceptibility data exhibit a discontinuity around 40 K that comparison with the end-member phase GaV_4S_8 [123] suggests is due to a structural distortion. The second lower temperature

anomaly in χ^{-1}(T), which corresponds to a marked increase in magnetisation, indicates that the ferromagnetic behaviour of GaV_4S_8 [123] is retained to $x \leq 0.7$, with $T_C \approx 20$ K. The magnitude of the low temperature susceptibility of the materials decreases with increasing germanium content, until at compositions with $x > 0.7$, the low-temperature magnetisation is greatly reduced and a local maximum is introduced into χ(T). It would thus appear that $Ga_{0.25}Ge_{0.75}V_4S_8$ exhibits antiferromagnetic order, similar to that of the end-member phase GeV_4S_8, with $T_N = 15$ K.

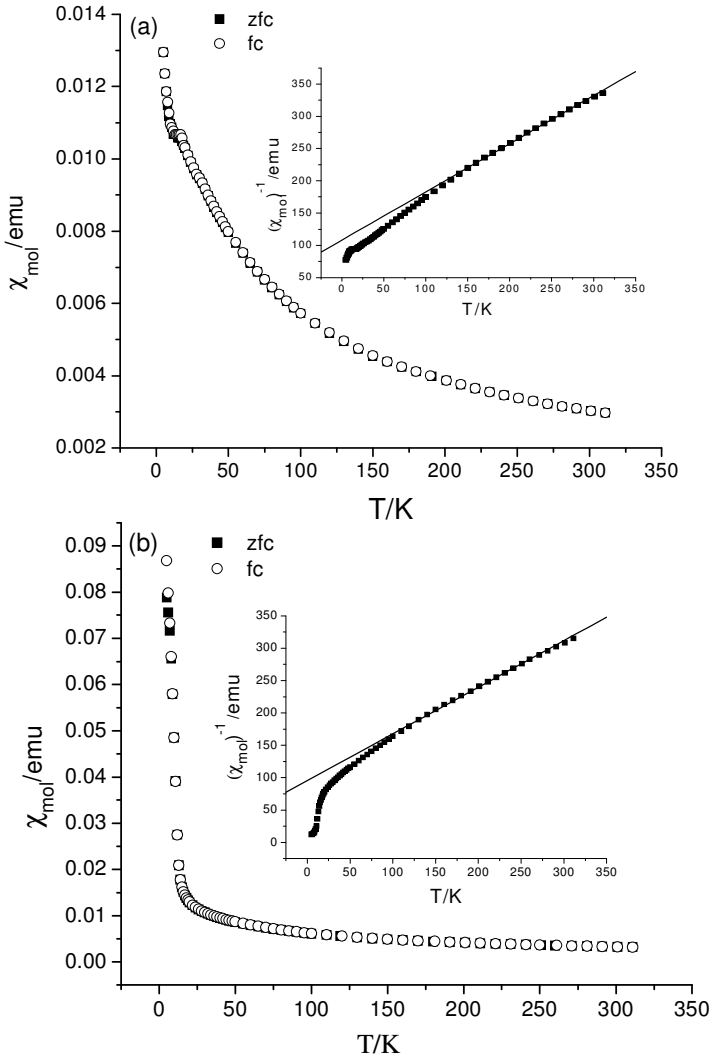

Figure 64: Zero-field-cooled (zfc) and field-cooled (fc) molar magnetic susceptibility data for: (a) $Ga_{0.25}Ge_{0.75}V_4S_8$, (b) $Ga_{0.3}Ge_{0.7}V_4S_8$, (c) $Ga_{0.35}Ge_{0.65}V_4S_8$, (d) $Ga_{0.4}Ge_{0.6}V_4S_8$, (e) $Ga_{0.45}Ge_{0.55}V_4S_8$, (f) $Ga_{0.5}Ge_{0.5}V_4S_8$ – (fc), (g) $Ga_{0.75}Ge_{0.25}V_4S_8$ data. *Inset:* Reciprocal magnetic susceptibility data showing the fit (solid line) to the Curie-Weiss law.

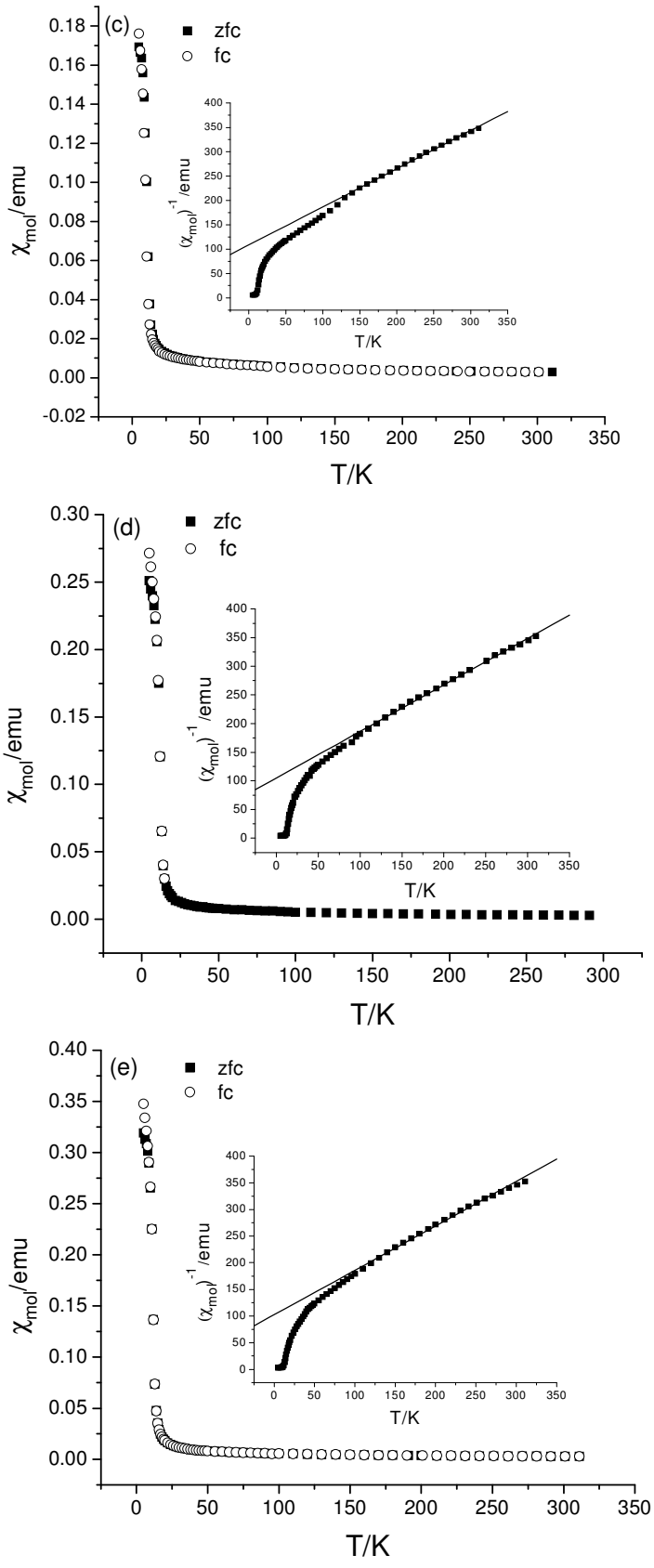

Figure 64: continued

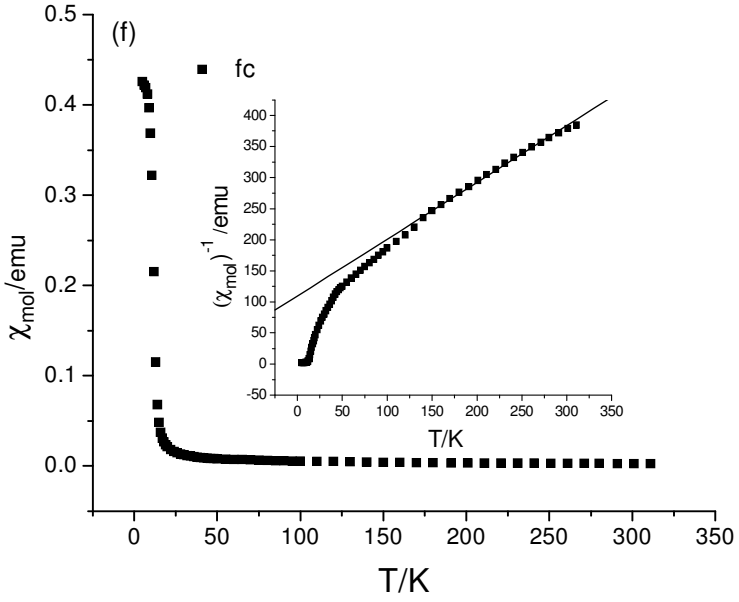

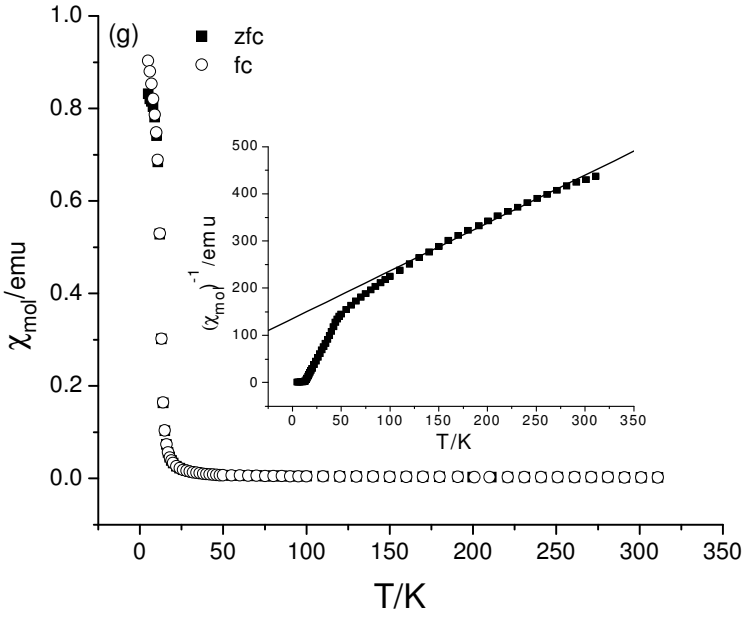

Figure 64: continued

Table 25: Parameters derived from magnetic susceptibility data using a Curie-Weiss law.

Material	Data range / K	C / cm^3 K mol^{-1}	θ / K	μ_{eff} per V_4 cluster
GaV_4S_8* [146]	45-295	0.304(3)	-12.4(6)	1.559(8)
$Ga_{0.75}Ge_{0.25}V_4S_8$	110-285	0.984(5)	-133.98(9)	2.81(8)
$Ga_{0.5}Ge_{0.5}V_4S_8$	130-300	1.102(4)	-123.04(9)	2.97(7)
$Ga_{0.45}Ge_{0.55}V_4S_8$	110-290	1.1994(3)	-122.9055(6)	3.10(8)
$Ga_{0.4}Ge_{0.6}V_4S_8$	100-300	1.2093(1)	-122.696(2)	3.11(3)
$Ga_{0.35}Ge_{0.65}V_4S_8$	140-300	1.2783(4)	-138.9386(6)	3.20(7)
$Ga_{0.3}Ge_{0.7}V_4S_8$	110-270	1.3869(3)	-68.9189(4)	3.33(8)
$Ga_{0.25}Ge_{0.75}V_4S_8$	130-300	1.328(5)	-142.08(4)	3.26(8)
GeV_4S_8** [146]	45-295	0.75(2)	-36.2(2)	2.45(3)

* Fit to a modified Curie-Weiss law incorporating a temperature-independent term, $\chi_0 = 4.3(1) \times 10^{-4}$ emu

** Fit to a modified Curie-Weiss law incorporating a temperature-independent term, $\chi_0 = 4.9(4) \times 10^{-4}$ emu

4.3.3.2 Electron Transport Properties

Electrical resistance data for all the samples were collected as described in Section 2.3.1 in Chapter 2. GaV_4S_8 exhibits semiconducting behaviour (Figure 65). The mechanism of the conductivity in GaV_4S_8 was investigated in detail by Rastogi *et al.* [144] who reported that the activation energy varies from 0.14 eV at room temperature to 0.04 eV at 80 K. It was proposed that this reduction is the result of multielectron hopping of carriers. By fitting the linear portion of the ln(ρ) *vs.* 1/T curve (Figure 66), an activation energy of 0.08(2) eV was obtained, which is within the range previously reported. The analogous plot for the other end-member is non-linear, indicating that it does not exhibit simple thermally activated conduction. However, the data were found to conform to a variable-range-hopping model [225] of the form

$$\rho = \rho_0 \left(\frac{T}{T_0}\right)^{1/2} \exp\left[\left(\frac{T_0}{T}\right)^{\nu}\right] \tag{56}$$

with the exponent $\nu = ¼$ indicating a three-dimensional conduction mechanism (Figure 67).

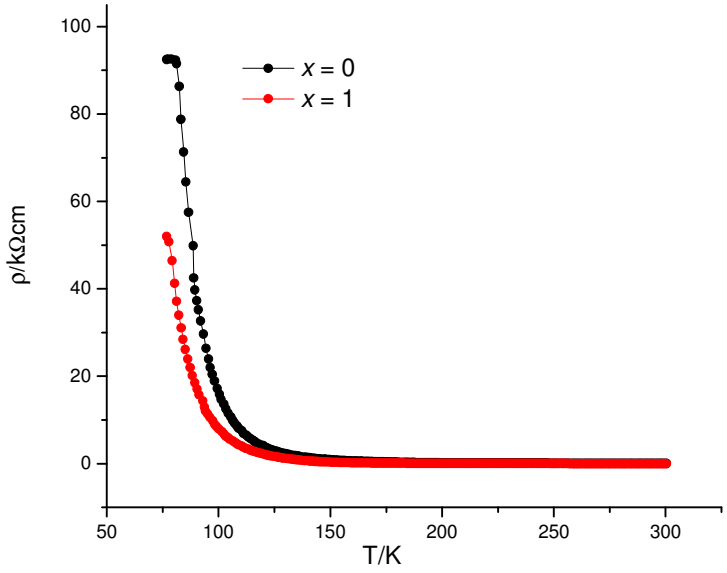

Figure 65: Electrical transport property data for end-members of the $Ga_{1-x}Ge_xV_4S_8$ series.

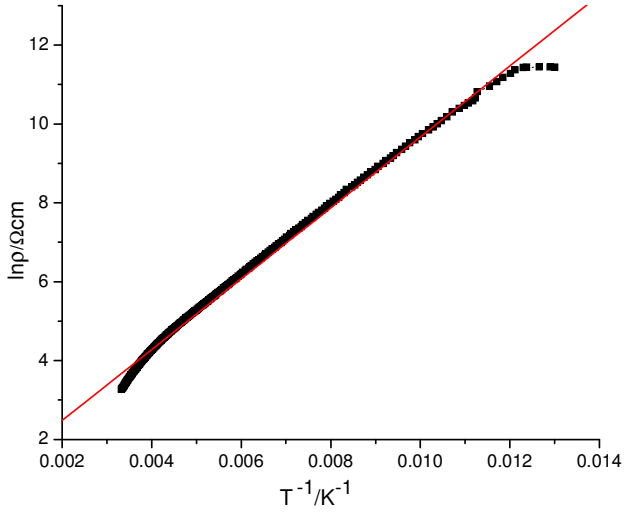

Figure 66: Temperature dependence of the electrical resistivity of GaV_4S_8.

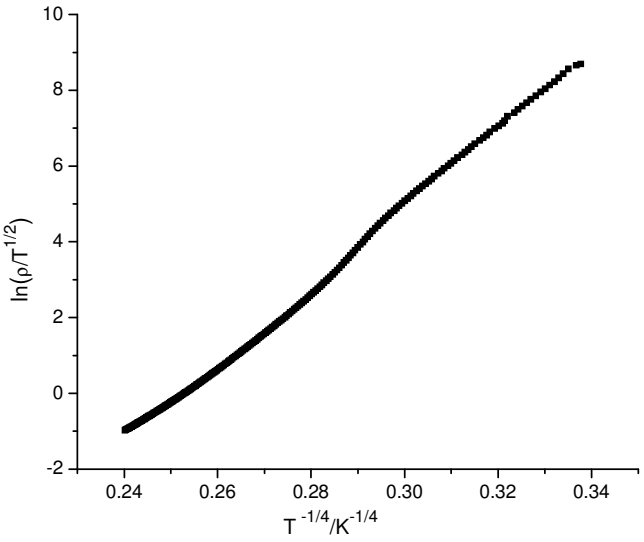

Figure 67: The VRH relation $\ln(\rho/T^{1/2})$ versus $T^{-\nu}$ with $\nu = ¼$ for GeV_4S_8.

The temperature dependence of the electrical resistivity of all quaternary phases (Figure 68) is also consistent with semiconducting behaviour. However, there is a significant reduction of the resistivity relative to that of either of the end-member phases (Figure 65). For materials containing both gallium and germanium, the magnitude of the resistivity decreases with increasing germanium content such that the resistivity of $Ga_{0.25}Ge_{0.75}V_4S_8$ at low temperature (*ca.* 80 K) is almost six orders of magnitude lower than that of GaV_4S_8.

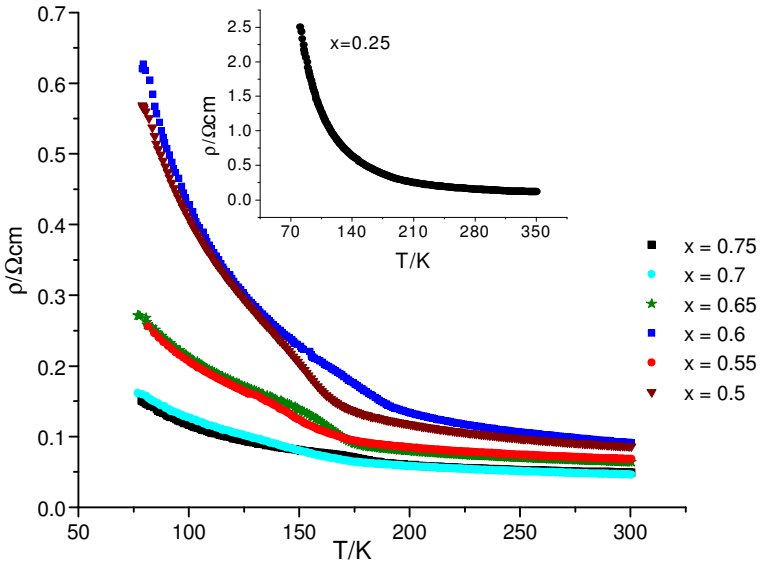

Figure 68: Electrical transport property data for $Ga_{1-x}Ge_xV_4S_8$.

For non-stoichiometric materials plots of ln(ρ) vs. T^{-1} are non-linear indicating that the conduction mechanism is not of the Arrhenius type. However, plots of $\ln(\rho/T^{1/2})$ vs. $T^{-1/4}$ (Figure 69) are linear over a wide range of temperatures, indicating that a variable-range hopping conduction mechanism is operative throughout the composition range ($0 < x \leq 1$) suggesting that the conduction is dominated by hopping of charge carriers between states localised on opposite sides of the Fermi energy. Furthermore, with the exception for $Ga_{0.75}Ge_{0.25}V_4S_8$, a resistivity anomaly, not present in the end members, is observed in the region 165 K – 182 K, depending on the composition. The origin of this anomaly is unclear. This anomaly might be due to small amount of V_2O_3 impurities. Pure V_2O_3 undergoes metal-insulator transition at *ca.* 150 K [226], marked by a sudden increase in the electrical resistivity data. However, powder X-ray diffraction data does not indicate any V_2O_3 impurities. A similar anomaly was also observed in NiV_2S_4 [227] at about 165 K and was demonstrated to be characteristic of this phase rather than an effect arising from V_2O_3 impurities. It was reported [227] as a first-order transition involving substantial changes in the electronic structure due to periodic displacement of the crystal lattice/lattice distortion. Johrendt has suggested [122] that the electronic structure of ordered-defect thiospinels is extremely sensitive to subtle structural distortions of the V_4 cluster from tetrahedral symmetry. Analysis of neutron diffraction data provide no evidence for a reduction from cubic symmetry at this temperature, suggesting that any such distortion would involve displacement of vanadium atoms.

Low-temperature X-ray diffraction data are required to investigate structural changes in this temperature region.

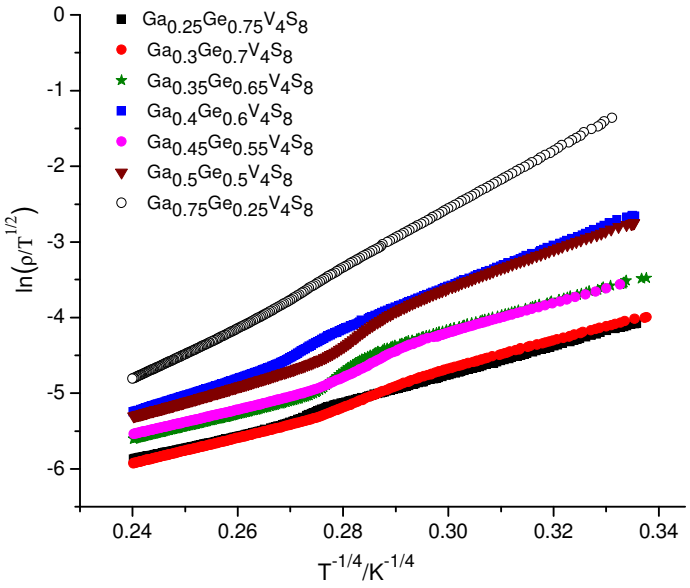

Figure 69: The VRH relation $\ln(\rho/T^{1/2})$ versus $T^{-\nu}$ with $\nu = ¼$ for non-stoichiometric phases.

4.3.3.3 Seebeck Coefficient Measurements

Seebeck coefficient measurements were performed over the temperature range $100 \leq T/K \leq 300$ as described in Section 2.3.2 in Chapter 2. The large negative Seebeck coefficient of GaV_4S_8 (Figure 70(a)) indicates that the dominant charge carriers are electrons. Although the data presented by Sahoo and Rastogi [144] appear to indicate *p*-type behaviour, they state clearly that it is an *n*-type semiconductor in agreement with the data collected in this work, suggesting an error in the plot in the latter work. They have shown however that the Seebeck coefficient of GaV_4S_8 is dependent on sample preparation and on gallium content. Quenching the sample significantly changes the values of Seebeck coefficient and 33 % gallium excess results in a change of sign at low temperatures [144]. The other end-member phase GeV_4S_8 exhibits hole-type conduction as evidenced by the positive Seebeck coefficient (Figure 70(b)), although its absolute value is significantly lower than that of GaV_4S_8. However, at intermediate compositions the Seebeck coefficient in the temperature range $100 \leq T/K \leq 300$ is negative (Figure 71). This indicates that the materials are *n*-type semiconductors in which conduction is dominated by electrons. The temperature dependence of the

Seebeck coefficient of the non-stoichiometric phases is much weaker than that of either of the end members. At a given temperature, the absolute value of the Seebeck coefficient decreases with increasing germanium content (Figure 72), which correlates with the marked reduction in resistivity with increasing levels of substitution.

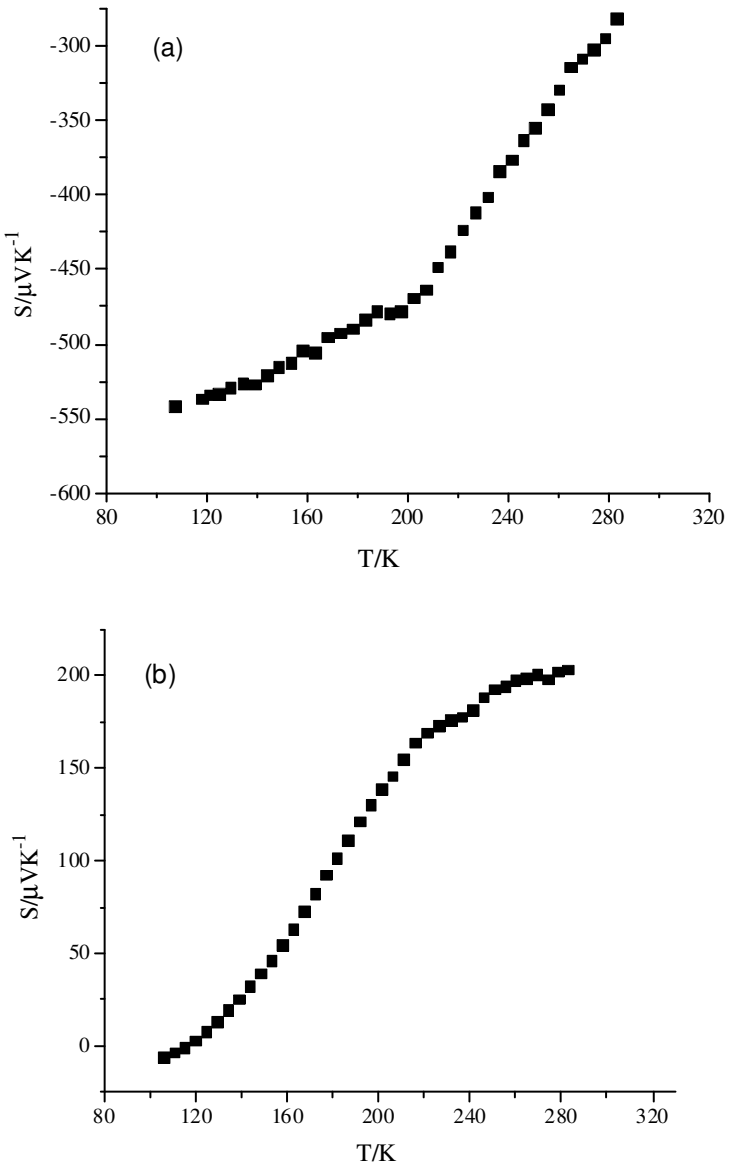

Figure 70: Seebeck coefficient data for: (a) GaV_4S_8 and (b) GeV_4S_8 collected over the temperature range $100 \leq T/K \leq 300$.

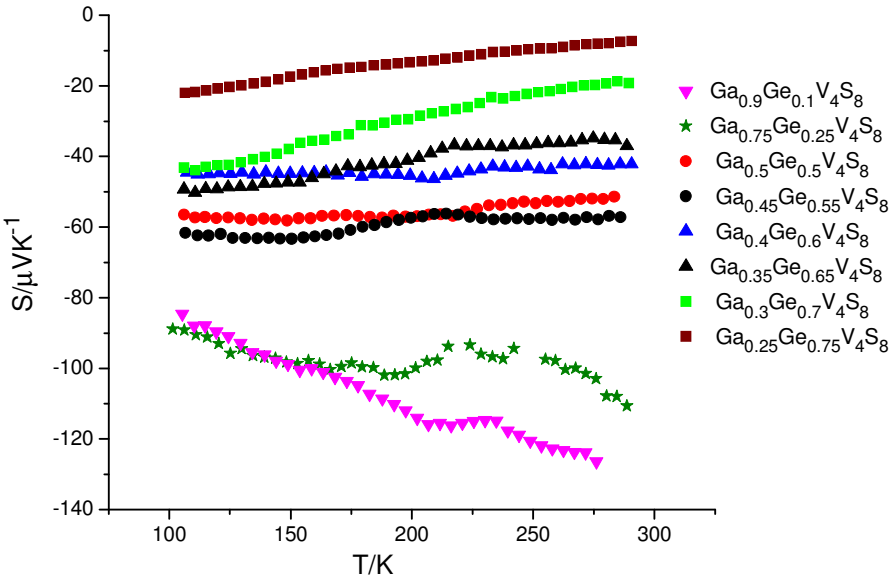

Figure 71: Seebeck coefficient data for non-stoichiometric materials $Ga_{1-x}Ge_xV_4S_8$ ($0 < x < 1$) collected over the temperature range $100 \leq T/K \leq 300$.

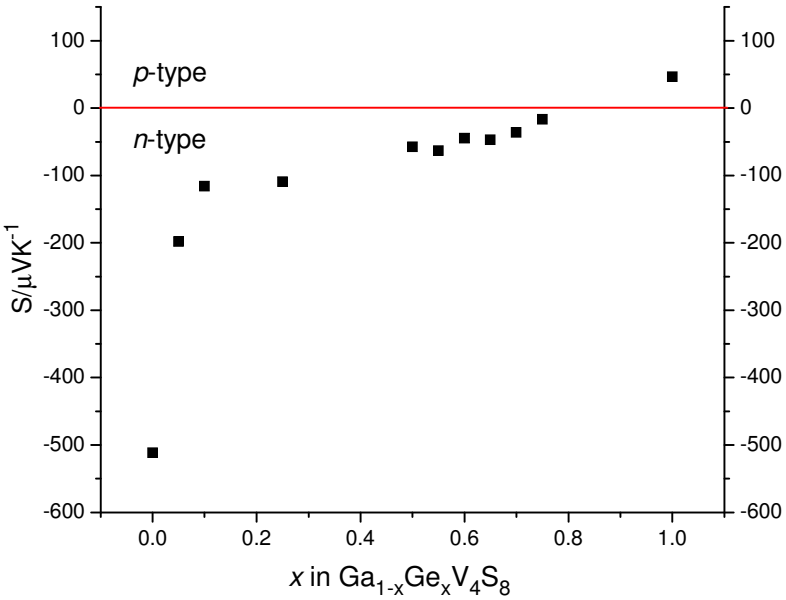

Figure 72: Seebeck data for the $Ga_{1-x}Ge_xV_4S_8$ series ($0 \leq x \leq 1$) at T = 215 K.

4.3.4 Low Temperature Neutron Diffraction Studies of the Ordered Defect Thiospinels

Selected materials from the $Ga_{1-x}Ge_xV_4S_8$ series were studied at low temperatures by powder neutron diffraction using the high resolution powder diffractometer D2B, ILL. Additional low temperature data at 48, 38, 28, 18 and 2 K, were collected on $Ga_{0.25}Ge_{0.75}V_4S_8$ using the high resolution D1A diffractometer, ILL, and at 2 K on POLARIS at ISIS. Data were collected for four samples at temperatures (Table 26) close to the temperature where a deviation from Curie Weiss law in magnetic data is observed and a phase transition could be expected to occur. The temperatures of data collection were chosen on the basis of the SQUID data, to be close to but above and below the temperature of expected structural phase transition.

Regions centered at d = 2.1 – 2.2 (data collected at ILL and ISIS), 1.5 – 1.6 and 1.2 – 1.3 Å (data collected at ISIS) in the low temperature neutron data were excluded from refinements owing to the presence of reflections due to vanadium (d_{110} = 2.14 Å, d_{200} = 1.52 Å and d_{211} = 1.24 Å) originating from the sample can.

Table 26: Temperatures at which neutron diffraction patterns were collected using the D2B diffractometer, ILL.

***x* in $Ga_{1-x}Ge_xV_4S_8$**	**0.9**	**0.85**	**0.75**	**0.65**	**0.3**
Temperature/K	298	298	200	298	298
		50	25	60	60
		30	3	30	30
		3		3	3

At each temperature the refined model at the next higher temperature was used as the starting point. Site occupancy factors were fixed at the values determined at room temperature and at 200 K for $Ga_{0.25}Ge_{0.75}V_4S_8$ and the refinement was performed in the same manner as for room temperature data. Rietveld analyses show that all the materials are well-described by a cubic structure down to a temperature of 25 K. Refinements of the structural models proceeded smoothly and the observed, calculated and difference profiles are shown Figure 73 – Figure 75. The results of the refinements are presented in Table 27 - Table 30.

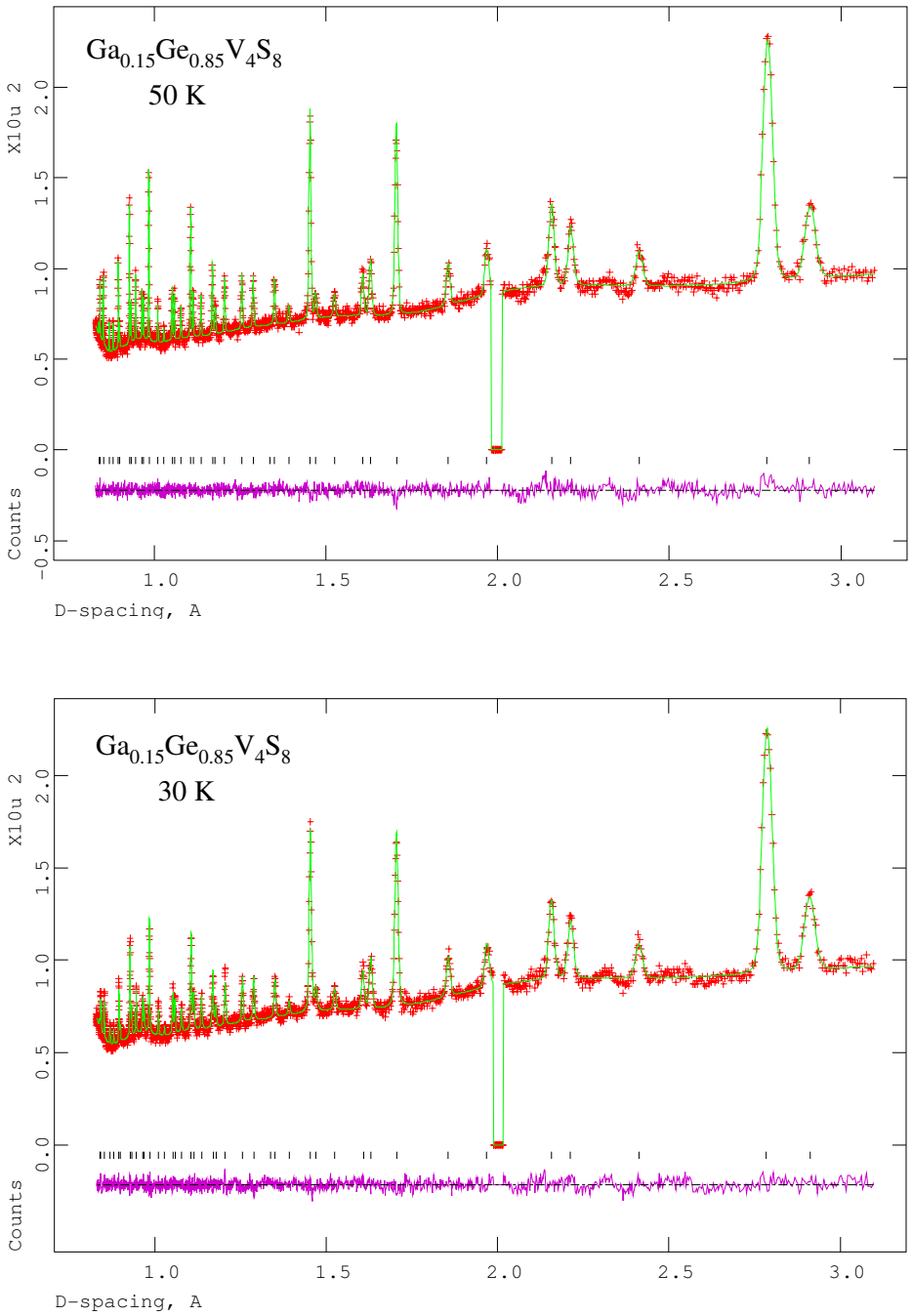

Figure 73: Final observed (crosses), calculated (upper full line) and difference (lower full line) profiles for $Ga_{0.15}Ge_{0.85}V_4S_8$. The excluded region is due to the presence of a peak from the vanadium sample can.

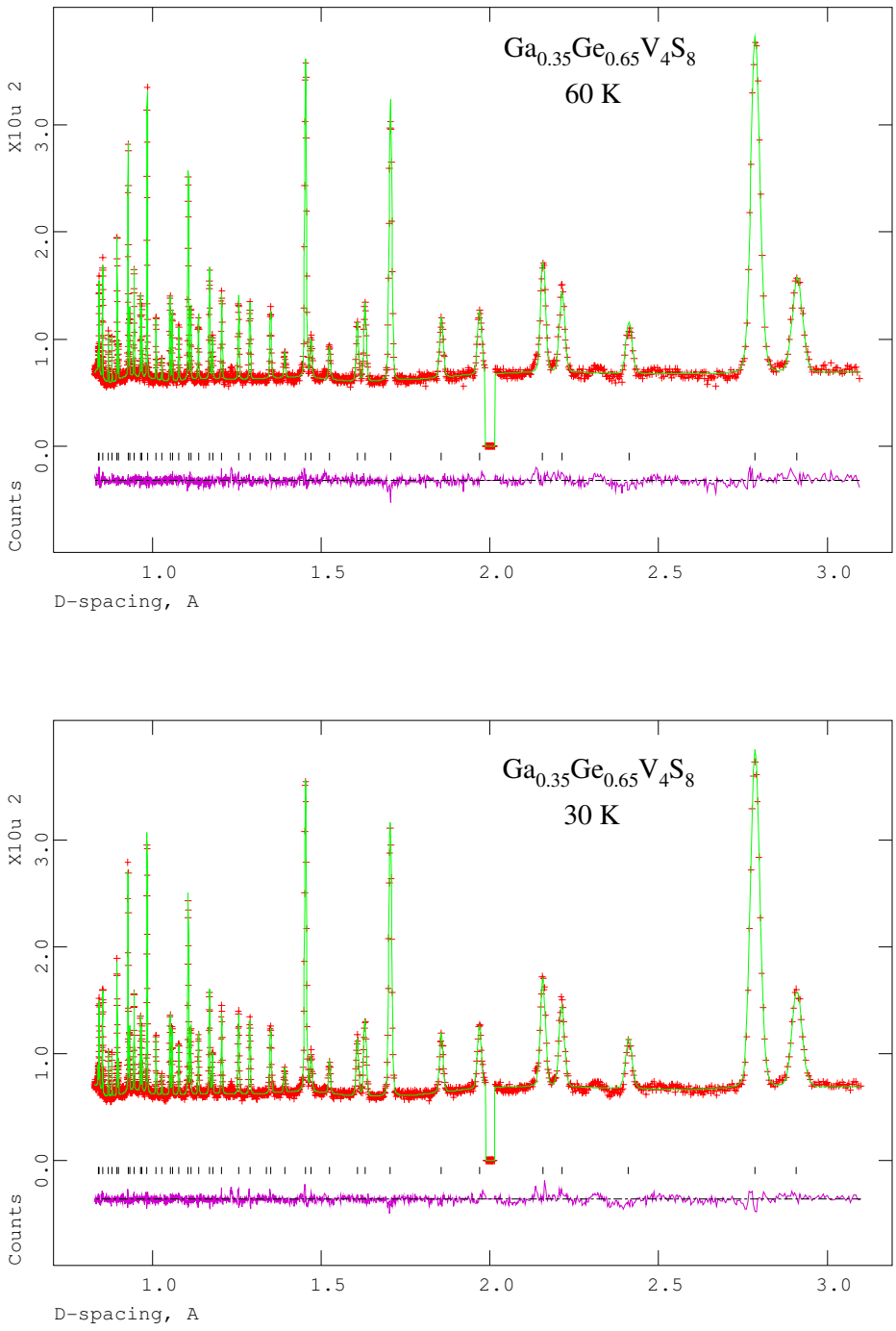

Figure 74: Final observed (crosses), calculated (upper full line) and difference (lower full line) profiles for $Ga_{0.35}Ge_{0.65}V_4S_8$. The excluded region is due to the presence of a peak from the vanadium sample can.

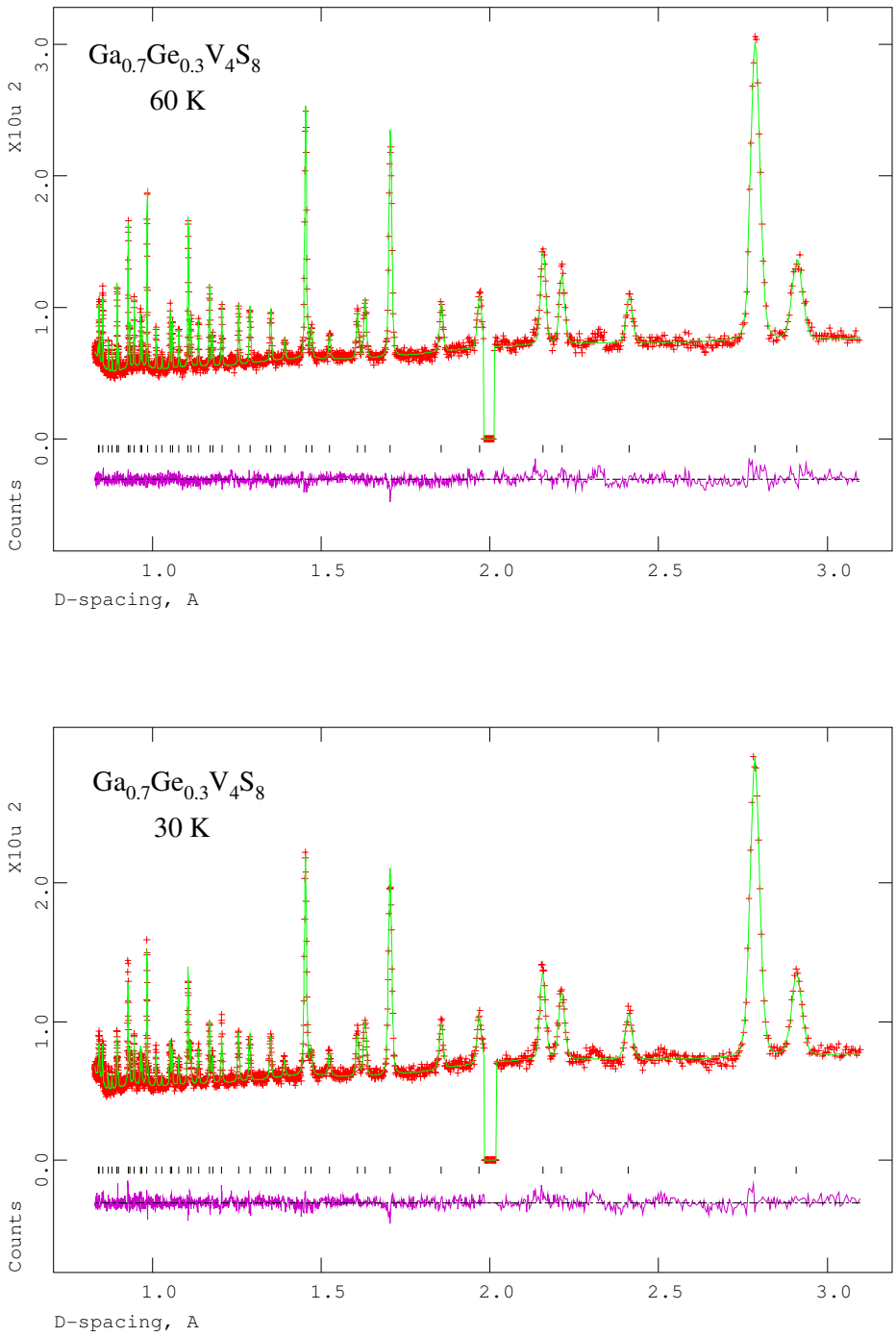

Figure 75: Final observed (crosses), calculated (upper full line) and difference (lower full line) profiles for $Ga_{0.7}Ge_{0.3}V_4S_8$. The excluded region is due to the presence of a peak from the vanadium sample can.

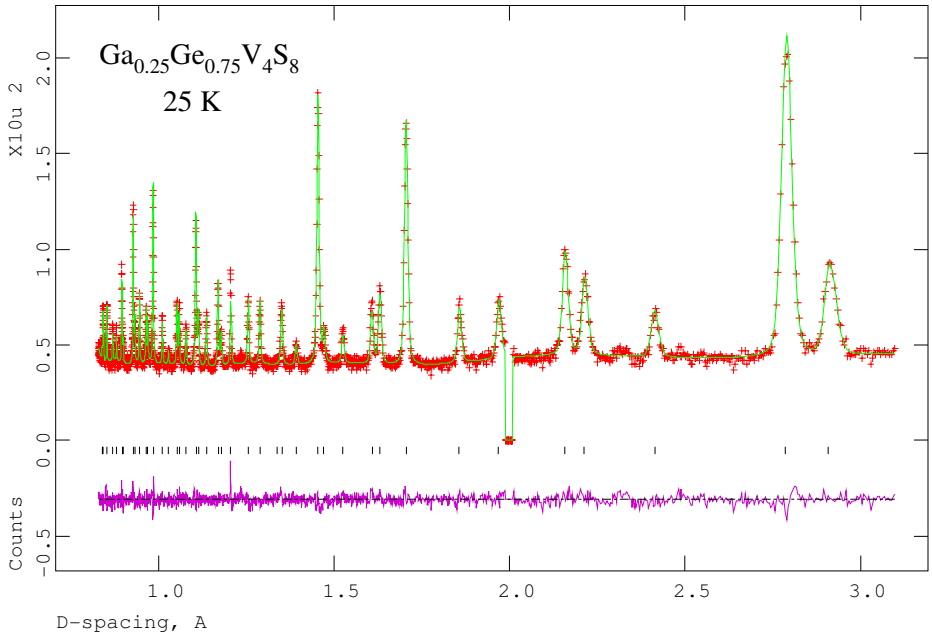

Figure 76: Final observed (crosses), calculated (upper full line) and difference (lower full line) profiles for $Ga_{0.25}Ge_{0.75}V_4S_8$. The excluded region is due to the presence of a peak from the vanadium sample can.

Table 27: Final refined parameters for the low-temperature cubic phase of $Ga_{1-x}Ge_xV_4S_8$ described in the space group $F\bar{4}3m$ *.

***x* in $Ga_{1-x}Ge_xV_4S_8$**		**0.85**	**0.65**	**0.3**
T/K		50	60	60
a/Å		9.64106(6)	9.64225(4)	9.64399(13)
Ga/Ge	B/Å^2	0.44(4)	0.11(3)	0.36(3)
	x	0	0	0
V	B/Å^2	0.51 (3)	0.21(3)	0.49(3)
	x	0.6045(9)	0.6041(7)	0.6060(9)
S(1)	B/Å^2	0.51(3)	0.21(3)	0.49(3)
	x	0.3694(2)	0.3696(1)	0.3698(2)
S(2)	B/Å^2	0.51(3)	0.21(3)	0.49(3)
	x	0.8650(2)	0.8649(1)	0.8644(2)
R_{wp}/% (neutron)		2.88	3.91	4.19
χ^2		1.35	1.87	1.58

* Ga and Ge on 4(*a*) (0, 0, 0) site; V, S(1) and S(2) on 16(*e*) (*x*,*x*,*x*) site.

Table 28: Final refined parameters for $Ga_{1-x}Ge_xV_4S_8$ at low temperatures ($F\bar{4}3m$)*.

***x* in $Ga_{1-x}Ge_xV_4S_8$**		**0.85**	**0.75**	**0.65**	**0.3**
T/K		30	25	30	30
a/Å		9.6418(1)	9.64411(9)	9.64106(3)	9.63956(11)
Ga/Ge	B/Å^2	0.28(4)	0.07(3)	0.10(2)	0.21(3)
	x	0	0	0	0
V	B/Å^2	0.38(4)	0.13(3)	0.18(2)	0.43(3)
	x	0.6057(11)	0.6077(9)	0.6061(5)	0.6062(10)
S(1)	B/Å^2	0.38(4)	0.13(3)	0.18(2)	0.43(3)
	x	0.3692(2)	0.3694(2)	0.3698(1)	0.3703(2)
S(2)	B/Å^2	0.38(4)	0.13(3)	0.18(2)	0.43(3)
	x	0.8648(3)	0.8645(2)	0.8648(1)	0.8648(2)
R_{wp}/% (neutron)		2.99	4.33	3.59	4.24
χ^2		1.44	2.52	1.84	1.92

Table 29: Bond distances (Å) and bond angles (°) for $Ga_{1-x}Ge_xV_4S_8$ at low temperatures ($F\bar{4}3m$).

***x* in $Ga_{1-x}Ge_xV_4S_8$**	**0.85**	**0.65**	**0.3**
T/K	50	60	60
M-S(2)	2.254(4) × 4	2.256(2) × 4	2.265 (3) × 4
V-S(1)	2.295(7) × 3	2.289(5) × 3	2.302(7) × 3
V-S(2)	2.545(11) × 3	2.550(8) × 3	2.524(11) × 3
V-V within the V_4 clusters	2.851(25) × 6	2.840(18) × 6	2.892(25) × 6
V-V between clusters	3.966(25)	3.978(18)	3.927(25)
S(2)-M-S(2)	109.471(0) × 6	109.471(0) × 6	109.471(0) × 6
S(1)-V-S(1)	101.8(4) × 3	101.9(3) × 3	101.0(4) × 3
S(1)-V-S(2)	89.61(15) × 6	89.64(11) × 6	90.03(14) × 6
S(2)-V-S(2)	76.1(4) × 3	75.8(3) × 3	76.4(4) × 3

* Ga and Ge on 4(*a*) (0, 0, 0) site; V, S(1) and S(2) on 16(*e*) (*x,x,x*) site.

Table 30: Bond distances (Å) and bond angles (^{o}) for $Ga_{1-x}Ge_xV_4S_8$ at low temperatures ($F\bar{4}3m$).

***x* in $Ga_{1-x}Ge_xV_4S_8$**	**0.85**	**0.75**	**0.65**	**0.3**
T/K	30	25	30	30
M-S(2)	2.257(4) × 4	2.263(3) × 4	2.257(2) × 4	2.257(4) × 4
V-S(1)	2.306(8) × 3	2.319(7) × 3	2.302(4) × 3	2.296(8) × 3
V-S(2)	2.530(13) × 3	2.506(10) × 3	2.525(6) × 3	2.524(12) × 3
V-V within the V_4 clusters	2.883(30) × 6	2.938(24) × 6	2.894(14) × 6	2.896(27) × 6
V-V between clusters	3.935(30)	3.881(24)	3.923(14)	3.921(27)
S(2)-M-S(2)	109.471(0) × 6	109.471(1) × 6	109.471(0) × 6	109.471(1) × 6
S(1)-V-S(1)	101.3(5) × 3	100.3(4) × 3	100.92(25) × 3	100.7(5) × 3
S(1)-V-S(2)	89.75(17) × 6	90.10(12) × 6	89.94(8) × 6	90.08(14) × 6
S(2)-V-S(2)	76.5(5) × 3	77.1(4) × 3	76.64(21) × 3	76.6(4) × 3

Rietveld refinement using powder neutron diffraction data collected on POLARIS at ISIS on $Ga_{0.25}Ge_{0.75}V_4S_8$ at 4 K shows that the cubic model of Pocha *at al.* [123] gives a good fit to the data (Figure 77), indicating that there is no phase transition at low temperature. The results of this refinement are presented in Table 31 and Table 32. Recently, a new series of the defect thiospinels $GaV_{4-x}Mo_xS_8$ was reported [133]. Non-stoichiometric materials from this series are also well fitted by a cubic structural model down to 4.2 K. On the other hand it is known [133] that the end-member phases of the $Ga_{1-x}Ge_xV_4S_8$ series transform to rhombohedral modification at low temperatures and that this phase transition is not complete and both cubic and rhombohedral phases coexist at low temperatures. Initially it appears that neutron data for $Ga_{1-x}Ge_xV_4S_8$ materials also can be described by cubic model to the lowest temperatures studied but close examination of the reflections in the data collected on the high resolution D2B and D1A diffractometers at ILL shows that one peak ($d \approx 0.98$ Å) is not fitted very well by cubic model (Figure 78), which may indicate a phase transition. However, the data collected do not provide enough information to describe the unit cell at low temperature. Refined parameters and final neutron diffraction profiles of the data collected at 3 K on D2B are in Appendix 4.3 and at several low temperatures on D1A in Appendix 4.4.

Table 31: Bond distances (Å) and bond angles (^{o}) for cubic $Ga_{0.25}Ge_{0.75}V_4S_8$ phase ($F\bar{4}3m$)[*]. Data collected at 4 K on POLARIS, ISIS.

$Ga_{0.25}Ge_{0.75}V_4S_8$		
a/Å		9.6453(1)
Ga/Ge	B/Å^2	0.02(1)
	x	0
V	B/Å^2	0.10(1)
	x	0.6056(2)
S(1)	B/Å^2	0.10(1)
	x	0.3700(1)
S(2)	B/Å^2	0.10(1)
	x	0.8648(1)
R_{wp}/% (neutron)		0.69
χ^2		1.00

[*] Ga and Ge on 4(*a*) (0, 0, 0) site; V, S(1) and S(2) on 16(*e*) (*x,x,x*) site.

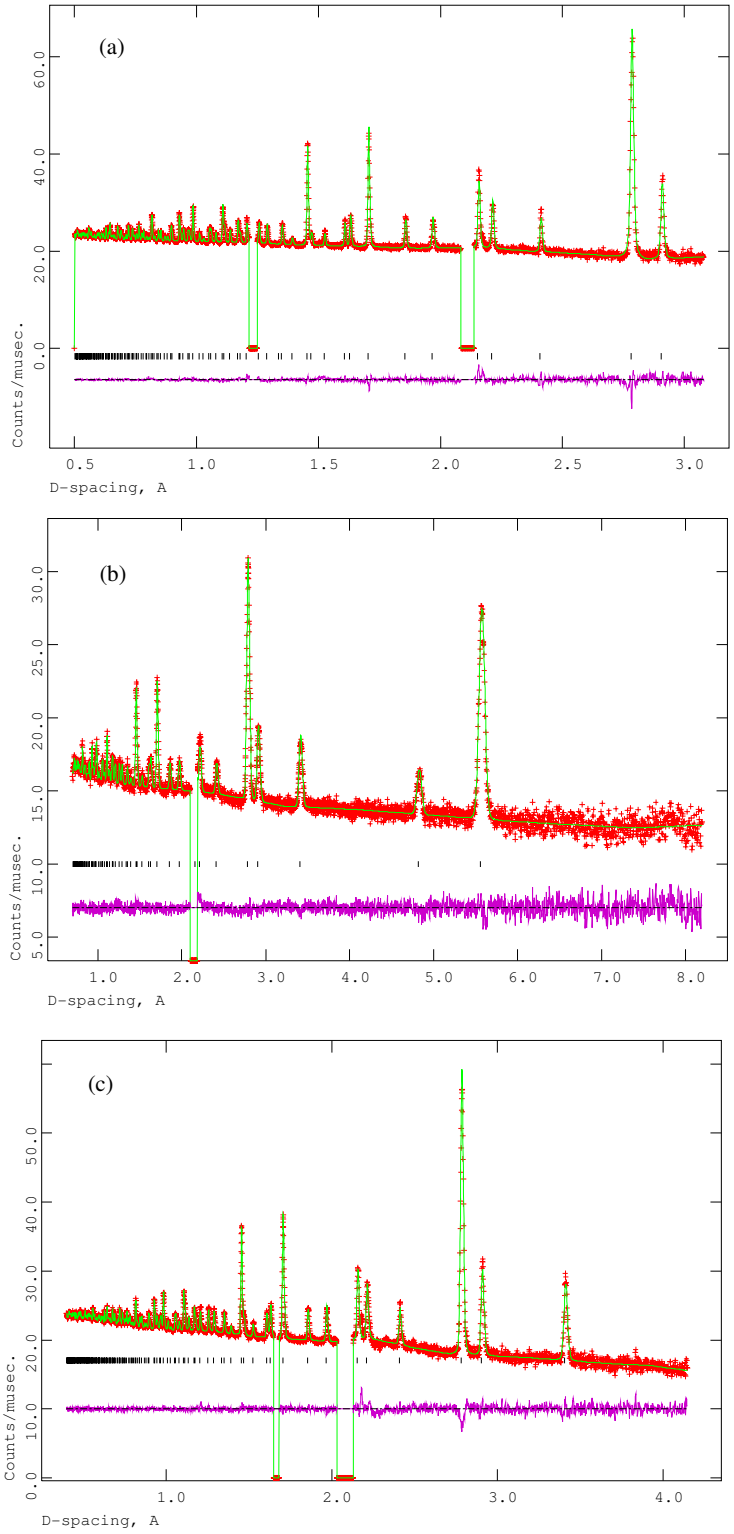

Figure 77: Final, observed (crosses), calculated (upper full line) and difference (lower full line) neutron diffraction profile of the cubic $Ga_{0.25}Ge_{0.75}V_4S_8$ at 4 K. Data collected on POLARIS at ISIS from (a) backscattering bank ($2\theta = 145°$), (b) low angle bank ($2\theta = 35°$) and (c) 90 degree bank. Vanadium reflections originating from the sample can are excluded.

Table 32: Bond distances (Å) and bond angles (^{o}) for low temperature (4 K) cubic $Ga_{0.25}Ge_{0.75}V_4S_8$ phases ($F\bar{4}3m$).

Bond/angle	
M-S(2)	$2.258(1) \times 4$
V-S(1)	$2.298(2) \times 3$
V-S(2)	$2.532(3) \times 3$
V-V within the V_4 clusters	$2.882(7) \times 6$
V-V between clusters	3.938(7)
S(2)-M-S(2)	$109.471(0) \times 6$
S(1)-V-S(1)	$101.08(12) \times 3$
S(1)-V-S(2)	$89.92(4) \times 6$
S(2)-V-S(2)	$76.42(11) \times 3$

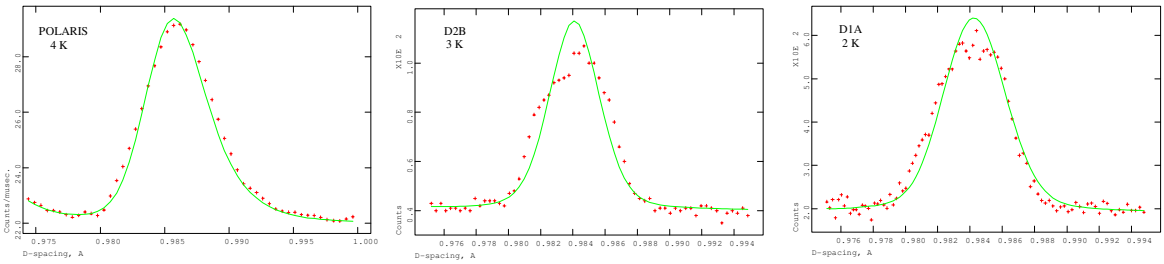

Figure 78: Comparison of the cubic (8 4 4) peak of $Ga_{0.25}Ge_{0.75}V_4S_8$ at low temperature using data collected on different instruments. *Key*: crosses, observed points and full line, calculated for cubic structural model.

4.4 Discussion

Structural refinement using a combination of powder X-ray and neutron diffraction confirms that germanium is incorporated exclusively at the tetrahedral 4(*a*) site, where it replaces gallium. This results in a reduction in the unit cell volume (Figure 79), consistent with the smaller ionic radius of Ge^{4+} (0.53 Å) compared with Ga^{3+} (0.62 Å) [228].

The intracluster V-V distance of GeV_4S_8 has been determined as 2.847(3) Å [122]. This is slightly shorter than that of the gallium analogue (2.896(2) Å) [123], consistent with the increased population of bonding states in the former. The short Mo-Mo distance of

2.814(3) Å is observed in the related phase $GaMo_4S_8$, in which there are 11 bonding electrons associated with the Mo_4S_4 cluster [123]. In the $Ga_{1-x}Ge_xV_4S_8$ phases, the intracluster V-V distance decreases with increasing levels of germanium substitution (Figure 80) which may be related to the increasing electron population of bonding states. Conversely the intercluster V-V separation increases with increasing germanium content (Figure 80). These two observations suggest that the deviation from the ideal spinel structure increases with increasing substitution at the *A*-site. This may be quantified [29] through the degree of clustering of the *B*-site cations ($D^{BB} = [(d_{B—B}/d_{B\text{-}B}) - 1] \times 100$ %) and the degree of distortion of the transition-metal coordination from the ideal octahedral geometry ($D^{BS} = [(d_{B\text{-}S2}/d_{B\text{-}S1}) - 1] \times 100$ %)). Both of these parameters show a strong correlation with the cluster electron count, corrected for the effects of sulphur deficiency (Figure 81). Both the degree of clustering and the distortion from octahedral symmetry increase with increasing electron count. This is consistent with the increased population on traversing the $Ga_{1-x}Ge_xV_4S_8$ series, of levels which molecular orbital calculations indicate have strong B-B bonding character. Similarly it has been shown [137] that depopulation of these levels in $Ga_{0.87}Ti_4S_8$ (*ca.* 3 e^- per cluster) leads to partial de-clustering as evidenced by longer B-B distances and less distortion of the local coordination around B.

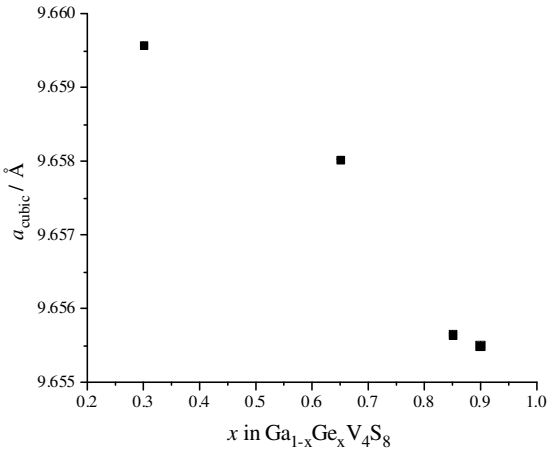

Figure 79: Cubic unit cell parameter at room temperature from simultaneous X-ray/neutron refinement as a function of composition. Errors are marked but typically smaller than the points.

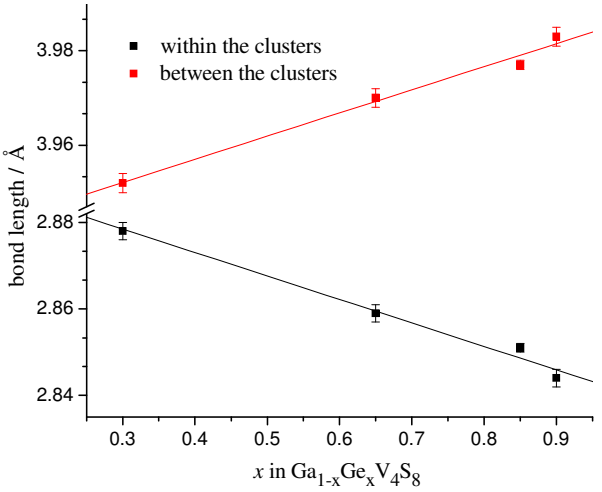

Figure 80: Variation with composition of V–V distances in $Ga_{1-x}Ge_xV_4S_8$ phases. Values determined from the combined refinement of neutron and powder X-ray diffraction data collected at room temperature.

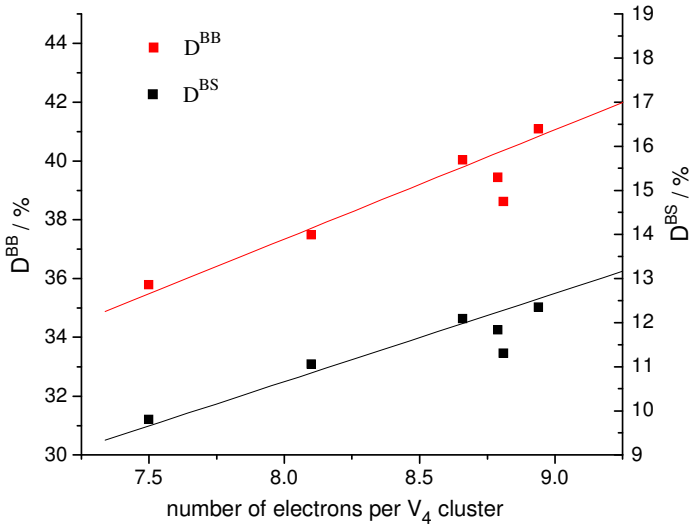

Figure 81: Variation of the D^{BB} and D^{BS} parameters with the number of *d*-electrons per V_4 cluster in $Ga_{1-x}Ge_xV_4S_8$. The number of electrons per metal cluster was calculated for experimentally determined composition, taking into account the sulphur deficiency.

It has been proposed [137] that partial de-clustering of the Ti_4S_4 cluster in $Ga_{0.87}Ti_4S_8$ is responsible for the metallic behaviour of this phase as a result of the strengthening of inter-cluster transfer integrals. This would suggest that the increased clustering with increasing germanium content that occurs in the $Ga_{1-x}Ge_xV_4S_8$ series of

phases reported here would weaken the transfer integrals, resulting in a decrease in electron mobility. However, both the resistivity and Seebeck data are consistent with the non-stoichiometric materials being more conductive than either of the end-member phases, although the materials remain semiconducting throughout the composition range and values of μ_{eff} indicate that localised electron behaviour is retained. This suggests that the changes in the electron transport properties of $Ga_{1-x}Ge_xV_4S_8$ may be associated with a change in charge carrier density rather than electron mobility.

Formal valence considerations suggest that the negative charge on the V_4S_4 cluster should reduce by one unit between $x = 0$ and $x = 1$ in the series $Ga_{1-x}Ge_xV_4S_8$. This would correspond to the addition of one electron to the cluster orbitals on traversing the series. However, thermogravimetric analysis reveals significant levels of sulphur deficiency across the entire range of compositions. Consequently the electron count associated with the vanadium-sulphur cluster is higher than expected on the basis of nominal stoichiometries. In particular, above $x = 0.3$, the electron count exceeds that expected for the end-member ($x = 1$) phase. The molecular orbital treatment of Pocha *et al*. [123] indicates that for the cubic phase, electrons are accommodated in orbitals (in ascending order of energy) of a_1, e and t_2 symmetry (see Figure 20 in Chapter 1). Therefore for all materials investigated in this work, it is the population of the highest lying t_2 orbitals that changes with germanium substitution. Band structure calculations have been performed for the end-member phases GaV_4S_8 [123] and GeV_4S_8 [122]. In GeV_4S_8, states in the region of the Fermi level, E_F, are almost purely V-V bonding levels, with little dispersion and hence a narrow bandwidth. It has been suggested that it is the narrowness of the bands relative to the on-site repulsion energy, U, that is responsible for the non-metallic character of GeV_4S_8, despite the absence of an energy gap at E_F. Similarly GaV_4S_8 exhibits a band of width *ca*. 0.7 eV at E_F. A general feature of these phases is therefore a highly-structured density of states, with sharp peaks in the region of E_F. As the density of states changes rapidly with increasing energy, it suggests that the charge-carrier density at E_F is an extremely sensitive function of the degree of band filling. Therefore it can be suggested that the increased conductivity in the substituted phases reflects an increase in charge-carrier density. The decrease in the absolute value of the Seebeck coefficient with increasing levels of germanium incorporation suggests that hole conduction assumes greater significance as the degree of band filling increases, with the result that the conductivity-weighted sum of hole and electron contributions to the Seebeck coefficient that is measured becomes less negative. At full germanium substitution, the highest-lying t_2 band is almost half-

full, and thus the spin-polarised density of states may be considered as having holes in the spin-up sub-band, which may account for the dominance of hole conduction in this materials.

The defect thiospinels, $Ga_{1-x}Ge_xV_4S_8$, should be studied using highest resolution neutron powder diffraction, for example HRPD at ISIS, to find the unit cell at low temperatures.

Results of this chapter were submitted to Journal of Material Chemistry.

Chapter 5: Ternary Erbium Chromium Sulphides

5.1 Introduction

Rare-earth transition-metal chalcogenides are relatively unexplored. In mixed-metal chalcogenides containing both rare-earth and transition metal cations, the latter exhibit primarily the two oxidation states: +2 and +3. The +3 oxidation state of a transition-metal cation in mixed chalcogenides of the rare earth elements is most often observed in the chromium derivatives, for example in Ln_3CrS_6 [177] and $LnCr_3S_6$ [178] phases for which the synthesis and lattice parameters have been reported but their crystal structure has not been determined. However, more usually for Cr the +2 oxidation state is observed. Ternary rare-earth materials containing Cr(II) include Ln_2CrS_4 [154, 229], Ln_4CrS_7 [165, 166], $La_6Cr_2S_{11}$ [174, 230] and $Er_8Cr_3S_{15}$ [174, 231]. However, for most mixed-metal chalcogenides containing both rare-earth and transition metal cations only lattice parameters are known and no detailed structure or property measurements were reported. In the case of erbium-chromium sulphides containing Cr(II) the structure has been determined only for Er_2CrS_4 [152] and $Er_6Cr_2S_{11}$ [176]. It has been suggested on the basis of powder X-ray diffraction data that Er_4CrS_7 is isostructural to Y_4CrS_7 and Ho_4FeS_7 with a Y_5S_7-type structure [165, 166]. Lattice parameters were reported for $Er_8Cr_3S_{15}$ [174, 231] but its structure has not been described. Table 33 summarises those rare-earth chromium sulphides whose existence have been reported.

This chapter presents the results of a systematic study of the structural and magnetic properties of selected ternary erbium chromium sulphides. The presence of long-range magnetic order at low temperatures is correlated with the detailed structures determined by single-crystal X-ray diffraction.

5.2 Synthesis

Erbium-chromium sulphides were prepared by high-temperature solid-state reaction. Stoichiometric quantities of high-purity erbium, chromium and sulphur powders were ground in an agate mortar inside an argon-filled glove-box and loaded into silica tubes. The chromium powder used in all the reactions was –325 mesh (< 44 micron). Larger particle sizes led to the formation of mixed phases. A small amount of iodine (*ca.* 5

mg) was added to all the reaction mixtures. Iodine was used to help removing any oxide from the erbium surface. The tubes were evacuated to < 10^{-4} Torr and sealed. The addition of the iodine required the reacting mixtures to be cooled using liquid nitrogen whilst evacuating the tubes prior to sealing. Bulk samples of Er_3CrS_6, Er_4CrS_7 and $Er_6Cr_2S_{11}$ were prepared by heating reaction mixtures at 1273 K for 1 week, whereas synthesis of powdered Er_2CrS_4 required 2 weeks at this temperature. In each case the reaction mixtures were placed in the furnace, heated up to 1273 K at the natural rate of the furnace and, after firing, the sample was allowed to cool to room temperature again at the natural rate of the furnace *(ca.* 5 K min^{-1}). After firing the tubes were opened in the glove-box, the contents were finely ground and analysed using powder X-ray diffraction. The products were fine, loose, dark grey powders.

Table 33: Rare-earth chromium sulphides.

Material	La	Ce	Pr	Nd	Sm	Eu	Gd	Tb	Dy	Ho	Er	Tm	Yb	Lu	Y
Ln_2CrS_4	✓*		✓			✓			✓	✓	✓	✓	✓		✓
$Ln_6Cr_2S_{11}$							✓	✓		✓	✓				
Ln_4CrS_7	✓	✓	✓	✓	✓		✓		✓	✓	✓	✓	✓	✓	✓
$Ln_8Cr_3S_{15}$											✓				
Ln_3CrS_6	✓	✓	✓	✓	✓		✓	✓	✓	✓	✓	✓	✓	✓	✓

* Actual stoichiometry: $La_{15.9(2)}Cr_{5.4(2)}S_{32}$ [156].

Single crystals of five erbium-chromium sulphides were grown using a chemical vapour transport method, from stoichiometric mixtures of the elements, using iodine (3 – 5 mg cm^{-3}) as the transporting agent. The charge and growth zones were held at 1273 K and 1223 K respectively for the growth of Er_3CrS_6 and $Er_6Cr_2S_{11}$, whilst a steeper gradient (1273 K to 1173 K) was required for the formation of single crystals of Er_2CrS_4 and Er_4CrS_7. For the preparation of crystals of the new phase $Er_8Cr_3S_{15}$ reported here, temperatures of 1273 K and 1223 K were used. In all cases crystals suitable for structure determination by single-crystal X-ray diffraction were obtained in 7 days.

5.3 Single Crystal X-ray Diffraction

Single-crystal X-ray diffraction data for all erbium-chromium sulphides were collected at 293 K using a Bruker X8 Apex 2 diffractometer (Mo-Kα radiation , λ = 0.71073 Å). Data were processed using the Apex-2 software [192]. The structures were solved by direct methods (SIR-92 [195]). Subsequent Fourier calculations and least-squares refinements were carried out using the CRYSTALS program suit [196].

The cif files for Er_2CrS_4, Er_3CrS_6, Er_4CrS_7, $Er_6Cr_2S_{11}$ and the new phase $Er_8Cr_3S_{15}$ are provided as on Appendix on CD.

5.3.1 Crystal Structure Description of Er_2CrS_4

Single-crystal X-ray diffraction data were collected at 293 K on a single crystal mounted on a glass fibre. Crystallographic information and refinement details for Er_2CrS_4 are given in Table 34. The data for Er_2CrS_4 were initially indexed in centrosymmetric space group *Pbca*. However, detailed examination of these data revealed a number of weak *(0kl)* reflections which violate the *k = 2n* condition of the *b* glide plane. The structure was subsequently solved in the non-centrosymmetric space group $P2_1ca$, as previously proposed by Tomas *et al.* [152]. With the exception of S(11) and S(12), the structure exhibits pseudosymmetry, and therefore similarity restraints were applied to the anisotropic thermal parameters during the least-squares refinements. There are two crystallographically-distinct chromium and four erbium ions in the asymmetric unit of Er_2CrS_4. All chromium ions exhibit a distorted octahedral coordination, with two long and four short Cr–S distances, of *ca.* 2.84 and 2.48 Å, respectively (Figure 82), consistent with a Jahn-Teller distortion associated with the degenerate ground state of the Cr^{2+}:d^4 ion, whose presence is required by formal valence considerations and supported by bond valence sums [232]. A comparable Jahn-Teller distortion has been characterised in the binary phase CrS [90] and Y_2CrS_4 [155]. The erbium ions exhibit two different coordination environments, octahedral and monocapped trigonal prismatic, with average Er–S bond lengths of *ca.* 2.67 Å and *ca.* 2.82 Å, respectively (Figure 82). Refined atomic coordinates and isotropic thermal parameters for Er_2CrS_4 are listed in Table 35, while bond distances and bond valence sums for each of the ions appear in Table 36.

The basic building unit in the structure of Er_2CrS_4 is the MS_3 double octahedral chain (Figure 83(a)) analogous to the isolated MSe_3 chains present in the structure of

$CeCrSe_3$ (Figure 84) [233]. However, in the structure of Er_2CrS_4, these chains are linked through shared edges to form a two-dimensional slab of stoichiometry M_2S_5 (Figure 83(b)), which serves as the building block for the structure of Er_2CrS_4. In Er_2CrS_4, (Figure 85) vertex linking of these slabs generates an M_2S_4 framework of linked octahedra. The Cr^{2+} and Er^{3+} ions are ordered within the slabs such that they alternate along the [001] direction within the chains of metal-centred octahedra. The resulting anionic framework of stoichiometry $[CrErS_4]^{3-}$ defines one-dimensional channels directed along [010], in which the seven-coordinate erbium cations, Er(l) and Er(2), that provide the charge-balancing reside. The complete ordering of Cr^{2+} and Er^{3+} in Er_2CrS_4 may be favoured by the Jahn-Teller distortion of Cr^{2+}:d^4.

Table 34: Crystallographic data for Er_2CrS_4.

Formula	**Er_2CrS_4**
M_r	514.78
Crystal Habit	Black needle
Dimensions/mm	$0.2 \times 0.04 \times 0.02$
Crystal System	Orthorhombic
Space group	$P2_1ca$
T/K	293
a/Å	12.4629(11)
b/Å	7.4882(6)
c/Å	12.4937(11)
β/°	90.0
V/Å^3	1165.97(17)
Z	8
Wavelength/Å	0.71073
μ/mm^{-1}	31.636
Measured data	3248
Unique data	3248
Observed data ($I/>3\sigma(I)$)	1528
$R(F_o)^*$	0.0328
$R_w(F_o)^{**}$	0.0128

* $R(F_o)=\Sigma(|F_o| - |F_c|)/\Sigma|F_o|$

** $R_w(F_o)=[\Sigma w(|F_o|-|F_c|)^2/\Sigma w|F_o|^2]^{1/2}$

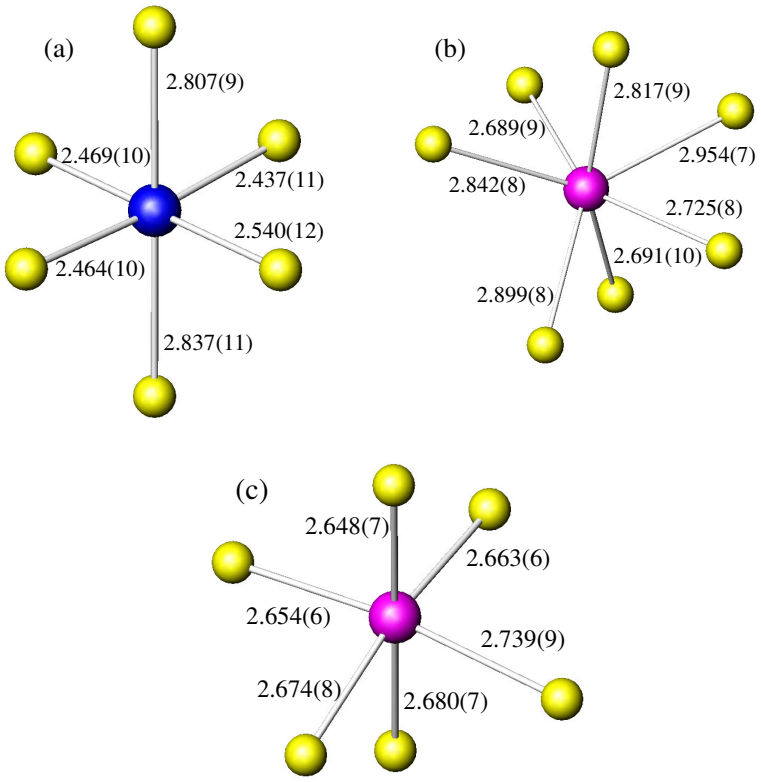

Figure 82: The local coordination geometry of (a) Cr(6), (b) Er(1) and (c) Er(4) in Er_2CrS_4. *Key*: chromium, blue circles; erbium, magenta circles; sulphur, yellow circles.

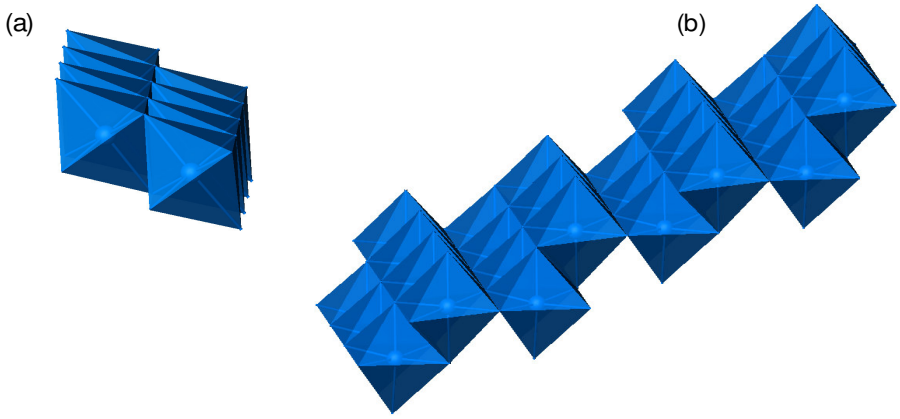

Figure 83: (a) double octahedral chain that forms the basic building unit for the structure of Er_2CrS_4 and (b) M_2S_5 slabs formed from linkage of double octahedral chains.

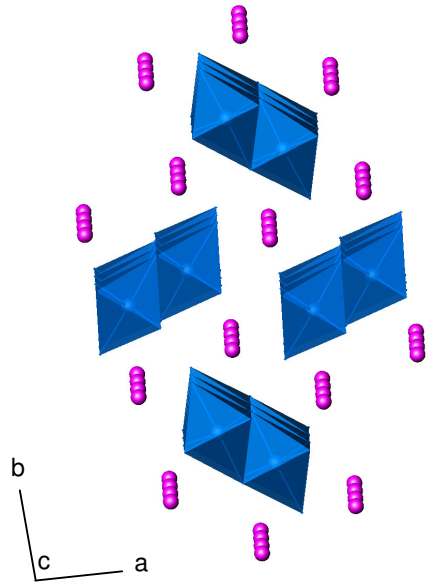

Figure 84: The crystal structure of $CeCrSe_3$ viewed along [001]. $CrSe_3$ chains are coloured blue, cerium cations are represented by magenta circles.

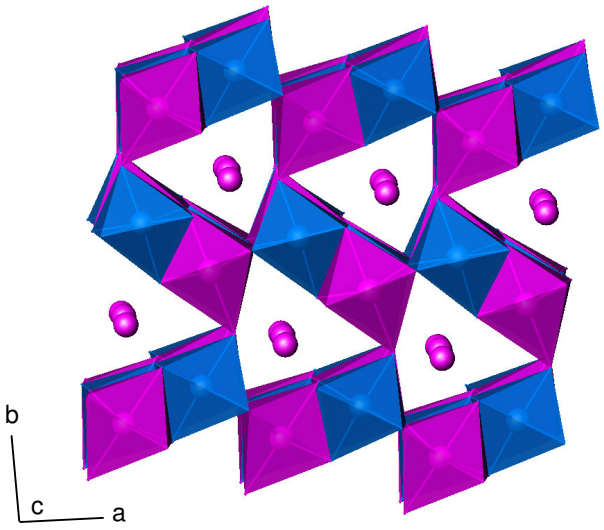

Figure 85: The structure of Er_2CrS_4 viewed along the [001] direction.

Table 35: Final refined coordinates and equivalent isotropic displacement parameters for Er_2CrS_4.

Atom	Site	*x*	*y*	*z*	U_{eq}(Å^2)
Er(1)	4(*a*)	0.58027(12)	0.6365(3)	1.13561(14)	0.0098(4)
Er(2)	4(*a*)	0.57184(11)	1.1359(3)	1.13675(15)	0.0116(4)
Er(3)	4(*a*)	0.7458(2)	0.8843(3)	1.37394(9)	0.0094(3)
Er(4)	4(*a*)	0.8845(2)	0.6139(3)	1.61095(9)	0.0095(3)
Cr(5)	4(*a*)	0.8792(8)	1.1153(11)	1.6094(3)	0.0105(9)
Cr(6)	4(*a*)	0.7495(7)	1.3822(12)	1.3771(3)	0.0098(8)
S(7)	4(*a*)	0.5498(4)	0.8824(17)	1.2896(5)	0.0086(11)
S(8)	4(*a*)	0.9380(5)	0.8836(14)	1.4728(4)	0.0096(10)
S(9)	4(*a*)	0.4322(5)	0.3878(13)	1.0477(4)	0.0087(10)
S(10)	4(*a*)	0.6933(5)	0.6167(15)	1.5128(5)	0.0086(10)
S(11)	4(*a*)	0.7984(6)	1.1502(8)	1.2453(5)	0.0120(10)
S(12)	4(*a*)	0.7990(5)	0.6476(8)	1.2263(5)	0.0100(10)
S(13)	4(*a*)	0.7004(5)	1.1151(13)	1.5305(4)	0.0088(10)
S(14)	4(*a*)	0.5735(5)	0.3902(16)	1.2921(5)	0.0094(10)

Table 36: Selected bond distances (Å) and bond valences (v.u.) for Er_2CrS_4.

Bond length		*v*	Bond length		*v*
Er(1) – S(7)	2.691(10)	0.36	Er(4) – S(8)	2.739(9)	0.47
Er(1) – S(8)	2.899(8)	0.31	Er(4) – S(9)	2.674(8)	0.56
Er(1) – S(9)	2.842(8)	0.36	Er(4) – S(10)	2.680(7)	0.50
Er(1) – S(10)	2.817(9)	0.38	Er(4) – S(11)	2.663(6)	0.58
Er(1) – S(12)	2.954(7)	0.26	Er(4) – S(12)	2.654(6)	0.59
Er(1) – S(13)	2.725(8)	0.49	Er(4) – S(14)	2.648(7)	0.60
Er(1) – S(14)	2.689(9)	0.54			
Mean Er(1) - S	**2.80**	**$\sum v$ = 2.70**	***Mean Er(4) - S***	**2.68**	**$\sum v$ = 3.30**
Er(2) – S(7)	2.707(10)	0.51	Cr(5) – S(7)	2.472(10)	0.45
Er(2) – S(8)	2.868(8)	0.33	Cr(5) – S(8)	2.541(11)	0.38
Er(2) – S(9)	2.797(8)	0.40	Cr(5) – S(9)	2.907(10)	0.14
Er(2) – S(10)	2.850(9)	0.35	Cr(5) – S(11)	2.802(9)	0.19
Er(2) – S(11)	3.134(8)	0.16	Cr(5) – S(12)	2.507(9)	0.41
Er(2) – S(13)	2.804(8)	0.40	Cr(5) – S(13)	2.437(12)	0.50
Er(2) – S(14)	2.719(10)	0.50			
Mean Er(2) - S	**2.84**	**$\sum v$ = 2.65**	***Mean Cr(5) - S***	**2.61**	**$\sum v$ = 2.07**
Er(3) – S(7)	2.660(6)	0.58	Cr(6) – S(9)	2.464(10)	0.46
Er(3) – S(8)	2.696(7)	0.53	Cr(6) – S(10)	2.540(12)	0.38
Er(3) – S(10)	2.729(9)	0.48	Cr(6) – S(11)	2.469(10)	0.46
Er(3) – S(11)	2.642(6)	0.61	Cr(6) – S(12)	2.807(9)	0.18
Er(3) – S(12)	2.643(6)	0.61	Cr(6) – S(13)	2.837(11)	0.17
Er(3) – S(13)	2.671(8)	0.56	Cr(6) – S(14)	2.437(11)	0.50
Mean Er(3) - S	**2.67**	**$\sum v$ = 3.37**	***Mean Cr(6) - S***	**2.59**	**$\sum v$ = 2.15**

5.3.2 Crystal Structure Description of Er_3CrS_6

Crystals of Er_3CrS_6 had the form of black needles. Single-crystal X-ray diffraction data were collected at 293 K on a single crystal mounted on a glass fibre. Crystallographic information and refinement details for Er_3CrS_6 are listed in Table 37 while final atomic coordinates and isotropic thermal parameters are given in Table 38.

The asymmetric unit of Er_3CrS_6 contains two and three crystallographically-distinct chromium and erbium ions, respectively. Both chromium ions are trivalent and exhibit a slightly distorted octahedral coordination, with an average Cr–S distance of 2.44 Å (Table 39). In contrast, two different coordination environments may be identified for the rare-earth cations. Er(1) and Er(3) are surrounded by eight sulphur atoms (Figure 86(a) and Figure 86(b)) in a bicapped trigonal-prismatic arrangement. Er(2) is seven coordinate and adopts a capped pseudo-octahedral arrangement with four S atoms in the equatorial plane and three other S atoms in a perpendicular plane (Figure 86(c)); this arrangement is usually described as a 7-octahedron with one apex split into two positions. The average Er–S distances (Table 39), which increase with increasing coordination number, are similar to those in the binary sulphide, Er_2S_3, [234] in which Er^{3+} cations exhibit coordination numbers in the range six to eight.

The structure of Er_3CrS_6 consists of $[CrS_4]^-$ chains of edge-sharing Cr^{3+}-centered octahedra directed along [001] (Figure 87). $Er(1)S_8$ polyhedra share opposite triangular faces to form ErS_5^{5-} chains, also directed parallel to the crystallographic *c*-axis. The ErS_5^{5-} chains share common edges and vertices with the CrS_4^{5-} chains and serve to link the latter to form a slab parallel to the (100) plane. These slabs are connected in the [010] direction by $Er(2)S_7$ and $Er(3)S_8$ one-dimensional chains, to generate a complex three-dimensional network. The erbium-sulphur matrix serves to isolate individual CrS_4^{5-} chains from each other; the closest inter-chain Cr(l)···Cr(2) separation being 6.85 Å.

Table 37: Crystallographic data for Er_3CrS_6.

Formula	**Er_3CrS_6**
M_r	746.17
Crystal Habit	Black needle
Dimensions/mm	$0.5 \times 0.04 \times 0.04$
Crystal System	Orthorhombic
Space group	*Pnnm*
T/K	293
a/Å	13.192(2)
b/Å	15.819(3)
c/Å	3.7333(6)
β/°	90.0
V/Å^3	779.1(2)
Z	4
Wavelength/Å	0.71073
μ/mm^{-1}	34.848
Measured data	17332
Unique data	2087
Observed data ($I/>3\sigma(I)$)	1729
$R(F_o)^*$	0.0186
$R_w(F_o)^{**}$	0.0188

Table 38: Final refined coordinates and equivalent isotropic displacement parameters for Er_3CrS_6.

Atom	**Site**	***x***	***y***	***z***	**U_{eq}(Å^2)**
Er(1)	4(*g*)	0.54922(1)	0.22090(1)	0	0.0042(1)
Er(2)	4(*g*)	0.31855(2)	0.35227(1)	0	0.0041(1)
Er(3)	4(*g*)	0.25639(2)	0.09874(1)	- ½	0.0048(1)
Cr(4)	2(*a*)	½	½	- ½	0.0033(2)
Cr(5)	2(*c*)	½	0	- ½	0.0028(2)
S(6)	4(*g*)	0.41659(8)	0.07611(7)	0	0.0052(2)
S(7)	4(*g*)	0.62050(8)	0.10867(7)	- ½	0.0052(2)
S(8)	4(*g*)	0.68796(8)	0.28959(7)	½	0.0050(2)
S(9)	4(*g*)	0.39569(8)	0.24634(7)	- ½	0.0048(2)
S(10)	4(*g*)	0.52197(8)	0.40137(7)	0	0.0051(2)
S(11)	4(*g*)	0.31847(8)	0.47972(7)	½	0.0051(2)

* $R(F_o)=\Sigma(|F_o| - |F_c|)/\Sigma|F_o|$

** $R_w(F_o)=[\Sigma w(|F_o|-|F_c|)^2/\Sigma w|F_o|^2]^{1/2}$

Table 39: Selected bond distances (Å) and bond valences (v.u.) for Er_3CrS_6.

Bond length		***v***	**Bond length**		***v***
Er(1) – S(6)	2.882(1)	0.32	Er(3) – S(6)	2.842(1) × 2	0.36
Er(1) – S(7)	2.742(1) × 2	0.47	Er(3) – S(8)	2.724(1) × 2	0.49
Er(1) – S(8)	2.831(1) × 2	0.37	Er(3) – S(9)	2.971(1)	0.25
Er(1) – S(9)	2.784(1) × 2	0.42	Er(3) – S(10)	3.092(1)	0.18
Er(1) – S(10)	2.877(1)	0.32	Er(3) – S(11)	2.829(1) × 2	0.37
Mean Er(1) – S	**2.81**	**$\sum v$ = 3.16**	***Mean Er(3) – S***	**2.86**	**$\sum v$ = 2.87**
Er(2) – S(7)	2.685(1)	0.54	Cr(4) – S(10)	2.450(1) × 4	0.48
Er(2) – S(8)	2.829(1)	0.37	Cr(4) – S(11)	2.416(1) × 2	0.53
Er(2) – S(9)	2.707(1) × 2	0.51	***Mean Cr(4) – S***	**2.44**	**$\sum v$ = 2.98**
Er(2) – S(10)	2.794(1)	0.41	Cr(5) – S(6)	2.479(1) × 4	0.44
Er(2) – S(11)	2.748(1) × 2	0.46	Cr(5) – S(7)	2.341(1) × 2	0.65
Mean Er(2) – S	**2.75**	**$\sum v$ = 2.8**	***Mean Cr(5) – S***	**2.43**	**$\sum v$ = 3.06**

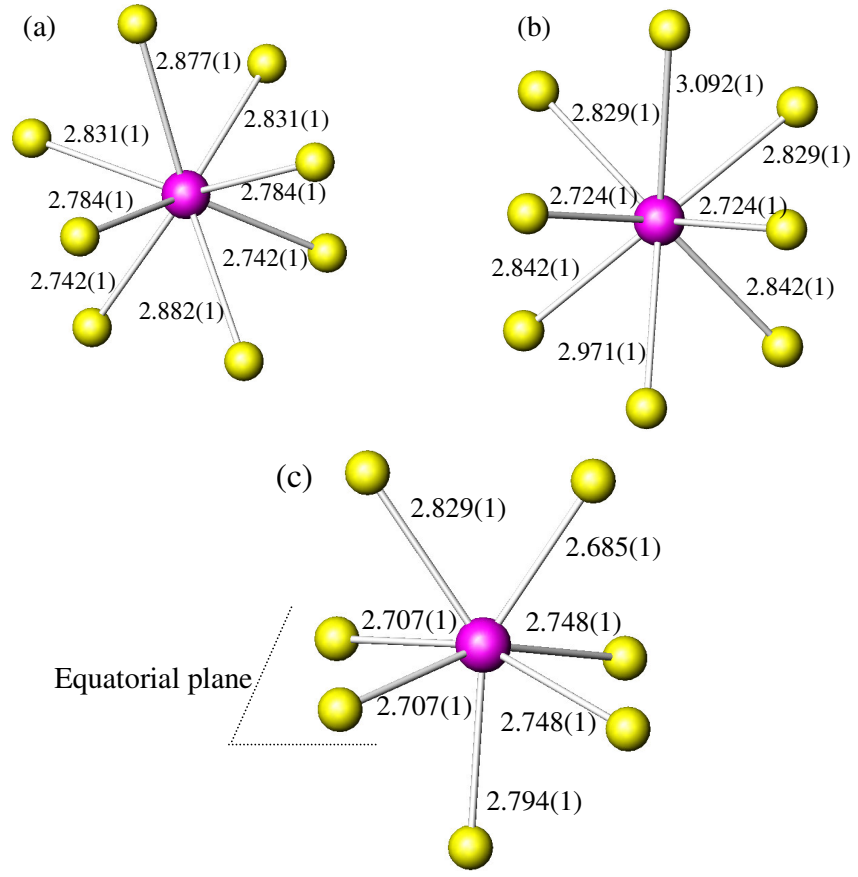

Figure 86: The local coordination of the erbium atoms in Er_3CrS_6: (a) Er(1), (b) Er(3) and (c) Er(2). *Key*: erbium, magenta circles; sulphur, yellow circles.

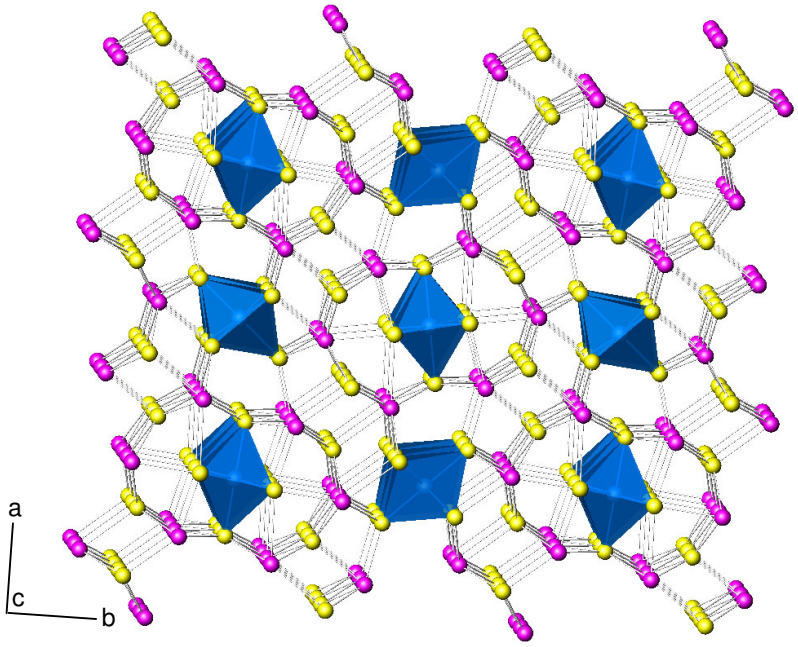

Figure 87: Polyhedral representation of the crystal structure of Er_3CrS_6 viewed along [001]. CrS_6 octahedra are coloured blue, erbium cations are represented by magenta circles and sulphide anions by yellow circles.

5.3.3 Crystal Structure Description of Er_4CrS_7

Crystals of Er_4CrS_7 were formed in black blocks. Crystallographic information and refinement details for Er_4CrS_7 are given in Table 40. Data were collected at room temperature. Final refined coordinates are shown in Table 41.

There are three crystallographically-independent cation sites in Er_4CrS_7, two of which are octahedrally coordinated by sulphur whilst the third is a seven-coordinate monocapped trigonal-prismatic site. Structural refinement using single-crystal X-ray diffraction data reveal that erbium and chromium ions are disordered over both octahedral sites, with the remaining erbium ions occupying the seven-coordinate site. The average metal-sulphur distance at the octahedral sites is *ca.* 2.66 Å (Table 42), which is slightly larger than that observed for divalent chromium in Er_2CrS_4, and is consistent with the presence of both chromium and the larger erbium cations at these sites. The average Er–S distance at the seven-coordinated site is *ca.* 2.82 Å (Figure 88), comparable to those found in the structures of Er_2CrS_4 and Er_3CrS_6 (Figure 82 and Figure 86, respectively). During initial structural refinements, the anion S(7) was located at a 2*(d)* (0.5,0,0.5) site. This resulted in large oblate anisotropic thermal parameters, suggesting that this ion might be disordered. In subsequent refinements S(7) was placed

at a 4*(i)* site (0.4861(4), 0, 0.4814(4)), with a site occupancy factor of 0.5. Similar disorder has previously been reported for the isostructural Tm_5S_7 [235].

Table 40: Crystallographic data for Er_4CrS_7.

Formula	**Er_4CrS_7**
M_r	940.93
Crystal Habit	Black block
Dimensions/mm	$0.16 \times 0.08 \times 0.05$
Crystal System	Monoclinic
Space group	*C2/m*
T/K	293
a/Å	12.5057(5)
b/Å	3.7650(2)
c/Å	11.2740(4)
β/°	105.85(2)
V/Å^3	510.64(4)
Z	2
Wavelength/Å	0.71073
μ/mm^{-1}	34.618
Measured data	6925
Unique data	878
Observed data ($I/>3\sigma(I)$)	735
$R(F_o)^*$	0.0332
$R_w(F_o)^{**}$	0.0279

Table 41: Final refined coordinates and equivalent isotropic displacement parameters for Er_4CrS_7.

Atom	**Site**	***x***	***y***	***z***	**U_{eq}(Å^2)**	**SOF**
Er(1)	4(*i*)	0.30774(3)	0	0.19747(3)	0.0129(1)	
M(2)	2(*a*)	½	½	0	0.0103(2)	Er:0.763(6) Cr:0.237(6)
M(3)	4(*i*)	0.61409(4)	½	0.42473(4)	0.0106(1)	Er:0.599(4) Cr:0.401(4)
S(4)	4(*i*)	0.16018(15)	½	0.05072(17)	0.0100(4)	
S(5)	4(*i*)	0.46519(16)	½	0.21708(19)	0.0149(5)	
S(6)	4(*i*)	0.75938(17)	½	0.64334(18)	0.0151(5)	
S(7)	4(*i*)	0.4861(4)	0	0.4814(4)	0.0184(8)	0.5(-)

* $R(F_o)=\Sigma(|F_o| - |F_c|)/\Sigma|F_o|$

** $R_w(F_o)=[\Sigma w(|F_o|-|F_c|)^2/\Sigma w|F_o|^2]^{1/2}$

Table 42: Selected bond distances (Å) for Er_4CrS_7.

Er(1) – S(6)	2.933(2) 2.832(1) × 2
Er(1) – S(7)	2.689(1) × 2
Er(1) – S(8)	2.880(2) × 2
Mean Er(1) – S	**2.82**
M(2) – S(6)	2.6940(13) × 4
M(2) – S(7)	2.600(2) × 2
Mean M(2) – S	**2.66**
M(3) – S(8)	2.7019(15) × 2
M(3) – S(9)	2.659(4) × 2 2.638(4) × 2
Mean M(3) – S	**2.66**

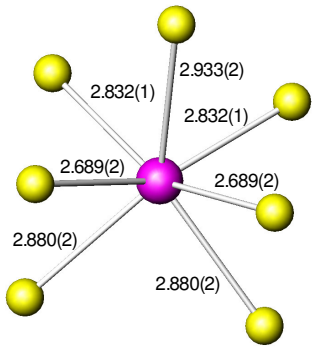

Figure 88: The local coordination of the Er(1) ion in Er_4CrS_7. *Key*: erbium, magenta circle; sulphur, yellow circles.

The structure of Er_4CrS_7 is presented in Figure 89. The M_2S_5 slabs in Er_4CrS_7 are not fused directly together as occurs in Er_2CrS_4, but are separated by one dimensional MS_4 chains of edge-sharing octahedra, analogous to those present in Er_3CrS_6. However, despite the presence of Cr^{+2}:d^4, the Er^{3+} and Cr^{2+} are disordered over the octahedral sites. Refinements using single crystal X-ray diffraction indicate that chromium cations show a preference for octahedral sites within the slab, which has a composition $(Er_{0.60}Cr_{0.40})_2S_5^{4.8-}$, whereas *ca.* 75 % of the octahedra in the single-octahedral chains contain erbium cations. The resulting $[Er_2CrS_7]^{6-}$ framework, contains channels parallel to the crystallographic *b*-axis, in which are located additional Er^{3+} ions (Er1) in a monocapped trigonal prismatic coordination geometry. The shortest cation-cation distances within the slab are *ca.* 3.70 Å, slightly shorter than the intra-chain distances of 3.77 Å.

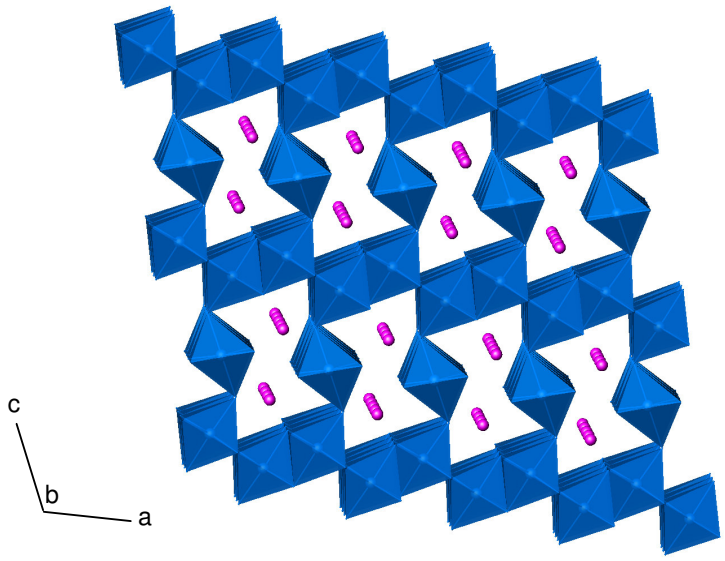

Figure 89: A polyhedral representation of the structure of Er_4CrS_7 viewed along the [010] direction.

5.3.4 Crystal Structure Description of $Er_6Cr_2S_{11}$

Crystals of $Er_6Cr_2S_{11}$ are black needles. A single crystal of $Er_6Cr_2S_{11}$ was selected for single-crystal X-ray diffraction and mounted on a glass fibre. The data were collected at 293 K. Crystallographic information and refinement details for $Er_6Cr_2S_{11}$ are given in Table 43. Final atomic coordinates, occupation factors and isotropic thermal parameters are given in Table 44.

$Er_6Cr_2S_{11}$ has been reported to crystallise in the non-centrosymmetric space group $Bb2_1m$, an alternative setting of $Cmc2_1$ [230]. However, application of Platon/Addsym [236, 237] to the data collected in this study, in order to identify missing symmetry elements indicates that there is an additional mirror plane, and that the structure is more correctly described in the centrosymmetric space group *Cmcm*. Refinements using single-crystal data were therefore carried out in *Cmcm,* and resulted in a low weighted residual of 2.35 %. The asymmetric unit contains three crystallographically-independent cation sites of octahedral coordination, together with two erbium sites of distorted trigonal prismatic and monocapped trigonal prismatic coordination (Figure 90).

The Cr^{2+} and Er^{3+} cations in $Er_6Cr_2S_{11}$ are again disordered over the octahedral sites with the average cation-sulphur distances (Table 45) comparable with those observed in Er_4CrS_7.

Table 43: Crystallographic data for $Er_6Cr_2S_{11}$.

Formula	**$Er_6Cr_2S_{11}$**
M_r	1462.48
Crystal Habit	Black needle
Dimensions/mm	$0.26 \times 0.08 \times 0.06$
Crystal System	Orthorhombic
Space group	*Cmcm*
T/K	293
a/Å	3.7551(3)
b/Å	12.5190(8)
c/Å	34.177(2)
β/°	90.0
V/Å^3	1606.7(2)
Z	4
Wavelength/Å	0.71073
μ/mm^{-1}	33.749
Measured data	18621
Unique data	1410
Observed data ($I/>3\sigma(I)$)	1086
$R(F_o)^*$	0.0229
$R_w(F_o)^{**}$	0.0235

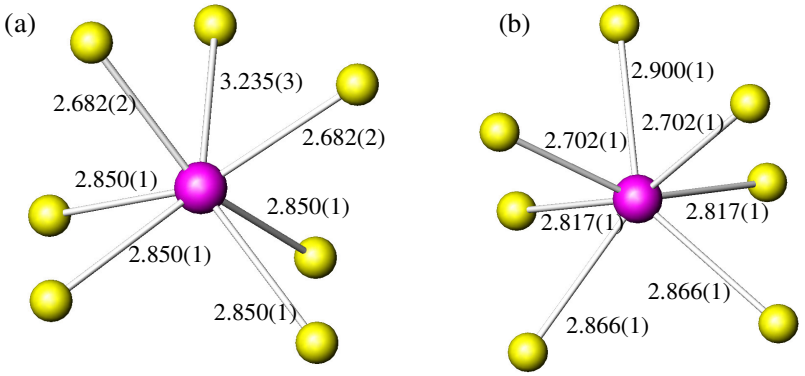

Figure 90: The local coordination of geometry of (a) Er(1) and (b) Er(2) in $Er_6Cr_2S_{11}$.

Key: erbium, magenta circles; sulphur, yellow circles.

* $R(F_o)=\Sigma(|F_o| - |F_c|)/\Sigma|F_o|$

** $R_w(F_o)=[\Sigma w(|F_o|-|F_c|)^2/\Sigma w|F_o|^2]^{1/2}$

Table 44: Final refined coordinates and equivalent isotropic displacement parameters for $Er_6Cr_2S_{11}$.

Atom	Site	*x*	*y*	*z*	U_{eq}(Å^2)	SOF
Er(1)	4(*c*)	0	0.49117(3)	¼	0.0159(1)	
Er(2)	8(*f*)	½	0.75959(2)	0.43838(1)	0.0093(1)	
M(3)	8(*f*)	0	0.74867(3)	0.31710(1)	0.0093(1)	Er:0.583(3) Cr:0.417(3)
M(4)	8(*f*)	½	0.51374(3)	0.36581(1)	0.0086(1)	Er:0.569(3) Cr:0.431(3)
M(5)	4(*a*)	½	½	½	0.0072(1)	Er:0.714(4) Cr:0.286(4)
S(6)	8(*f*)	½	0.60363(14)	0.29733(5)	0.0146(4)	
S(7)	4(*c*)	½	0.33818(17)	¼	0.0154(6)	
S(8)	8(*f*)	0	0.65877(13)	0.38691(5)	0.0122(4)	
S(9)	8(*f*)	½	0.41348(12)	0.43103(5)	0.0119(4)	
S(10)	8(*f*)	0	0.64706(10)	0.48397(4)	0.0068(3)	
S(11)	8(*f*)	½	0.88752(17)	0.33672(8)	0.0303(6)	

Table 45: Selected bond distances (Å) for $Er_6Cr_2S_{11}$.

Er(1) – S(9)	2.850(1) × 4
Er(1) – S(10)	2.682(2) × 2
Er(1) – S(14)	3.235(3)
Mean Er(1) – S	**2.86**
Er(2) – S(11)	2.866(1) × 2
Er(2) – S(12)	2.702(1) × 2
Er(2) – S(13)	2.817(1) × 2 2.900(1)
Mean Er(2) – S	**2.81**
M(3) – S(9)	2.698(1) × 2
M(3) – S(10)	2.552(1)
M(3) – S(11)	2.638(2)
M(3) – S(14)	2.645(1) × 2
Mean M(3) – S	**2.65**
M(4) – S(9)	2.597(2)
M(4) – S(11)	2.710(1) × 2
M(4) – S(12)	2.558(2)
M(4) – S(14)	2.648(1) × 2
Mean M(4) – S	**2.65**
M(5) – S(12)	2.594(2) × 2
M(5) – S(13)	2.686(1) × 4
Mean M(5) – S	**2.66**

In the structure of $Er_6Cr_2S_{11}$ (Figure 91), pairs of M_2S_5 units are fused to create a double slab. There is disorder of Er^{3+} and Cr^{2+} cations over the available sites within this network of octahedra, with *ca.* 85 % of the chromium cations residing in sites within the slab, whilst the ratio of Er^{3+}:Cr^{2+} within the octahedral chains is similar to that in Er_4CrS_7 at 3:1. Successive double slabs are linked by sharing common vertices with single MS_4 octahedral chains to produce a framework of composition $[Er_3Cr_2S_{11}]^{9-}$. This network of octahedra contains two types of channel running parallel to the crystallographic *a*-axis. The channels are occupied by six-coordinate Er(l) and seven-coordinate Er(2) cations which serve to balance the charge of the framework.

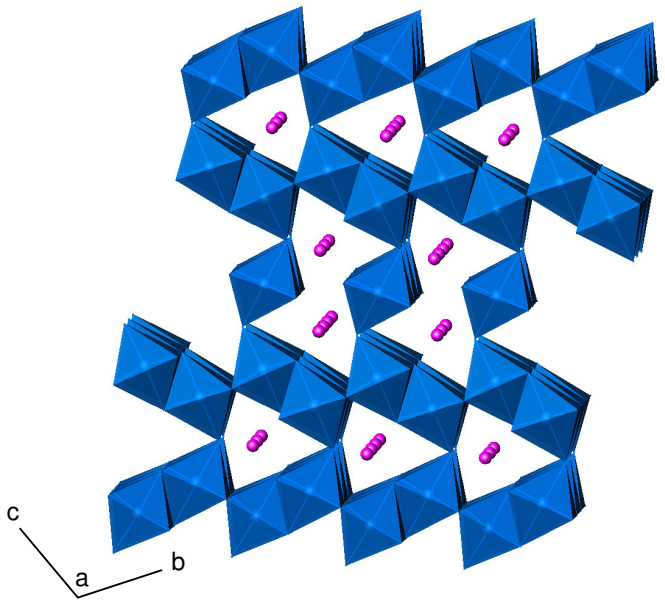

Figure 91: Structure of $Er_6Cr_2S_{11}$ viewed along the [100] direction.

Single crystal X-ray diffraction studies showed that the structures of Er_2CrS_4, Er_4CrS_7 and $Er_6Cr_2S_{11}$ are closely related. The basic building unit in these structures is MS_3 double octahedral chains which are linked to form two-dimensional M_2S_5 slab. In the structure of Er_4CrS_7 and $Er_6Cr_2S_{11}$ single and double slabs are observed. Further reactions were carried out in an attempt to synthesise a new compound with triple M_2S_5 slabs.

5.3.5 Crystal Structure Description of $Er_8Cr_3S_{15}$

The reaction in an attempt to synthesise new $Er_8Cr_3S_{15}$ was successful and black crystals were obtained. Single-crystal X-ray diffraction data were collected at 293 K on

a single crystal mounted on a glass fibre. Crystallographic information and refinement details for $Er_8Cr_3S_{15}$ are given in Table 46.

Systematic extinction conditions for the $Er_8Cr_3S_{15}$ crystal were compatible with space groups *C2/m*, *Cm* and *C2*. The values of R_{merge} for all three space groups were comparable, and therefore the structure was solved in space group *C2/m*, the highest symmetry group of the three. Refinement of the structure shows that there are six crystallographically-independent cation sites in $Er_8Cr_3S_{15}$. There are four cation sites of octahedral coordination and two erbium sites of distorted trigonal prismatic and monocapped trigonal prismatic coordination. Similar to Er_4CrS_7 and $Er_6Cr_2S_{11}$, the Cr^{2+} and Er^{3+} cations are disordered over the octahedral sites. The average metal-sulphur distance at the octahedral sites is *ca.* 2.64 Å and *ca.* 2.82 Å for Er–S at the seven-coordinate site (Figure 92). These are comparable with those observed in Er_4CrS_7 and $Er_6Cr_2S_{11}$. During initial structural refinement of $Er_8Cr_3S_{15}$ S(14) was located at a 2(*a*) (½, ½, ½) site. The anisotropic thermal factor for this ion showed large oblate thermal parameters. In subsequent refinements S(14) was placed at a 4*(i)* site (0.4907(5), 0.5, 0.5081(2)), with a site occupancy factor of 0.5. Similar disorder of one of the sulphur atoms was observed in the structure of Er_4CrS_7. Final atomic coordinates, site occupancy factors and isotropic thermal parameters are given in Table 47 while bond distances are listed in Table 48.

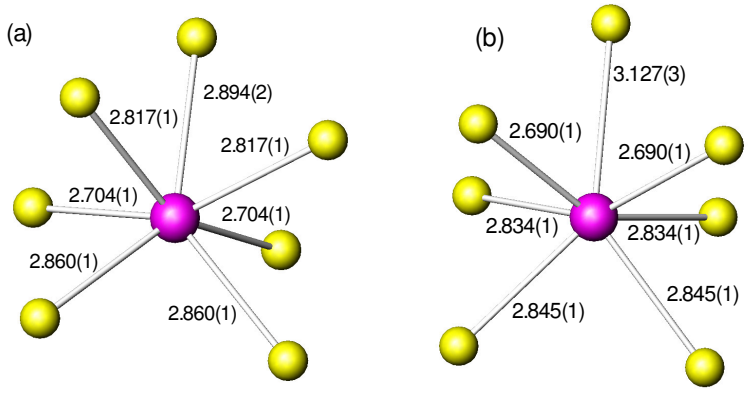

Figure 92: The local coordination of the Er(1) and Er(2) atoms in $Er_8Cr_3S_{15}$.
Key: erbium, magenta circles; sulphur, yellow circles.

Table 46: Crystallographic data for a new $Er_8Cr_3S_{15}$ phase.

Formula	**$Er_8Cr_3S_{15}$**
M_r	1974.59
Crystal Habit	Black needle
Dimensions/mm	$0.36 \times 0.08 \times 0.04$
Crystal System	Monoclinic
Space group	*C2/m*
T/K	293
a/Å	12.5048(5)
b/Å	3.7533(1)
c/Å	23.4935(8)
β/°	97.641(2)
V/Å^3	1092.86(6)
Z	1
Wavelength/Å	0.71073
μ/mm^{-1}	32.875
Measured data	15243
Unique data	1914
Observed data ($I/>3\sigma(I)$)	1596
$R(F_o)^*$	0.0333
$R_w(F_o)^{**}$	0.0313

$Er_8Cr_3S_{15}$ is a new erbium chromium sulphide in which triple M_2S_5 slabs are linked through octahedral chains (Figure 93). The octahedra in the single-octahedral chain contain *ca.* 70 % of the erbium cations. Similar to the Er_4CrS_7 and $Er_6Cr_2S_{11}$ structures, Er^{3+} and Cr^{2+} are disordered over the octahedral sites. Triple M_2S_5 slabs are linked again by octahedral chains resulting in a framework of composition $[Er_4Cr_3S_{15}]^{12-}$. This framework contains channels running parallel to the crystallographic *b*-axis. The channels are occupied by seven-coordinate Er(1) and Er(2). The existence of the $Er_8Cr_3S_{15}$ phase has been proposed [174, 231] but its structure has not been described and there are no other isostructural phases known to date.

* $R(F_o)=\Sigma(|F_o| - |F_c|)/\Sigma|F_o|$

** $R_w(F_o)=[\Sigma w(|F_o|-|F_c|)^2/\Sigma w|F_o|^2]^{1/2}$

Table 47: Final refined coordinates and equivalent isotropic displacement parameters for $Er_8Cr_3S_{15}$.

Atom	Site	*x*	*y*	*z*	U_{eq}(Å^2)	SOF
Er(1)	4(*i*)	0.78224(3)	0	0.09038(1)	0.0105(1)	
Er(2)	4(*i*)	0.58080(3)	½	0.36365(2)	0.0169(1)	
M(3)	4(*i*)	0.56356(4)	0	0.19666(2)	0.0111(2)	Er:0.548(4) Cr:0.452(4)
M(4)	4(*i*)	0.31675(4)	0	0.26839(2)	0.0106(2)	Er:0.540(4) Cr:0.460(4)
M(5)	4(*i*)	0.35910(4)	0	0.46403(2)	0.0109(2)	Er:0.514(4) Cr:0.486(4)
M(6)	2(*a*)	½	0	0	0.0090(2)	Er:0.708(5) Cr:0.292(5)
S(7)	4(*i*)	0.42763(14)	0	0.36690 (10)	0.0195(6)	
S(8)	4(*i*)	0.70576(17)	1	0.43526(8)	0.0178(6)	
S(9)	4(*i*)	0.65297(13)	½	0.02338(7)	0.0089(4)	
S(10)	4(*i*)	0.43928(14)	0	0.10144(8)	0.0144(5)	
S(11)	4(*i*)	0.20188(16)	0	0.16619(7)	0.0146(5)	
S(12)	4(*i*)	0.4495(2)	- ½	0.24071(12)	0.0313(8)	
S(13)	4(*i*)	0.67861(17)	0	0.29637(8)	0.0172(6)	
S(14)	4(*i*)	0.4907(5)	½	0.5081(2)	0.0319(11)	0.5(-)

Table 48: Bond distances (Å) for $Er_8Cr_3S_{15}$.

Er(1) – S(13)	2.894(2)	M(4) – S(11)	2.535(2)
Er(1) – S(13)	2.817(1) × 2	M(4) – S(15)	2.629(2)
Er(1) – S(14)	2.704(1) × 2	M(4) – S(16)	2.643(2) × 2
Er(1) – S(15)	2.860(1) × 2	M(4) – S(17)	2.691(1) × 2
Mean Er(1) – S	**2.81**	***Mean M(4) – S***	**2.64**
Er(2) – S(11)	2.690(1) × 2	M(5) – S(11)	2.542(2)
Er(2) – S(12)	2.845(1) × 2	M(5) – S(12)	2.617(2)
Er(2) – S(16)	3.127(3)	M(5) – S(12)	2.704(2) × 2
Er(2) – S(17)	2.834(1) × 2	M(5) – S(18)	2.674(5) × 2
Mean Er(2) – S	**2.84**	***Mean M(5) – S***	**2.63**
M(3) – S(14)	2.552(2)	M(6) – S(13)	2.684(1) × 4
M(3) – S(15)	2.712(1) × 2	M(6) – S(14)	2.596(2) × 2
M(3) – S(16)	2.649(2) × 2		
M(3) – S(17)	2.548(2)		
Mean M(3) – S	**2.64**	***Mean M(6) – S***	**2.65**

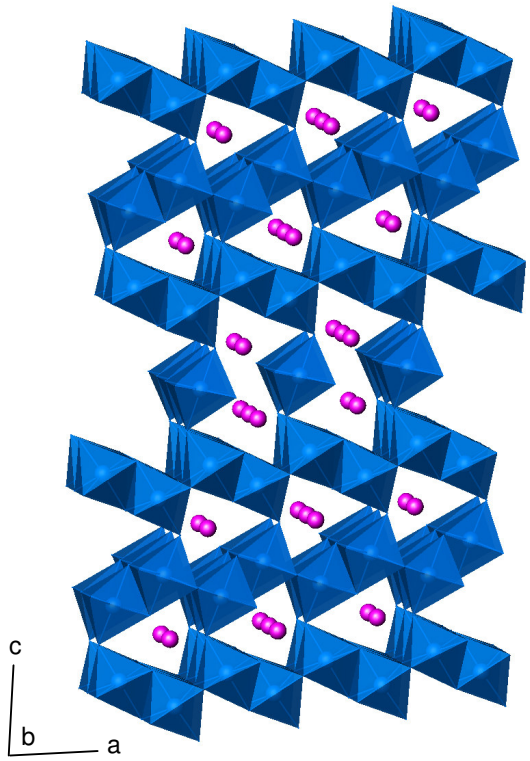

Figure 93: Structure of $Er_8Cr_3S_{15}$ viewed along the [010] direction.

5.3.6 Powder X-ray Analysis

Bulk samples of four erbium chromium sulphides were prepared. Powder X-ray diffraction data for powdered samples are consistent with the formation of single phase products. The data can be indexed on the basis of the unit-cells determined by single-crystal X-ray diffraction, with refined parameters (Table 49) that are in good agreement with those obtained in the single-crystal study. The unit cell parameters were determined from the raw powder X-ray diffraction data using the Topas software (Bruker AXS).

Table 49: Lattice parameters of bulk samples of ternary erbium chromium sulphides determined by powder X-ray diffraction.

Formula	Er_2CrS_4	Er_3CrS_6	Er_4CrS_7	$Er_6Cr_2S_{11}$
a/Å	12.4463(5)	13.1815(4)	12.5007(9)	3.7568(3)
b/Å	7.4892(3)	15.8363(5)	3.7602(3)	12.513(1)
c/Å	12.4839(6)	3.7293(2)	11.2637(8)	34.121(3)
β/°	90	90	105.977(5)	90

5.4 Magnetic Properties

Magnetic measurements were performed on four bulk samples (Er_3CrS_6, Er_4CrS_7, $Er_6Cr_2S_{11}$ and Er_2CrS_4) in a manner described in Chapter 2. Magnetic susceptibility data (Figure 94) reveal that all materials follow Curie-Weiss behaviour at high temperatures. Magnetic parameters derived from data obtained by the VSM technique are given in Table 50. The effective magnetic moments, μ_{eff}, of erbium chromium sulphide materials are in good agreement with expectations based on spin-only behaviour for the chromium cations and a value of 9.58 μ_B, calculated from the Landé formula, for the μ_{eff} of the Er^{3+} cations. The observation of a small negative Weiss constant for Er_4CrS_7, suggests that the dominant magnetic interactions are antiferromagnetic in origin. However, these interactions are of insufficient strength to produce long-range magnetic order and the material remains paramagnetic to the lowest temperature studied (Figure 94(a)). Initially, it appears that behaviour of $Er_6Cr_2S_{11}$ is also consistent with paramagnetic behaviour down to 5 K and leads to a very small positive Weiss constant. However, a significant deviation from Curie-Weiss behaviour is observed below *ca.* 20 K. Subtraction of the contribution to the magnetic susceptibility arising from the erbium ions, assuming Curie-Weiss behaviour and an effective magnetic moment of 9.58 μ_B, reveals an underlying antiferromagnetic transition, with T_N = 11.4 K (Figure 94(b)). This suggests ordering of the Cr^{2+} sub-lattice occurs on cooling, the signature of which is masked by the much larger magnetic response of the rare-earth ion. A similar subtraction applied to the data for Er_4CrS_7 does not reveal a corresponding ordering transition of the Cr^{2+} sub-lattice in this phase. The magnetic susceptibility data for Er_3CrS_6 (Figure 94(c)) exhibit Curie-Weiss behaviour at high temperatures with a value of μ_{eff} consistent with trivalent rare-earth and transition-metal cations. However, Er_3CrS_6 shows more complex behaviour at low temperatures, with slight divergence of fc and zfc data in the temperature range $5 < T/K < 45$. Moreover, on cooling below 50 K, the $\chi(T)$ curve exhibits an inflection at 30 K, followed by a steep rise at 10 K, suggesting two successive magnetic transitions. Further support for this is provided by examination of the temperature dependence of the effective magnetic moment, μ_{eff}, per cation (Figure 95), as measured by the quantity $[(8\chi T)/4]^{1/2}$. On cooling, μ_{eff} remains close to the expected value for Er^{3+} and Cr^{3+} over a wide range of temperature, until at *ca.* 50 K it begins to increase markedly, reaching a maximum of 21.8 μ_B at 30 K. Below this temperature μ_{eff} falls, reaches a minimum at 9.4 K, before increasing slightly on further cooling. Measurement of the magnetisation

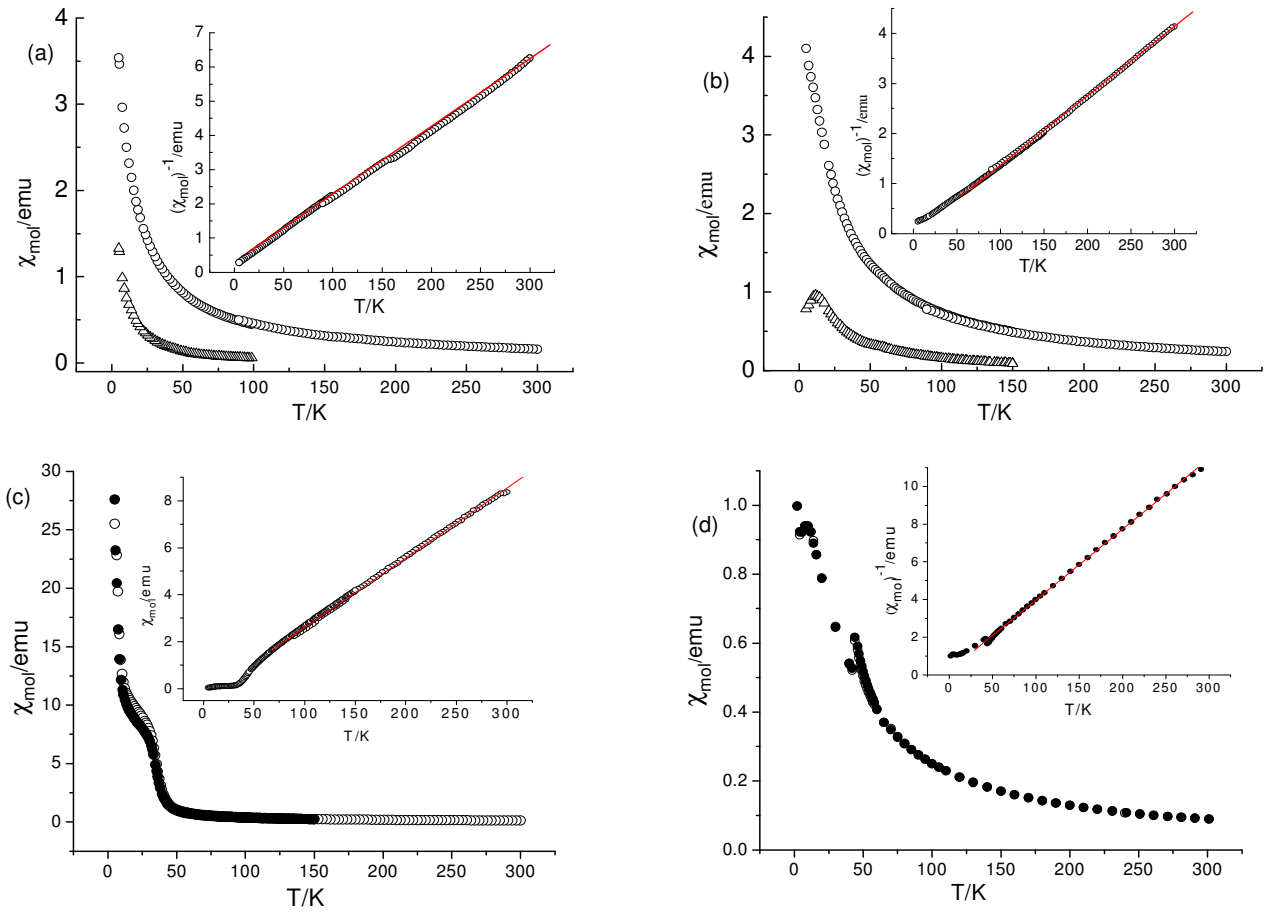

Figure 94: Magnetic susceptibility data for (a) Er_4CrS_7, (b) $Er_6Cr_2S_{11}$, (c) Er_3CrS_6 and (d) Er_2CrS_4. Solid points denote field-cooled data and open points zero-field cooled data measured by SQUID magnetometry. In (a) and (b), open triangles represent the magnetic susceptibilities obtained following subtraction of the contribution due to the erbium moments. The inset shows the fit of a Curie-Weiss expression to high-temperature data collected using a vibrating sample magnetometer.

Table 50: Magnetic properties of erbium chromium sulphide materials derived from fits to a Curie-Weiss expression.

Material	Fitting range/ K	C_{exp} / cm^3 K mol^{-1}	C_{th} / cm^3 K mol^{-1}	μ_{eff}/μ_B	μ_{th}/μ_B	θ / K
Er_3CrS_6	80 – 300	34.32(4)	36.3	8.28(1)	8.52	+8.0(2)
Er_2CrS_4	80 – 300	27.47(15)	25.95	8.56(3)	8.31	-10(1)
Er_4CrS_7	88 – 300	49.46(13)	48.9	8.90(1)	8.85	-6.4(5)
$Er_6Cr_2S_{11}$	88 – 300	72.15(16)	74.9	8.49(1)	8.65	+2.4(4)

as a function of field confirms the existence of a spontaneous magnetisation at 5 K (Figure 96). This approaches saturation in an applied field of 10 kG. The saturated moment was estimated by taking the intercept on the moment axis of linear fits to the high-field region of μ *vs. 1/H* plots, leading to a value of 7.97(9) μ_B per formula unit.

Two magnetic transitions are apparent at low temperature in the magnetic susceptibility data of Er_2CrS_4 (Figure 94(d)). The value of μ_{eff}, extracted from the Curie-Weiss fit to the high-temperature data, is consistent with the presence of Er^{3+} and Cr^{2+} ions. On cooling, the magnetic susceptibility shows a peak at 44 K. Below 42 K, χ rises and exhibits a second broad maximum at 9 K, before rising again below 4 K. The negative Weiss constant indicates that the dominant magnetic exchange interactions are antiferromagnetic in origin. The effective magnetic moment is almost invariant with temperature down to *ca.* 44 K (Figure 97), below which μ_{eff} decreases markedly, suggesting that the peak in χ(T) at 42 K is associated with long-range antiferromagnetic ordering of the chromium sub-lattice; the second lower-temperature anomaly corresponding to ordering of the erbium sub-lattice.

The magnetisation of Er_2CrS_4 shows an almost linear dependence on magnetic field (Figure 98) and does not approach saturation even at the highest field used. This, together with the relatively low value of *ca.* 0.5 μ_B per cation at l0 kG indicates that there is no uncompensated moment associated with either the erbium or chromium sub-lattices.

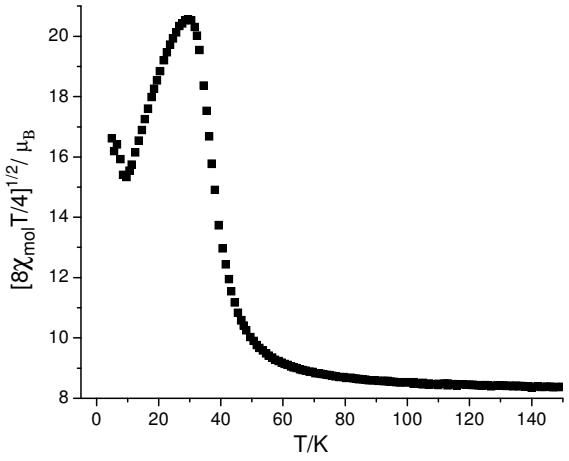

Figure 95: Temperature dependence of the effective magnetic moment per ion of Er_3CrS_6, as measured by the quantity $(8\chi T/4)^{1/2}$.

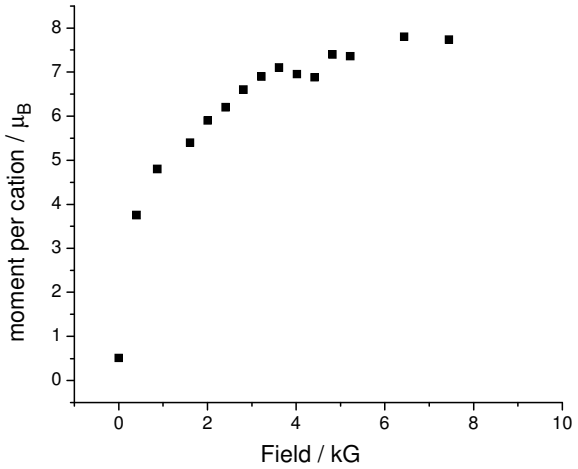

Figure 96: Variation in the magnetic moment per cation of Er_3CrS_6 as a function of applied magnetic field at 5 K.

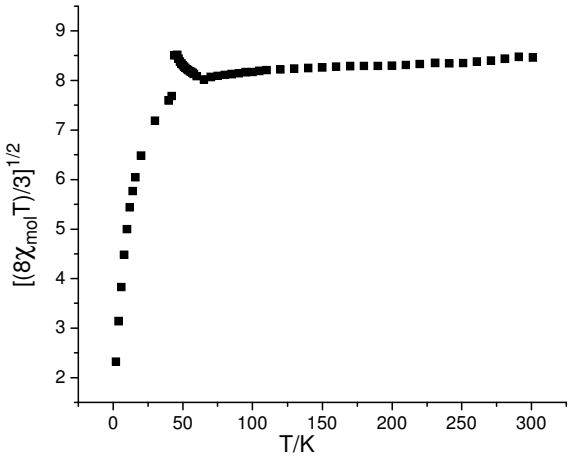

Figure 97: Temperature dependence of the effective magnetic moment per ion of Er_2CrS_4, as measured by the quantity $(8\chi T/3)^{1/2}$.

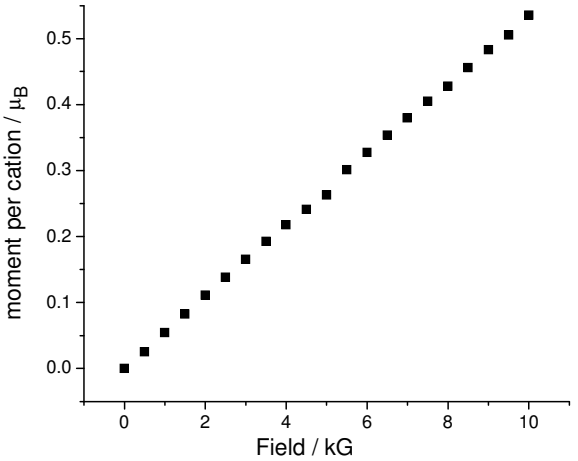

Figure 98: Variation in the magnetic moment per cation of Er_2CrS_4 as a function of applied magnetic field at 5 K.

5.5 Neutron Diffraction

Neutron diffraction studies were performed on the four erbium-chromium sulphides using the POLARIS diffractometer. Additionally Er_3CrS_6 was studied using the OSIRIS diffractometer. Neutron diffraction was used in order to investigate further the magnetic properties of these materials. Furthermore, it allowed determination of the magnetic structure of Er_3CrS_6 sample and the thermal evolution of the magnetic structure to be followed. Data were collected as described in Chapter 2. Typically ~1.5 g of the powdered sample was placed in 6 mm vanadium sample can which was then attached to the end of a sample stick and placed in a standard orange cryostat. Data were collected at room temperature for all the samples and at selected low temperatures close to the temperature where a deviation from Curie Weiss law in magnetic data was observed. Initial data manipulation and reduction was carried out using Genie [207] spectrum manipulation software. Rietveld refinement was performed with GSAS program [189] using the EXPGUI interface [190]. The initial models were the structures determined using single crystal X-ray diffraction as described in Section 5.3 of this Chapter. The background of the neutron data was modelled using a linear interpolation function with the coefficients included as refinable parameters. Peak shape was refined using a convolution of back-to-back exponentials with a pseudo-Voigt function. Following initial refinement of scale factors, background terms, positional and lattice parameters, thermal parameters were introduced as variables into the refinement. A wavelength-dependent absorption correction was included in all the refinements. In the case of Er_4CrS_7 and $Er_6Cr_2S_{11}$ materials, site occupancy factors (SOF) associated with disordered cations were introduced as variables with the constraint that overall stoichiometry was maintained. Values of SOF were fixed at the values determined at room temperature. Finally, in case of the magnetic structures, magnetic moments were refined. The reflections originating from the vanadium sample can (d_{110} = 2.14 Å, d_{200}=1.52 Å and d_{211}=1.24 Å) were excluded from the refinements where appropriate.

5.5.1 Neutron Studies of Er_4CrS_7

Powder neutron diffraction data of Er_4CrS_7 were collected at room temperature and at 2 K on POLARIS at ISIS. Data obtained from the high-resolution backscattering detector bank ($2\theta = 145^o$), the low angle and the 90^o banks provide no evidence of long range order in this material. The neutron diffraction patterns collected at 2 K and room

temperature were both well fitted with the structure described in the space group *C2/m*. Er_4CrS_7 appears to be paramagnetic to the lowest temperatures studied. Results of the refinements using neutron data show that the unit cell contracts on cooling (Table 51). Final refined profiles of neutron data are presented in Figure 99 and Figure 100, while refined parameters are listed in Table 51. Site occupancy factors of disordered erbium and chromium atoms were refined giving composition $Er_{4.10(1)}Cr_{0.90(1)}S_7$ which is in good agreement with the nominal composition of the initial reaction mixture.

Table 51: Final refined parameters for Er_4CrS_7 (space group *C2/m*)[**].

Temperature/K		2 K	RT
a /Å		12.4757(7)	12.4837(3)
b /Å		3.7551(2)	3.7572(1)
c /Å		11.2441(7)	11.2530(2)
β (°)		105.913(5)	105.960(2)
M(1)	*x*	0.3072(2)	0.3079(1)
	z	0.1990(3)	0.1979(1)
	B/Å^2	0.82(2)	0.98(1)
M(2)	B/Å^2	0.82(2)	0.98(1)
	SOF(Er)	0.80(-)	0.80(1)
	SOF(Cr)	0.20(-)	0.20(1)
M(3)	*x*	0.6138(3)	0.6154(1)
	z	0.4256(4)	0.4252(1)
	B/Å^2	0.82(2)	0.98(1)
	SOF(Er)	0.65(-)	0.65(1)
	SOF(Cr)	0.35(-)	0.35(1)
S(1)	*x*	0.1614(7)	0.1632(3)
	z	0.0472(7)	0.0495(3)
	B/Å^2	0.55(4)	0.63(2)
S(2)	*x*	0.4636(7)	0.4641(3)
	z	0.2175(8)	0.2137(3)
	B/Å^2	0.55(4)	0.63(2)
S(3)	*x*	0.7574(7)	0.7589(3)
	z	0.6421(7)	0.6452(3)
	B/Å^2	0.55(4)	0.63(2)
S(4)	*x*	0.4859(16)	0.4850(6)
	z	0.4834(15)	0.4794(5)
	B/Å^2	0.55(4)	0.63(2)
R_{wp}/%	Bank 2: $2\theta = 145^o$	0.64	1.37
	Bank 3: $2\theta = 35^o$	2.38	2.72
	Bank 1: $2\theta = 90^o$	1.25	1.76
χ^2		0.81	1.13

[**] M(1) and S(4) on 4(*i*), (*x*, 0, *z*); M(2) on 2(*a*), (½, ½, 0); M(3), S(1), S(2), S(3) on 4(*i*), (*x*, ½, *z*).

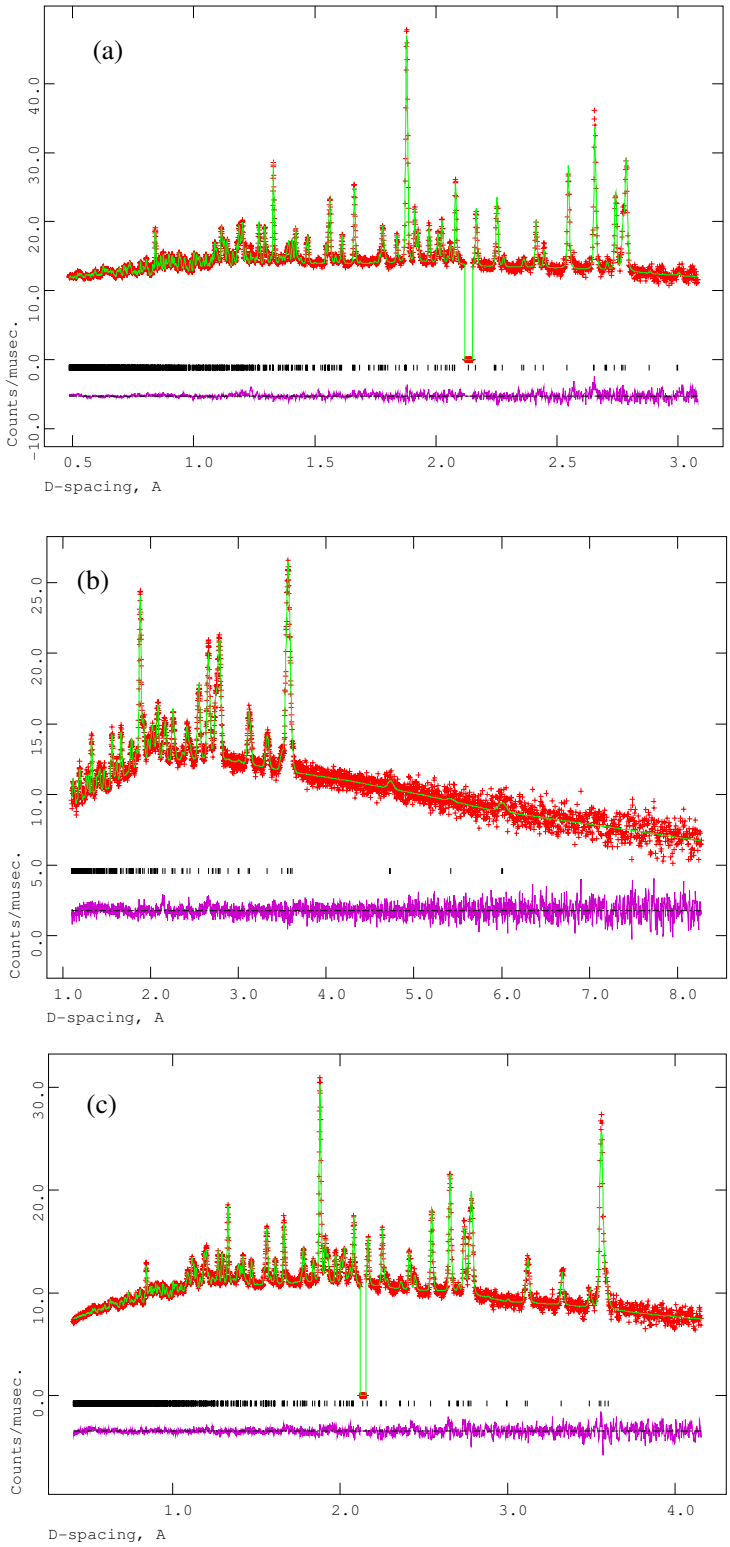

Figure 99: Final observed (crosses), calculated (upper full line) and difference (lower full line) neutron diffraction profiles for Er_4CrS_7 at room temperature: data collected from (a) backscattering bank ($2\theta = 145°$), (b) low angle bank ($2\theta = 35°$) and (c) 90° bank. Reflection positions are marked. Vanadium reflections originating from the sample can and cryostat are excluded.

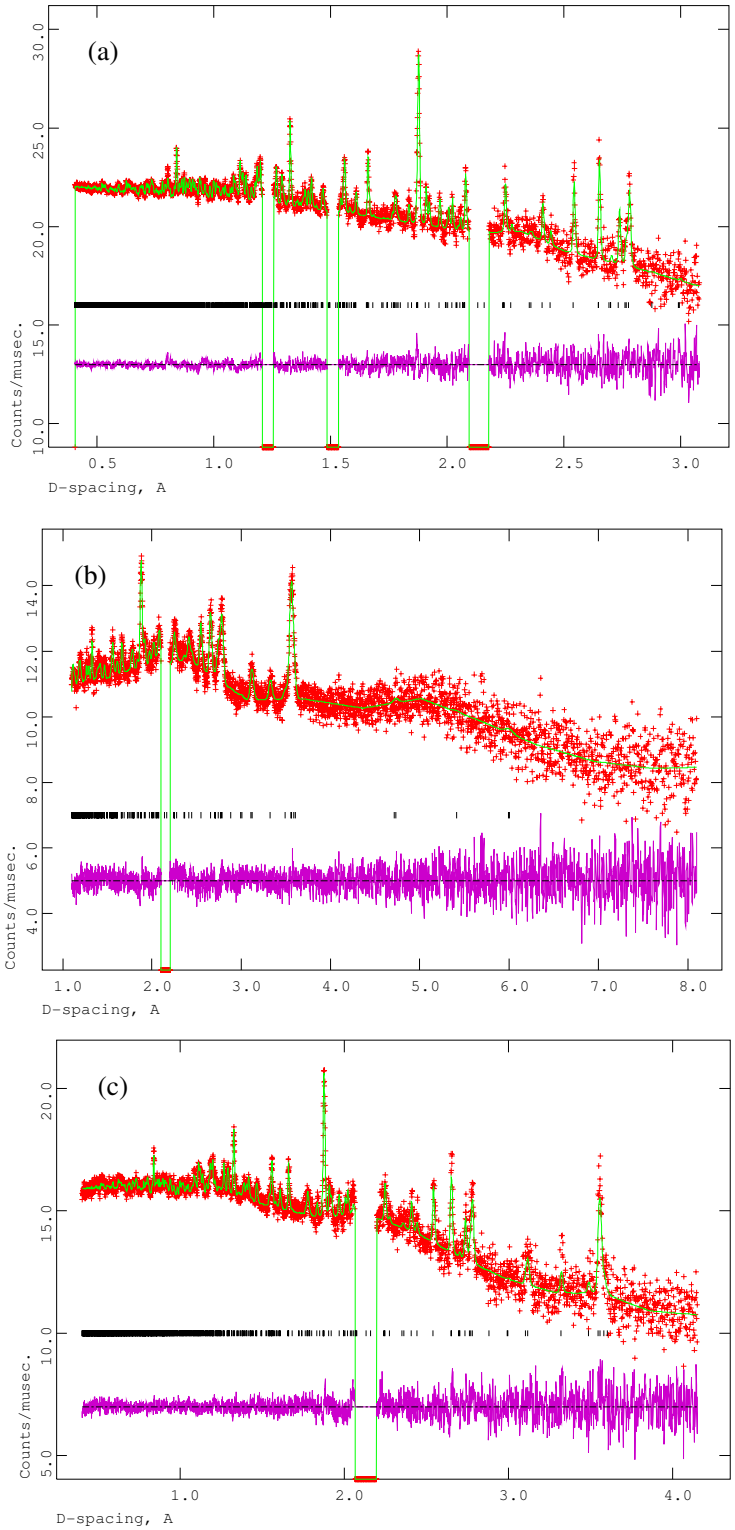

Figure 100: Final observed (crosses), calculated (upper full line) and difference (lower full line) neutron diffraction profiles for Er_4CrS_7 at 2 K: data collected from (a) backscattering bank ($2\theta = 145°$), (b) low angle bank ($2\theta = 35°$) and (c) 90° bank. Reflection positions are marked. Vanadium reflections originating from the sample can and cryostat are excluded.

5.5.2 Neutron Studies of $Er_6Cr_2S_{11}$

Powder neutron diffraction data for $Er_6Cr_2S_{11}$ were collected at room temperature and at 20, 14, 8 and 4 K on POLARIS at ISIS. The neutron diffraction patterns collected at room temperature, 20 K and 14 K show that the orthorhombic model (space group *Cmcm*) obtained from single crystal X-ray diffraction gives a good fit to the data. Final refined profiles of the neutron data collected at room temperature are presented in Figure 101.

Site occupancy factors of disordered erbium and chromium cations were fixed at the values determined at room temperature. Disordered erbium and chromium atoms occupy two crystallographically-distinct cation sites (8(*f*) and 4(*a*)). Initially the site occupancy factors for the cations at the two 8(*f*) sites in the double slabs were allowed to vary with the constraint that the overall stoichiometry of these layers was maintained. Next, the site occupancy factor of the 4(*a*) site was refined with a constraint that the stoichiometry of this site was maintained. Later all three site occupancy factors were refined maintaining the original constraints. This procedure led to the composition $Er_{5.98(1)}Cr_{1.92(1)}S_{11}$ which is in good agreement with the nominal composition.

Initially, it appears that there is no magnetic order in $Er_6Cr_2S_{11}$ to the lowest temperature studied. However, close examination of the data collected at 4 and 8 K show two additional very weak reflections at d = 3.14 and d = 3.17 Å suggesting a magnetic transition (Figure 102). The anomaly observed in the magnetic data suggests that these peaks are due to ordering of chromium sub-lattice. The extra peaks can be indexed on the basis of the crystallographic unit cell suggesting that the magnetic propagation vector is a zero vector **k** = (0, 0, 0). These peaks disappear on heating and are not present in the data collected at 14 K. The data collected at 4 and 8 K can be fitted very well using the nuclear unit cell, indicating that the magnetic contribution is very small. The data do not provide enough information to solve the magnetic structure of $Er_6Cr_2S_{11}$ sample at low temperature. Final refined profiles of the data collected at 4 K are shown in Figure 103 while these at 20, 14 and 8 K are provided in Appendix 5.1. Results of the refinements using neutron data are listed in Table 52.

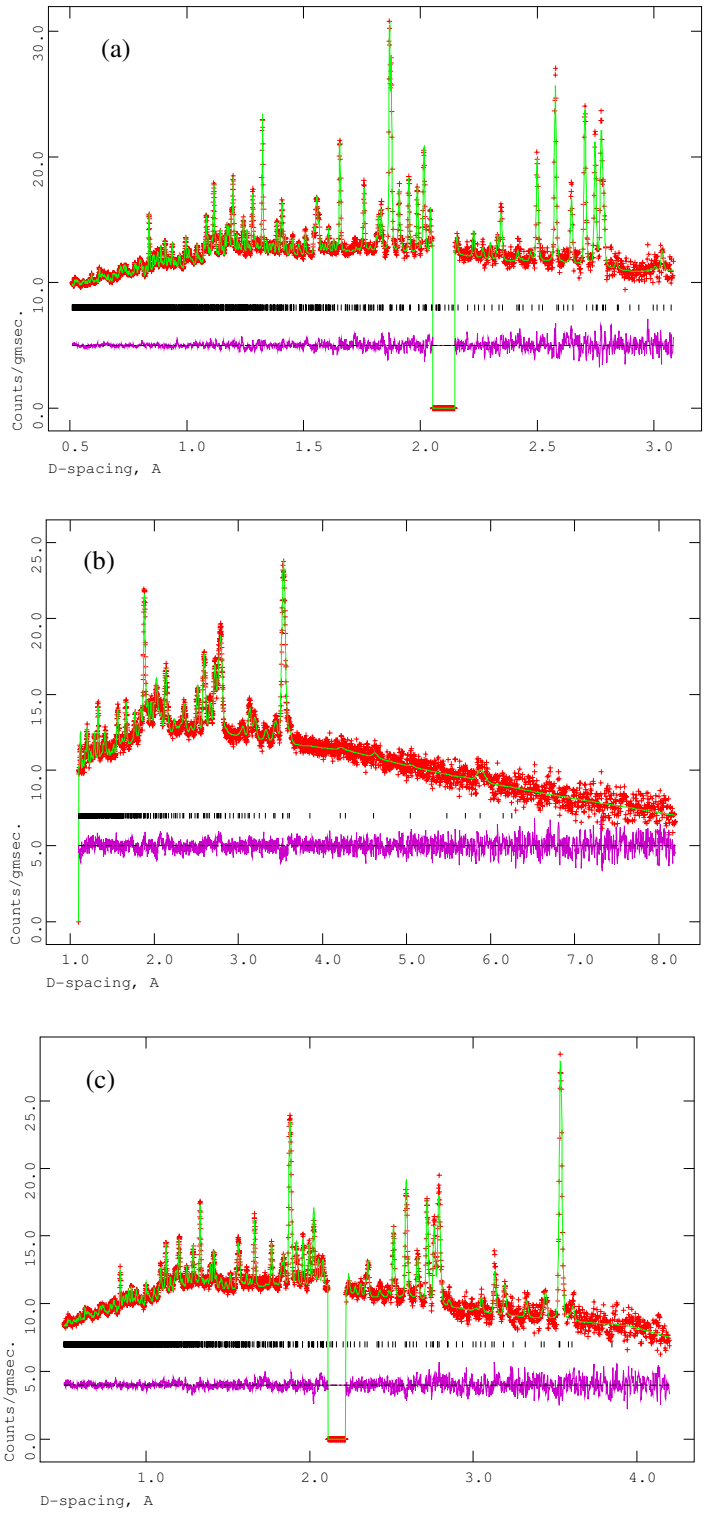

Figure 101: Final, observed (crosses), calculated (upper full line) and difference (lower full line) neutron diffraction profile of $Er_6Cr_2S_{11}$ at room temperature. Data collected on POLARIS at ISIS from (a) backscattering bank (2θ = 145°), (b) low angle bank (2θ = 35°) and (c) 90 degree bank. The excluded regions are due to the presence of a peaks originating from the vanadium sample can.

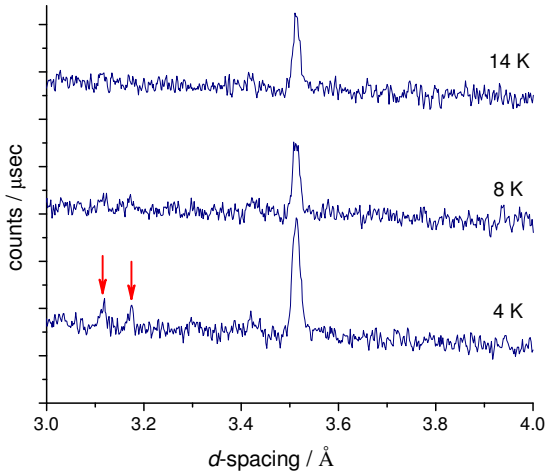

Figure 102: Powder neutron diffraction data collected for $Er_6Cr_2S_{11}$ at 4 K, 8 K and 14 K, illustrating the disappearance of weak reflections at 3.14 and 3.17 Å on heating through the temperature at which the maximum in the magnetic susceptibility is observed (11.4 K) following subtraction of the contribution due to Er^{3+}.

5.5.3 Neutron Studies of Er_2CrS_4

Powder neutron diffraction data for Er_2CrS_4 were collected at room temperature on the POLARIS diffractometer, ISIS. Data were collected in a manner described in Chapter 2. Data collected on POLARIS used for Rietveld refinement were those from the high-resolution backscattering detector bank (2θ = 145°), 90° bank and the low angle bank. The initial structural model used in the refinement was the orthorhombic model obtained from single crystal X-ray diffraction and described in the space group $P2_1ca$. The refinement using neutron data showed that this model gives a good fit to the data. During the refinement it was necessary to use one thermal parameter for cations and anions to produce a stable refinement. Final observed, calculated and difference powder diffraction profiles of Er_2CrS_4 at room temperature are shown in Figure 104. The refined structural parameters at room temperature are presented in Table 53.

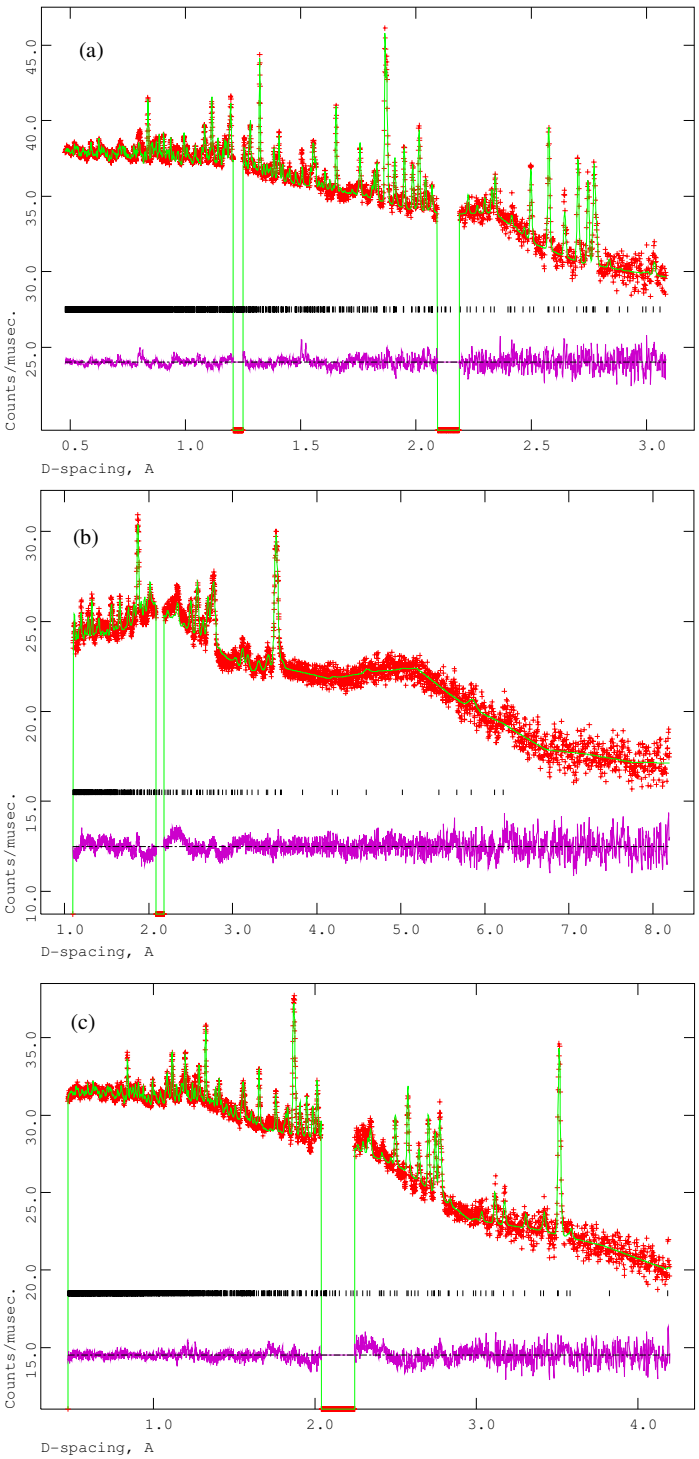

Figure 103: Final, observed (crosses), calculated (upper full line) and difference (lower full line) neutron diffraction profile of $Er_6Cr_2S_{11}$ at 4 K. Data collected on POLARIS at ISIS from (a) backscattering bank (2θ = 145°), (b) low angle bank (2θ = 35°) and (c) 90 degree bank. Vanadium reflections originating from the sample can are excluded.

Table 52: Final refined parameters for $Er_6Cr_2S_{11}$ (space group *Cmcm*)*.

Temperature/K		4	8	14	20	298
a /Å		3.7440(1)	3.7437(1)	3.7437(1)	3.7438(1)	3.7658(1)
b /Å		12.4463(4)	12.4438(5)	12.4458(5)	12.4455(5)	12.5185(2)
c /Å		34.0145(12)	34.0145(17)	34.0183(16)	34.0140(2)	34.2067(8)
M(1)	*y*	0.4892(4)	0.4914(6)	0.4925(5)	0.4908(5)	0.4898(3)
	B/Å^2	0.44(3)	0.91(4)	0.62(3)	0.70(4)	0.87(2)
M(2)	*y*	0.7577(3)	0.7592(4)	0.7606(3)	0.7595(3)	0.7577(2)
	z	0.4376(1)	0.4374(1)	0.4373(1)	0.4371(1)	0.4377(1)
	B/Å^2	0.44(3)	0.91(4)	0.62(3)	0.70(4)	0.87(2)
M(3)	*y*	0.7503(4)	0.7495(6)	0.7490(5)	0.7490(5)	0.7488(3)
	z	0.3170(1)	0.3171(2)	0.3171(2)	0.3170(2)	0.3171(1)
	B/Å^2	0.47(5)	0.96(8)	0.53(7)	0.71(7)	0.79(4)
	SOF(Er)	0.45(-)	0.45(-)	0.45(-)	0.45(-)	0.45(1)
	SOF(Cr)	0.55(-)	0.55(-)	0.55(-)	0.55(-)	0.55(1)
M(4)	*y*	0.5134(4)	0.5117(5)	0.5130(5)	0.5131(4)	0.5137(2)
	z	0.3657(1)	0.3661(2)	0.3658(2)	0.3656(2)	0.3653(1)
	B/Å^2	0.38(5)	0.83(7)	0.81(7)	0.80(7)	0.98(5)
	SOF(Er)	0.60(-)	0.60(-)	0.60(-)	0.60(-)	0.60(1)
	SOF(Cr)	0.40(-)	0.40(-)	0.40(-)	0.40(-)	0.40(1)
M(5)	B/Å^2	0.40(9)	1.56(16)	0.86(17)	1.08(14)	0.82(8)
	SOF(Er)	0.68(-)	0.68(-)	0.68(-)	0.68(-)	0.68(2)
	SOF(Cr)	0.32(-)	0.32(-)	0.32(-)	0.32(-)	0.32(2)
S(1)	*y*	0.6088(8)	0.6108(11)	0.6101(10)	0.6095(10)	0.6034(5)
	z	0.2979(2)	0.2977(3)	0.2982(3)	0.2977(3)	0.2968(2)
	B/Å^2	0.14(3)	0.46(3)	0.28(3)	0.31(4)	0.60(2)
S(2)	*y*	0.3370(11)	0.3368(15)	0.3398(14)	0.3392(14)	0.3384(7)
	B/Å^2	0.14(3)	0.46(3)	0.28(3)	0.31(4)	0.60(2)
S(3)	*y*	0.6615(8)	0.6575(9)	0.6612(9)	0.6598(9)	0.6608(5)
	z	0.3861(3)	0.3900(3)	0.3899(3)	0.3877(3)	0.3868(2)
	B/Å^2	0.14(3)	0.46(3)	0.28(3)	0.31(4)	0.60(2)
S(4)	*y*	0.4102(6)	0.4135(9)	0.4118(8)	0.4120(8)	0.4107(4)
	z	0.4288(2)	0.4308(3)	0.4318(3)	0.4304(3)	0.4326(2)
	B/Å^2	0.14(3)	0.46(3)	0.28(3)	0.31(4)	0.60(2)
S(5)	*y*	0.6500(7)	0.6496(9)	0.6511(9)	0.6499(9)	0.6508(5)
	z	0.4868(2)	0.4868(3)	0.4858(3)	0.4864(3)	0.4848(2)
	B/Å^2	0.14(3)	0.46(3)	0.28(3)	0.31(4)	0.60(2)
S(6)	*y*	0.8925(7)	0.8923(9)	0.8931(8)	0.8921(8)	0.8893(5)
	z	0.3356(2)	0.3349(3)	0.3336(3)	0.3356(3)	0.3350(2)
	B/Å^2	0.14(3)	0.46(3)	0.28(3)	0.31(4)	0.60(2)
R_{wp}/%		0.54	0.66	0.65	0.64	1.17
χ^2		1.35	0.78	0.74	0.79	0.97

* M(1) on 4(*c*), (0, y, ¼); M(2), M(4), S(1), S(4), S(6) on 8(*f*), (½, y, z); M(3), S(3), S(5) on 8(*f*), (0, y, z); M(5) on 4(*a*), (½, ½, ½) and S(2) on 4(*c*), (½, y, ¼).

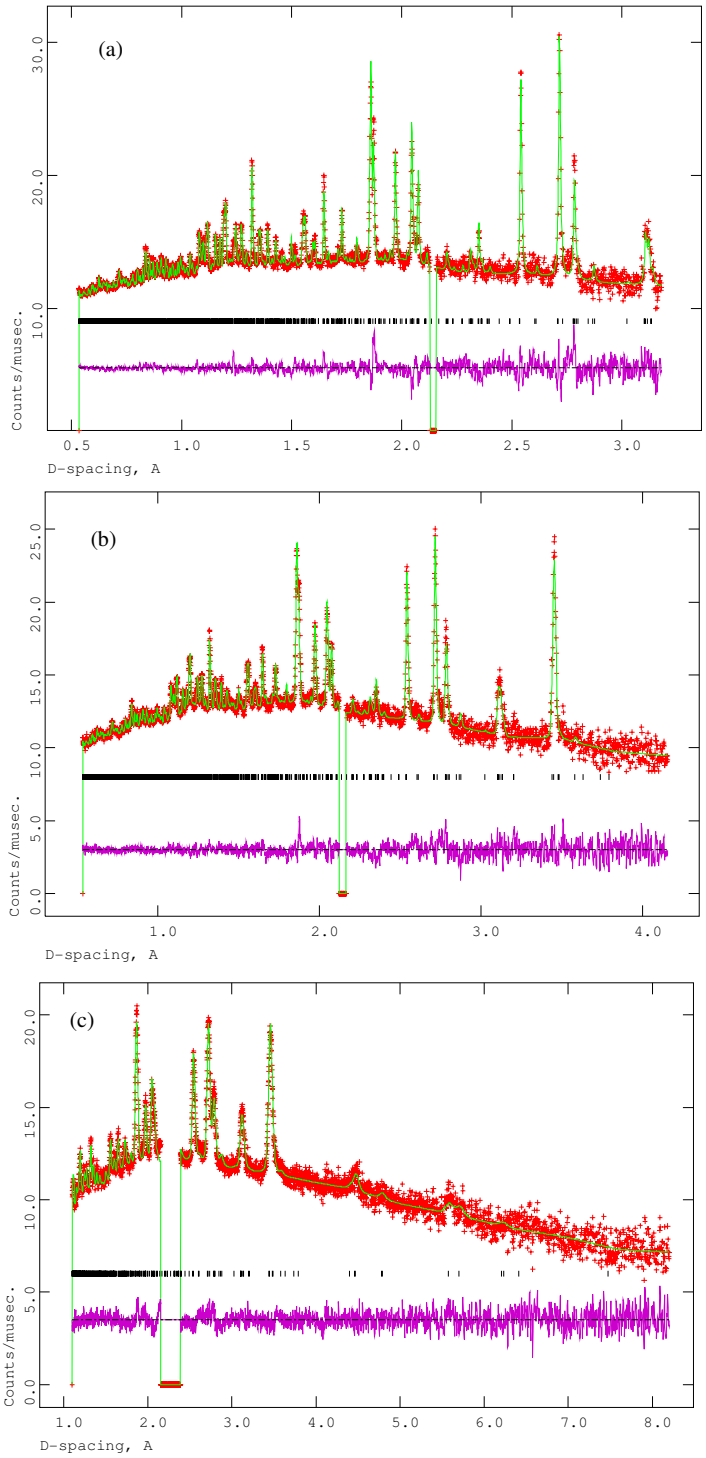

Figure 104: Final, observed (crosses), calculated (upper full line) and difference (lower full line) neutron diffraction profile of the Er_2CrS_4 at 298 K. Data collected on POLARIS from (a) backscattering bank ($2\theta = 145°$), (b) 90 degree bank and (c) low angle bank ($2\theta = 35°$). Reflection positions are marked. The excluded region is due to the presence of a peak from the vanadium sample can.

Table 53: Final refined parameters for Er_2CrS_4 (space group $P2_1ca$)*.

Temperature/K		298 K
a /Å		12.4363(4)
b /Å		7.4820(2)
c /Å		12.4809(3)
Er(1)	*x*	0.5806(3)
	y	0.6381(8)
	z	0.1300(4)
	B/Å^2	0.42(2)
Er(2)	*x*	0.5768(4)
	y	0.1360(8)
	z	0.1403(4)
	B/Å^2	0.42(2)
Er(3)	*x*	0.7489(3)
	y	0.8836(9)
	z	0.3762(3)
	B/Å^2	0.42(2)
Er(4)	*x*	0.8879(3)
	y	0.6199(10)
	z	0.6091(3)
	B/Å^2	0.42(2)
Cr(1)	*x*	0.8637(6)
	y	0.1223(19)
	z	0.6186(7)
	B/Å^2	0.42(2)
Cr(2)	*x*	0.7094(6)
	y	0.3727(18)
	z	0.3720(7)
	B/Å^2	0.42(2)
S(1)	*x*	0.5581(9)
	y	0.8787(25)
	z	0.2886(12)
	B/Å^2	0.42(2)
S(2)	*x*	0.9382(9)
	y	0.8834(29)
	z	0.4688(10)
	B/Å^2	0.42(2)
S(3)	*x*	0.4257(9)
	y	0.3682(27)
	z	0.0408(10)
	B/Å^2	0.42(2)
S(4)	*x*	0.6950(9)
	y	0.6231(26)
	z	0.5092(10)
	B/Å^2	0.42(2)

* All atoms are on 4(*a*), (*x*, *y*, *z*) site.

Table 53: continued

S(5)	*x*	0.7876(9)
	y	0.1449(18)
	z	0.2312(12)
	B/Å^2	0.42(2)
S(6)	*x*	0.8054(9)
	y	0.6374(23)
	z	0.2317(10)
	B/Å^2	0.42(2)
S(7)	*x*	0.6884(9)
	y	0.1072(25)
	z	0.5249(11)
	B/Å^2	0.42(2)
S(7)	*x*	0.5756(9)
	y	0.3872(24)
	z	0.2930(11)
	B/Å^2	0.42(2)
R_{wp}/%	bank 2: $2\theta = 145^o$	1.31
	bank 3: $2\theta = 35^o$	2.78
	bank 1: $2\theta = 90^o$	1.67
χ^2		1.09

5.5.4 Magnetic Structure Determination of Er_3CrS_6

Neutron diffraction studies were performed on the Er_3CrS_6 sample over the temperature range $2 \leq T/K \leq 298$ using the POLARIS and OSIRIS diffractometers in order to determine the magnetic structure and the thermal evolution of magnetic structure. Data were collected as described in Chapter 2. Data with better statistics were collected over a longer period at 2, 20, 36 and 298 K on POLARIS and at 4, 20, 55 and 298 K on OSIRIS. Diffraction data collected on POLARIS from the high-resolution backscattering detector bank ($2\theta = 145°$), 90° bank and the low angle bank were used for Rietveld refinement. Data from OSIRIS were collected in eight time windows, which were then combined to produce diffraction patterns suitable for input into Rietveld refinement. The initial structural model used for Rietveld refinement was the orthorhombic model obtained from single crystal study and described in the space group *Pnnm*. This model fits very well the data collected at room temperature. Final observed, calculated and difference powder diffraction profiles of Er_3CrS_6 at room temperature are shown in Figure 105.

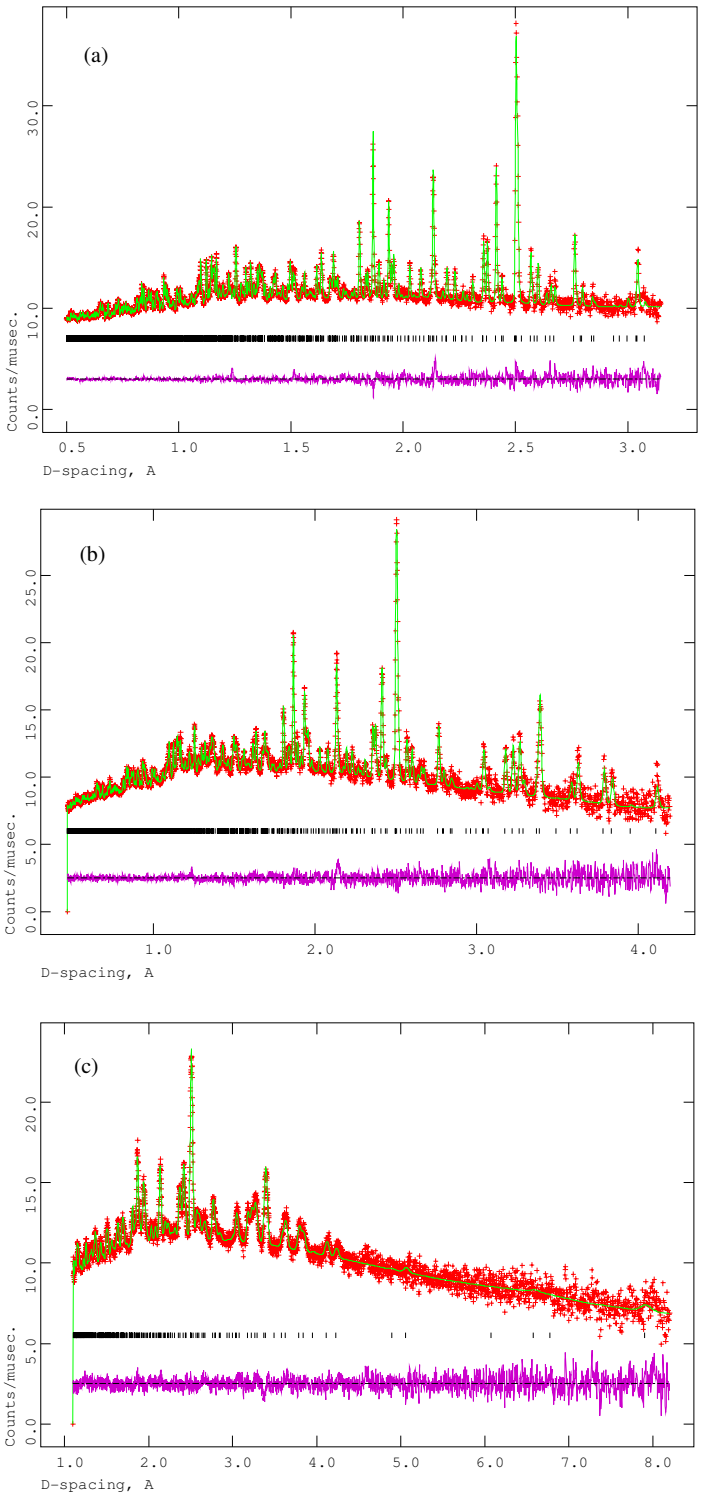

Figure 105: Final, observed (crosses), calculated (upper full line) and difference (lower full line) neutron diffraction profile of the Er_3CrS_6 at 298 K. Data collected on POLARIS from (a) backscattering bank ($2\theta = 145°$), (b) 90 degree bank and (c) low angle bank ($2\theta = 35°$). Reflection positions are marked.

The refined structure at room temperature was used as a trial model for analysis of the data collected at 2 K on POLARIS. However, low temperature neutron diffraction data for Er_3CrS_6 revealed several additional Bragg peaks which are not present in the data collected at room temperature. These reflections are magnetic in origin and they can be indexed on the same crystallographic unit cell. This indicates that the magnetic propagation vector **k** = (0, 0, 0). Under this condition, the possible magnetic structures were calculated by the representation analysis technique using program SARAh [238]. Information that is required for these calculations are the propagation vector **k**, the crystallographic space group and the atomic coordinates of the magnetic atoms before the magnetic phase transition. Representational analysis leads to the irreducible magnetic representation:

4(*g*) site [(Er(1)-Er(3)]

$$\Gamma_{mag} = \Gamma_1 + 2\Gamma_2 + 2\Gamma_3 + \Gamma_4 + 2\Gamma_5 + \Gamma_6 + \Gamma_7 + 2\Gamma_8$$

while that of a 2(*a*) site [Cr(1)] and 2(*c*) site [Cr(2)] is:

$$\Gamma_{mag} = \Gamma_1 + 2\Gamma_3 + 2\Gamma_5 + \Gamma_7$$

For the t_{2g}^3 configuration of Cr^{3+}, the 90° d_π–p_π/p_σ–d_σ interaction is predicted to be ferromagnetic. It was thus assumed that chromium orders ferromagnetically within the chains, reducing number of possibilities. Only Γ_3, Γ_5 and Γ_7 on erbium permit this assumption.

There are five magnetic ions in the crystallographic unit cell; three erbium ions, Er(1), Er(2) and Er(3), all of them occupying 4(*g*) site and two crystallographically-distinct chromium ions, Cr(1) and Cr(2), occupying 2(*a*) and 2(*c*) positions of the orthorhombic space group *Pnnm*. It means that there are 16 magnetic atoms in the magnetic unit cell. The moments of erbium ions associated with a given Wyckoff site can be denoted $\mathbf{S_1}$, $\mathbf{S_2}$, $\mathbf{S_3}$ and $\mathbf{S_4}$, and four types of magnetic arrangements are possible (Table 54), while chromium ions with magnetic moments $\mathbf{S_5}$ and $\mathbf{S_6}$ have two possible magnetic arrangements.

Table 54: Basis vectors spanned by each of the irreducible representations of the little group G_k [239].

Irreducible representation	Basis vectors	
	4(*g*) site	2(*a*) and 2(*c*) sites
Γ_3	F_x, A_y	F_x', G_y'
Γ_5	A_x, F_y	G_x', F_y'
Γ_7	F_z	-
	$F = \mathbf{S_1} + \mathbf{S_2} + \mathbf{S_3} + \mathbf{S_4}$	
	$G = \mathbf{S_1} - \mathbf{S_2} + \mathbf{S_3} - \mathbf{S_4}$	$F' = \mathbf{S_5} + \mathbf{S_6}$
	$C = \mathbf{S_1} + \mathbf{S_2} - \mathbf{S_3} - \mathbf{S_4}$	$G' = \mathbf{S_5} - \mathbf{S_6}$
	$A = \mathbf{S_1} - \mathbf{S_2} - \mathbf{S_3} + \mathbf{S_4}$	

Calculations using program SARAh-Refine [238] indicated that $\Gamma_3(F_x)$ on Er(1), $\Gamma_3(F_x, A_y)$ on Er(3) and $\Gamma_7(F_z)$ on Er(2) offered the best agreement with observed data. In this structure, magnetic moments of all chromium ions order ferromagnetically in the *x* direction and they have antiferromagnetic *y* component. All subsequent refinements of the magnetic structure were based on this solution. The magnetic phase described in the space group *P1* was introduced as a second phase into GSAS [189] and the free-ion form factors [240] for Cr^{3+} and Er^{3+} were used to describe the wavelength dependence of the magnetic scattering. The unit cell parameters and the thermal parameters in the magnetic phase were constrained to be identical with those of the crystallographic phase. An overall thermal parameter for cations and for anions was used. It was assumed that the ordered magnetic moments of chromium ions at the two sets of 2(*a*) and 2(*c*) sites had the same magnitude and they were constrained to be equal. The magnetic moments of erbium ions for each magnetic sub-lattice were also constrained to be equal before the refinement and allowed to vary independently of the other sub-lattices giving the magnetic structure shown in Figure 106. Final observed, calculated and difference profiles of the neutron data collected at 2 K are presented in Figure 107. The magnetic structure of Er_3CrS_6 at 2K is a non-collinear magnetic structure. In this structure one of the Er moments is directed perpendicular to the other two.

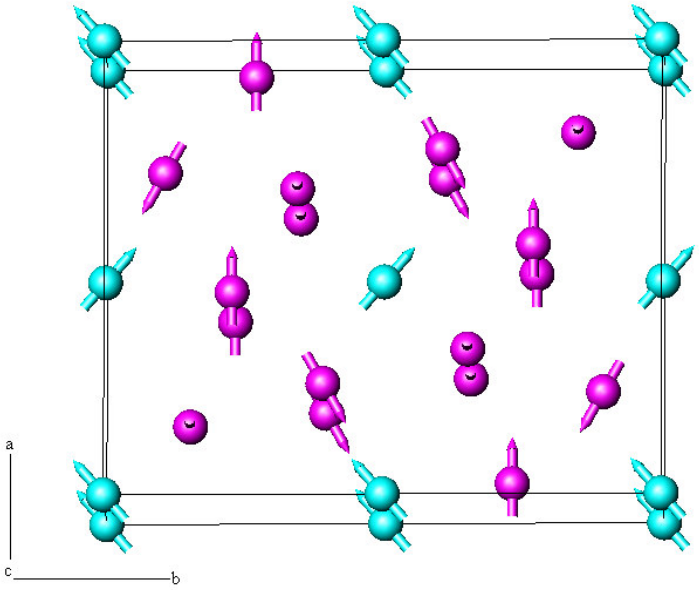

Figure 106: The magnetic structure of Er_3CrS_6 at 2 K. (*Key*: erbium atoms are represented by magenta circles and chromium atoms by cyan circles. Sulphide anions are omitted for clarity.

The patterns collected on POLARIS at 20 and 36 K suggested that there is an impurity phase. The reflections of the impurity phases were observed at the different *d*-spacing in the patterns collected at 20 and 36 K (Figure 108). However, no extra reflections due to impurities were observed in the neutron data collected on OSIRIS. Close examination of these peaks suggest that they are due to coating of solid nitrogen on the walls of the cryostat sample chamber caused by a small leak on the centre stick seal allowing air into the sample space. The nitrogen in the air then froze solid and gave a diffraction pattern. Nitrogen exhibits phase transition from α- do β- modification at 36 K [241] and this is the reason why the extra reflections are observed at different *d*-spacing in the patterns collected at 20 and 36 K. Moreover, the reflections are shifted from the expected *d*-spacing because solid nitrogen was not at the sample position. The different flight paths and scattering angles when compared to the sample position itself mean that the *d*-spacing occurs at the "wrong" time of flight. The data collected at 20 K were those from OSIRIS (Figure 109) while in the refinement of the data collected at 36 K on POLARIS, the nitrogen was introduced as an impurity phase. A full set of observed, calculated and difference profiles from both POLARIS and OSIRIS diffractometers at the remaining temperature collections may be found in Appendix 5.2.

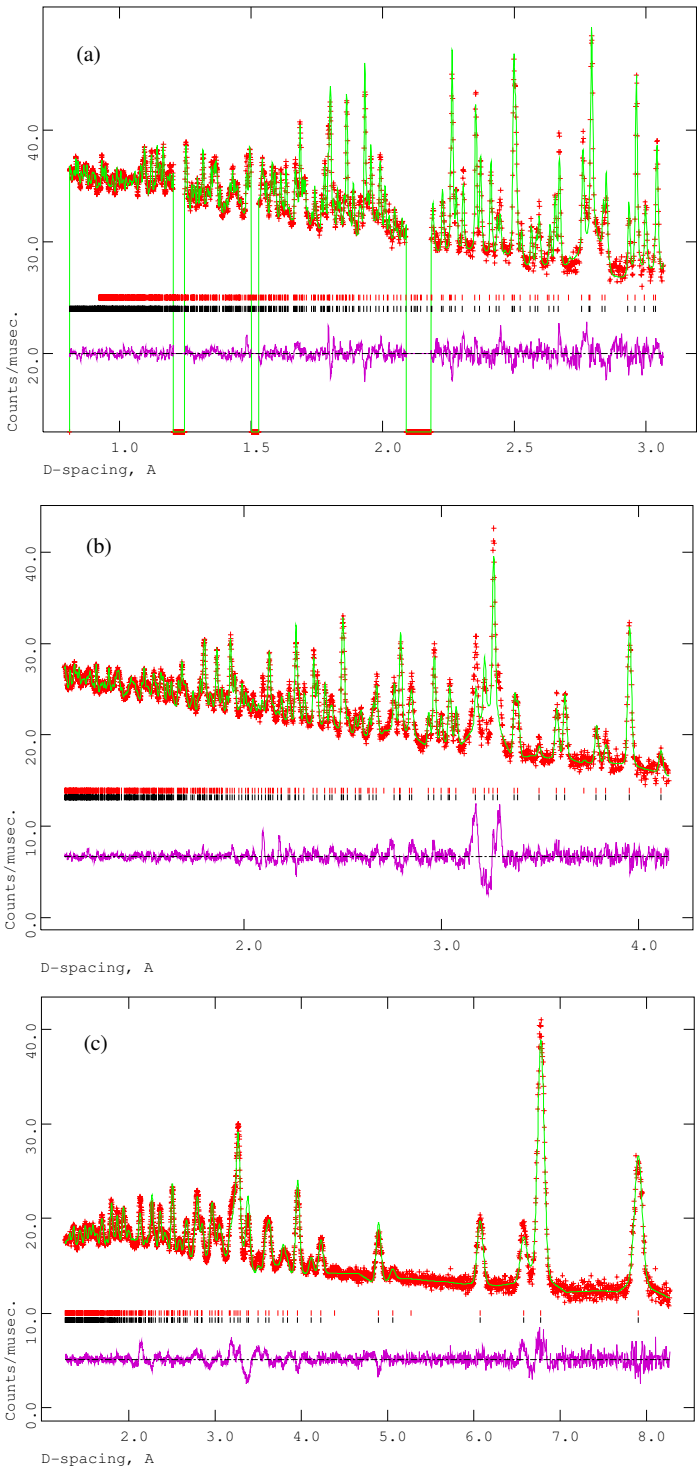

Figure 107: Final, observed (crosses), calculated (upper full line) and difference (lower full line) neutron diffraction profile of the Er_3CrS_6 at 2 K. Data collected on POLARIS from (a) backscattering bank (2θ = 145°), (b) 90 degree bank and (c) low angle bank (2θ = 35°). Reflection positions are marked. The lower markers refer to the crystallographic unit cell and the upper markers to the magnetic unit cell described in the space group *P1*. Vanadium reflections originating from the sample can are excluded.

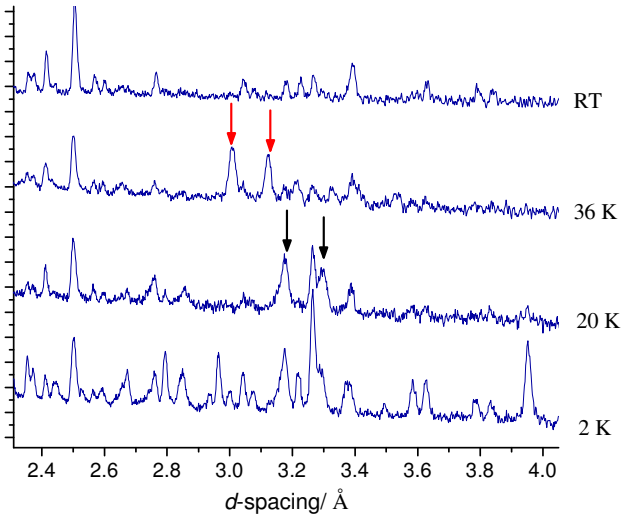

Figure 108: Powder neutron patterns collected on POLARIS. (*Key*: red arrows illustrate the extra reflections at 3.01 and 3.12 Å which are due to β-N_2 phase and black arrows at 3.18 and 3.29 Å due to α-N_2 phase.

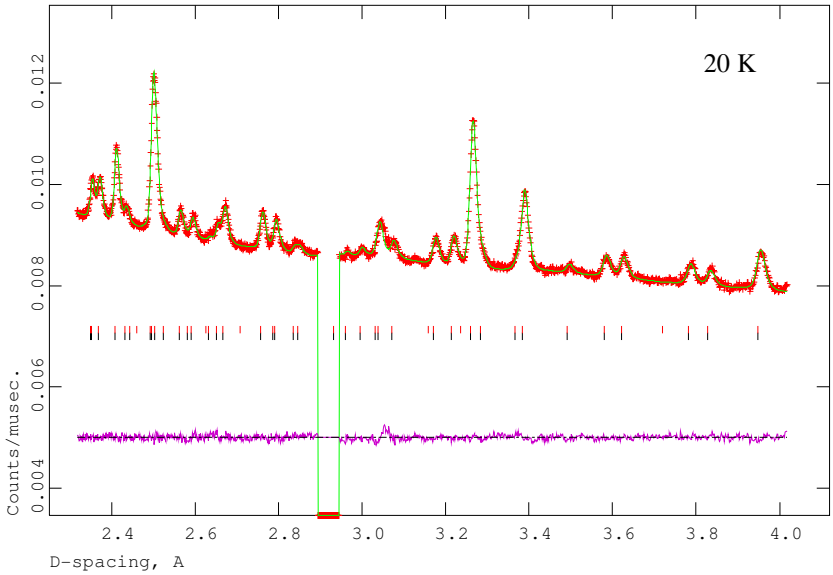

Figure 109: Final, observed (crosses), calculated (upper full line) and difference (lower full line) neutron diffraction profile of Er_3CrS_6 at 20 K. Data collected on the OSIRIS diffractometer. Reflection positions are marked. The lower markers refer to the crystallographic unit cell and the upper markers to the magnetic unit cell described in the space group *P1*. A reflection originating from the instrument was excluded.

The structural parameters determined at 2 K using POLARIS data were used for the trial nuclear and magnetic structures for the analysis of the data collected on OSIRIS. The refinement procedure was similar to that applied to the analysis of the POLARIS data, with the exception of the simultaneous use of data from three detector banks in Rietveld refinement. The refined magnetic structure using data collected at 4 K on OSIRIS is in agreement to that determined at 2 K, with slightly reduced magnetic moments. The results of Rietveld refinement of the neutron data are presented in Table 55. The refinements of neutron data revealed that the unit cell parameters increase with increasing temperature.

5.6 Discussion

Single-crystal X-ray diffraction reveals that Er_3CrS_6 adopts the U_3ScS_6-type structure [181], with complete ordering of Cr^{3+} cations into the octahedral sites. It appears likely on the basis of powder X-ray diffraction data that other sulphides of stoichiometry Ln_3CrS_6 (Ln = La – Lu) [177] are isostructural, although determination of the degree of Ln^{3+}/Cr^{3+} ordering requires detailed structural measurements. While isostructural phases containing other transition metals have not been reported, it is possible to substitute chromium by indium, to form the closely related Ln_3InS_6 (Ln = Sm to Tb) phases [242, 243].

Although the intra-chain Cr–Cr distances in the structure of Er_3CrS_6 are considerably shorter at 3.733 Å, this is significantly greater than the critical distance (R_c ≈ 3.1 Å) [244] below which a direct t_{2g}–t_{2g} interaction could occur. Intra-chain magnetic exchange is therefore through a 90° superexchange interaction *via* an intervening sulphide anion. For the t_{2g}^3 configuration of Cr^{3+}, the 90° d_π–p_π/p_σ–d_σ interaction is predicted to be ferromagnetic [244]. This suggests that the magnetic transition that occurs at 30 K involves ferromagnetic ordering of the chromium ions within the CrS_2^- chains. Rietveld refinement using neutron data revealed that chromium ions order ferromagnetically along [100]. The magnetic moment of chromium ion at 20 K is equal to 2.22(6) μ_B and 0.9(2) μ_B at 36 K. However, at these temperatures still Er(1) orders ferromagnetically in the *x* direction at the 4(*g*) site, while Er(2) and Er(3) at 4(*g*) site are not magnetically ordered. On further cooling, the weaker interactions associated with the rare-earth ions become significant. The second anomaly in magnetic data at 11 K may therefore be associated with ordering of the erbium sub-lattice. Neutron data show that all of the

Table 55: Final refined parameters for Er_3CrS_6 (space group *Pnnm*)*.

Temperature/K		**2**	**4**	**20**	**36**	**55**	**298**
Diffractometer		POLARIS	OSIRIS	OSIRIS	POLARIS	OSIRIS	POLARIS
a/Å		13.1414(2)	13.1411(1)	13.1427(2)	13.1432(3)	13.1436(3)	13.1727(2)
b/Å		15.8023(3)	15.8019(2)	15.8046(4)	15.8054(4)	15.8060(5)	15.8225(3)
c/Å		3.7230(0)	3.7230(0)	3.7230(0)	3.72304(1)	3.72305(1)	3.7269(1)
Er(1)	*x*	0.5508(4)	0.5491(11)	0.5523(10)	0.5491(4)	0.5519(9)	0.5497(1)
	y	0.2176(4)	0.2208(11)	0.2230(9)	0.2222(3)	0.2206(7)	0.2207(1)
	μ_x	-9.01(5)	-8.64(4)	-5.31(4)	-2.52(14)	-0.9(2)	0
	μ_y	0	0	0	0	0	0
	μ_z	0	0	0	0	0	0
	Moment/μ_B	9.01(5)	8.64(4)	5.31(4)	2.52(14)	0.9(2)	0
	B/Å^2	1.10(3)	0.4(2)	0.69(13)	0.99(2)	0.45(14)	0.47(1)
Er(2)	*x*	0.3200(4)	0.3114(13)	0.3117(10)	0.3212(3)	0.3128(9)	0.3189(1)
	y	0.3523(3)	0.3510(8)	0.3538(6)	0.3535(2)	0.3551(6)	0.3521(1)
	μ_x	0	0	0	0	0	0
	μ_y	0	0	0	0	0	0
	μ_z	-8.72(4)	-8.05(5)	0	0	0	0
	Moment/μ_B	8.72(4)	8.05(4)	0	0	0	0
	B/Å^2	1.10(3)	0.4(2)	0.69(13)	0.99(2)	0.45(14)	0.47(1)
Er(3)	*x*	0.2534(4)	0.2593(15)	0.2621(11)	0.2567(3)	0.2641(10)	0.2561(1)
	y	0.0982(4)	0.0963(9)	0.0988(7)	0.0976(3)	0.0959(6)	0.0992(1)
	μ_x	6.18(4)	3.44(5)	0	0	0	0
	μ_y	-2.99(9)	-1.84(11)	0	0	0	0
	μ_z	0	0	0	0	0	0
	Moment/μ_B	6.864(6)	3.91(7)	0	0	0	0

* Er(1), Er(2), S(1), S(5) on 4(*g*), (*x*, *y*, 0); Er(3), S(2), S(3), S(4), S(6) on 4(*g*) (*x*, *y*, ½); Cr(1) on 2(*a*) (½, ½, ½) and Cr(2) on 2(*c*) (½, 0, ½).

Table 55: continued

	B/Å^2	1.10(3)	0.4(2)	0.69(13)	0.99(2)	0.45(14)	0.47(1)
Cr(1)	μ_x	-2.22(5)	-1.97(4)	-2.22(6)	-0.9(2)	0	0
	μ_y	0.67(11)	0	0	0	0	0
	μ_z	0	0	0	0	0	0
	Moment/μ_B	2.32(6)	1.97(4)	2.22(6)	0.9(2)	0	0
	B/Å^2	1.10(3)	0.4(2)	0.69(13)	0.99(2)	0.45(14)	0.47(1)
Cr(2)	μ_x	-2.22(5)	-1.97(4)	-2.22(6)	-0.9(2)	0	0
	μ_y	-0.67(11)	0	0	0	0	0
	μ_z	0	0	0	0	0	0
	Moment/μ_B	2.32(6)	1.97(4)	2.22(6)	0.9(2)	0	0
	B/Å^2	1.10(3)	0.4(2)	0.69(13)	0.99(2)	0.45(14)	0.47(1)
S(1)	x	0.4191(10)	0.430(4)	0.4133(28)	0.4234(9)	0.4151(23)	0.4148(2)
	y	0.0873(9)	0.0882(21)	0.0858(18)	0.0768(9)	0.0817(16)	0.0769(2)
	B/Å^2	0.70(6)	0.4(2)	0.69(13)	0.99(2)	0.45(14)	0.27(2)
S(2)	x	0.6190(11)	0.5963(25)	0.6125(25)	0.6199(10)	0.6094(21)	0.6216(3)
	y	0.1040(9)	0.1111(31)	0.1132(23)	0.1081(8)	0.1142(18)	0.1096(2)
	B/Å^2	0.70(6)	0.4(2)	0.69(13)	0.99(2)	0.45(14)	0.27(2)
S(3)	x	0.6900(12)	0.6844(33)	0.6709(34)	0.6790(11)	0.6660(26)	0.6858(3)
	y	0.2733(9)	0.2876(27)	0.2869(22)	0.2940(7)	0.2797(16)	0.2897(2)
	B/Å^2	0.70(6)	0.4(2)	0.69(13)	0.99(2)	0.45(14)	0.27(2)
S(4)	x	0.4059(11)	0.3804(34)	0.3949(32)	0.3936(10)	0.4109(30)	0.3960(2)
	y	0.2561(9)	0.2367(32)	0.2507(27)	0.2463(8)	0.2479(21)	0.2468(2)
	B/Å^2	0.70(6)	0.4(2)	0.69(13)	0.99(2)	0.45(14)	0.27(2)
S(5)	x	0.5293(10)	0.487(4)	0.4929(30)	0.5167(9)	0.4993(27)	0.5222(2)
	y	0.4077(10)	0.383(5)	0.375(4)	0.3973(9)	0.3794(26)	0.4014(2)
	B/Å^2	0.70(6)	0.4(2)	0.69(13)	0.99(2)	0.45(14)	0.27(2)

Table 55: continued

S(6)	*x*	0.3183(13)	0.3101(34)	0.3138(24)	0.3183(12)	0.3095(21)	0.3178(3)
	y	0.4770(8)	0.4825(30)	0.4792(21)	0.4798(7)	0.4706(16)	0.4787(2)
	B/Å^2	0.70(6)	0.4(2)	0.69(13)	0.99(2)	0.45(14)	0.27(2)
R_{wp}/%[††]	bank 2: $2\theta = 145^o$	0.94	0.65	0.55	0.81	0.54	1.15
	bank 3: $2\theta = 35^o$	2.75			2.00		2.64
	bank 1: $2\theta = 90^o$	1.79			1.25		1.66
χ^2		2.88	-	-	1.62	-	0.84

[††] Data from OSIRIS were collected in eight time windows, which were then combined to one produce diffraction patterns suitable for input into Rietveld refinement.

most intense magnetic reflections disappear above 12 K (Figure 110), suggesting that this feature is related to magnetic ordering of the Er^{3+} sub-lattice. Weaker reflections remain to *ca.* 30 K. Moreover, Rietveld refinement using neutron data collected at 55 K revealed that there are still very weak magnetic moments (0.9(2) μ_B) on Er(1) at 4(*g*) site (Table 55). The saturation moment of 7.97(9) μ_B per formula unit at 5 K suggests that it arises from a single uncompensated erbium moment, for which the free-ion value, $g_J J = 9\ \mu_B$. This would require the two crystallographically-distinct ferromagnetic chains of chromium-centred octahedra to be antiferromagnetically coupled and the moments associated with one of the erbium sub-lattices to be anti-parallel to that of the other two. Neutron diffraction measurements carried out on POLARIS and OSIRIS showed that the magnetic structure of Er_3CrS_6 at low temperatures is a complex non-collinear magnetically ordered structure. The observation of a spontaneous magnetisation for Er_3CrS_6 at 5 K is consistent with the complex magnetically-ordered structure determined by powder neutron diffraction.

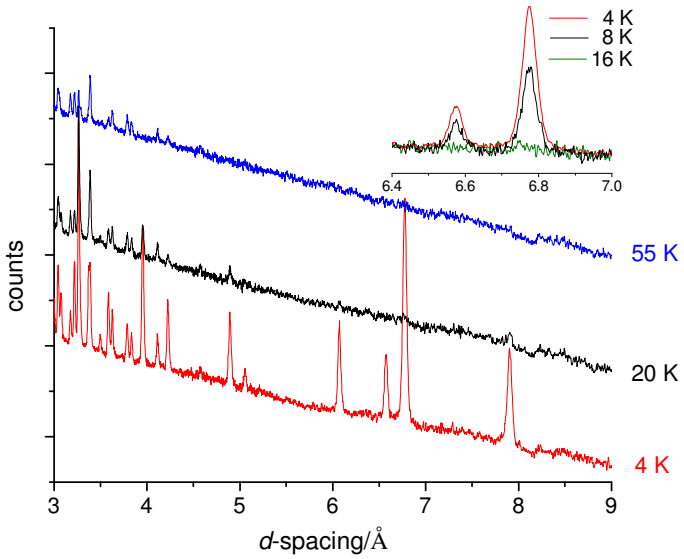

Figure 110: Neutron diffraction patterns of Er_3CrS_6. Data collected on OSIRIS diffractometer.

The structures of the remaining erbium-chromium sulphides; Er_4CrS_7, Er_2CrS_4, $Er_6Cr_2S_{11}$ and the new $Er_8Cr_3S_{15}$ phase investigated in this work are closely related. Structural relationships of ternary sulphides within the MnS – Er_2S_3 and MnS – Y_2S_3 pseudo-binary systems [170, 173] have previously been formulated on the basis of chemical twinning, [245] in which a homologous series of phases may be generated

from a parent rock-salt type structure through repeated reflection twinning on the {113} planes [245, 246]. It has been proposed that this description could also be applied to describe ternary phases within the Er–Cr–S system [231]. However, identification of a common building block on the basis of the crystallographic studies performed in this work, shows that the structures of these materials may be better considered as arising from these blocks.

$Er_8Cr_3S_{15}$ is a new material with three M_2S_5 slabs. The presence of M_2S_5 slabs of variable thickness in the structures of each of the ternary phases, Er_2CrS_4, $Er_6Cr_2S_{11}$, Er_4CrS_7 and $Er_8Cr_3S_{15}$ suggests a common description can be applied to the structure of these materials. The slabs provide a structural component, $[M_{2n}S_{4n+1}]$. This unit shares terminal sulphide ions with MS_4 chains of edge-linked octahedra, to generate an anionic framework that may be expressed by the general formula, $[M_{2n+1}S_{4n+3}]^{x-}$, where the charge is determined by the oxidation state of chromium and the Ln/Cr ratio within the framework. The charge balance is provided by additional rare-earth cations which reside at sites of higher coordination number within one-dimensional channels defined by the framework. The anionic network of Er_4CrS_7, $Er_6Cr_2S_{11}$ and $Er_8Cr_3S_{15}$ can thus be considered the n = 1, n = 2 and n = 3 members of a homologous series, whilst Er_2CrS_4 in which the single octahedral chains are absent is the n = ∞ end-member of this family.

The structure of Er_2CrS_4 is related to that of $CaTi_2O_4$ (*Cmcm*) [247] and its Jahn-Teller distorted variant, $CaMn_2O_4$ (*Pbcm*) [248]. On the basis of powder X-ray diffraction, it has been suggested that materials Ln_2MS_4 (Ln = Tb – Tm; M = Mg, Mn, Fe) [151] adopt a structure described in the space group *Cmcm,* which is closely related to that of $CaTi_2O_4$. A subsequent single-crystal diffraction study on non-stoichiometric Yb_2MnS_4 confirms this close-relationship, although led to the description of the structure in the space group $Cmc2_1$ [158]. In contrast with the Ln_2MnS_4 structures, in which the rare-earth and the transition-metal atoms are disordered over all the available octahedral sites, in Er_2CrS_4 ordering of erbium and chromium atoms results in a doubling of the *b*-axis, together with a lowering of the symmetry to $P2_1ca$. A similar enlargement of the unit cell has been identified, from powder X-ray diffraction data, for other Ln_2CrS_4 (Ln = Y, Ho, Tm, Yb) phases [154], suggesting that they are isostructural with Er_2CrS_4. This is supported by a recent powder neutron diffraction study on Y_2CrS_4 [155]. Single crystal X-ray diffraction data collected in this work revealed that Er_2CrS_4 crystallises in the orthorhombic system with a space group $P2_1ca$. The refinement

using neutron data collected at 298 K showed that this model gives a good fit to the data.

The M_2S_5 slab of metal-centred octahedra is also encountered in the structure of Er_4CrS_7, which is isostructural with the binary sulphides Ln_5S_7 [161, 235]. Refinements using powder neutron diffraction data give a composition of the slab $(Er_{0.65}Cr_{0.35})_2S_5^{4.7-}$ which is in good agreement with that obtained from single crystal X-ray diffraction ($(Er_{0.60}Cr_{0.40})_2S_5^{4.8-}$). These refinements show that ca. 80 % of the octahedra in the single-octahedral chains contain erbium cations. The distribution of rare-earth and transition-metal cations is similar to that in the isostructural Y_4FeS_7 [161, 162] and Ho_4FeS_7 [162], the only two examples of this structure type for which detailed structural characterisation has been performed to date.

The $Er_6Cr_2S_{11}$ structure is analogous to that of the binary sulphide Tm_8S_{11} [249], whilst the degree of disorder of Er^{3+} and Cr^{2+} over the octahedral sites is similar to that of Yb^{3+} and Fe^{2+} in $Yb_6Fe_2S_{11}$ [175]. It seems that Ln_8S_{11} stoichiometry has not been observed for any other binary rare-earth sulphide, the lattice parameters of the ternary compounds $Ln_6Mn_2S_{11}$ (Ln = Y, Er) [170, 173] and $Yb_6Mg_2S_{11}$ [171] determined by electron diffraction, suggest they crystallise in the same structural type. Whilst the synthesis of the ternary chromium sulphides $Ln_6Cr_2S_{11}$ (Ln = Gd, Tb, Ho), has been described [173], structural characterisation is yet to be performed.

The magnetic properties of the n = l, 2, and ∞ members of this family of ternary phases show significant variation, which can be related to the detailed structure and, in particular, degree of cation ordering. The paramagnetism of Er_4CrS_7 may be traced to the disorder of Er^{3+} and Cr^{2+} over sites in the $Er_3CrS_7^{3-}$ framework. In particular the occupancy of only 40 % of the sites in the slab by Cr^{2+} ions may be sufficient to prevent a long-range magnetic exchange pathway from being established. By contrast, in $Er_6Cr_2S_{11}$ where the fraction of octahedral sites in the double slab is only marginally higher at 42 %, the degree of coverage appears to exceed the percolation threshold for this topology and ordering of Cr^{2+} cations appears to occur at low temperatures. Further evidence for long-range order below 11.4 K in $Er_6Cr_2S_{11}$ is provided by powder neutron diffraction data collected at 4, 8 and 14 K, which reveal that weak reflections present in the 4 K data at 3.14 and 3.17 Å disappear on heating through the temperature of the maximum in χ(T).

The complete Cr^{2+}/Er^{3+} ordering that occurs in Er_2CrS_4 results in a zig-zag magnetic exchange pathway between Cr(l) and Cr(2) ions within the double chains of octahedra that constitute the $ErCrS_4^{3-}$ slab (Figure 111). These interactions are *via*

intervening sulphide anions and are of the 180° superexchange type, involving long and short Cr-S bonds on either side of the anion. The magnitude of the Jahn-Teller distortion ($d_{ax}/d_{eq} \approx 1.14$), suggests that the e_g electron density of Cr^{2+} is located in dz^2 orbitals. Therefore exchange between Cr(5) and Cr(6) occurs through overlap of a filled dz^2 and empty dx^2-y^2 with the *p*-orbital of a sulphide anion. The σ-interaction is predicted to be ferromagnetic in origin, with a moderate antiferromagnetic π-component [244]. There are additional intra-slab 90° antiferromagnetic d_σ-p_σ/p_π-d_π superexchange interactions between chromium ions located in adjacent double chains. These predictions suggest that within the $ErCrS_5^{5-}$ slab, chromium ions within a given octahedral chain should be ferromagnetically ordered along the [010] direction, with antiferromagnetic coupling between adjacent chains within the double chain. The double chains would in turn be antiferromagnetically coupled. Inter-slab interactions between chromium cations occur *via* the erbium-centred octahedra and are therefore likely to be weaker in strength. An attempt to solve a magnetic structure of Er_2CrS_4 to confirm this proposed model should be performed.

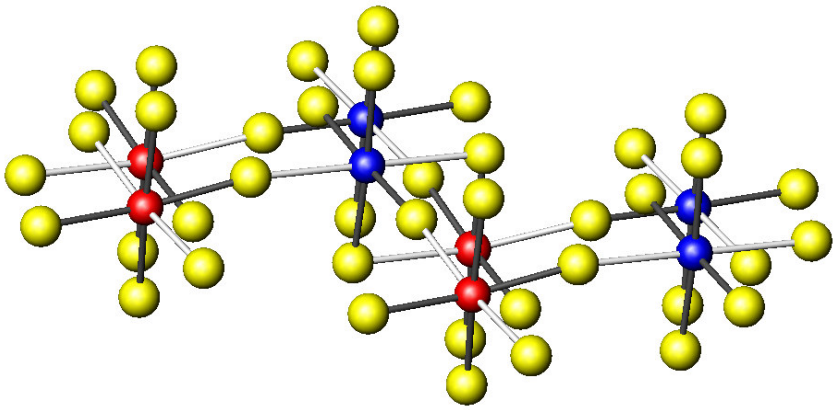

Figure 111: The magnetic exchange pathway due to Er^{3+}/Cr^{2+} ordering in the octahedral framework of Er_2CrS_4. Red circles represent Cr(5), blue circles Cr(6) and yellow circles sulphur. Erbium cations are omitted for clarity. Short and long Cr-S distances are indicated respectively by filled and unfilled bonds.

The results in parts presented in this Chapter have been accepted for publication in Inorganic Chemistry.

Chapter 6: Conclusions and Suggestions for Further Work

During this study a diverse range of materials have been studied using a variety of synthetic and analytical techniques.

The phases which are formed in metal oxide systems are interesting not only for research but also for industrial purposes. The most promising are systems containing Bi_2O_3, V_2O_5 and MO, where M is a transition metal. It is known that bismuth-containing oxides exhibit interesting properties such as high oxygen ion conductivity, they are bright yellow pigments and selective oxidation catalysts [51-53]. This is the reason why they are worth of study.

In this work the diagrams of phase relations have been worked out for three systems ZnO – $BiVO_4$, $Pb_2V_2O_7$ – $BiVO_4$ and PbO – $BiVO_4$ over the whole component concentration range up to 1273 K. Two new compounds have been synthesised in these systems: $BiZn_2VO_6$ and $Pb_2BiV_3O_{11}$. Both of them were obtained as a result of solid state reaction between appropriate oxides mixed at stoichiometric quantities. The results of this work showed that bismuth forms with zinc a compound which belongs to BiA_2MO_6 family. The diffractogram of $BiZn_2VO_6$ did not show either any similarity to the diffractograms of other BiA_2MO_6-type phases, where A = divalent cation, M = pentavalent cation. It can be concluded that a new compound was obtained with its formula $BiZn_2VO_6$. However, this compound is not isostructural with other compounds of the type BiA_2MO_6 described in the literature.

$Pb_2BiV_3O_{11}$ is a new compound which belongs to the $M^{II}_2M^{III}V_3O_{11}$ family of materials. It has been shown that $Pb_2BiV_3O_{11}$ is not isostructural with the compounds of the general formula $M^{II}_2BiV_3O_{11}$. Furthermore, it can be concluded that a sample which corresponds to the composition of the compound $Pb_6Bi_2V_8O_{29}$ reported in work [69] is a mixture of $Pb_2V_2O_7$ and $Pb_2BiV_3O_{11}$ phases.

A new family of defect thiospinels $Ga_{1-x}Ge_xV_4S_8$ ($0 \leq x \leq 1$) has been prepared and characterised. *A*-site substitution in this series has been used to tune the electron count associated with the vanadium-sulphur cluster. Powder X-ray diffraction data for $Ga_{1-x}Ge_xV_4S_8$ reveal solid solution behaviour over the range $0 \leq x \leq 1$. Substitution markedly changes the electrical properties. The results demonstrate that the electrical transport properties are a sensitive function of the electron count, which is consistent

with previous suggestions that it is narrow band states arising from V-V interactions within the cluster which principally determine the physical properties. All materials show an appreciable sulphur deficiency. In this work it has been shown that properties of defect thiospinels are strongly influenced by this deficiency.

Erbium-chromium sulphides have been synthesised and characterised using X-ray and neutron diffraction and SQUID magnetometry. It has been demonstrated that the magnetic properties of erbium chromium sulphides are influenced by the degree of rare-earth/transition-metal ordering. In particular on cooling, successive transitions associated with the chromium and erbium sub-lattices are observed in Er_3CrS_6 and Er_2CrS_4 in which cation ordering is complete, suggesting an interaction between the *d*- and *f*-electrons of the two types of cation. The cation-disordered phase $Er_6Cr_2S_{11}$ shows magnetic ordering of the chromium sub-lattice only. Significantly, it has been shown by single-crystal X-ray diffraction that the structures of Er_2CrS_4, Er_4CrS_7, $Er_6Cr_2S_{11}$ and the new $Er_8Cr_3S_{15}$ phase may be described in terms of a common building block (Figure 112). This suggests that synthesis of new members of this family of materials, containing thicker slabs of octahedra, may be possible. Variable thickness layers are common for instance in perovskites. There exist a number of layered perovskites which can be identified as Aurivillius ($(Bi_2O_2)(A_{n-1}B_nO_{3n+1})$) [250-252], Ruddlesden-Popper ($(A_2[A_{n-1}'B_nO_{3n+1}])$ [253, 254] and Dion-Jacobson ($(A[A_{n-1}'B_nO_{3n+1}))$ [255, 256] phases, where A - alkali metal, A' - alkaline earth and B - transition metal. They consist of infinite perovskite 2D slabs which are separated by some motif. In the Ruddlesden-Popper phases the perovskite layers are separated by an individual AO rock-salt layer. The separating motif for the Aurivillius phases is a Bi_2O_2 layer. Dion-Jacobson phases differ from the other layered phases by having a layer of alkali metal as the separating motif. The layered perovskites are of special interest in view of the possibility of carrying out interesting interlayer chemistry between the perovskite slabs.

Linkage of M_2S_5 slabs of varying thickness produces the octahedral frameworks of Er_4CrS_7 $Er_6Cr_2S_{11}$, $Er_8Cr_3S_{15}$ and Er_2CrS_4: the n = 1, 2, 3 and ∞ members of a series whose anionic framework is described by the general formula $[M_{2n+1}S_{4n+3}]^{x-}$. The presence of long range magnetic order may be related to the degree of Er/Cr ordering.

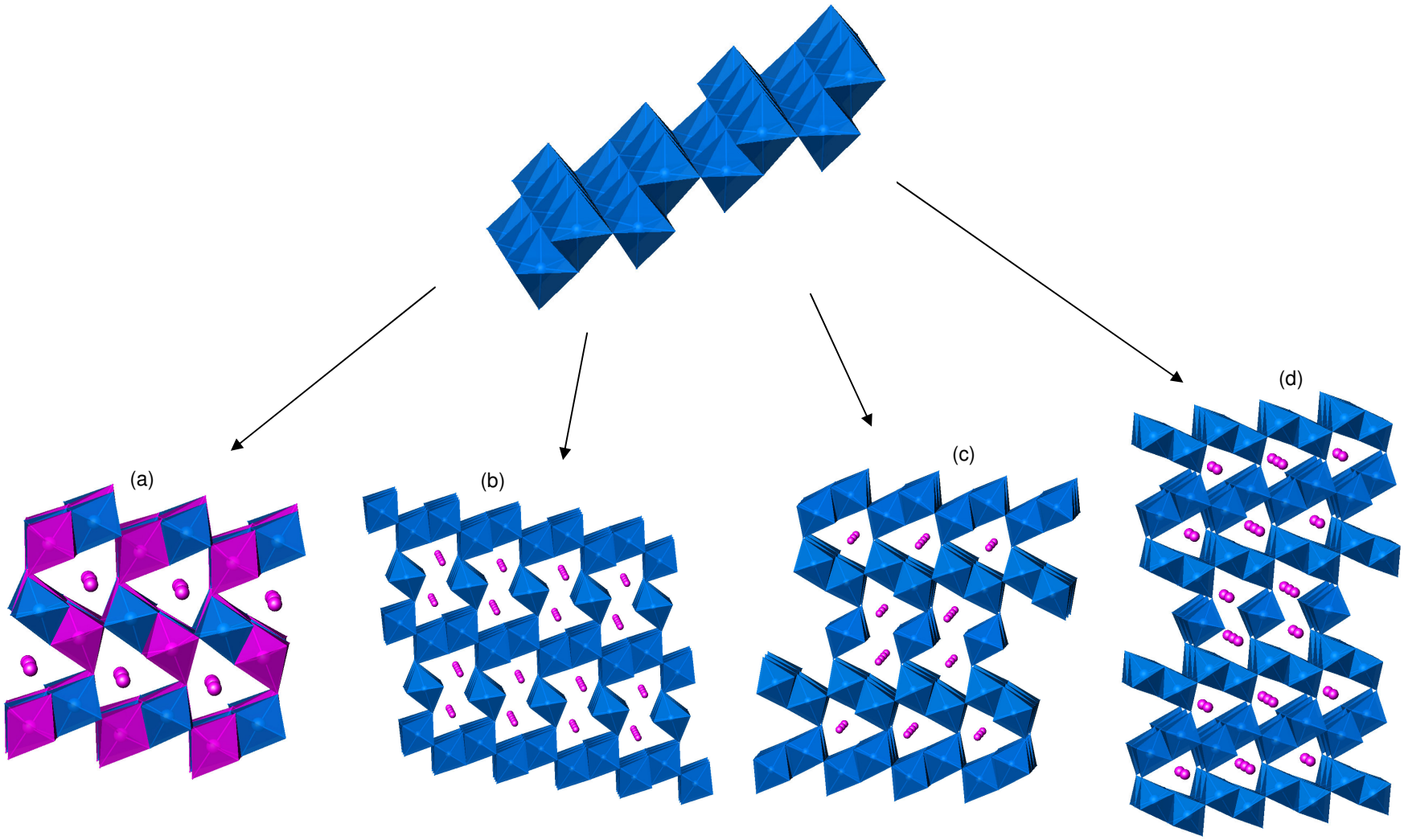

Figure 112: Series of $[M_{2n+1}S_{4n+3}]^{x-}$ materials: (a) Er_2CrS_4, (b) Er_4CrS_7 (c) $Er_6Cr_2S_{11}$ and (d) $Er_8Cr_3S_{15}$.

This study suggests that further work in a number of areas would be rewarding:

1. Single crystals of $BiZn_2VO_6$ and $Pb_2BiV_3O_{11}$ could be grown from powder sample melting and examined using single crystal X-ray diffraction in aim to solve their structures.

2. The new solid solution series $Ga_{1-x}Ge_xV_4S_8$ should be studied at low temperatures using high resolution powder neutron diffraction. Experiments on HRPD at ISIS would be useful for more accurate determination of the structure of these materials. Long term objectives might include investigation of new *B*-site substituted defect thiospinels, for example $Ge(Mo, V)_4S_8$ systems.

3. Magnetic measurements and neutron diffraction studies of the new $Er_8Cr_3S_{15}$ sample should be performed as well as an attempt to solve a magnetic structure of Er_2CrS_4.

4. Synthesis of new members of the $[M_{2n+1}S_{4n+3}]^{x-}$ family of materials should be attempted. This part of work could be extended further for other rare earth elements and transition metals.

References

[1] T. Jiang, A. Lough, G. A. Ozin, R. L. Bedard and R. Broach, J. Mater. Chem., **8**, (3), 721-732 (1998).

[2] N. Imanaka, T. Masui and M. Itaya, Chem. Lett., **32**, (4), 400-401 (2003).

[3] P. Šulcová and M. Trojan, Dyes and Pigments, **36**, (4), 287-293 (1998).

[4] H. Kronmüller and S. Parkin, Editors-in-Chief, *Handbook of Magnetism and Advanced Magnetic Materials*, John Wiley & Sons: (2007).

[5] J. Rouxel, *Physics and Chemistry of Low-Dimensional Inorganic Conductors*, Vol. Series B: Physics vol. 354, (1996).

[6] C. I. Pearce, R. A. D. Pattrick and D. J. Vaughan, Rev. Mineral. Geochem., **61**, 127-180 (2006).

[7] A. West, *Basic Solid State Chemistry*, 2nd ed.; Wiley: NewYork, (1999).

[8] P. P. Edwards and C. N. R. Rao, *Metal-Insulator Transitions, Revisited*. Edited by; Taylor and Francis: London, (1995).

[9] A. Sommerfeld, Zeits. f. Physik, **47**, 1-32 (1928).

[10] P. A. Cox, *The Electronic Structure and Chemistry of Solids*, Oxford University Press: Oxford, (1987).

[11] S. M. Sze, *Physics of Semiconductor Devices*, 2nd ed.; John Wiley & Sons: NewYork, (1981).

[12] B. G. Streetman and S. Banerjee, *Solid State Electronic Devices*, Prentice Hall: New Jersey, (2000).

[13] N. F. Mott, *Metal-Insulator Transitions*, Taylor&Francis: London, (1990).

[14] P. W. Anderson, Phys. Rev., **109**, 1492-1505 (1958).

[15] E. Abrahams and G. Kotliar, Science, **274**, 1853-1854 (1996).

[16] F. J. Morin, Phys. Rev. Lett., **3**, 34-36 (1959).

[17] T. Furubayashi, T. Matsumoto, T. Hagino and S. Nagata, J. Phys. Soc. Japan, **63**, 3333-3339 (1994).

[18] L. S. Martinson, J. W. Schweitzer and N. C. Baenziger, Phys. Rev. Lett., **71**, 125-128 (1993).

[19] H. K. Onnes, *Commun. Phys. Lab. Univ. Leiden*; No 120b, 1911.

[20] J. G. Bednorz and K. A. Müller, Z. Physik, **B64**, (2), 189-193 (1986).

[21] M. Wu, J. Ashburn, C. Torng, P. Hor, R. Meng, L. Gao, Z. Huang, Y. Wang and C. Chu, Phys. Rev. Lett., **58**, (9), 908-910 (1987).

[22] S. N. Putilin, E. V. Antipov, O. Chmaissern and M. Marezio, Nature, **362**, 226-228 (1993).

[23] A. Schilling, M. Cantoni, J. D. Guo and H. R. Ott, Nature, **363**, 56-58 (1993).

[24] L. F. Mattheiss and D. R. Hamann, Phys. Rev. B, **26**, 2686-2689 (1982).

[25] O. Fischer, Applied Physics B, **16**, (1), 1-28 (1978).

[26] M. T. F. Telling and K. H. Andersen, Phys. Chem. Chem. Phys., **7**, 1255-1261 (2005).

[27] O. Peña, F. Le Berre, J. Padiou, T. Marchand, R. Horyn and A. Wojakowski, J. Solid State Chem., **136**, 160-166 (1998).

[28] R. S. Roth and J. L. Waring, The American Mineralogist, **48**, 1348-1356 (1963).

[29] R. Pocha, D. Johrendt, B. Ni and M. M. Abd-Elmeguid, J. Am. Chem. Soc., **127**, 8732-8740 (2005).

[30] A. F. Orchard, *Magnetochemistry*, Oxford University Press Inc.: New York, (2003).

[31] G. Toulouse, Commun. Phys. (London), **2**, 115-119 (1977).

[32] J. E. Greedan, J. Mater. Chem., **11**, 37-53 (2001).

[33] J. Dumas and C. Schlenker, Phys. Rev., **B20**, 3913-3925 (1979).

[34] D. Stauffer and A. Aharony, *Introduction to Percolation Theory*, Taylor and Francis: London, (1994).

[35] J. Adler, Y. Meir, A. Aharony and A. B. Harris, Phys. Rev. B, **41**, (13), 9183-9206 (1990).

[36] R. M. Ziff, Phys. Rev. E, **73**, 016134 (6pages) (2006).

[37] S. C. van der Marck, Phys. Rev. E, **55**, (2), 1514-1517 (1997).

[38] R. Parvianinen, J. Phys. A: Math. Theor., **40**, 9253-9258 (2007).

[39] H. G. Ballesteros, L. A. Fernández, V. Martín-Mayor, A. Munoz Sudupe, G. Parisi and J. J. Ruiz-Lorenzo, J. Phys. A: Math. Gen., **32**, 1-13 (1999).

[40] P. N. Suding and R. M. Ziff, Phys. Rev. E, **60**, (1), 275-283 (1999).

[41] C. D. Lorenz and R. M. Ziff, J. Phys. A: Math. Gen., **31**, 8147-8157 (1998).

[42] M. Drache, P. Roussel and J. P. Wignacourt, Chem. Rev., **107**, 80-96 (2007).

[43] P. Šulcová and M. Trojan, J. Therm. Anal. Cal., **60**, 209-213 (2000).

[44] L. M. Levinson and H. Philipp, R, Am. Ceram. Soc. bull., **65**, 639-646 (1986).

[45] J. K. Tsai and T. B. Wu, J. Appl. Phys., **76**, (8), 4817-4822 (1994).

[46] P. Rybarczyk, H. Berndt, J. Radnik, M. M. Pohl, O. Buyevskaya, M. Bearns and A. Brückner, Journal of Catalysis, **202**, 45-58 (2001).

[47] H. H. Kung and M. C. Kung, Appl. Catal. A, **157**, 105-116 (1997).

[48] P. Šulcová and M. Trojan, J. Therm. Anal. Cal., **83**, (3), 557-559 (2006).

[49] M. A. de la Rubia, J. F. Fernandez and A. C. Caballero, J. Europ. Ceram. Soc., **25**,

2215-2217 (2005).

[50] J. C. Boivin and G. Mairesse, Chem. Mater., **10**, 2870-2888 (1998).

[51] F. Abraham, M. F. Debreuille-Gresse, G. Mariesse and G. Nowogrocki, Solid State Ionics, **28-30**, 529-536 (1988).

[52] T. Takahashi and H. Iwahara, Mater. Res. Bull, **13**, 1447-1453 (1978).

[53] A. W. Sleight, Science, **208**, 895-900 (1980).

[54] I. Radosavljevic, J. S. O. Evans and A. W. Sleight, J. Solid State Chem., **137**, 143-147 (1998).

[55] X. Xun, S. Uma and A. W. Sleight, J. Solid State Chem., **167**, 245-248 (2002).

[56] I. Radosavljevic, J. S. O. Evans and A. W. Sleight, J. Alloys Comp., **284**, 99-103 (1999).

[57] J. Huang, Q. Gu and A. W. Sleight, J. Solid State Chem., **105**, 599-606 (1993).

[58] E. Ketatni, B. Mernari, F. Abraham and O. Mentre, J. Solid State Chem., **153**, 48-54 (2000).

[59] J. Huang and A. W. Sleight, J. Solid State Chem., **100**, 170-178 (1992).

[60] I. Radosavljevic, J. S. O. Evans and A. W. Sleight, J. Solid State Chem., **141**, 149-154 (1998).

[61] I. Radosavljevic and A. W. Sleight, J. Solid State Chem., **149**, 143-148 (2000).

[62] A. Mizrahi, J. P. Wignacourt, M. Drache and P. Conflant, J. Mater. Chem., **5**, (6), 901-904 (1995).

[63] F. Abraham, E. Ketatni, G. Mariesse and B. Mernari, Eur. J. Solid State Inorg. Chem., **31**, 313-321 (1994).

[64] I. Radosavljevic, J. A. K. Howard, J. S. O. Withers and J. S. O. Evans, Chem. Commun., **19**, 1984-1985 (2001).

[65] A. Mizrahi, J. P. Wignacourt and H. Steinfink, J. Solid State Chem., **133**, 516-521 (1997).

[66] I. Radosavljevic Evans, J. S. O. Evans and J. A. K. Howard, J. Mater. Chem., **12**, (9), 2648-2652 (2002).

[67] I. Radosavljevic, J. A. K. Howard and A. Sleight, Int. J. Inorg. Mater., **2**, 543-550 (2000).

[68] N. P. Smolyaninov and I. N. Belyaev, J. Inorg. Chem., **8**, 632-634 (1963).

[69] A. A. Fotiev, B. V. Slobodin and M. Y. Khodos, *Vanadaty, sostav, sintez, struktura svoistva*, Izd. Nauka: Moscow (1988).

[70] L. H. Brixner and C. M. Foris, Mater. Res. Bull., **9**, 273-276 (1974).

[71] P. Roussel, S. Giraud, E. Suard, J. P. Wignacourt and H. Steinfink, Solid State

Sciences, **4**, 1143-1152 (2002).

[72] Y. C. Jie and W. Eysel, Powder Diffr., **10**, (2), 76-80 (1995).

[73] S. Giraud, M. Drache, P. Conflant, J. P. Wignacourt and H. Steinfink, J. Solid State Chem., **154**, 435-443 (2000).

[74] M. Kurzawa, I. Rychlowska-Himmel, A. Blonska-Tabero, M. Bosacka and G. Dabrowska, Solid State Phenom., **90-91**, 347-352 (2003).

[75] M. Kurzawa, I. Rychlowska-Himmel, M. Bosacka and G. Dabrowska, Solid State Phenom., **90-91**, 353-358 (2003).

[76] M. Bosacka and M. Kurzawa In *Book of abstracts*, Solid State Chemistry, Prague, Czech Republic, 2004, p 183.

[77] X. Wang, D. A. V. Griend, C. L. Stern and K. R. Poeppelmeier, J. Alloys Comp., **298**, 119-124 (2000).

[78] M. A. Lafontaine, J. M. Greneche, Y. Laligant and G. Ferey, J. Solid State Chem., **108**, 1-10 (1994).

[79] M. Kurzawa and A. Blonska-Tabero, Mater. Res. Bull., **37**, 849-858 (2002).

[80] J. D. Pless, B. B. Bardin, H. S. Kim, D. Ko, M. T. Smith, R. R. Hammond, P. C. Stair and K. R. Poeppelmeier, J. Catal., **223**, 419-431 (2004).

[81] J. Huang and A. Sleight, J. Solid State Chem., **97**, 228-232 (1992).

[82] J. Huang, Q. Gu and A. Sleight, J. Solid State Chem., **110**, 226-233 (1994).

[83] S. Giraud, A. Mizrahi, M. Drache, P. Conflant, J. P. Wignacourt and H. Steinfink, Solid State Science, **3**, 593-602 (2001).

[84] O. Labidi, J. P. Wignacourt, P. Roussel, M. Drache, P. Conflant and H. Steinfink, Solid State Science, **6**, 783-790 (2004).

[85] I. R. Evans, J. S. O. Evans and J. A. K. Howard, J. Mater. Chem., **12**, 2648-2652 (2002).

[86] P. L. Wang and D. Y. Li, Acta Phys., **34**, 235-240 (1985).

[87] S. Giraud, J. Wignacourt, M. Drache, G. Nowogrocki and H. Steinfink, J. Solid State Chem., **142**, 80-88 (1999).

[88] D. J. Vaughan, *Sulfide Minerology and Geochemistry*, J. J. Rosso Edited; University of Manchester, United Kingdom: Vol. 61, (2006).

[89] E. Makovicky, Reviews in Mineralogy and Geochemistry, **61**, 7-125 (2006).

[90] F. Jellinek, Acta Cryst., **10**, 620-628 (1957).

[91] A. Wold and K. Dwight, *Solid State Chemistry:Synthesis, Structure and Properties of Selected Oxides and Sulfides*, Chapman and Hall: New York, (1993).

[92] R. P. Stapele, *Ferromagnetic Materials*, Netherlands, Vol. 3, (1982).

[93] A. M. Umarji, C. S. Sunandana and G. V. S. Rao, Mat. Res. Bull., **14**, 1025-1031 (1979).

[94] P. Vaqueiro, A. V. Powell, S. Hull and D. A. Keen, Phys. Rev. B, **63**, (6), 064106-1-064106-6 (2001).

[95] D. J. Vaughan and J. R. Craig, *Mineral Chemistry of Metal Sulphides*, Cambridge University Press: Cambridge, (1978).

[96] J. Dereń, J. Haber and R. Pampuch, *Chemia ciała stałego*, PWN: Warszawa, (1975).

[97] A. Nakatsura, Y. Ikeda, N. Nakayama and T. Mizota, Acta Cryst., **E62**, i109-i111 (2006).

[98] B. Antic, D. Rodic, A. S. Nikolic, Z. Kacarevic-Popovic and L. Karanovic, J. Alloys Comp., **336**, (1-2), 286-291 (2002).

[99] E. J. W. Verwey, Nature, **144**, 327-328 (1939).

[100] J. M. Tarascon, E. Wang, F. K. Shokoohi, W. R. McKinnon and S. Colson, J. Electrochem. Soc., **138**, 2859-2864 (1991).

[101] D. C. Johnston, J. Low Temp. Phys., **25**, (1-2), 145-175 (1976).

[102] J. Hemberger, P. Lunkenheimer, R. Fichtl, H. A. Krug von Nidda, V. Tsurkan and A. Loidl, Nature, **434**, 364-367 (2005).

[103] V. Fritsch, J. Hemberger, N. Büttgen, E. W. Scheidt, H. A. Krug von nidda, A. Loidl and V. Tsurkan, Phys. Rev. Lett., **92**, 116401-1 -116401-4 (2004).

[104] R. Fichtl, V. Tsurkan, P. Lunkenheimer, J. Hemberger, V. Fritsch and H. A. Krug von Nidda, Phys. Rev. Lett., **94**, 027601-1 - 027601-4 (2005).

[105] T. Hagino, Y. Seki, N. Wada, S. Tsuji, T. Shirane, K. I. Kumagai and S. Nagata, Phys. Rev. B, **51**, 12673-12684 (1995).

[106] A. P. Ramirez, R. J. Cava and J. Krajewski, Nature, (386), 156-159 (1997).

[107] P. K. Baltzer, P. J. Wojtowicz, M. Robbins and E. Lopatin, Phys. Rev., **151**, 367-377 (1966).

[108] V. Shamrai, H. Mädge, T. Mydlarz and G. Leitus, J. Low Temp. Phys., **49**, (1-2), 123-133 (1982).

[109] P. W. Anderson, Phys. Rev., **102**, 1008-1013 (1956).

[110] G. Blasse and J. F. Fast, Philips Res. Rept., **18**, 393-399 (1963).

[111] K. Siratori, J. Phys. Soc. Japan, **30**, 709-719 (1971).

[112] N. Menyuk, K. Dwidgt and A. Wold, J. Appl. Phys., **36**, 1688-1700 (1965).

[113] E. F. Bertaut, V. Van Qui, R. Pauthenet and A. Murasik, J. Phys. France, **25**, 516-521 (1964).

[114] T. Motida and K. Miyahara, J. Phys. Soc. Japan, **28**, 1188-1196 (1970).

[115] T. Akino and K. Motizuki, J. Phys. Soc. Japan, **31**, 691-705 (1971).

[116] V. F. Shamrai and G. M. Leitus, Izv. Akad. Nauk. SSSR Met., **1**, 162-167 (1983).

[117] O. Peña, H. Ben Yaich, M. Potel and M. Sergent, Physica B, **163**, 435-437 (1990).

[118] A. Kjekshus and W. B. Pearson, Prog. Solid State Chem, **1**, 83-174 (1964).

[119] P. Vaqueiro and A. V. Powell, Chem. Mater., **12**, 2705-2714 (2000).

[120] J. M. Vandenberg and D. Brasen, J. Solid State Chem., **14**, 203-208 (1975).

[121] C. Perrin, R. Chevrel and M. Sergent, C.R. Acad. Sci. Paris, **280C**, 949-951 (1975).

[122] D. Johrendt, Z. Anorg. Allg. Chem., **624**, 952-958 (1998).

[123] R. Pocha, D. Johrendt and R. Pöttigen, Chem. Mater., **12**, 2882-2887 (2000).

[124] H. Barz, Mater. Res. Bull., **8**, 983-988 (1973).

[125] H. Ben Yaich, M. Jegaden, M. Potel, M. Sergent, A. K. Rastogi and R. Tournier, J. Less Common Met., **102**, (1), 9-22 (1984).

[126] H. Ben Yaich, J. C. Jegaden, M. Potel, R. Chevrel, M. Sergent, A. Berton, J. Chaussy, A. K. Rastogi and R. Tournier, J. Solid State Chem., **51**, 212-217 (1984).

[127] D. Brasen, J. M. Vandenberg, M. Robbins, R. H. Willens, W. A. Reed, R. C. Sherwood and X. J. Pinder, J. Solid State Chem., **13**, 298-303 (1975).

[128] I. Nakatani, J. Solid State Chem., **35**, 50-58 (1980).

[129] V. F. Shamrai and G. M. Leitus, Sov. Phys. Solid State **29**, 1312-1315 (1987).

[130] A. K. Rastogi, A. Berton, J. Chaussy, R. Tournier, M. Potel, R. Chevrel and M. Sergent, J. Low Temp. Phys., **52**, 539-557 (1983).

[131] Y. Sahoo and A. K. Rastogi, J. Phys. Chem Solids **57**, 467-474 (1996).

[132] Y. Sahoo and A. K. Rastogi, Physica B, **215**, 233-242 (1995).

[133] A. V. Powell, A. McDowall, I. Szkoda, K. S. Knight, B. J. Kennedy and T. Vogt, Chem. Mater., **19**, 5035-5044 (2007).

[134] D. Bichler and D. Johrendt, Chem. Mater., **19**, 4316-4321 (2007).

[135] C. Perrin, R. Chevrel and M. Sergent, J. Solid State Chem. , **19**, 305-308 (1976).

[136] M. Paranthaman, G. Aravamudan and G. V. Subba Rao, Mat. Res. Bull., **24**, 931-938 (1989).

[137] C. Vaju, J. Martial, E. Janod, B. Corraze, V. Fernandez and L. Cario, Chem. Mater., **20**, 2382-2387 (2008).

[138] A. Le Beuze, M. C. Zerrouki, H. Loirat and R. Lissillour, J. Alloys Comp., **190**, 1-11 (1992).

[139] A. Le Beuze, H. Loirat, M. C. Zerrouki and R. Lissillour, J. Solid State Chem.,

120, 80-89 (1995).

[140] N. Shanthi and D. D. Sarma, J. Solid State Chem., **148**, 143-149 (1999).

[141] M. Francois, W. Lengauer, K. Yvon, H. B. Yaich-Aerrache, P. Gougen, M. Potel and M. Sergent, Z. Krist. , **196**, 111-120 (1991).

[142] M. Francois, O. V. Alexandrow, K. Yvon, H. Ben Yaich-Aerrache, P. Gougeon, M. Potel and M. Sergent, Z. Krist., **200**, 47-55 (1992).

[143] H. Müller, W. Kockelmann and D. Johrendt, Chem. Mater., **18**, 2174-2180 (2006).

[144] Y. Sahoo and A. K. Rastogi, J. Phys.: Condens. Matter, **5**, 5953-5962 (1993).

[145] A. K. Rastogi and A. Niazi, Physica B, **223&224** 588-590 (1996).

[146] A. D. McDowall. Ph.D. Thesis, Heriot-Watt University, 2003.

[147] H. Chudo, C. Michioka, H. Nakamura and K. Yoshimura, Physica B, **378-380**, 1150-1151 (2006).

[148] D. Bichler, V. Zinth, D. Johrendt, O. Heyer, M. K. Forthaus, T. Lorenz and M. M. Abd-Elmeguid, Phys. Rev. B, **77**, 212102 (4 pages) (2008).

[149] R. Pocha. Ph.D. Thesis, Ludwig-Maximilians-Universität München, 2004.

[150] K. Mitchell and J. A. Ibers, Chem. Rev., **102**, 1929-1952 (2002).

[151] M. Patrie and R. Chevalier, C.R. Acad. Sc. Paris, Series C, **263**, 1061-1064 (1966).

[152] A. Tomas, R. Chevalier, P. Laurelle and B. Bachet, Acta Cryst. B, **32**, 3287-3289 (1976).

[153] B. W. Eichhorn, Progr. Inorg. Chem., **42**, 139-237 (1994).

[154] A. Tomas, M. Guittard, R. Chevalier and J. Flahaut, C.R. Acad. Sci. Paris, **282C**, 587-589 (1976).

[155] K. Tezuka, Y. J. Shan, H. Imoto and K. Ohoyama, J. Phys. Chem Solids, **68**, 2133-2137 (2007).

[156] J. B. Litteer, S. A. Sirchio, J. C. Fettinger, V. Smolyaninova, B. W. Eichhorn and R. L. Greene, Chem. Mater., **11**, 1179-1182 (1999).

[157] A. M. Mills, D. Bräunling and M. Ruck, Acta Cryst. C, **62**, i70-i72 (2006).

[158] P. P. Lemoine, A. Tomas and M. Guittard, Acta Cryst. C, **48**, 774-776 (1992).

[159] H. H. Heikens, R. S. Kuindersma, C. F. Van Bruggen and C. Haas, Phys. Stat. Sol., **46**, 687-695 (1978).

[160] C. Adolphe, M. Guittard and P. Laruelle, C. R. Acad. Sc. Paris, **258**, 4773-4775 (1964).

[161] C. Adolphe, Ann. Chim., **10**, 271-297 (1965).

[162] C. Adolphe and P. Laruelle, Bull. Soc. Fr. Mineral. Cristallogr., **91**, 219-232 (1968).
[163] G. Collin, F. Rouyer and J. Loriers, C.R. Acad. Sc. Paris, Series C, **266**, 689-691 (1968).
[164] A. M. Mills and M. Ruck, Acta Cryst. C, **60**, i71-i72 (2004).
[165] O. M. Aliev, T. K. Kurbanov, T. V. Imanova and G. G. Khasaev, Neorganicheskie Materialy, **22**, (1), 19-21 (1986).
[166] O. M. Aliev, G. G. Khasaev and T. K. Kurbanov, Bull. Soc. Chim. Fr., **1**, 26-28 (1986).
[167] A. B. Agaev, V. O. Aliev and O. M. Aliev, Russian Journal of Inorganic Chemistry, **41**, (2), 306-312 (1996).
[168] J. Float, P. Laruelle and R. Holitrsut, Zhu. Vses. Khim. O-va Im. D. I. Mendeleeva, **26**, (6), 664-672 (1981).
[169] A. Tomas, M. Robert, C. Adolphe and M. Guittard, Mat. Res. Bull., **19**, 1643-1646 (1984).
[170] A. R. Landa-Canovas and L. C. Otero-Diaz, Aust. J. Chem., **45**, 1473-1487 (1992).
[171] E. Urones-Garrote, A. Gómez-Herrero, A. R. Landa-Cánovas and L. C. Otero-Díaz, Eur. J. Inorg. Chem., (7), 1436-1443 (2006).
[172] G. Collin and P. Laurelle, Acta Cryst. B, **30**, 1134-1139 (1974).
[173] M. Bakker and B. G. Hyde, Philos. Mag. A, **38**, (6), 615-628 (1978).
[174] A. V. Einullaev, N. V. Mamedov, R. Z. Sadykhov and A. B. Agaev, Inorg. Mater., **36**, (1), 10-11 (2000).
[175] S. M. Chaquor, A. Tomas, P. Lemoine, M. Palazzi and M. Guittard, Acta Cryst. C, **50**, 1655-1657 (1994).
[176] A. Tomas, J. Rigoult, M. Guittard and P. Laruelle, Acta Cryst. B, **36**, 1987-1989 (1980).
[177] P. G. Rustamov, T. K. Kurbanov, O. M. Aliev and I. P. Aliev, Inorg. Mater., **20**, 1664-1666 (1984).
[178] T. Takahashi, K. Ametani and O. Yamada, J. Crystal Growth, **24/25**, 151-153 (1974).
[179] O. Tougait and J. A. Ibers, Inorg. Mater., **39**, 1790-1794 (2000).
[180] G. G. Guseinov, V. A. Gasymov, I. P. Aliev and K. S. Mamedov, Inorg. Mater., **17**, (5), 556-558 (1981).
[181] P. N. Rodier and V. Tien, Acta Cryst., Sect. B: Struct. Crystallogr. Cryst. Chem.,

32, 2705-2707 (1976).

[182] P. Hagenmuller, *Preparative methods in solid state chemistry* Academic Press: New York, London, (1972).

[183] H. Schäfer, *Chemical transport reactions*, Academic Press: New York, (1964).

[184] R. Nitsche, H. U. Bölsterli and M. Lichtensteiger, J. Phys. Chem. Solids, **21**, 199-205 (1961).

[185] D. A. Fletcher, R. F. McMeeking and D. Parkin, J. Chem. Inf. Comput. Sci., (The United Kingdom Chemical Database Service), **36**, 746-749 (1996).

[186] *PDF-2 Database sets, International Centre for Diffraction Data Dataware Technologies*, PA, USA, 2007.

[187] H. M. Rietveld, Acta Cryst., **22**, 151-152 (1967).

[188] H. M. Rietveld, J. Appl. Cryst., **2**, 65-71 (1969).

[189] A. C. Larson and R. B. von Dreele, *General Structural Analysis System*; LAUR 85-748; Los Alamos Laboratory: Los Alamos, NM 87545, 1994.

[190] B. H. Toby, J. Appl. Cryst., **34**, 210-213 (2001).

[191] *Bruker X8 APEX2*, Version 1.0-8; Bruker AXS Inc. Madison: WI USA, 2003.

[192] *Apex-2 Software*, Bruker-AXS: Madison, Wisconsin, USA, 2004.

[193] G. M. Sheldrick *SADABS*, University of Göttingen, Germany: 1996.

[194] W. Clegg, *Crystal Structure Determination*, Oxford University Press Inc.: New York, (1998).

[195] A. Altomare, G. Cascarano, C. Giacovazzo, A. Guangliardi, M. Burla, G. Polidori and M. Camalli, J. Appl. Cryst. Sect. A, **27**, 435-436 (1994).

[196] D. J. Watkin, C. K. Prout, J. R. Carruthers and P. W. Betteridge *CRYSTALS, ISSUE 10*, Chemical Crystallography Laboratory, University of Oxford, UK: 1996.

[197] J. R. Carruthers and D. J. Watkin, Acta Cryst. A, **35**, 698-699 (1979).

[198] D. M. Rowe, *CRC Handbook of Thermoelectrics*, CRC press: Boca Raton, FL, (1995).

[199] S. A. Kasap, *Principles of Electrical Engineering Materials and Devices*, McGraw-Hill Press: p 274, (1997).

[200] C. Wood, Rep. Prog. Phys., **51**, 459-539 (1988).

[201] R. R. Heikes and R. W. Ure, *Thermoelectricity: Science and Engineering*, Interscience Publishers, Inc.: New York, (1961).

[202] The Yellow Book 2005, *Guide to Neutron Research Facilities, ILL.*

[203] A. Hewat, *Super-D2B, EPDIC-IX*; Prague, 2004.

[204] *ISIS Facility Annual Report*; 2004.

[205] http://www.isis.rl.ac.uk/, ISIS Spallation Neutron & Muon Source.

[206] D. Engberg, *Rutherford Appleton Laboratory Technical Report*; RAL-TR-1999-068; 1999.

[207] W. I. F. David, M. W. Johnson, K. J. Knowles, C. M. Moreton-Smith, G. D. Crisbie, E. P. Campbell, S. P. Graham and J. S. Lyall, RAL-86-102; Rutherford Appleton Laboratory: 1986.

[208] R. I. Smith and S. Hull, *User Guide for the Polaris Powder Diffractometer at ISIS*; Rutherford Appleton Laboratory Report, RAL-TR-97-038: 1997.

[209] L. B. McCusker, R. B. Von Dreele, D. E. Cox, D. Louër and P. Scardi, J. Appl. Cryst., **32**, 36-50 (1999).

[210] R. A. Young, *The Rietveld Method*. Edited by; R. A. Young, Oxford University Press: (1993).

[211] E. Jansen, W. Schäfer and G. Will, J. Appl. Cryst., **27**, 492-496 (1994).

[212] C. Changkang, Prog. Crystal Growth and Charact, **36**, 1-97 (1998).

[213] J. McMurdie, Powder Diff. J., **1**, 40-44 (1986).

[214] J. D. Bierlein and A. W. Sleight, Solid State Communications, **16**, 69-70 (1975).

[215] A. K. Bhattacharya, K. K. Mallick and A. Hartridge, Mater. Lett., **30**, 7-13 (1997).

[216] J. B. Liu, H. Wang, S. Wang and H. Yan, Mater. Sci. Eng., **B 104**, 36-36 (2003).

[217] S. Uma, R. Bliesner and A. W. Sleight, Solid State Sci., **4**, 329-333 (2002).

[218] D. Taupin, J. Appl. Cryst., **6**, 380-385 (1973).

[219] Z. Kluz and I. Waclawska, Rocz. Chem., **49**, 839-849 (1975).

[220] M. Bosacka, M. Kurzawa, I. Rychlowska-Himmel and I. Szkoda, Thermochimica Acta, **428**, 51-55 (2005).

[221] A. A. Fotiev, V. K. Trunov and Zhuravlev, *Vanadaty Dvukhvalentnykh Metallov*, Izd. Nauka: Moscow, (1985).

[222] M. Kurzawa, M. Bosacka and I. Szkoda, Journal of Phase Equilibria and Diffusion, **28**, (5), 412-416 (2007).

[223] *Powder Diffraction File, International Centre for Diffraction Data, Fil Nos.:83-1700, 77-2262, 50-0494, 50-0493*, Swarthmore, USA.

[224] M. Bosacka and I. Szkoda In *Book of abstracts*, 9th European Symposium on Thermal Analysis and Calorimetry, Krakow, Poland, 2006.

[225] B. I. Shklovskii and A. L. Efros, *Electronic Properties of Doped Semiconductors*, Springer-Verlag: Berlin, (1984).

[226] S. A. Carter, J. Yang, T. F. Rosenbaum, J. Spalek and J. M. Honig, Phys. Rev. B, **43**, 607-614 (1991).

[227] Y. K. Kuo, K. M. Sivakumar, J. Y. Lin, C. N. Kuo and C. S. Lue, J. Phys.: Condens. Matter, **19**, 216210 (7pages) (2007).
[228] R. D. Shannon, Acta Cryst., **A32**, (5), 751-767 (1976).
[229] P. G. Rustamov, G. G. Guseinov, T. K. Kurbanov, A. V. Einullaev and O. M. Aliev, Inorg. Mater., **14**, (4), 504-506 (1978).
[230] A. Tomas, J. Rigoult, M. Guittard and P. Laruelle, Acta Cryst. Sect B, **36**, 1987-1989 (1980).
[231] A. Tomas and M. Guittard, Mat. Res. Bull., **15**, 1547-1556 (1980).
[232] N. E. Brese and M. O'Keeffe, Acta Cryst. B, **47**, 192-197 (1991).
[233] H. D. Nguyen, J. Etienne and P. Laruelle, Bull. Soc. Chim. Fr., **1971**, 2433-2437 (1971).
[234] C. M. Fang, A. Meetsma, G. A. Wiegers and G. Boom, J. Alloys Comp., **201**, 255-259 (1993).
[235] K. J. Range, F. Rau and U. Klement, Z. Kristallogr., **208**, 97-98 (1993).
[236] A. L. Speck, J. Appl. Cryst., **36**, 7 (2003).
[237] A. L. Speck, J. Appl. Cryst., **21**, 578 (1988).
[238] A. S. Wills, Physica B, **277-278**, 680-681 (2000).
[239] *International Tables for Crystallography*, T. Hahn Edited; Kluwer: Dordrecht Vol. A, (1992).
[240] *International Tables for Crystallography*, A. J. C. Wilson Edited; Kluwer Academic Publishers: Dordrecht Vol. C, (1995).
[241] W. L. Vos and J. A. Schouten, J. Chem. Phys., **91**, (10), 6302-6305 (1989).
[242] D. Messain, D. Carré and L. P, Acta Cryst. B, **33**, 2540-2542 (1977).
[243] M. Guittard, D. Carré and T. S. Kabré, Mat. Res. Bull., **13**, 279-286 (1978).
[244] J. Goodenough, *Magnetism and the Chemical Bond*, Wiley: New York, (1963).
[245] B. G. Hyde, S. Andersson, M. Bakker, C. M. Plug and M. O'Keeffe, Prog. Solid State Chem., **12**, 273-327 (1979).
[246] G. Ferraris, E. Makovicky and S. Merlino, *Crystallography of modular Materials*, Oxford University Press: (2004).
[247] E. F. Bertaut and P. Blum, Acta Cryst., **9**, 121-126 (1956).
[248] H. G. Giesber, W. T. Pennington and J. W. Kolis, Acta Cryst. C, **57**, 329-330 (2001).
[249] Y. Zhang, H. F. Franzen and B. Harbrecht, J. Less-Common Metals, **166**, 135-140 (1990).
[250] B. Aurivillius, Ark. Kemi., **1**, 499-512 (1949).

[251] B. Aurivillius, Ark. Kemi., **2**, 519-527 (1950).

[252] B. Aurivillius, Ark. Kemi., **1**, 463-480 (1949).

[253] S. N. Ruddlesden and P. Popper, Acta Cryst., **10**, 538-539 (1957).

[254] S. N. Ruddlesden and P. Popper, Acta Cryst., **11**, 54-55 (1958).

[255] M. Dion, M. Ganne and M. Tournoux, Mat. Res. Bull., **16**, (11), 1429-1435 (1981).

[256] A. J. Jacobson, J. W. Johnson and J. T. Lewandowski, Inorg. Chem., **24**, 3727-3729 (1985).